UiT
THE ARCTIC UNIVERSITY OF NORWAY

Faculty of Science and Technology
Department of Geosciences

Cross-disciplinary investigation of gas seepage at Storbanken high and the Olga basin, The northern Barents Sea

Frank Andreas Amdal

Master's thesis in Geology, GEO-3900
May 2019

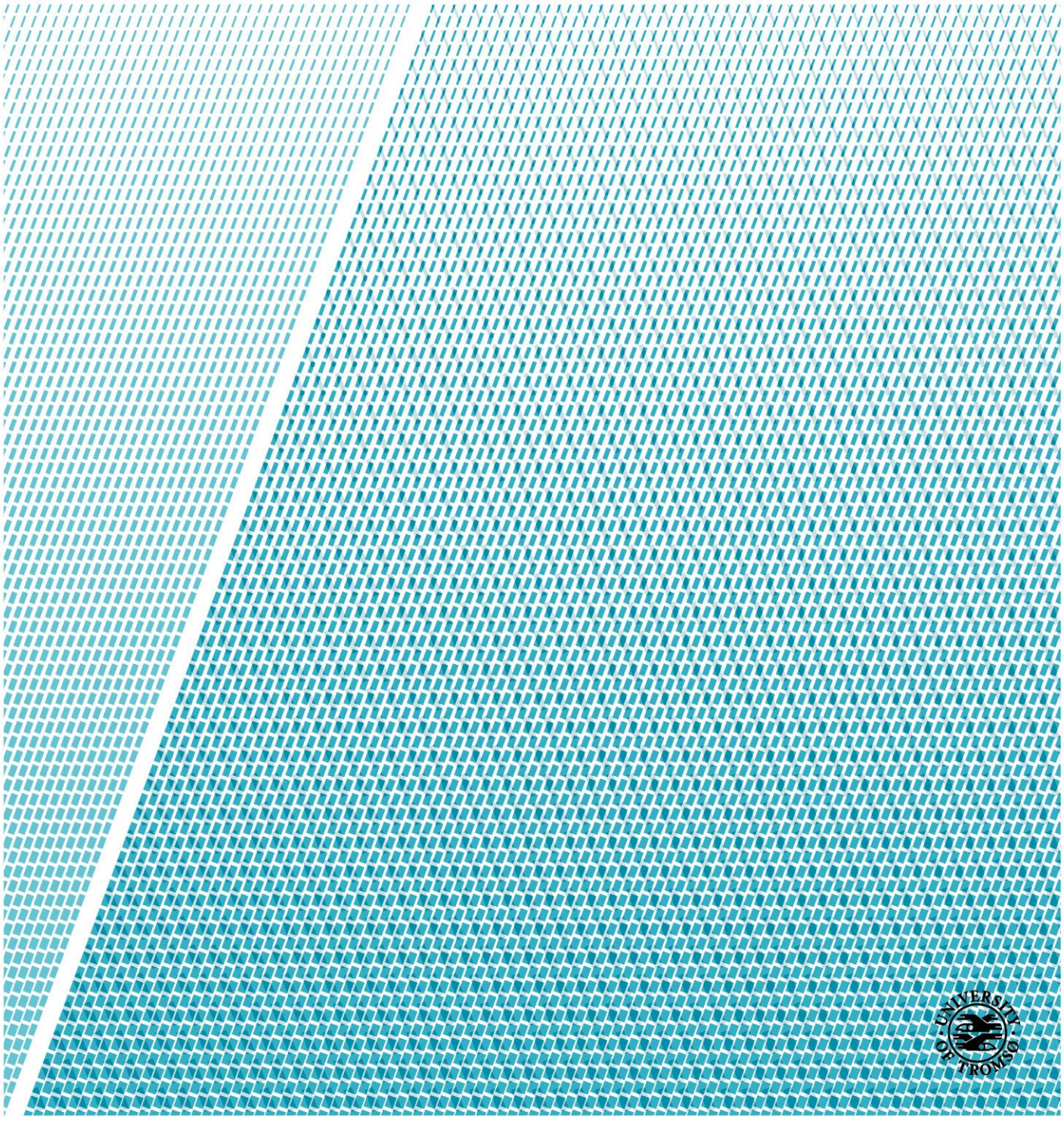

Abstract

The eastern parts of the northern Barents Sea is a little explored sector of the Barents Sea which currently is not open for petroleum activity. This thesis focuses on the processes and mechanisms controlling gas seepage activity in the Olga basin and Storbanken high. 2D seismic and bathymetric data has been correlated with water column acoustic data to identify gas bubbles in the water column and active seeping sites.

A simplified maturation modeling of source rocks suggested that the Botneheia Formation and Billefjorden Group is gas generating. Gas is believed to migrate vertically from these formations through leaking faults (F1, F2, F4, F6 and FZ) and gas chimneys (GC1-GC3 and GCZ). Direct migration from the Botneheia Formation source rock to the reservoir of De Geerdalen/Snadd Formation is also possible in the gas mature areas of the Olga basin and potentially in the deeper parts of the Storbanken high. Post-Early Cretaceous extension, most likely related to the uplift of Storbanken high, is believed to developed NW-SE striking normal faults (FZ). The normal fault zone (FZ) is regarded as a vital migration pathway potentially transporting gas from the Botneheia Formation source rock and distributing gas from the reservoir of the De Geerdalen/Snadd Formation to the Realgrunnen Subgroup. NE-SW striking reverse faults (F5) at the Kong Karls Land platform has suggested compression in Early Cretaceous, an important tectonic event tilting the stratigraphy towards the northwest favoring lateral migration towards the Storbanken high. Gas flares identified above outcropping formations has indicated lateral migration along the cap rocks of the Flatsalen Formation and Agardhfjellet Formation.

Pockmarks were mainly restricted to the intersection of the Olga basin and Storbanken high. The distinct distribution is believed to be governed by the glacigenic sediments which accumulated within a glacial trough carved by the lithologically controlled erosion of the Agardhfjellet Formation. The pockmarks, craters and craters with associated mounds were found to be inactive. Earlier massive gas expulsion related to the retreating ice sheet acting as a seal or the dissociation of sub-glacial gas hydrates after the LGM is therefore suggested as a potential generating mechanism. Modeling of the gas hydrate stability zone has indicated favorable conditions for gas hydrates S_{II} at Storbanken high suggesting the potential for ongoing gas hydrate dissociation as a gas leakage mechanism in the study area.

Acknowledgement

Da var det dags for ett siste tastetrykk på masteren. 5 år har flydd forbi og man har fått æren av å bli kjent med utrolig mange hyggelige folk. Det er mange som fortjener å takkes for at denne masteren går i land, men enkelte fortjener å bli nevnt ved navn.

Først og fremst må jeg takke hovedveileder Andreia Plaza-Faverola (CAGE) og Bi-veileder Rune Mattingsdal (NPD) for å ha gitt meg muligheten til å få skrive slik en spennende oppgave i et relativt lite utforsket området. Jeg setter stor pris og takker for all veiledning jeg har fått gjennom hele masterprossesen, det har vært til stor hjelp. En takk må også rettes til Sunil Vadakkepuliyambatta (CAGE) for lån av GUI til modellering av gasshydratstabilitetssone.

Sigurd Tonstad fortjener også en takk for god hjelp med rettskriving og ellers være tilgjengelig for spørsmål. Kontorkollega Truls Thorsen takkes for all den gode kaffen og hyggelige pauser. Sist men ikke minst fortjener mamma og pappa en stor takk for å være de viktigste støttespilleren mine, masteren hadde ikke komt i havn uten dere.

Frank Andreas Amdal

Tromsø, Mai 2019

Contents

1 Introduction

The northern Barents Sea is a remote and little explored area which currently is not open for petroleum activity. However Norwegian Petroleum Directorate (NPD) has since 2012 worked to get a better understanding of the geology in the area (NPD, 2017). Seismic and water acoustic investigations have indicated a complex geology with large prominent structures and high seepage activity. Understanding the seepage activity in relation to the geology is of high interest as the gas seepage imposes changes to ecosystems, threats to the environment and climate change as well as being a great indicator for hydrocarbon prospects.

1.1 Objective

The main objective of this thesis is to investigate and get a broader understanding of the processes controlling seepage activity in the study area of Storbanken high and Olga basin in the northern Barents Sea (Fig.1.1). The emphasis will therefore be to introduce stratigraphic constraints, interpret geological structures and fluid flow features in the seismic in addition to seabed morphology in bathymetric data and examine how these features correlate to seepage activity. The potential for gas hydrates will also be examined by a 1D modeling of the gas hydrate stability zone.

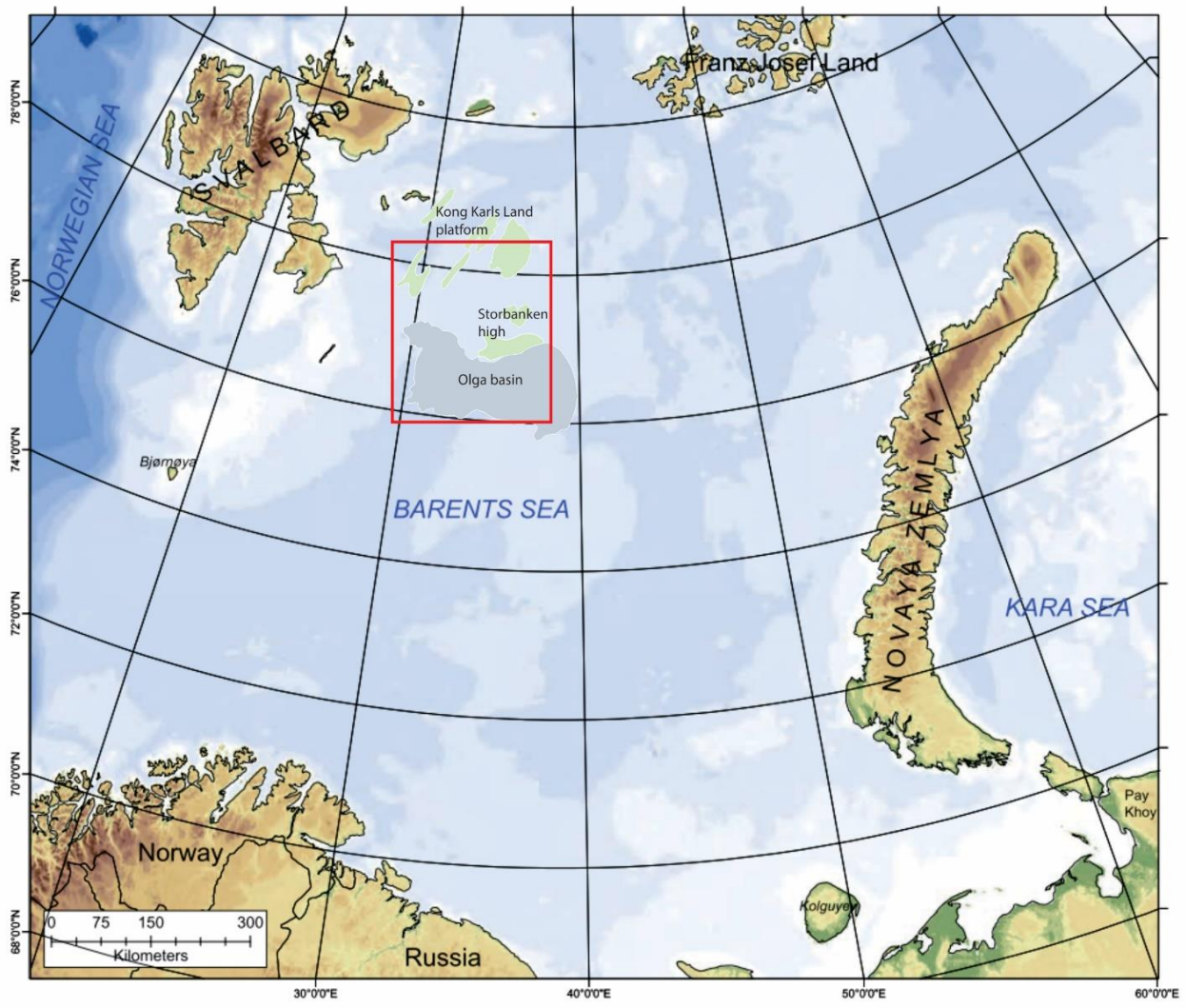

Fig.1.1: The Structural elements within the study area delineated by the red square. Modified from Smelror et al. (2009) and (NPD, 2017).

2 Theoretical Background

This Chapter is dedicated to defining the theoretical framework for this thesis.

2.1 Petroleum system

A petroleum system consists of all the geological elements and processes needed in order to generate petroleum accumulations (Magoon & Dow, 1994). Geological elements such as a source rock, reservoir rock, cap rock, overburden, migration pathway and trap are all essentials for the generation, migration and accumulation of hydrocarbons (Selley & Sonnenberg, 2014). All these elements need to be arranged correctly in time and space in order to have a functioning petroleum system.

The source rock constitutes a high content of organic matter (kerogen) capable of generating hydrocarbons when buried and exposed to the right temperature and pressure conditions (Selley & Sonnenberg, 2014). The reservoir rock is the rock in which hydrocarbons are accumulated. The reservoir rock needs to be permeable (the ability of a rock to let a fluid flow through it) in order for hydrocarbons to migrate freely and porous (pore space within the rock) or fractured in order to store the hydrocarbons (Bjørlykke, 2015). The cap rock is the impermeable barrier formed above and around the reservoir preventing the hydrocarbons from migrating past the reservoir (Selley & Sonnenberg, 2014).

The generation of hydrocarbons in the form of oil or gas is mainly controlled by the kerogen type and temperature in which the source rock is exposed to. There exist three kerogen types capable of generating hydrocarbons: Type I is mainly generating oil and usually deposited in a Lacustrine environment, Type II kerogen is both oil and gas generating and usually deposited in a marine environment while the Type III kerogen mainly generates gas and is deposited in a terrestrial environment (Selley & Sonnenberg, 2014). Oil will primarily be generated at lower temperatures approximately between 60 and 120 ^{o}C while temperatures between 120 and 225 ^{o}C are favorable for gas generation, the temperatures are however approximate and dependent on kerogen type (Selley & Sonnenberg, 2014).

2.2 Faults

Faults are the result of compressional and extensional forces within the earth. The faults form certain alignment of fractures that can result in a relative displacement from centimeters to hundreds of kilometers of two or more rock unit. The faulting and fracturing of rocks are caused by the effective stress acting on a plane and overcoming the internal strength of the rock unit (Twiss & Moores, 2007). Reactivation of older fault planes will require less energy than the initiation of new ones as a developed fracture plane becomes a zone of weakness and new stress will be distributed to the already developed fracture plane and cause frictional sliding (Fossen & Gabrielsen, 2005; Twiss & Moores, 2007). Faults are of great interest as gases and fluids, or a solution of both can migrate through the faults as they act as great migration pathways (Guzzetta & Cinquegrana, 1987).

2.2.1 Fault types

Faults can be classified and characterized based on two important criteria's: angle of the dip along the fault plane and slip which is the net distance and directional movement of the hanging wall relative to the footwall (Fig.2.1) (Twiss & Moores, 2007).

The fault is characterized as a low-angled fault if the angle of the dip is less than 45^{o} or high-angled fault if the dip is higher than 45^{o} (Twiss & Moores, 2007). Based on the slip the faults are further sub-divided into the following three categories according to Twiss & Moores, (2007), dip-slip is where the slip is approximately parallel to the dip, strike-slip where the slip is horizontal and parallel to the strike and oblique-slip where the slip is inclined obliquely on the fault surface. The faults are further divided into normal or reverse and dextral or sinistral (strike-slip) based on the relationship between the hanging wall and footwall (Fig.2.1). Normal faulting is associated with extensional forces and the hanging wall moving down relative to the footwall (Fig.2.1). Reverse faulting is associated with compressional forces and the hanging wall moving up relative to the footwall (Fig.2.1). The strike-slip faulting is associated with horizontal forces commonly along transform plate boundaries, if the block has moved to the right from the observation point it is termed dextral, and sinistral if the block moved to the left (Fig.2.1).

The normal dip-slip faults are commonly high angled faults as they usually have a dip angle of approximately 60°, while the reverse dip-slip faults usually have dip angle greater than 45° (Fossen & Gabrielsen, 2005; Twiss & Moores, 2007). Reverse dip-slip faults can however be termed low-angled usually associated with thrust faults which are characterized by fault surfaces cutting through the stratigraphy placing older rock succession above younger (DiPietro, 2013).

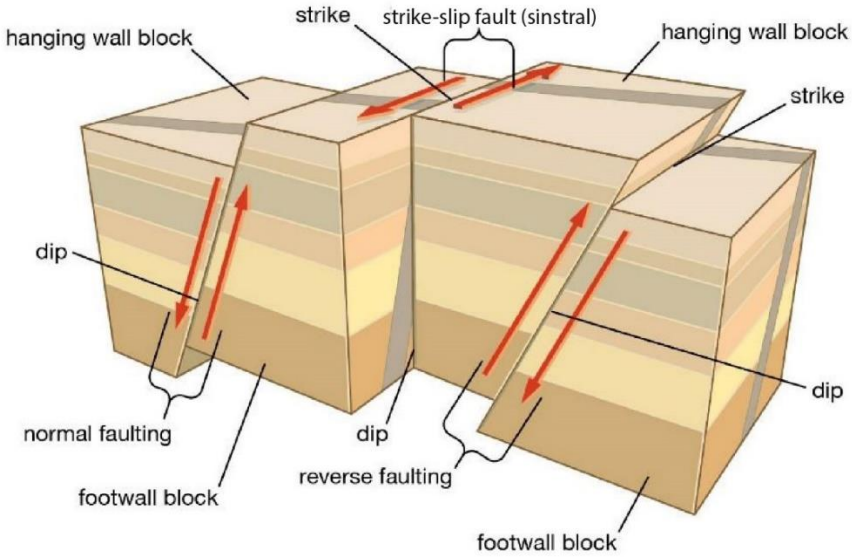

Fig.2.1: Overview of the different fault types, red arrows indicate the direction of stress. Modified from (Kall, 2016).

2.2.2 Gas migration through faults

Faults are known to be one of the main conduits for migration in basins worldwide (Ligtenberg, 2005; Cartwright et al., 2007). Fluids are conducted through local, weak sections and the faults leaking or sealing potential is governed by the faults complexity, intersection (e.g., many faults connected to form a larger fracture network) and the fault plan irregularities (Ligtenberg, 2005; Cartwright et al., 2007). Fault planes can also have sealing potential as fine-grained sediments known as fault gouge or smearing is produced by the active fault planes sliding against each other, this clay-like substance has poor permeability and bad connectivity between pores and fractures (Ligtenberg, 2005; Cartwright et al., 2007). In order to examine if a fault is leaking or sealing there could be seen clear evidence of gas plumes in the water column, pockmarks at the seafloor or carbonate mounds located above faults (Naeth

et al., 2005; Cartwright et al., 2007; Løseth et al., 2009). All these are signs indicating that a fault might be leaking or has leaked at a certain point in time.

2.3 Seismic reflection theory

Reflection seismic is an essential tool for mapping and understanding the subsurface structures and features. An artificial source generates a pulse and sends out seismic waves which propagate through the subsurface and gets reflected by the interfaces between layers (reflectors) (Veeken, 2013). The signal gets recorded by geophones on land or hydrophones in the water commonly termed receivers (Veeken, 2013). Every layer has its own acoustic impedance properties (Z), acoustic impedance is the result of density (p) and wave velocity propagating through the layer (v) (Equation 2.1) (Veeken, 2013). The seismic reflectors represent the contrast in acoustic impedance and are commonly associated with the boundary between two stratigraphic layers (Badley, 1985).

The strength of contrast in acoustic impedance for a reflection between two layers can best be described with the reflection coefficient. The reflection coefficient is a numerical value from -1 to 1 where a positive value indicates an increase in acoustic impedance and a negative value indicates a decrease in acoustic impedance as the energy propagates downward in the subsurface (Equation 2.2) (Badley, 1985). A reflection coefficient with a value of -1 or 1 indicates a high contrast in acoustic impedance between two layers and all seismic energy reflected, whereas a value of 0 would indicate no contrast in acoustic impedance properties between two layers and all energy transmitted.

Equation 2.1 Acoustic impedance

$$Z = \rho V$$

Equation 2.1 The acoustic impedance (Z) is equal to the result of p= density (Kg/m^3) multiplied with V= wave velocity (m/s).

Equation 2.2 Reflection Coefficient

$$R = \frac{Z_2 - Z_1}{Z_2 + Z_1} = \frac{\rho_2 V_2 - \rho_1 V_1}{\rho_2 V_2 + \rho_1 V_1}$$

Equation 2.2. The reflection coefficient (R) is determined by the difference in Acoustic impedance properties (Z). Z_1 and Z_2 indicate the relative position of the two layers, where Z_1 is the uppermost layer, if $Z_2 > Z_1$ the reflection coefficient will be positive and negative if $Z_2 < Z_1$.

2.3.1 Seismic resolution

In order to detect specific features in the subsurface it is important that the seismic resolution is of sufficient quality. The resolution quantifies the level of precision and can be defined as the smallest feature or sedimentary layer which can be detected in the subsurface by a seismic wave and expressed as an acoustic impedance contrast (Brown, 1999; Zhou, 2014). The potential seismic resolution relies on both the acquisition and processing of the seismic. There are three parameters governing the seismic resolution: Wavelength (λ), velocity (v) and frequency (f), the relationship between these parameters can best be described by (Equation 2.3), where the fluctuation in one of these parameters will influence the resolution (Brown, 1999; Kearery et al., 2002). Furthermore the seismic resolution can be divided into vertical and horizontal aspects (Brown, 1999).

Equation 2.3 Relationship between wavelength, velocity and frequency

$$\lambda = \frac{v}{f}$$

Equation 2.3: λ= wavelength (m), v= velocity (m/s) and f= frequency (Hertz).

As a wavelet travels downwards to greater depths the relationship between wavelength, velocity and frequency will be influenced (Fig.2.2). Velocity will increase as sediments become compacted and experience diagenesis with depth, frequency will decrease as the high-frequency signals will attenuate and get absorbed by the medium with increasing depth (Brown, 1999). The result of increasing velocity and decreasing frequency is an increasing wavelength with depth hence conclude a poorer seismic resolution with increasing depth (Brown, 1999) (Fig.2.2).

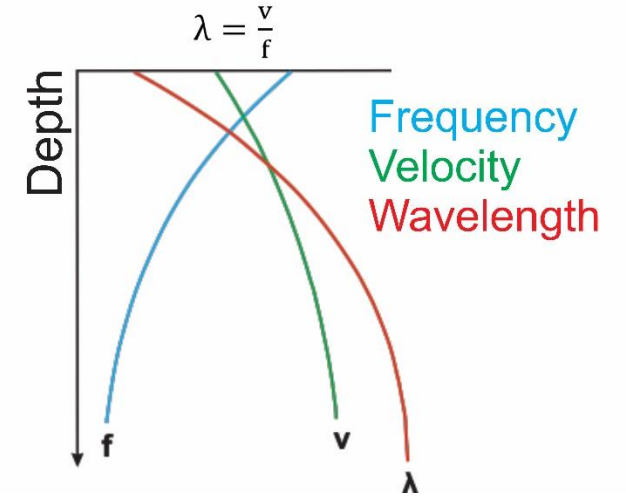

Fig.2.2: Relationship between frequency, velocity and wavelength as depth increases. Modified from (Brown, 1999).

2.3.1.1 Vertical resolution

Vertical resolution can be thought of as the ability to distinguish two closely spaced points, in other words, it can be a measurement for how thick a bed has to be in order to be detected (Zhou, 2014). Regarding vertical resolution, there are two limitations, the limit of separability and the limit of visibility (Sheriff, 1985; Brown, 1999). The limit of separability is the limit for separation of two wavelets in a certain bandwidth, if the thickness of a layer is greater than one-quarter of a wavelength it's within the limit of separability which means that the top and bottom can be distinguished (Fig.2.3) (Brown, 1999; Zhou, 2014). If however the thickness of a layer is less than the limit of separability then amplitudes will continuously be attenuated until the limit of visibility is reached and the reflected signal will be eliminated by background noise (Fig.2.3) (Brown, 1999). Calculations of the vertical resolution can therefore best be described by (Equation 2.4) (Brown, 1999).

Equation 2.4 Vertical resolution.

$$v_r = \frac{\lambda}{4}$$

Equation 2.4: vertical resolution (v_r) is a result of λ divided by 4.

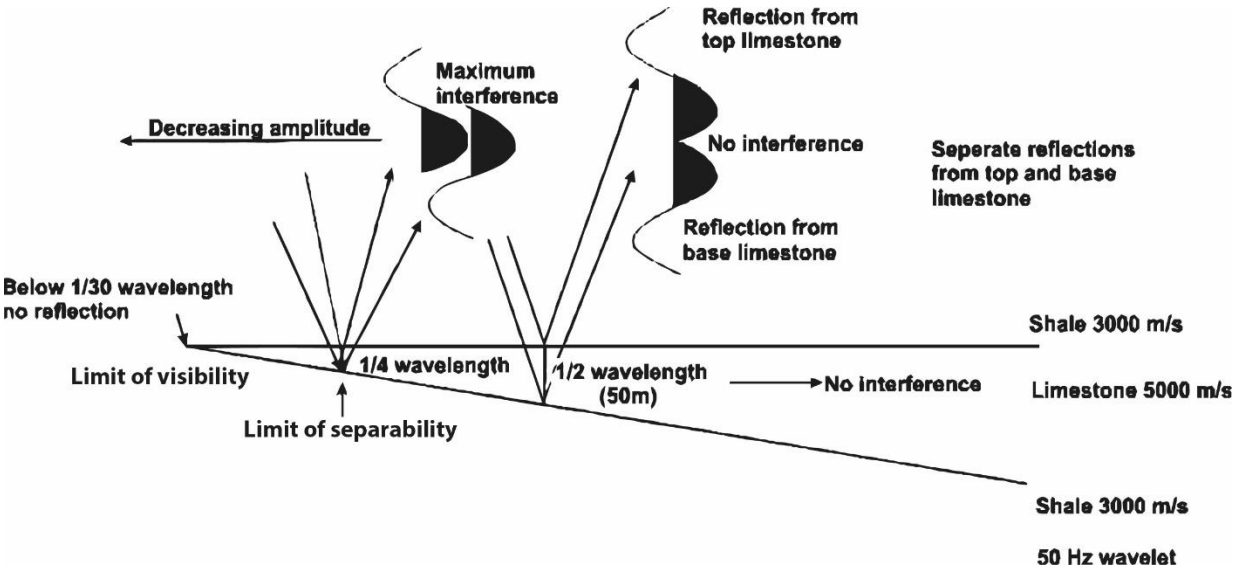

Fig.2.3: Vertical resolution and the effect of a wedge-shaped layer with higher acoustic impedance properties. Modified from (Badley, 1985).

2.3.1.2 Horizontal resolution

Seismic waves spread out from the source and travel spherical in three dimensions, the wavefront interacts with a reflecting boundary and a circular area of the interface becomes reflected and recorded by the receivers (Brown, 1999; Kearery et al., 2002). This circular area termed the Fresnel zone can best be defined as the horizontal seismic resolution (Fig.2.4). Sheriff (1985) defines the radius of the Fresnel zone for an un-migrated seismic section with Equation 2.5.

Equation 2.5 Horizontal resolution pre-migration (radius of Fresnel zone).

$$rf = \frac{v}{2}\sqrt{\frac{t}{f}}$$

Equation 2.5: rf= radius of Fresnel zone (m), v= average velocity (m/s), t= two-way travel time (s), f= dominating frequency (Hz). The radius of the Fresnel zone increases with depth, velocity and decreasing frequency.

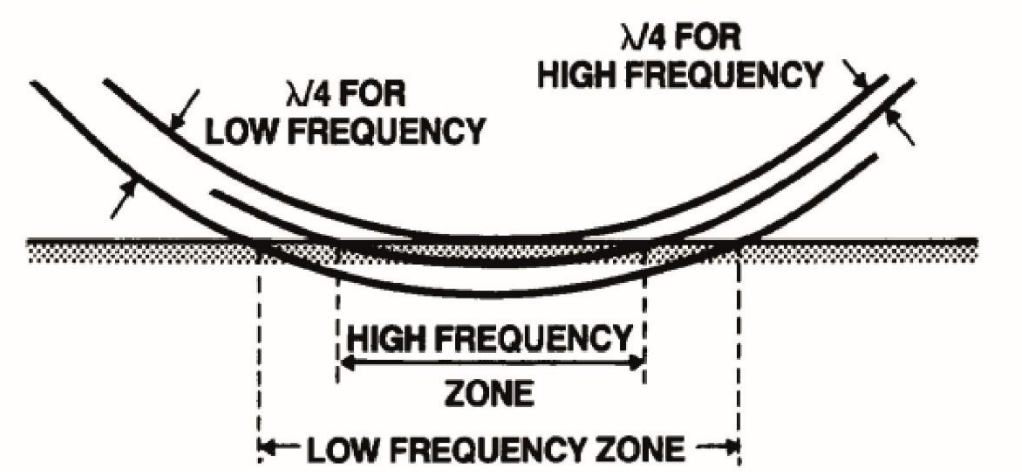

Fig.2.4: Post-migrated seismic illustrating a smaller Fresnel zone with higher frequency. From (Sheriff, 1985).

The horizontal resolution can be improved by processing and migration of the seismic data, this will decrease the Fresnel zone and therefore also decrease the width needed for a feature to be detected. Migration is a processing step which improves the seismic resolution by repositioning the misplaced reflections commonly caused by seismic features such as dipping layers, faults and salt domes (Brown, 1999; Veeken, 2007). 2D seismic can only be migrated along the seismic line in one direction, the Fresnel zone will therefore be reduced to an ellipsoid perpendicular to the line when 2D migrated, while 3D migration will collapse the Fresnel zone to a small circle as seismic waves are migrated in both inline and xline direction (Fig.2.5) (Brown, 1999). According to Brown (1999) is the post-migration Fresnel zone calculated with (Equation 2.6).

Equation 2.6 Horizontal resolution post-migration (radius of Fresnel zone).

$$rf = \frac{\mathrm{v}}{4\mathrm{f}}$$

Equation 2.6: rf = radius of Fresnel zone migrated seismic (m), 4f= four times the frequency (Hz).

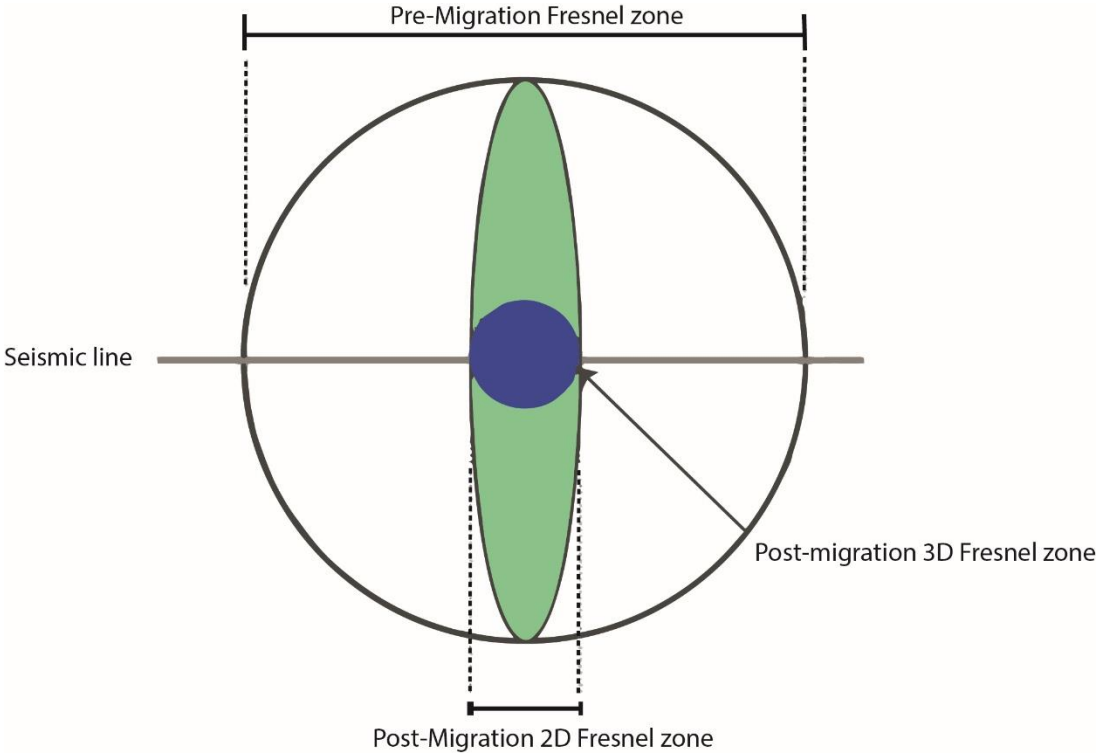

Fig.2.5: Migration of the Fresnel zone, green ellipsoid indicates 2D migration, while the blue circle indicates 3D migration. Modified from (Brown, 1999).

2.3.2 Seismic indications of gas and fluids

The presence of fluids, especially gas in the seismic drastically reduces the p-wave velocity, Veeken, (2013) specifies that as little as five percent gas saturation in a formation can impose a reflection with a high amplitude contrast. Gas can therefore be identified in the seismic based on several indicators, as the gas infers a high acoustic impedance disturbance to the rock medium, these are commonly known as hydrocarbon indicators. Due to the scope of this thesis will only some of these indicators be discussed.

Bright spot

A bright spot is a local increase in amplitude due to a high reflection coefficient either negative or positive (Fig.2.6) (Kearery et al., 2002). The bright spots are commonly associated with gas zones and a strong negative reflection coefficient, as the gas imposes a significant reduction in velocity. The acoustic impedance is therefore lowered as indicated by a reversed polarity reflection opposite of the seabed reflection. The bright spots can however have a strong positive reflection coefficient associated with lithology changes, e.g. with carbonates, salt or magmatic intrusions (Badley, 1985).

Dim spot

A dim spot in contrast to a bright spot is a local reduction in amplitude compared to its surrounding, appearing as a faded zone with a weak positive reflection in the seismic (Fig.2.6) (Løseth et al., 2009). The dim spot is usually caused by the overlying unit having similar acoustic impedance properties as the underlying hydrocarbon-filled reservoir, the reservoir initially having higher acoustic impedance than the overburden but when hydrocarbon-filled its velocity is reduced (Løseth et al., 2009; Nanda, 2016).

Flat spot

A flat spot is a flat positive reflector cross-cutting the surrounding stratigraphic reflectors representing the hydrocarbon contacts, either gas-oil contact, gas-water contact or oil-water contact (Fig.2.6) (Løseth et al., 2009). The gas-oil contact or gas-water contact is strongest and easier identified as the acoustic impedance contrast is larger going from gas to liquid in opposed from oil to water.

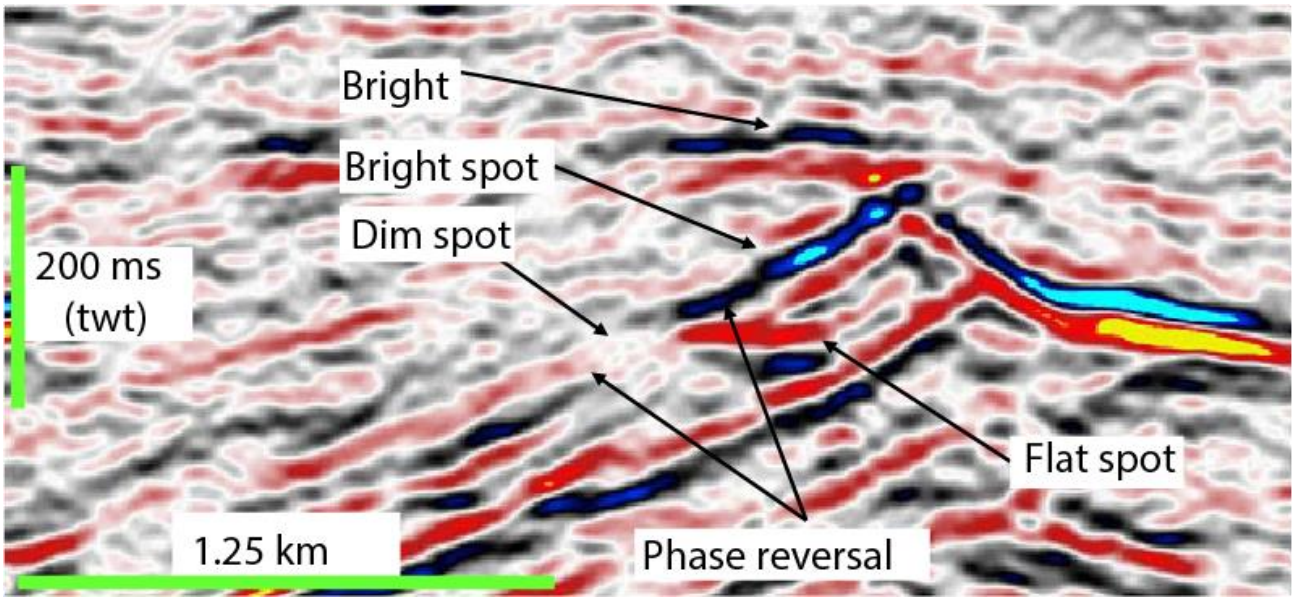

Fig.2.6: The hydrocarbon indicators: bright spot, dim spot, flat spot and phase reversal displayed in a seismic section. From (Løseth et al., 2009).

Velocity push-down

The Velocity push-down effect is the result of gas-bearing sediments imposing a low-velocity anomaly compared to the surrounding sediments with no gas, the reflector therefor appears with a little bend at the gas induced area (Fig.2.7a) (Løseth et al., 2009). The push-down effect can however be associated with lithological changes, e.g. imposed by local areas of sediments with lower velocity (Løseth et al., 2009).

Acoustic masking

Acoustic masking refers to an area which the seismic is highly distorted having a chaotic reflection pattern or with a low seismic reflectivity in contrast to its surroundings (Fig.2.7a) (Andreassen et al., 2007). Acoustic masking in association with other gas indicators such as push-down and bright spots might indicate scattering of acoustic energy caused by fluctuations in the acoustic properties which the gas imposes on the sediments (Fig.2.7a) (Andreassen et al., 2007). The acoustic masking is a result of hydro-fractures generated by fast flowing gas, extending from different depths, commonly associated to emanate from crestal regions such as folded anticlines, tilted fault blocks or isolated sand-bodies with

positive topography, however there has been documented pipes emanating from flat-lying units as well (Berndt et al., 2003; Cartwright et al., 2007).

Gas chimney

Gas chimneys are large vertical to near vertical columns with zones of scattered acoustic energy seen as acoustic masking and push-down characteristics inferred by free gas in the sediments (Anka et al., 2014). The gas chimneys commonly have a deep origin transporting thermogenic gas from deep-seated hydrocarbon reservoir which where the cap rock has been fractured and the gas can migrate vertically towards the surface (Fig.2.7b) (Løseth et al., 2009). On its way to the surface the gas might be trapped and can therefore be seen with associated bright spots, it is also common with surface expressions such as pockmarks and craters above the gas chimneys (Fig.2.7).

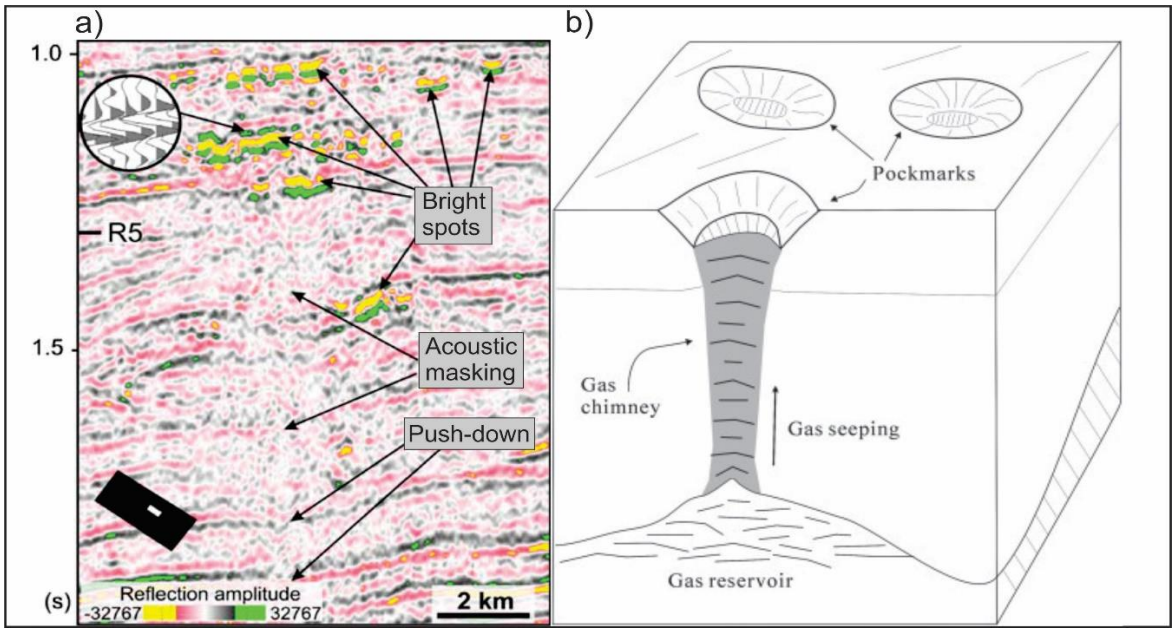

Fig.2.7:a) The hydrocarbon indicator: bright spot, acoustic masking and push down displayed in a seismic section. b) Conceptual sketch of a gas chimney with associated pockmarks. Figure (a) modified from (Andreassen et al., 2007) *and (b) from* (Cathles et al., 2010).

2.4 Surface expression of gas seepage: Pockmarks

The most common evidence for gas seepage on the seafloor is probably pockmarks (Fig.2.7). Pockmarks are small circular to sub-circular and sometimes slightly elliptical depressions with relatively steep walls representing discharge of fluids or gas from the subsurface (Fig.2.7) (Chand et al., 2009; Anka et al., 2014). The pockmarks are often to be found in relation to seismic amplitude anomalies e.g. gas chimneys and dissociation of gas hydrates or subsurface structures such as faults. The size and shape varies from 1 - 35 m in depth and 200 m in diameter and they are found at both active and passive continental margins in a variety of marine settings at documented water depths from <2 m – 5000 m (Judd & Hovland, 2009; Løseth et al., 2009; Anka et al., 2014). The pockmarks often occur in clusters where large areas of the seafloor are covered by pockmarks, but these features can however also occur as single isolated features. The pockmarks are mainly found in soft fine-grained sediments as the finer grained sediments have a better preservation potential than coarser material (Solheim & Elverhøi, 1985; Chand et al., 2009).

2.5 Fluid migration dynamics

Fluid migration is a natural phenomenon which influences not only the geology but also different aspects such as ecosystems, climate changes, predictions of hydrocarbons or triggers for geohazards such as submarine landslides or tsunamis (Berndt, 2005). The fluid migration can be described as liquids, gases or solutions of both existing in porous space and fractures within sediments and rocks migrating through a medium with sufficient porosity and permeability driven mainly by pressure and temperature gradients in the subsurface (Guzzetta & Cinquegrana, 1987; Berndt, 2005; Selley & Sonnenberg, 2014). As fluid migration will be discussed in this chapter it's on behalf of both liquids and gas.

The fluid migration follows some common concepts which apply to all kind of fluids flowing through a porous and permeable medium. Darcy's Law is central for fluid flows, this law simply describes the fluid migration as a result of the rock's ability to conduct a fluid and the pore-water pressure difference between two ends of the flow (Berndt, 2005). Highly permeable rock medium, fluids of low viscosity and large pressure differences are criteria's which allows for easier fluid migrations through a specific medium (Berndt, 2005).

Sediments generally lose porosity and permeability as they get compacted and buried deeper by overburden sediments, this increases the density and lowers the conductivity of the rocks as it experiences diagenesis (Berndt, 2005). The compaction and diagenetic processes are however highly variable depending on lithology, as for example sandstone density mainly increases linearly with depth (Berndt, 2005). while claystone has a higher increase in density within the first 1000 m and after the 3000 m interval because of internal clay mineral alignment and due to loss of internal formation water (Berndt, 2005).

A second important concept for fluids to migrate into a formation is the fluids ability to overcome the capillary pressure. The Capillary pressure is the pressure difference between an interface of two immiscible fluids of a certain area, in order for oil or gas to migrate through a water-wet formation it has to overcome the capillary pressure (Fanchi, 2006). The capillary pressure is the resisting force acting against the forces of buoyancy (density differences between two solutions) and groundwater-flow force (pushing the petroleum) (Hindle, 1997). Due to the high-density contrast between gas and fluids, this allows for easier migration.

2.5.1 Hydrostatic pressure, under pressure and overpressure.

Hydrostatic pressure is the pressure imposed by the overlying fluids, lithostatic pressure is the pressure exerted by the overall weight of the overburden, both fluids and matrix (Deming, 2002). If the fluid pressure were to be below the hydrostatic pressure there will be underpressure, if however the pressure is higher than the hydrostatic pressure then there will be overpressure, and fluids are then forced to migrate through permeable layers until normal hydrostatic pressure is reached (Fig.2.8) (Deming, 2002).

Overpressure is common to appear if the overburden rock does not have sufficient permeability due to, e.g. rapid sedimentation and compaction which prevent the fluids from flowing through the medium and reaching normal hydrostatic pressure. Overpressure can also occur by the generation of biogenic or thermogenic gases imposing high pressure on the overburden rocks (Osborne & Swarbrick, 1997; Berndt, 2005). The high overpressured fluids also have a tendency to fracture sealing cap rocks and may also impose hazardous to drilling as fluids will rush up to the wellbore with high speed and cause blowouts (Deming, 2002).

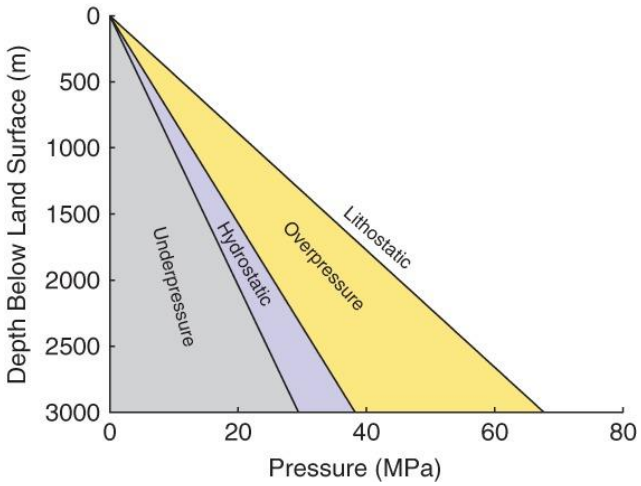

Fig.2.8: Relationship between the different pressure gradients, if the pore pressure is overpressured it can crack the overburden formations and fluids can migrate upward until hydrostatic pressure is reached. Figure from (Flewelling & Sharma, 2014).

2.5.2 Fluid migration models

The distance for which petroleum can migrate within sedimentary basins has been a debated topic. However measurements examining the distance between petroleum accumulations and the closest mature source rock has indicated migration distances up to 1000 km in the West Canadian basin, however this is an unusually long migration distance and distances of 100 km lateral and 2 km vertical is more common (England et al., 1987; Selley & Sonnenberg, 2014).

Lateral migration

Sedimentary basins which have not been subjected to tectonic activity favors lateral fluid migration through permeable carrier beds for longer distances as the fluids migrate along and below sealing surfaces (Hindle, 1997).

Vertical migration

As earlier discussed, the fluids will migrate vertically if the buoyancy and water-flow force are sufficient to overcome the capillary pressure of a certain rock medium with adequate permeability and porosity. If fluids however encounter a sealing rock of high capillary

pressure and can't migrate through it, this would trap the fluids and keep them there until the trap is filled to spill or the overpressure is sufficient to impose fracturing to the formation. The fluids will migrate upward until a new seal is encountered or all the way through the seabed and into the water column (England et al., 1987). Diapiric structures (salt/mud), tectonic activities (faulting and fracturing) and rapid sedimentation of muddy deposits (leading to overpressure) all favor vertical fluid migrations (Thrasher et al., 1996).

2.6 Gas hydrates

Gas hydrates are solid ice-like crystalline structures of water containing trapped gas molecules (Plaza-Faverola et al., 2017). The gas hydrates consist mainly of methane but often occur in association with other heavier gases, the hydrates are formed under high pressure and low temperatures in both marine and permafrost sediments and are commonly found in large parts of the continental margins and arctic regions (Judd & Hovland, 2009; Plaza-Faverola et al., 2017). The gas hydrates stability zone is best described as the zone where gas hydrates occur naturally under certain conditions governed by water depth, water bottom temperature, geothermal gradient, pore water salinity and gas composition, where low temperature and high pressure favors gas hydrate stability (Fig.2.9) (Plaza-Faverola et al., 2017). The gas hydrates are usually stable at water depths exceeding 500 m, however with a higher number of associated heavier gases such as ethane and propane the gas hydrates can be stable and form in much wider pressure-temperature regimes in contrast to pure methane gas hydrates (Fig.2.9) (Plaza-Faverola et al., 2017).

The structure of the gas hydrates is mostly controlled by the mixture of gases. Structure I (S_I) commonly forms with almost pure methane gas composition and is commonly associated with microbial sourced gas (Paganoni et al., 2016). The gas hydrate structures II (S_{II}) and H (S_H) have a much wider gas hydrate stability zone and can be found at much shallower water depths compared to S_I gas hydrates (Fig.2.9). They usually host a mixture of various heavier gases such as propane and ethane in combination with methane (Paganoni et al., 2016). These gas hydrates structures are commonly associated with a thermogenic source representing leakage from deep-seated reservoirs (Paganoni et al., 2016).

The gas hydrates can best be identified in the seismic by the bottom-simulating reflector (BSR) which indicates the base of the gas hydrate stability zone and the transition from underlying free gas and stable gas hydrates. The BSR is characterized by a high amplitude

reflector crosscutting other stratigraphic layers and mimicking the seafloor with an opposite reflection amplitude (Plaza-Faverola et al., 2017). The BSR often appear in association with other seismic fluid flow features, such as above gas chimneys where the BSR blocks the seepage for further vertical migration. Evidence for gas hydrates can also be observed at the seafloor with pockmarks, craters and authigenic carbonate which could indicate dissociation of gas hydrates (Cremiere et al., 2011; Andreassen et al., 2017).

The gas hydrates are of great interest due to the large untapped energy potential which they constitute, they also imposes potential evidence for deeper-seated hydrocarbon reservoirs. The research for gas hydrates is also important in the case of global warming as methane is a potent greenhouse gas which can amplify climate change and also cause geohazards related slope instability associated with the dissociation of gas hydrates.

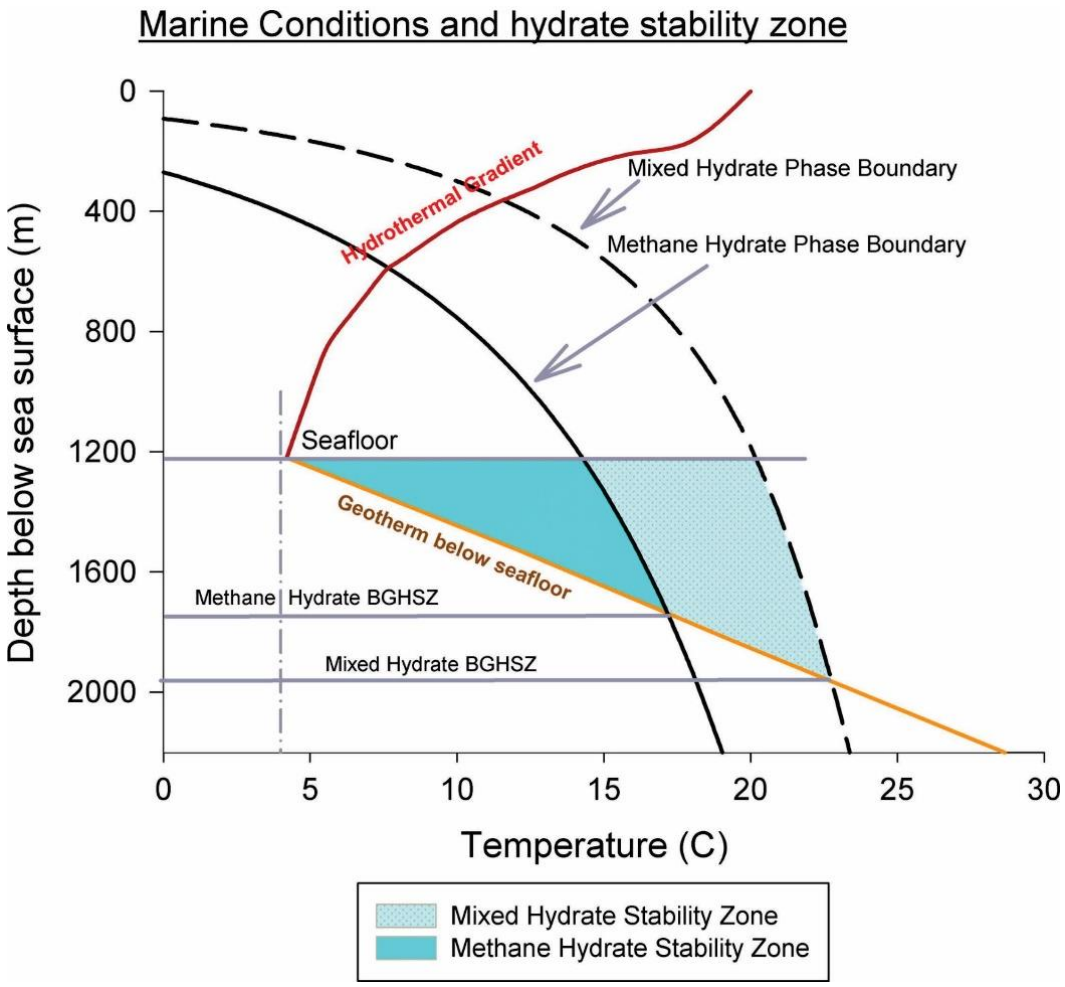

Fig.2.9: conceptual illustration of how the gas hydrate stability zone is influenced under similar conditions with different gas composition. Notice how the mixed compositional gas hydrates have a much wider stability zone. Figure from (Chong et al., 2015).

3 Study area

The study area of Storbanken high and Olga basin is located at the eastern parts of the northern Barents Sea, approximately 250 km east for Edgøya (Fig.3.1). This is an area with a complex geology influenced by various tectonic regimes and depositional environments.

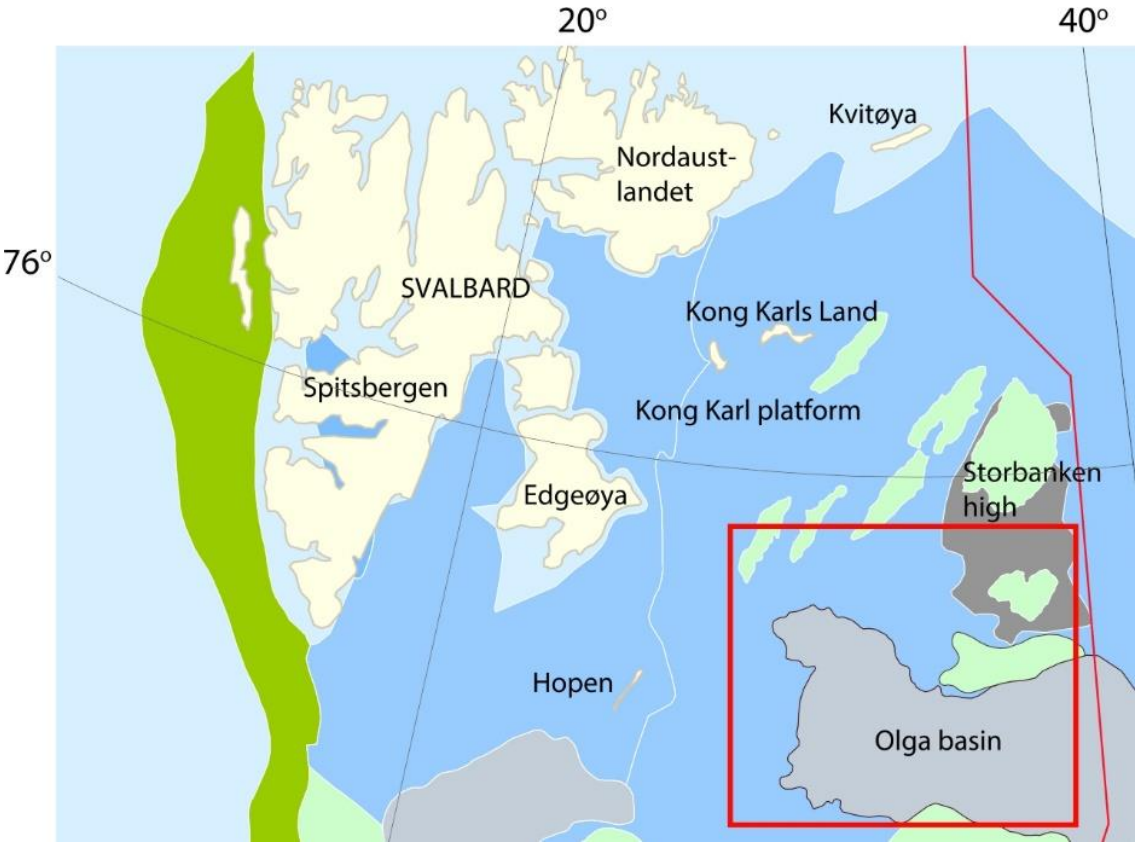

Fig.3.1: Overview of the structural elements in the northern Barents Sea. The red rectangle indicates the study area, the red line delineates the border between Norway and Russia. modified from (NPD, 2017).

3.1 Geologic history of the northern Barents Sea

The Barents Sea is an epicontinental sea which covers large areas of shallow waters in the Arctic, and with an average depth of 300 m it is one of the world's largest continental shelves (Dore, 1995; Smelror et al., 2009). The area of the Barents sea encompasses approximately 1,3 million km^2 and is bounded in the east by Novaya Zemlya and the Kara Sea, the Svalbard archipelago and Franz Josef Land in the north, the Norwegian-Greenland Sea in the west and the Norwegian and Russian coast in the south (Dore, 1995; Smelror et al., 2009).

The geology of the Barents Sea is a complex combination of different plate tectonic regimes, changing climatic conditions and varying depositional environments throughout hundreds of million years (Smelror et al., 2009).

3.2 Tectonic development

The most important tectonic events impacting the regional development of the northern Barents Sea can shortly be summarized with the following events: The Caledonian orogeny in the Ordovician to Early Devonian with associated Devonian and Carboniferous rifting (Smelror et al., 2009; Minakov et al., 2012). The Uralian Orogeny in Permian to Early Triassic with following regional subsidence, Late Jurassic and Early Cretaceous rifting and compression (Smelror et al., 2009; Kairanov et al., 2018). Cretaceous magmatic intrusions and regional Cretaceous uplift, Paleogene compression, and Neogene glacial related erosion and subsequently isostatic uplift (Smelror et al., 2009; Minakov et al., 2012; NPD, 2017; Kairanov et al., 2018).

3.2.1 Paleozoic (541-251Ma)

In the Early Ordovician to Early Devonian the two continental plates Laurentia and Baltica drifted towards each other and formed the Caledonian orogeny and the continent Laurussia as a result of the collision between the two continents (Smelror et al., 2009). The collision resulted in a regional metamorphosis and development of a crystalline basement along the Norwegian shelf. The transition from a compressional regime and conclusion of the Caledonian mountains to an extensional setting is characterized by rifting, erosion of hinterland and depositional basins of terrestrial sand, the rifting initiated in the early Carboniferous across the Barents Shelf (Anell et al., 2014; Dallmann et al., 2015). The widespread extensional post-Caledonian rifting event developed rift basins and horst and graben structures (Smelror et al., 2009).

The extensional rifting ceased in early Permian, and the western shelf became a quiet and tectonic stable region (Smelror et al., 2009). The eastern Barents Shelf were however in a collision of the Yamal-Gydan plate and an island arc bordering the Novaya Zemlya marginal basin to coincide the first Uralian orogeny phase and to close the Ural ocean and form the Uralian mountains south of Pay-Khoy (Smelror et al., 2009). During late Permian age the

northern Barents Sea was also subjected to uplift and several highs were exposed which led to the erosion of Paleozoic strata (Smelror et al., 2009; NPD, 2017).

3.2.2 Mesozoic (251-65Ma)

The Triassic is regarded as a quiet tectonic period In the Barents Sea, however in the transition from Permian to Early Triassic the final phase of the Uralian Orogeny led to the closure of the Novaya Zemlya Marginal basin (Golonka et al., 2003; Smelror et al., 2009). Following the Uralian Orogeny was regional subsidence associated with the continental collision processes culminating with the Uralian Orogeny (Gudlaugsson et al., 1998; Anell et al., 2014). There were also small transgressions and regressions associated with global sea level changes and local lobe subsidence related to the prograding sediments sourced from the Ural mountains (Anell et al., 2014; NPD, 2017).

In the Late Jurassic the Pangea break-up was completed with North America and Eurasia plates drifting away from Gondwana, a narrow ocean, which was to be the Atlantic Ocean was created between Gondwana and Laurasia (Dallmann et al., 2015). In the northern parts of this ocean there was a major flooding event creating a shallow sea during Early to Middle Jurassic (Dallmann et al., 2015).

The transition from Jurassic to Cretaceous saw a shift to a warmer climate due to massive volcanism and seafloor spreading, basaltic lava and intrusions have been documented east for Kong Karls Land platform and further north at Franz Josef (Dallmann et al., 2015; Kairanov et al., 2018). The magmatic activity is related to the High Arctic Large Igneous Province (HALIP) which developed during the opening of the Amerasian Basin (Døssing et al., 2013; Dallmann et al., 2015; Marin et al., 2017). Polar ice cap melting in combination with active rifting and sea-floor spreading resulted in a very high eustatic sea level, continental and lowland areas therefor became flooded to form shallow shelf and epicontinental seas (Dallmann et al., 2015). The tectonic events from Late Jurassic to Early Cretaceous with compression, volcanism and salt movement led to different degrees of uplift and inversion in the northern Barents Sea and the formation of NE-SW and E-W aligned structural highs and anticlines (Dallmann et al., 2015; Kairanov et al., 2018). The Compressional forces and uplift of the highs and platforms in the northern Barents Sea are to the present day not clear. However, Kairanov et al, (2018) have suggested that the compression most likely is related to Late Jurrasic – Early Cretaceous opening of the Amerasia Basin, the dextral transpression

along Novaya Zemlya, HALIP or the compression between NE Greenland and the NW Barents Sea.

3.2.3 Cenozoic (65Ma-present)

Cenozoic is generally characterized to be a period dominated by regional uplift related to seafloor spreading, a tectonic event which caused the northern Barents Sea to be uplifted in a magnitude of 500 - 2000 m, with most uplift along the northwestern margin at Svalbard (Grogan et al., 1999; Henriksen et al., 2011a).

The Paleogene initiated its period with warm and humid climate but got gradually cooler and drier as a result of the formation of the Antarctic Circumpolar Current which originated after the breakdown of the Gondwana continent in late Mesozoic (Dallmann et al., 2015). Seafloor spreading between the Norwegian – Greenland Sea initiated in early Eocene (56ma) and led to regional uplift in the Barents Sea (Henriksen et al., 2011b). The seafloor spreading pattern reorganized in middle Eocene (48ma) and later developed a dextral stress field along the Senja-Hornsund alignment (Steel et al., 1985; Henriksen et al., 2011b). Compression along this fault zone between Svalbard and north Greenland caused fold-and-thrust belt on Svalbard as well as fault inversions and compressional features across the northern Barents Sea (Steel et al., 1985; Henriksen et al., 2011b; Kairanov et al., 2018). This event is also believed to be an important tectonic episode governing the uplift in the northern Barents Sea.

The late Neogene and Quaternary were characterized throughout the whole period with repeated glacial subsidence, uplift and erosion, with sedimentation mainly restricted to the western shelf margin (Worsley, 2008). During late Cenozoic was Svalbard and the northern Barents Sea dominated by erosion whereas most of the Paleogene and Cretaceous strata was eroded in Pliocene and Pleistocene due to glacial erosion and isostatic uplift (Worsley, 2008; NPD, 2017).

3.3 Stratigraphy and Depositional environment

Correlation between geology and fieldwork on Svalbard, wells from the Barents Sea South, shallow boreholes in the north and seismic surveys have indicated a great similarity between Svalbard and the northern Barents Sea regarding the chronostratigraphic and lithostratigraphic framework (NPD, 2017). The general trend for the paleoenvironment reflects a climatic shift from humid and tropical equatorial conditions in Devonian-Carboniferous to a more northern temperate climate in Paleogene and Neogene (Dallmann et al., 2015; NPD, 2017). The northern Barents Sea is dominated mainly by siliciclastic and marine sediments but also exhibits carbonate rocks and evaporites deposited from late Carboniferous to early Permian age (Smelror et al., 2009; NPD, 2017). The stratigraphy in the northern Barents Sea is mainly dominated by Late Devonian to Late Cretaceous sediments (NPD, 2017; Kairanov et al., 2018). The underlying basement is most likely to be crystalline basement from the Caledonian orogeny but information is scarce as it hasn't been proved by drilling (Gudlaugsson et al., 1998).

3.3.1 Paleozoic

During the Devonian, sediments were mainly immature unsorted coarse-grained debris of eroded crystalline basement from the Caledonian Mountains deposited as colluvial and alluvial fans and braided river systems (Dallmann et al., 2015). The Devonian was a period with high sea levels and warm oceans, the Barents shelf was located around equatorial areas and had an arid climate (Dallmann et al., 2015). During early Carboniferous there was a shift in climate to tropical and organic-rich conditions, were humid swampy forests flourished and regional coal deposits could originate in combination with fluvial and lacustrine clastic sand deposited as syn-rift sediments (Fig.3.2a) (Worsley, 2008; Anell et al., 2014).

3.3.2 Mesozoic

The Permian-Triassic transition is marked with a hiatus of silica-rich shale from Permian age to a non-siliceous shale in Triassic age (Worsley, 2008). The drastic change in lithology for the two ages reflect the global tectonic changes resulting in a warmer ocean and the closure of the seaway connection between Tethys Ocean and Boreal sea caused by the formation of the Uralian Mountains (Worsley, 2008; Dallmann et al., 2015).

The Uralian mountains fed the Barents Sea with prograding deltas from the south-east providing large amounts of sand, the prograding deltasystems reached the Olga basin in late Induan age (251-249 ma) (Fig.3.2b and 3.3) (Worsley, 2008; Dallmann et al., 2015; NPD, 2017).

The Triassic sediment package is extensive across the whole northern Barents Sea due to high amounts of sediments fed from the Uralian Mountains in combination with regional subsidence causing a large accommodation space. During Olenekian-Anisian age (249-237ma) there was a rapid sea level rise in an open shelf environment along with upwelling of waters in combination with high biological activity and little oxygen (Krajewski, 2008). This led to a highly anoxic environment and the development of the Botneheia Formation also known as the time-transgressive Steinkobbe Formation in the southern Barents Sea (Mørk & Elvebakk, 1999; Krajewski, 2008; Lundschien et al., 2014).

The Western Barents Sea region transformed from a marine shelf with a deeper through in Anisian age (245-237ma) to a paralic platform in late Carnian age (216ma), as a result of delta progradation from the southeast sourced by the Urals (Fig.3.2b) (Riis et al., 2008). The Triassic was also subjected to local transgressions and regressions throughout the period, which is linked to the result of lobe shifting and subsidence, this process was an important contributor for the varied sediment distribution of sand, silt and clay in the northern Barents Sea in this time period (NPD, 2017). Continued sediment input from the Urals deposited in deltaic and floodplain environments rapidly established across the northern Barents shelf throughout Carnian age (228-216ma) (Riis et al., 2008; Worsley, 2008).

In early Norian age (215ma) there was a widespread regional transgression which established a marine connection between the Tethyan and Boreal ocean, the Barents shelf saw a decrease in sedimentation rate and subsidence (Worsley, 2008). The Uralian sourced sedimentation were no longer dominating, and the transgression led to a shallow marine mudstone dominated deposits also known as the Flatsalen Formation (Riis et al., 2008; Ryseth, 2014). The mudstone gradually passed into sand with a coarsening upward trend reflecting a prograding coastal dominated environment. The new environment reflected a more mature sandstone which had undergone extensive reworking and the generation of the Realgrunnen Subgroup (Riis et al., 2008; Worsley, 2008).

The transition from the Triassic to Jurassic was characterized by a shift in climate from arid to humid with frequently sea-level changes caused by the reorganization of continental plates associated with the break-up of Pangea (Smelror et al., 2009; Worsley, 2008). In Late Jurassic land areas were flooded as a new transgression submerged the highs and platforms as well as provided conditions for calcareous mudstone and anoxic black organic-rich shale in Callovian/Oxfordian age (165-155ma) giving rise to the Agardhfjellet Formation also known as the Hekkingen and Fuglen formations in the southern Barents Sea (Fig.3.2c and 3.3).

A major change in depositional environment initiated around the Jurassic-Cretaceous transition related to a lowering of sea level and the general development of a more open marine environment with better bottom circulation (Worsley, 2008). The northern margin during Late Cretaceous was dominated by uplift, volcanism and erosion with fluvial conglomerate and sand deposits (Fig.3.2d) (Worsley, 2008; Dallmann et al., 2015). Due to the great uplift and erosion in the northern Barents Sea there was a forced regression shoreline and southward directed clinoforms were formed (Fig.3.2d) (Marin et al., 2017; Kairanov et al., 2018).

3.3.3 Cenozoic

As a result of tectonic episodes and uplift related to the opening of the Norwegian-Greenland Sea in Paleogene and repeatedly glaciations in Neogene and Quaternary with following isostatic uplift, the northern Barents Sea was subjected to large amounts of erosion. Sediments from Cenozoic age are therefore not well preserved at the northern margin (Fig.3.2e).

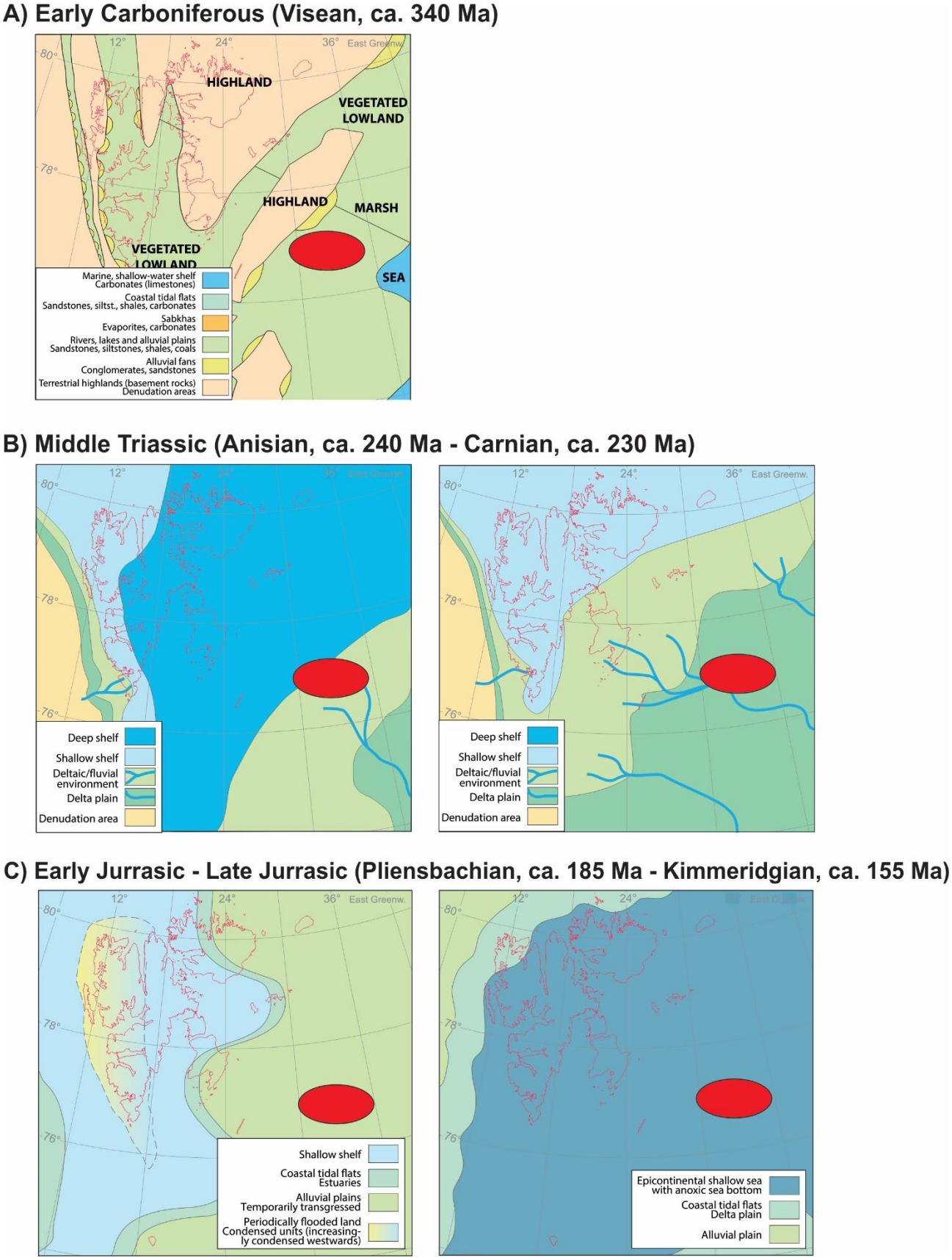

Fig.3.2: Paleographic reconstruction of the northern Barents Sea from early Carbon to late Pleistocene, approximately location of Olga basin is indicated by a red dot. Modified from (Dallmann et al., 2015).

D) Early Cretaceous (Barremian, ca. 125 Ma - Albian, ca. 110 Ma)

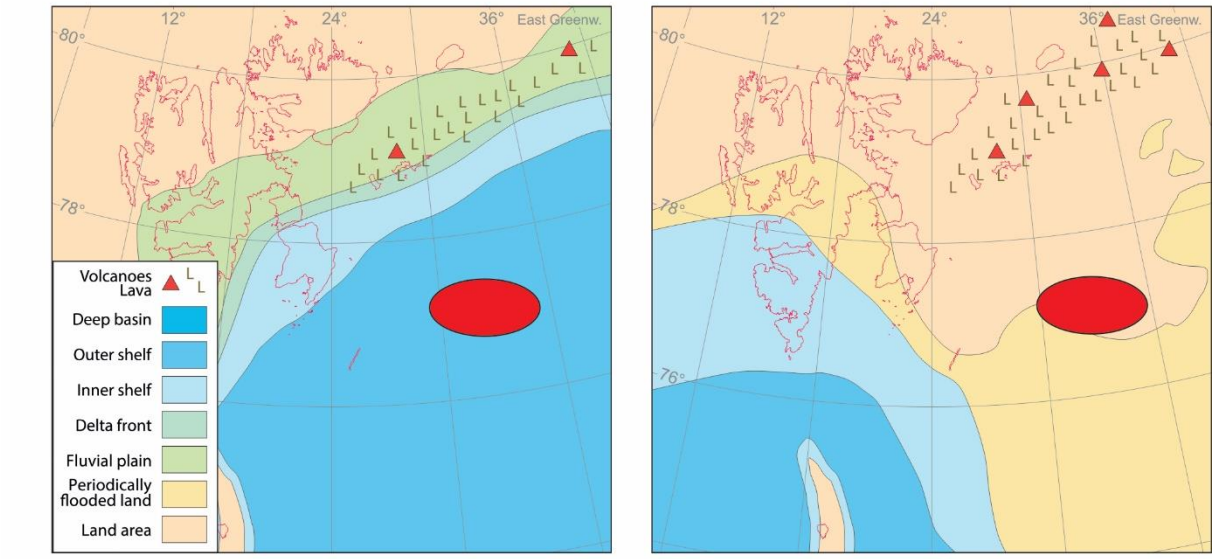

E) Late Quarternary (Late Glacial Maximum, ca. 20 Ka)

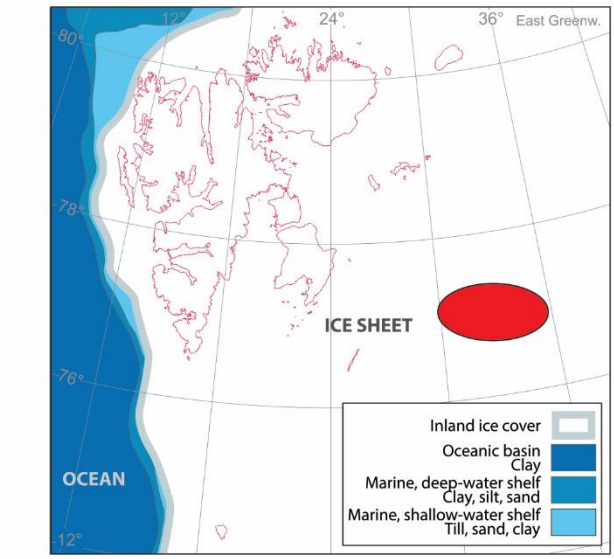

Fig.3.2: Continued.

3.4 Groups and Formations

The northern Barents Sea has sediments from Late Devonian to Late Cretaceous age (Fig.3.3) (Grogan et al., 1999; NPD, 2017). The groups and formations of: Billefjorden Group, Botneheia Formation, De Geerdalen/Snadd Formation, Flatsalen Formation, Realgrunnen Subgroup and Agardhfjellet Formation are important in regards to source, reservoir and cap rock. These groups and formations are believed to be important controlling the gas seepage activity in the study area and will therefore constitute as the main stratigraphic units for this thesis.

3.4.1 Billefjorden Group

The Billefjorden Group extends from Late Devonian, Famennian age to middle Carboniferous, Visean age (374-326ma) (Worsley, 2008). The group consists mainly of fluvial and lacustrine material deposited as syn-rift sediments in a humid and warm terrestrial environment (Fig.3.3) (Worsley, 2008). Erosion from faulted graben and horst margins led to the deposition of clastic immature sand and conglomerates, the swampy and humid environment caused deposition of local organic-rich coal deposits. (Grogan et al., 1999; Worsley, 2008; NPD, 2017).

3.4.2 Botneheia Formation

The Botneheia Formation is the time-transgressive formation for the Steinkobbe Formation in the southern Barents Sea, the formation is oldest in the southern Barents Sea and gets progressively younger towards the north and Svalbard (Fig.3.3). The Steinkobbe is deposited in late Olenekian to late Anisian at the Svalis Dome area, while the Botneheia Formation was deposited throughout the Anisian and Ladinian age in the central and eastern parts of Svalbard (Lundschien et al., 2014). Based on studied prograding clinoform break systems by Lundschien et al, (2014) is the Botneheia Formation most likely deposited in the Olga basin and Storbanken high from late Olenekian (245ma) to late Anisian (237ma), the same age corresponding to the Steinkobbe Formation deposited at the Svalis Dome. The Botneheia Formation is characterized as a soft dark organic-rich shale/mudstone (Fig.3.3) (Mørk & Elvebakk, 1999; Vigran et al., 2014).

The formation was developed during a rapid sea level rise and a retrogradation of the prograding delta system, which led to a deep shelf anoxic environment with interrupted short periods of oxygenation as an indication of high biological productivity and sporadic bioturbation (Mørk & Elvebakk, 1999). The formation has a documented Kerogen type of II and III with a high content of total organic compound (TOC) varying from 1-15 %, characterizing it as a prominent source rock in the study area (Grogan et al., 1999; Abay et al., 2014).

3.4.3 De Geerdalen/Snadd Formation

The De Geerdalen Formation at Svalbard is time-equivalent with the upper parts of the Snadd Formation in the Barents Sea (Fig.3.3). This formation is deposited as a dynamic paralic depositional environment representing mainly tidal and fluvial channelized sand deposits in late Middle Triassic to Late Triassic (Klausen & Mørk, 2014). Paleocurrent measurements in the channelized sand within the De Geerdalen/Snadd Formation has indicated progradation towards the northwest and therefore progressively older sediments in the southern Barents Sea compared to the northern Barents Sea (Klausen & Mørk, 2014; Dallmann et al., 2015). It should also be noticed that shaley prodelta deposits of the De Geerdalen/Snadd Formation has been observed in outcrops on Svalbard and is referred here to as the Tschermakfjellet Formation (Fig.3.3) (Klausen et al., 2015). This formation is time-equvivalent with the lower parts of the Snadd Formation in the Barents Sea and marks the transition from organic-rich offshore deposits of the Botneheia Formation to paralic deposits of De Geerdalen/Snadd Formation (Fig.3.3) (Klausen et al., 2015).

3.4.4 Flatsalen Formation

The Flatsalen Formation marks the Norian regional transgression which indicates a transition from a terrestrial environment with clastic sediments from the De Geerdalen/Snadd Formation to a marine environment (Fig.3.3). The Flatsalen Formation is characterized by an overall coarsening upward trend reflecting an offshore/transitional environment to a lower shoreface environment (Dallmann et al., 2015). The formation consists mainly of dark impermeable shale with thin siltstone intervals and is considered as an effective cap rock (Dallmann et al., 2015; Klausen et al., 2015).

3.4.5 Realgrunnen subgroup

Realgrunnen subgroup is part of the Upper Kapp Toscana Group and is correlative with the Wilhelmøya Subgroup at Svalbard, the Subgroup consists mainly of sand deposited in a shallow marine and coastal environment (Fig.3.3) (Riis et al., 2008). The subgroup consists of the following formations Kongsøya and Svenskøya at the eastern Svalbard also known as Stø and Tubåen in the Southern Barents Sea and the Fruholmen Formation (Fig.3.3). The sand of Realgrunnen subgroup is highly mature with a high permeability and documented porosity up to 25% as a result of coastal reworking and therefore constitutes as a great reservoir for the study area (Grogan et al., 1999; NPD, 2017).

3.4.6 Agardhfjellet Formation

The Agardhfjellet Formation of Late Jurrasic age corresponding to the Hekkingen and Fuglen formations further south (Fig.3.3). This formation was deposited mainly in an outer shelf/prodelta and lower shoreface/distal deltaic environment with anoxic shelf conditions (Dallmann et al., 2015). Minor siltstone, sandstone and carbonate concretions are common within this dark soft and plastic shale dominated formation, organic-rich mudstone intervals with TOC up to 10 % have been documented at Central Spitsbergen of Svalbard (Koevoets et al., 2018). The corresponding Hekkingen Formation is regarded as one of the most important source rocks in the southern Barents Sea (Koevoets et al., 2018).

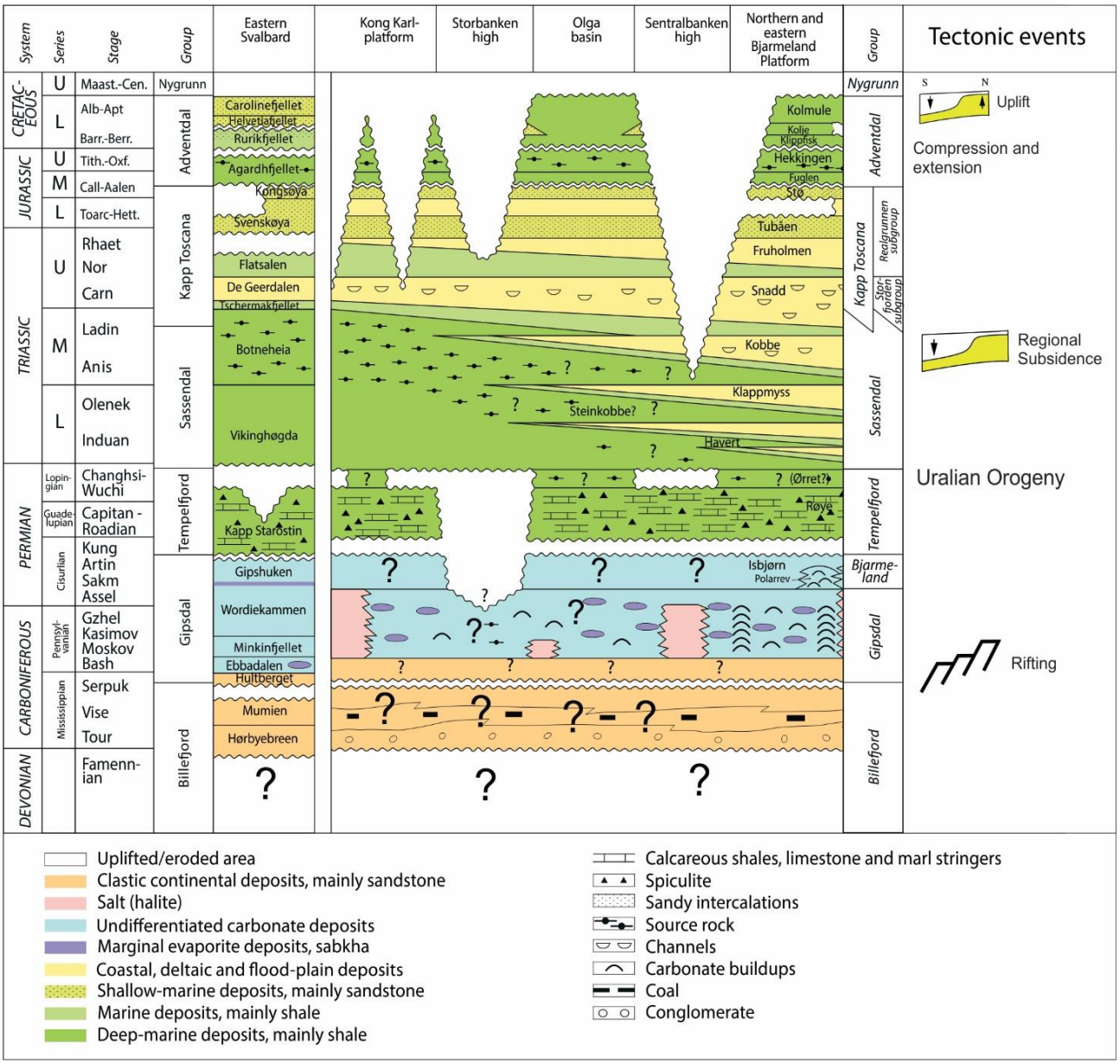

Fig.3.3: Stratigraphic overview of the main structural elements within the study area and how they correlate further south with the Southern Barents Sea and the Bjarmeland Platform. Modified from (Ostanin et al., 2012; NPD, 2017).

3.5 Structural elements

The Structural elements of the eastern parts of the northern Barents Sea can be divided into geological basins, highs and platforms with a relatively continuous sedimentary succession of late Paleozoic to early Cenozoic sediments (NPD, 2017).

Kong Karls Land platform

Kong Karls Land platform is believed to be a basement platoue as seismic data from NPD has indicated a chaotic reflection pattern in large parts beneath the Carboniferous sedimentary strata (NPD, 2017). The Kong Karls Land platform is mainly dominated by compressional anticlines oriented in a northeast-southwest direction which most likely is related to the reversal of older Paleozoic rifting and the inversion of old basins or grabens in late Mesozoic (Grogan et al., 2000). The Kong Karls Land platform has also been affected by salt tectonics initiating its movement after Late Triassic and magmatic intrusions following the bedding planes as sills and dykes related to the Early Cretaceous magmatic activity HALIP (Grogan et al., 1999; NPD, 2017).

Storbanken high

The Storbanken High is a large anticline bordering the Olga basin to the north, this structure is believed to be a basement platoue of Palaeozoic age with renewed uplift during the Late Jurassic – Early Cretaceous (Antonsen et al., 1991; NPD, 2017). This uplifted geological structure consists of several normal faulted horst and graben structures striking in an east-west direction, these extensional faults are prevailing from the seafloor and are believed to be related to the Late Jurrasic-Early Cretaceous uplift (Antonsen et al., 1991). The high consist of sediments from Paleozoic to late Mesozoic age, with a thin sedimentary package of Upper Carboniferous and Permian sediments, a large package of Triassic strata thinning northwards, and a thin package of Cretaceous and Jurassic sediments (Fig.3.4) (Grogan et al., 1999; NPD, 2017).

Olga basin

The Olga basin is an elongated syncline oriented in an east-west direction, the basin was initiated in Late Devonian to early Carboniferous related to the post-Caledonian Carboniferous rifting (Klitzke et al., 2019) (Fig.3.4). The basin is believed to been evolved as a W-E striking half-graben along a major normal fault in the north and with a smaller normal fault to the south as a result of transtensional deformation inheriting older lineaments from the Timanian orogeny to control the final W-E alignment of the basin (Klitzke et al., 2019). The basin also experienced renewed subsidence in Early Cretaceous as the flanks of the Olga Basin was uplifted with the Storbanken High to the north and Sentralbanken high to the south, this led to the deposition of Early Cretaceous sediments in the central parts of the basin (Antonsen et al., 1991; NPD, 2017). The Olga basin has large amounts of well-preserved successions of Cretaceous and Jurassic sediments which are highly eroded at the highs and platforms in the northern Barents Sea (Fig.3.4). The Olga Basin is therefore an important structure for understanding the Late Jurassic-Cretaceous development for the northern Barents Sea (Antonsen et al., 1991).

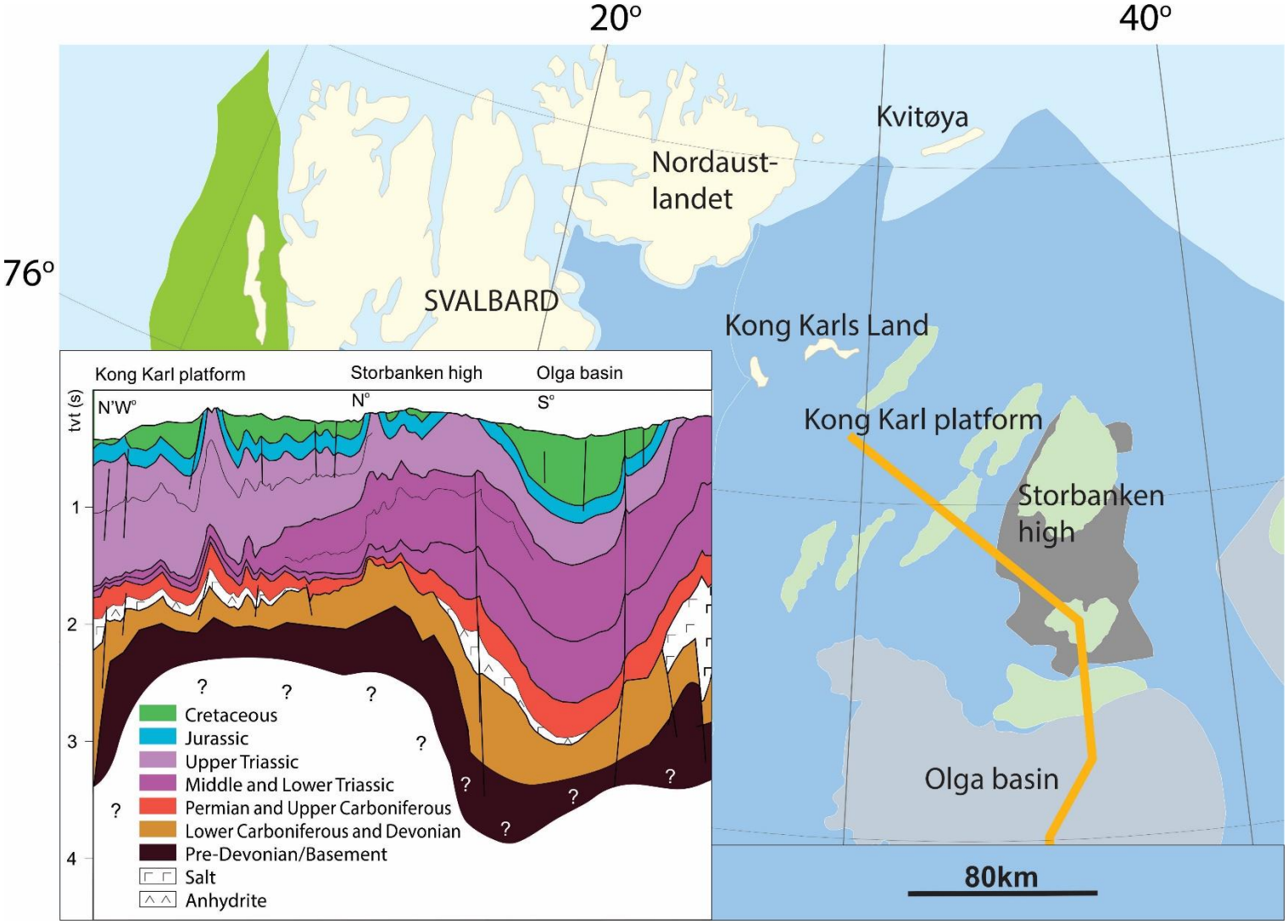

Fig.3.4: Structural elements of the northern Barents Sea within the study area, Orange line indicates the geoseismic profile. Modified from (NPD, 2017).

3.6 Glacial History

The northern Barents Sea has experienced multiple glaciations throughout the Quaternary, these glaciations can be summarized in three phases (Knies et al., 2009; Newton & Huuse, 2017). First the initial growth phase (3.6 Ma–2.4 Ma), then followed by the transitional growth stage (≈2.4-1.0 Ma) and lastly the final growth phase (≈1Ma) indicating the maximum extent of the ice sheet (Knies et al., 2009). During the last 1.5 Ma grounded ice and glaciation are believed to have reached the Barents shelf edge as much as eight times (Andreassen et al., 2004; Svendsen et al., 2004a).

The Barents Sea Ice Sheet (BSIS) reached the shelf edge one last time between 21.5-18.1 Ka BP and was connected to the glaciated mainland of Norway, also referred to as the Fennoscandian Ice Sheet (FIS) during the Late Glacial Maximum (LGM) (Fig.3.5a) (Newton & Huuse, 2017; Patton et al., 2017). The deglaciation and retreat of BSIS possibly initiated around 18-16Ka BP in Bjørnøyrenna, and the connection between FIS and BIS was probably disconnected between 16-15Ka BP (Newton & Huuse, 2017). The last stage of deglaciation in the Barents Sea occurred at the northern Barents Sea 10Ka BP after the Younger Dryas (12Ka BP) as the ice retreated towards Svalbard probably initiated by an abrupt Holocene climatic warming (Fig.3.5b) (Svendsen et al., 2004b).

Erosion related to the glaciation was extensive in the northern Barents Sea, with deposition of sediments mainly restricted to the western margin (Smelror et al., 2009). The repeated glaciations and periods of subsequent uplift in the northern areas around Svalbard led to the removal of as much as 2-3 Km of sediments and most of the Paleogene and Cretaceous sediments to be eroded during the Neogene (Ramberg et al., 2007; Smelror et al., 2009).

The repeated episodes of ice sheet loading and unloading caused episodes of pressurization and depressurization of thermogenic gases during the Pleistocene, these are events which could lead to large fluxes of natural gas to migrate upward in the subsurface (Andreassen et al., 2017).

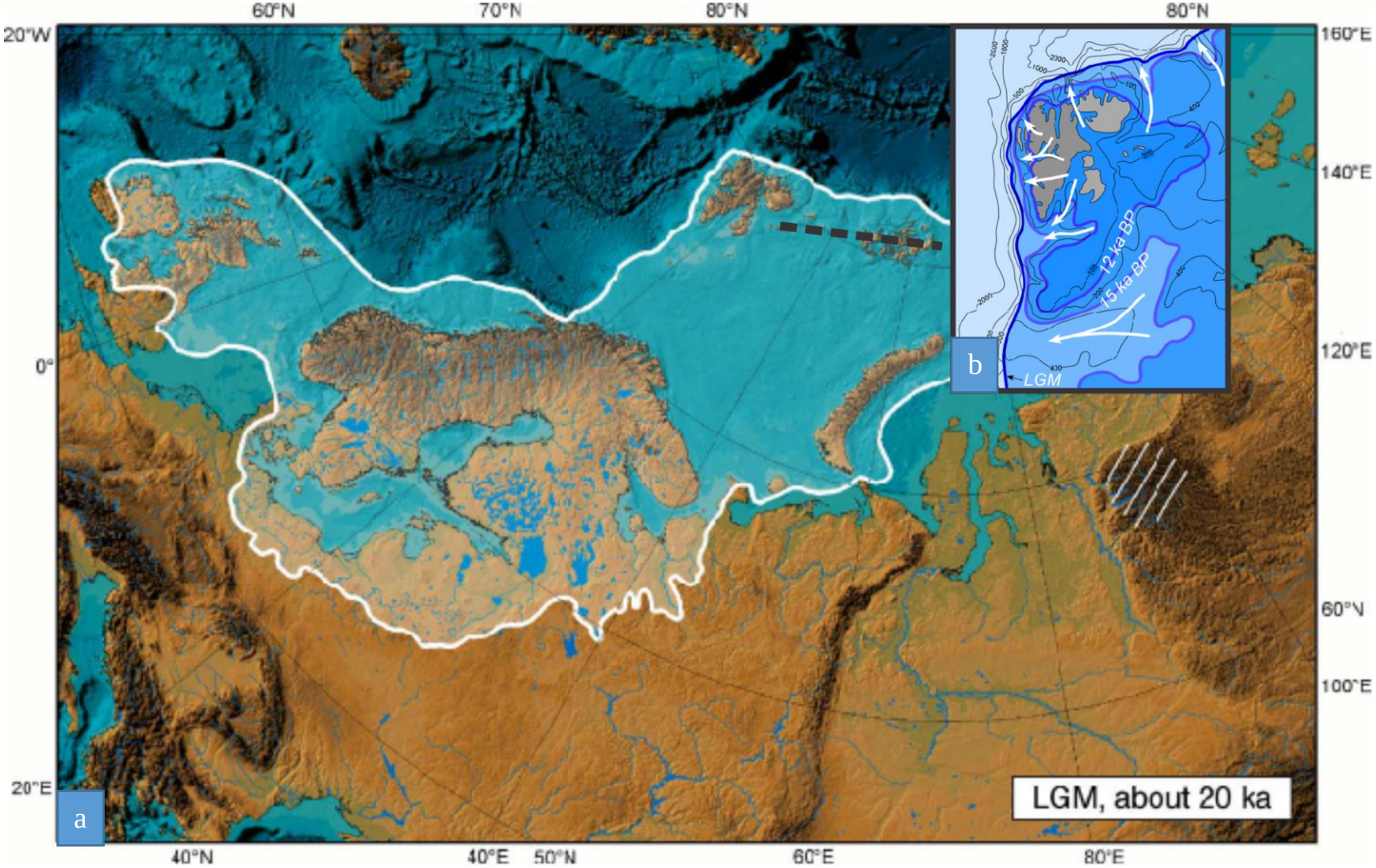

Fig.3.5: (a) Regional Glacial extent in the Barents Sea during Late Glacial Maximum (LGM). (b) Retreating pattern during LGM in proximity of Svalbard and the northern Barents Sea. Figure modified from (A): (Svendsen et al., 2004b)*(B):* (Ingólfsson & Landvik, 2013).

4 Data and methodology

4.1 Data

During the recently scientific cruise by CAGE-18-1 in May 2018, there were obtained different kinds of data along the North-western flank of the Olga basin and at the Storbanken high. The recently gathered 2D seismic, bathymetry and water acoustic data from CAGE in combination with 2D regional seismic lines from NPD, high-resolution bathymetric data from Mareano and well data from the southern Barents Sea provided by the University of Tromsø will constitute as a solid database for addressing the objectives for this thesis.

4.1.1 Well Data

As there are no available wells within the study area there has been used one well in the southern Barents Sea located at the Bjarmeland Platform (Well 7226/2-1) this well was drilled by Statoil in 2008 on the coordinates 72° 53' 31.6" N, 26° 35' 39.5" E (NPDfactpages) (Fig.4.1). The intention of this well is to correlate stratigraphic velocity from the southern Barents Sea with the northern Barents Sea, this will be further elaborated in chapter 4.2.3.

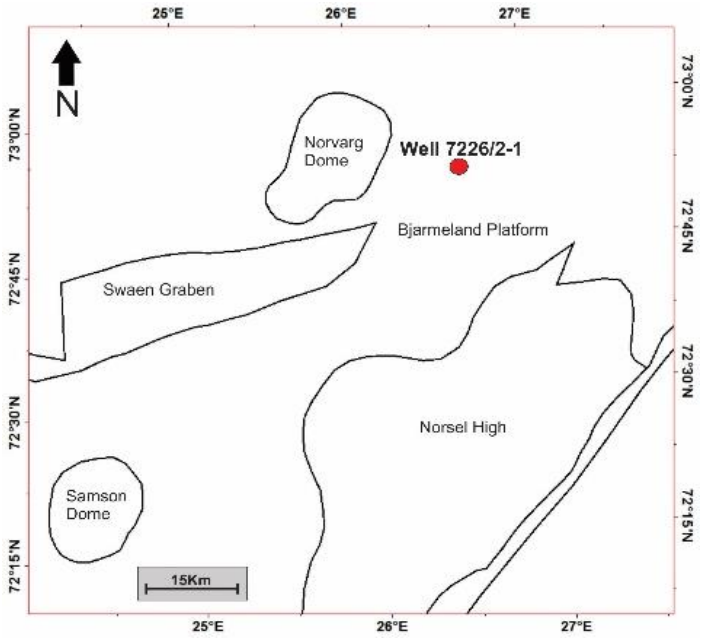

Fig.4.1: Location of the well 7226/2-1 used for stratigraphic velocity correlation for the Barents Sea South and the northern Barents Sea.

4.1.2 Seismic

The seismic interpretation of this study has been carried out based on a total of 26 regional 2D seismic lines from five different surveys distributed by the Norwegian Petroleum Directorate (NPD) and 29 high-resolution 2D seismic lines from CAGE (Fig.4.2 and Fig.4.3). Table 4.1 illustrates information for the six different seismic surveys and the available data used. Within survey NPD-STOB-90 there were obtained four lines of higher resolution, the characteristics of these are indicated with parenthesis in Table 4.1 and 4.2. The vertical extent of the different surveys is variable, especially the CAGE 18-1 survey which is highly affected by seafloor multiples, therefore the interpretable vertical extent is limited to the double Two-way traveltime (TWT) of the seafloor reflection for this survey and everything beneath the seafloor multiple is regarded as noise and not trustworthy (Table 4.1). The CAGE seismic is also affected by ghost reflections. In April 2019 the CAGE 18-1 survey was reprocessed by the NPD, the ghost reflection was attenuated but primary reflections below the seafloor multiple was not recovered properly most likely due to an insufficient source and potentially hard bedrock absorbing lots of energy. The original seismic from the CAGE 18-1 survey was best on visualizing structures in the seismic, the reprocessed seismic was however used as a supplement for detecting amplitude anomalies.

The 2D seismic lines of NPD was located 20 ms two-way traveltime (TWT) deeper than the CAGE seismic lines, this mismatch could easily be identified by the interpretation of the seabed reflection and intersecting seismic lines between CAGE and NPD seismic lines. The depth of the seabed in the seismic was examined relative to the high-resolution bathymetric data from CAGE, this indicated a seabed depth corresponding to the depth of the CAGE seismic. All the NPD lines were therefor uplifted with 20 ms to have a corresponding vertical depth as the CAGE seismic and the high-resolution bathymetry.

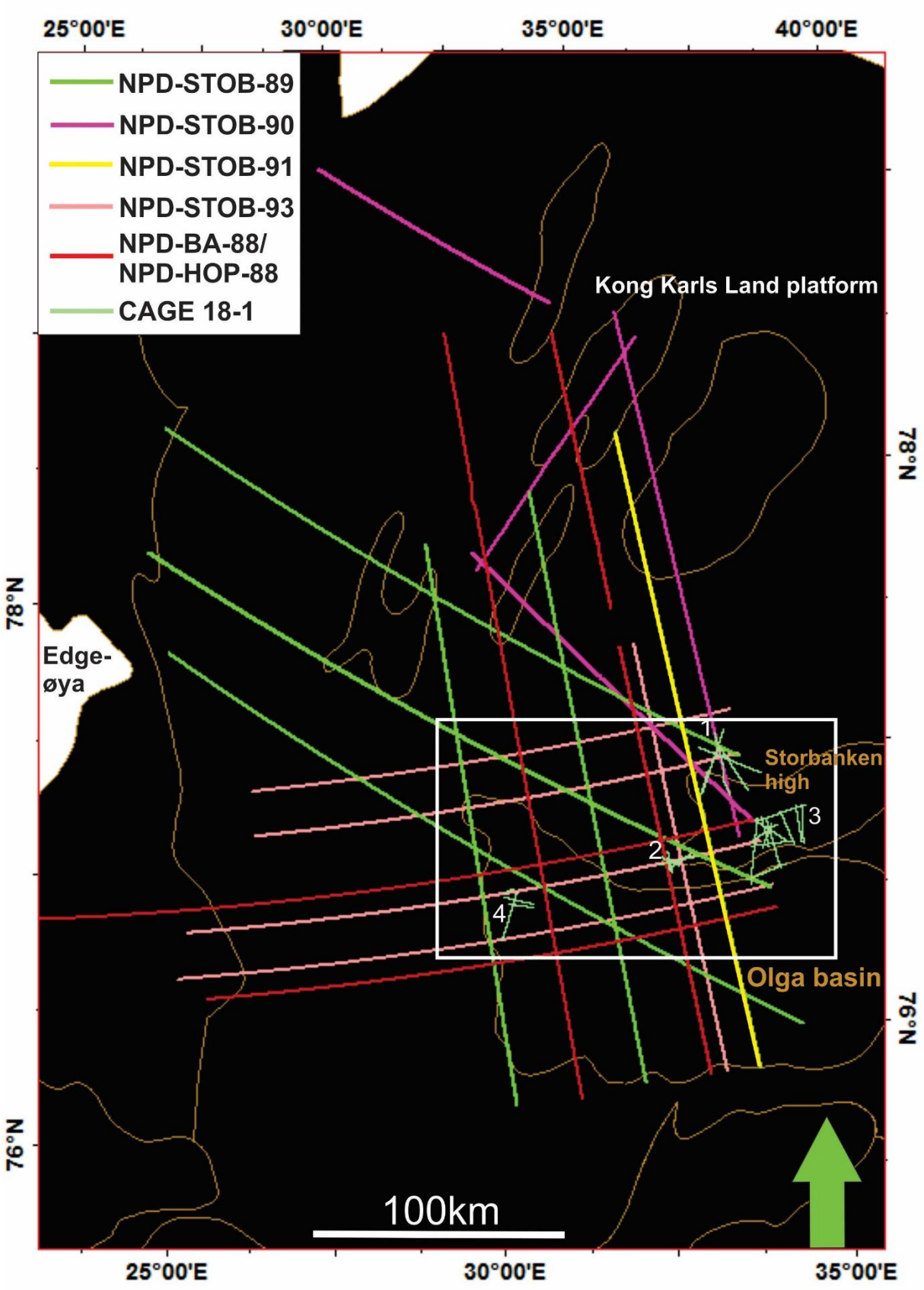

Fig.4.2: Location of the different seismic lines. The numbers 1-4 represents the different locations for the CAGE 18-1 seismic bound by the white rectangle as illustrated in Fig.4.3. The orange polygons represent the structural elements in the study area.

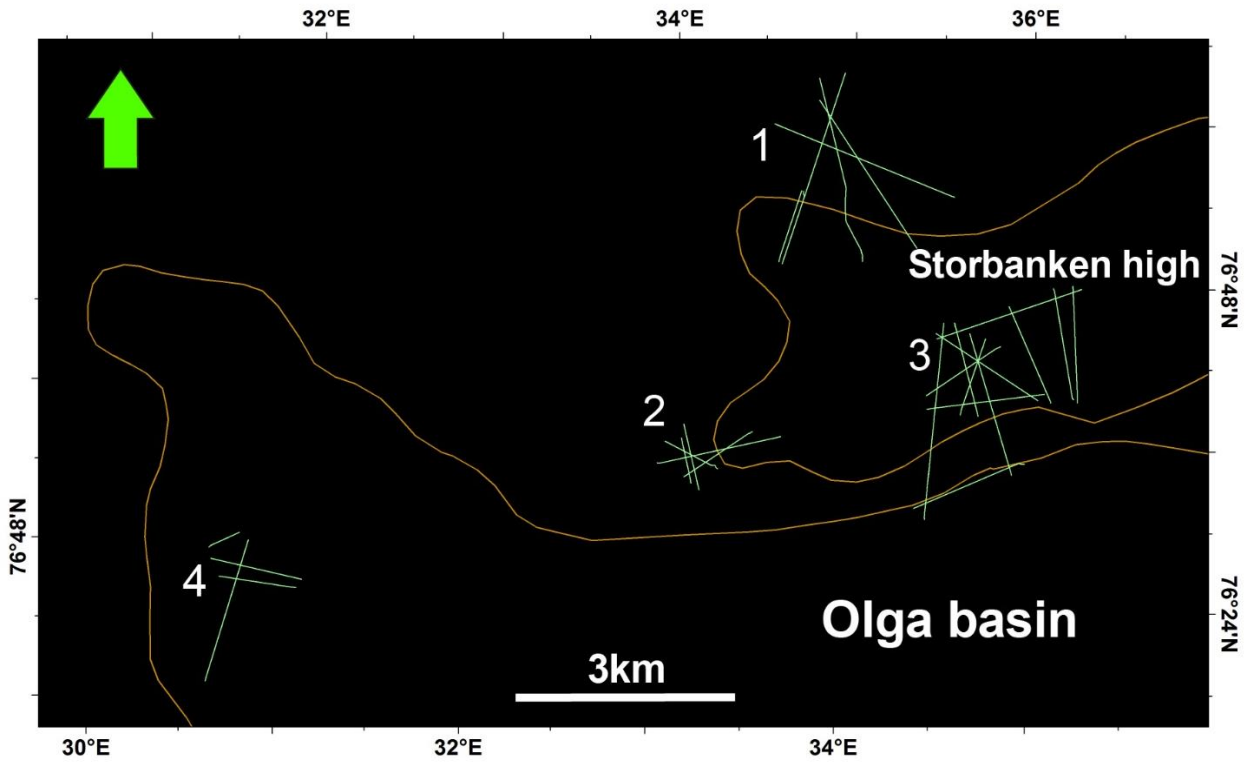

Fig.4.3 Closer overview of the seismic lines from the CAGE 18-1 survey. The location of the seismic lines in a regional perspective is illustrated in Fig.4.2 bound by the white rectangle. The orange polygons represent the structural elements of the Olga basin and Storbanken high.

Table 4.1: Overview of the six different seismic surveys used. () indicates the high-resolution seismic lines of NPD.

Survey Name	*Company responsible*	*Gathered by*	*Number of lines*	*Total length*	*Interpretable Vertical depth (TWT)*
CAGE 18-1	CAGE	CAGE	29	435 Km	300 to 800 ms
NPD-STOB-89	NPD	GECO	8	1355 Km	6000 ms
NPD-STOB-90	NPD	GECO-PRAKLA	2 (4)	382(608)Km	5000(1000) ms
NPD-STOB-91	NPD	MASTER	1	27 km	6000 ms
NPD-STOB-93	NPD	GEO-TEAM	6	1277 Km	7000 ms
NPD-BA-88/ NPD-HOP-88	NPD	Unspecified	5	1179 Km	6000 ms

There are two main conventions regarding the phase of seismic, these are minimum-phase and zero-phase (Fig.4.4). There also exist two polarity conventions, the polarity convention of Badly (1985) and the Society of Exploration Geophysicists (SEG) polarity convention of Sheriff (1999). These are two opposites when referring to polarity, this means a positive reflection coefficient would be represented with normal polarity as two small side peaks and a central trough with the Badly convention (1985) and two small side troughs and a central peak with the Sheriff convention (1999) for a zero-phase signal (Fig.4.4) (Veeken, 2013). A minimum phase signal with normal polarity in Sheriff convention (1999) would be represented with a small trough and a big peak and vice versa for Badly convention (1985). For simplicity will only the convention of Sheriff (1999) be used in this thesis when referring to polarity. The data used in this thesis is of both minimum phase and zero-phase, the phase and polarity were examined by using the positive high reflection coefficient exerted by the seafloor displayed in wiggle display (Fig.4.4). Information regarding the Polarity, phase and dominant frequency of the different surveys are illustrated in Table 4.2.

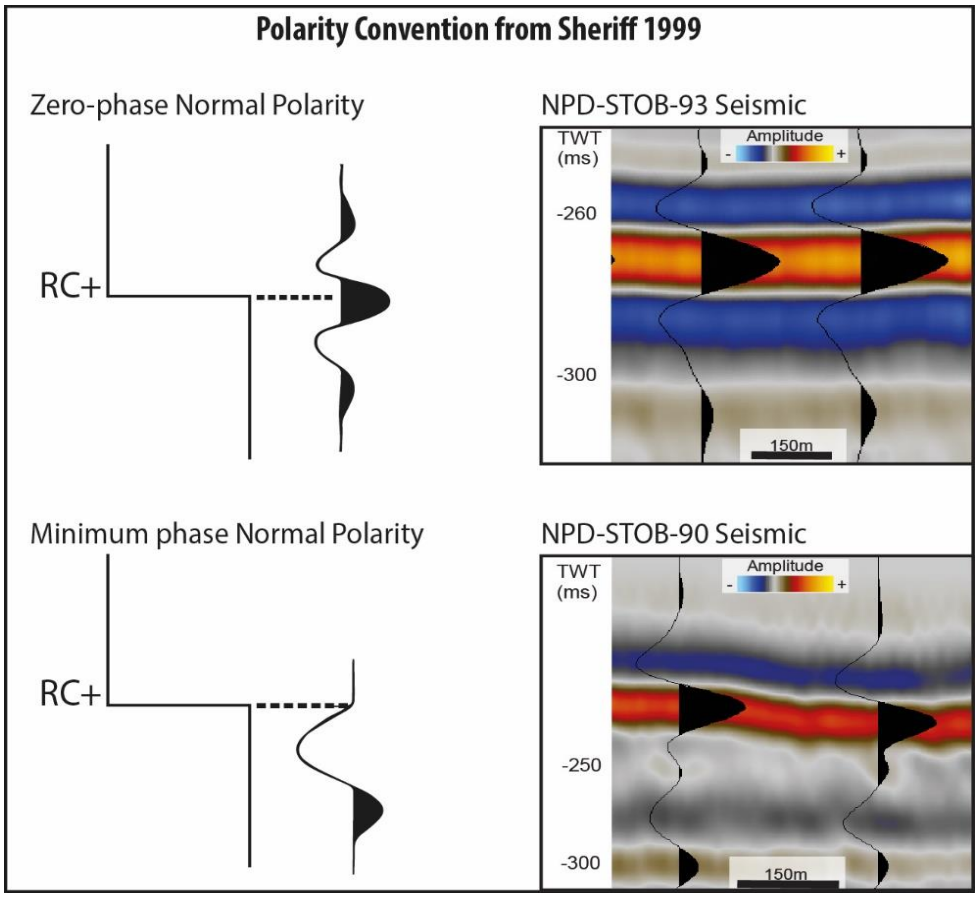

Fig.4.4: The seismic from the NPD surveys STOB-93 and STOB-90 illustrating the reflection exerted by the seafloor.

Table 4.2: Overview of the frequency, polarity and phase of the six different surveys used. () indicates the high-resolution seismic lines from NPD.

Seismic Survey	*Dominant frequency (Hz)*	*Polarity (Sheriff convention)*	*Phase*
CAGE 18-1	68	Normal	Minimum phase
NPD-STOB-89	18	Normal	Zero-Phase
NPD-STOB-90	20(50)	Normal(Reversed)	Minimum Phase
NPD-STOB-91	19	Normal	Zero-Phase
NPD-STOB-93	15	Normal	Zero-Phase
NPD-BA-88/ NPD-HOP-88	20	Normal	Minimum Phase

Based on Equation 2.4 and Equation 2.5 defined in chapter 2.3.1, both the vertical resolution and Fresnel was calculated for two different depth intervals (Table 4.3). The horizontal resolution is drastically improved by seismic migration and collapsing of the Fresnel zone, in general is the horizontal resolution for migrated seismic reduced to the trace spacing (Veeken, 2007). Both the NPD and CAGE seismic was migrated and had a trace spacing of 12,5 m and 3,125 m examined in the wiggle display. By using the frequency spectral analyzing tool the dominating frequencies could be determined for the seafloor and the Agardhfjellet Formation. As the NPD seismic had very similar frequencies while the CAGE seismic had notable higher frequencies, these were separated into two groups as they would have significantly different resolutions. The mean value of dominating frequency of all the NPD seismic lines from the different surveys was calculated while the mean value of dominating frequency was calculated from the CAGE seismic to use in the calculation for a rough estimation of vertical and horizontal resolution (Table.4.3). As there were no available wells in the area velocities had to be assumed, a velocity of 1500 m/s was used for calculations of seafloor resolution as this is a common velocity for saltwater. The interval velocity of Agardhfjellet Formation was found to be approximately 2650 m/s based on the corresponding interval velocity of the Hekkingen and Fuglen formations measured with the sonic log of Well 7226/2-1 (Appendix A).

Table 4.3: Calculation of vertical resolution and Fresnel zone for the different surveys at the Olga basin. Notice how the resolution is affected by velocity and frequency.

Dataset	Measured interval	Average interval Velocity (v)	Depth Two-way travel time (t)	Frequency (f)	Wavelength $\lambda = \frac{v}{f}$	Vertical resolution $v_r = \frac{\lambda}{4}$	First Fresnel zone $rf = \frac{v}{2}\sqrt{\frac{t}{f}}$
CAGE 18-1	Seafloor	1500 m/s	0,375 s	72 Hz	20,8 m	5,2 m	54,1 m
CAGE 18-1	Agardhfjellet Formation	2650 m/s	0,6 s	51 Hz	52 m	13 m	143,7 m
NPD	Seafloor	1500 m/s	0,375 s	26 Hz	57,7 m	14,4 m	90,1 m
NPD	Agardhfjellet Formation	2650 m/s	0,6 s	21 Hz	126,2 m	31,5 m	224 m

4.1.3 Multibeam Echosounder

During the cruise of CAGE-18-1 in May 2018 there were in addition to seismic data also gathered bathymetric and water acoustic data. A Kongsberg Simrad EM 302 multi-beam echo sounder was used, this multi-beam system measures the two-way travel time for a sound wave to reach the seafloor. The pulses of sound waves had a frequency of 30 kHz which produces the high-resolution bathymetric maps, in addition to scanning the seafloor there were also obtained water acoustic data which detects gas bubbles as acoustic flares in the water column.

4.1.3.1 Bathymetry

The CAGE multibeam bathymetric data were collected at the same locations as the high-resolution CAGE 2D seismic lines, plus an additional rectangle of approximately 57km^2 obtained (Fig.4.5). The bathymetric data of CAGE was recorded with a beam angle of 60/60 with two transducers generating 432 beams each, this produced a swath width of approximately 1100 m at the deepest parts of the N'W Olga basin and a width of

approximately 500 m at the shallowest areas of Storbanken high. The bathymetry is separated into four different surveys corresponding to the four areas of seismic acquisition, the four bathymetric surveys have all different degree of resolution (Table. 4.4). In addition to Bathymetric data gathered by CAGE, there was also available high-resolution bathymetric data gathered by Mareano. This data was obtained in 2015 by using a Kongsberg Simrad EM710 echo sounder covering an area of approximately 525km^2 with a high resolution of 5 m at the Storbanken high (Mareano, 2017) (Fig.4.5).

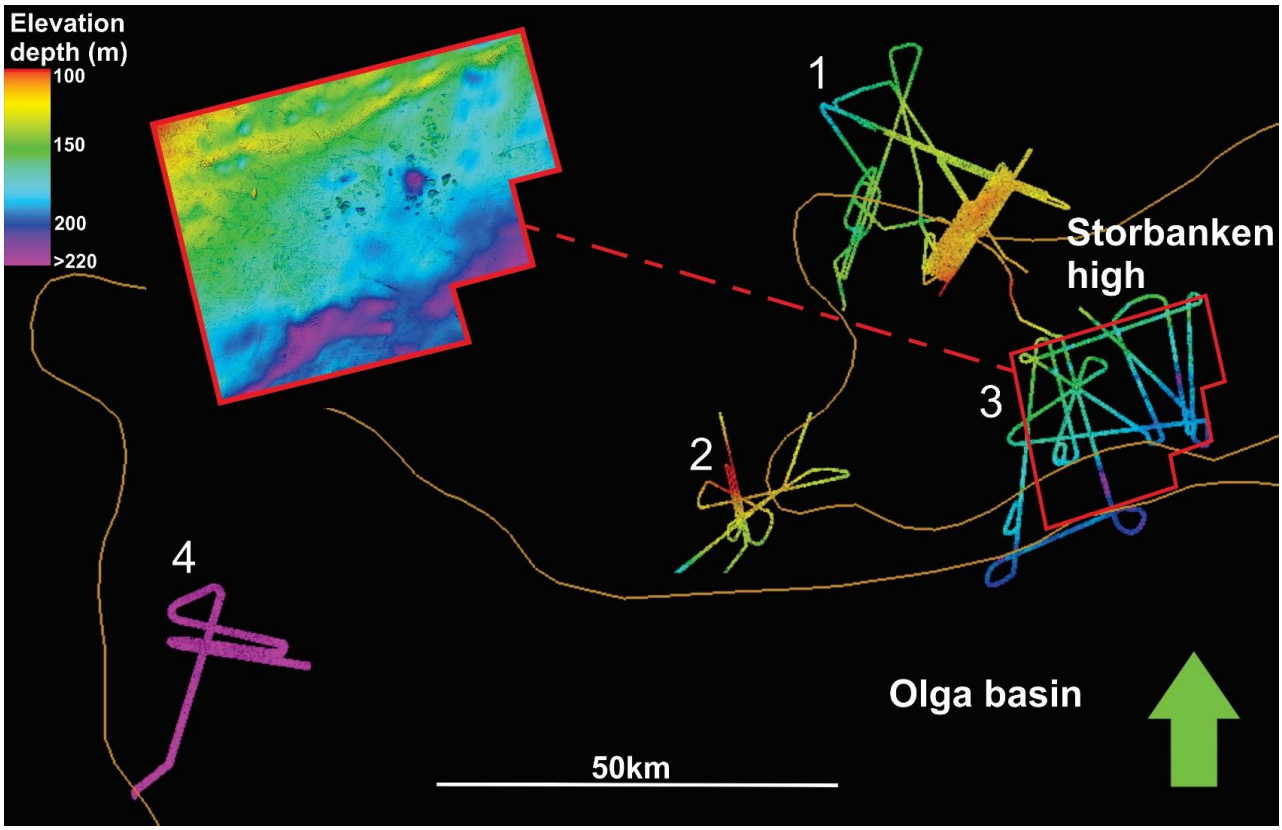

Fig.4.5: The four different bathymetric data collected by CAGE, the numbers represent the same locations as indicated in Fig.4.2. The red polygon represents the bathymetric data distributed by Mareano. Orange polygon delineates the structural elements of the Olga basin and Storbanken high.

Tabell 4.3 Bathymetric resolution of the data illustrated in Fig.3.4.

Bathymetric survey	**Resolution (m)**
CAGE-1	3
CAGE-2	4
CAGE-3	4
CAGE-4	10
Mareano	5

4.1.3.2 Water column acoustic data

The Simrad EM 302 multibeam echosounder system was also used to record water column acoustic data. Gas bubbles in the water column enforce large changes in the acoustic properties of the water column and are therefore easily recorded as the gas imposes strong velocity and density contrast between the bubbles and the water-column (Jansson, 2018). The gas flares is a reliable indication of active gas seepage sites and are therefore used as a supplement for detecting active leaking subsurface structures. The search width of the investigated area corresponds to the swath width of the bathymetric data. There were recorded a total of 380 gas flares distributed along the investigated area (Fig.4.6).

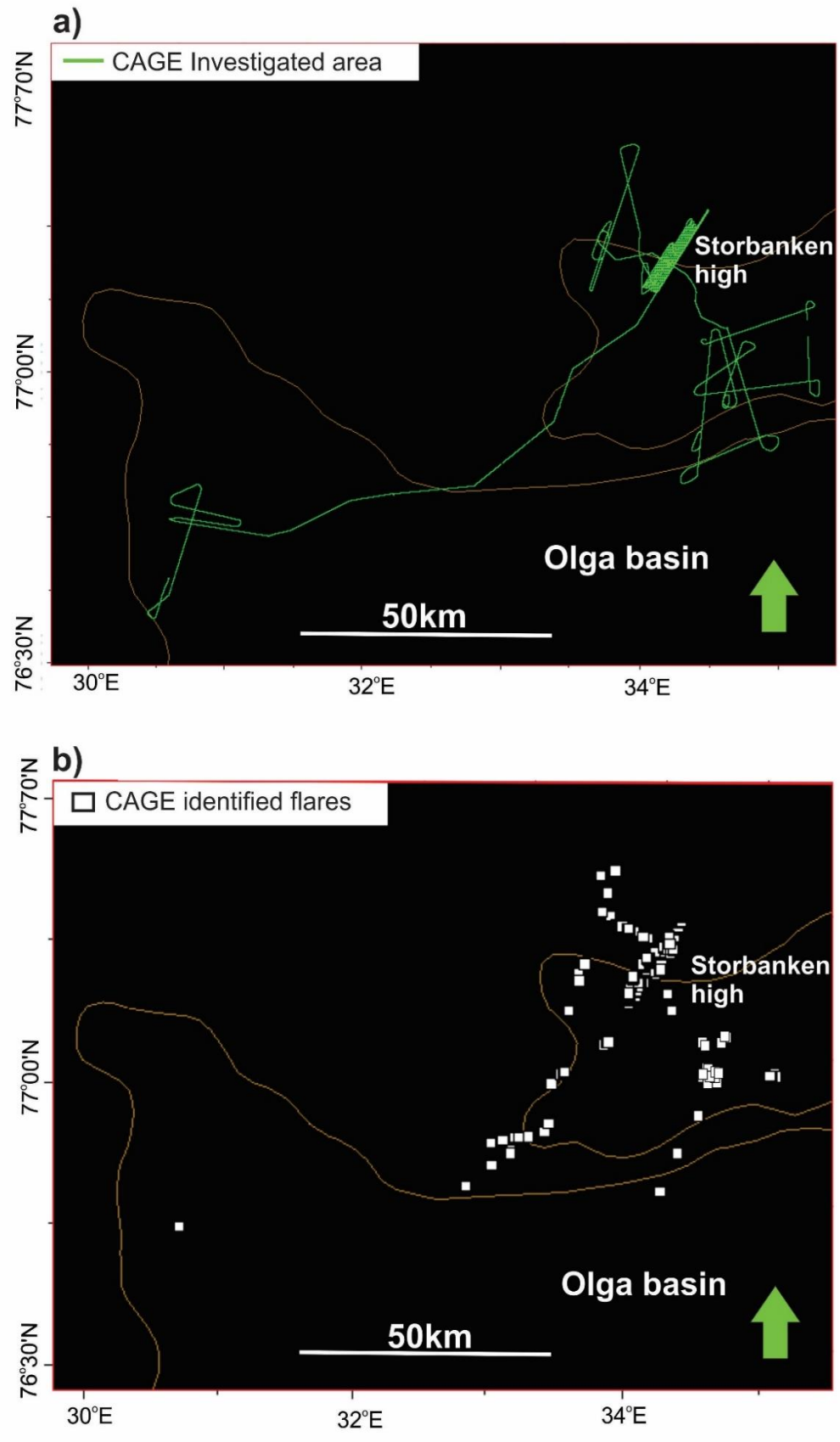

Fig.4.6: a) Areas investigated with EM-302 multibeam echosounder for water column acoustic data. B) Areas with identified gas flares. The orange polygons delineate the structural elements of the Olga basin and Storbanken high.

4.2 Methodology

All the interpretation and visualization of seismic, bathymetric data and gas flares have been carried out by the usage of the Schlumberger's software Petrel 2017. The Fledermous Mid water software was used for picking acoustic flares which were done by CAGE, in addition has Fledermous been used for interpretation of bathymetric data and presenting geomorphological cross-sectional profiles. All figures and illustrations have been made in the graphical software's CorelDraw 2017 and Adobe Illustrator.

4.2.1 Stratigraphic analysis

As there were no available wells in the study area the stratigraphy has been determined by expertise help from NPD and the usage of the NPD geological assessment report of petroleum resources in the eastern parts of the northern Barents Sea (NPD, 2017) to pick the correct reflectors. The reflectors are primarily interpreted manually, with seeded 2D autotrack only used at the most continuous reflectors mainly in areas at the Olga basin. Due to the lack of well data confirming the correct placement for the formations and large distances between the seismic lines there have been some challenges with the interpretations.

4.2.2 Structural analysis

In order to examine the faults and potential gas chimneys in the study area the seismic attribute variance edge method was used in petrel. This attribute measures the trace-to-trace variance for a particular interval and generates a variance coefficient independent of amplitude (Schlumberger, 2011). Areas with a high variance coefficient represent reflectors with a high degree of discontinuity commonly associated with seismic features such as faults, gas chimneys, salt, basement, etc. While areas with a low variance coefficient represent reflectors with a high continuity commonly associated with undisrupted conform stratigraphic layers.

4.2.3 Stratigraphic velocity correlation

In order to examine the maturity and gas hydrate stability zone which will be further elaborated in chapter 6.2 and 6.5 it's important to know the mean interval velocity for the different formations in the study area. The well at the Bjarmeland Platform was therefore used for the correlation as it to some degree shares the same lithologies and has according to Henriksen et al, (2011a) been exposed to approximately the same amount of erosion and uplift as the study area in the northern Barents Sea (Fig.3.3 and 4.7). The erosion and uplift is regarded due to burial history which influences the maturity of source rocks but also compaction which governs porosity and velocity of the sediments.

The correlation of the formations is based on the chronostratigraphic and lithostratigraphic diagram of NPD, (2017) the net erosion model by Henriksen et al, (2011a) and the sonic log of Well 7226/2-1 (Appendix A) (Fig.3.3 and 4.7). The sonic log measured the formations from Nordland Group to the Havert Formation at the Bjarmeland Platform as seen in Appendix A, the mean interval velocity of the Hekkingen/Fuglen, Tubåen, Fruholmen, Snadd and Kobbe Formation were extracted to correlate velocity for formations in the northern Barents Sea. The mean velocity of Realgrunnen subgroup had to be based on the Fruholmen- and Tubåen formations as the Nordmela and Stø formations were not present in the velocity log. As the open shelf marine shale of Kobbe share some similarities with the Botneheia Formation excluding the locally organic-rich intervals of Botneheia Formation was these two correlated to each other (Fig.3.3).

When correlating these two formations it's worth taking into consideration the effect which the organic-rich intervals of Botneheia Formation impose on the velocity. Studies by Harris, (2015) has indicated a systematically decrease of velocity by 20-25 % when there is a TOC increase from 0 to 10%. Progressively reduced formation interval velocity as a result of increasing TOC has also been confirmed by Løseth et al, (2011) in the Barents Sea with the source rock of the Hekkingen Formation. Due to little information regarding the extent of the locally high TOC intervals of the Botneheia Formation and the effect on the velocity it was assumed that the Botneheia Formation had a lower interval velocity of 400 m/s less than the Kobbe Formation.

Interval velocities for the different formations are indicated in Table 4.5, the mean interval velocity of the Botneheia Formation is annotated with parenthesis. Mean formation velocity of the Flatsalen Formation and lithologies located deeper than the Havert Formation was not

examined by well 7226/2-1. The sediment velocities (Upper Triassic, Lower Triassic, Permian and Carboniferous) was therefore correlated by the velocities at the Bjarmeland Platform used by Ktenas et al, (2018) in his multi-layer velocity inversion model for examining compaction-based net apparent erosion (Appendix B).

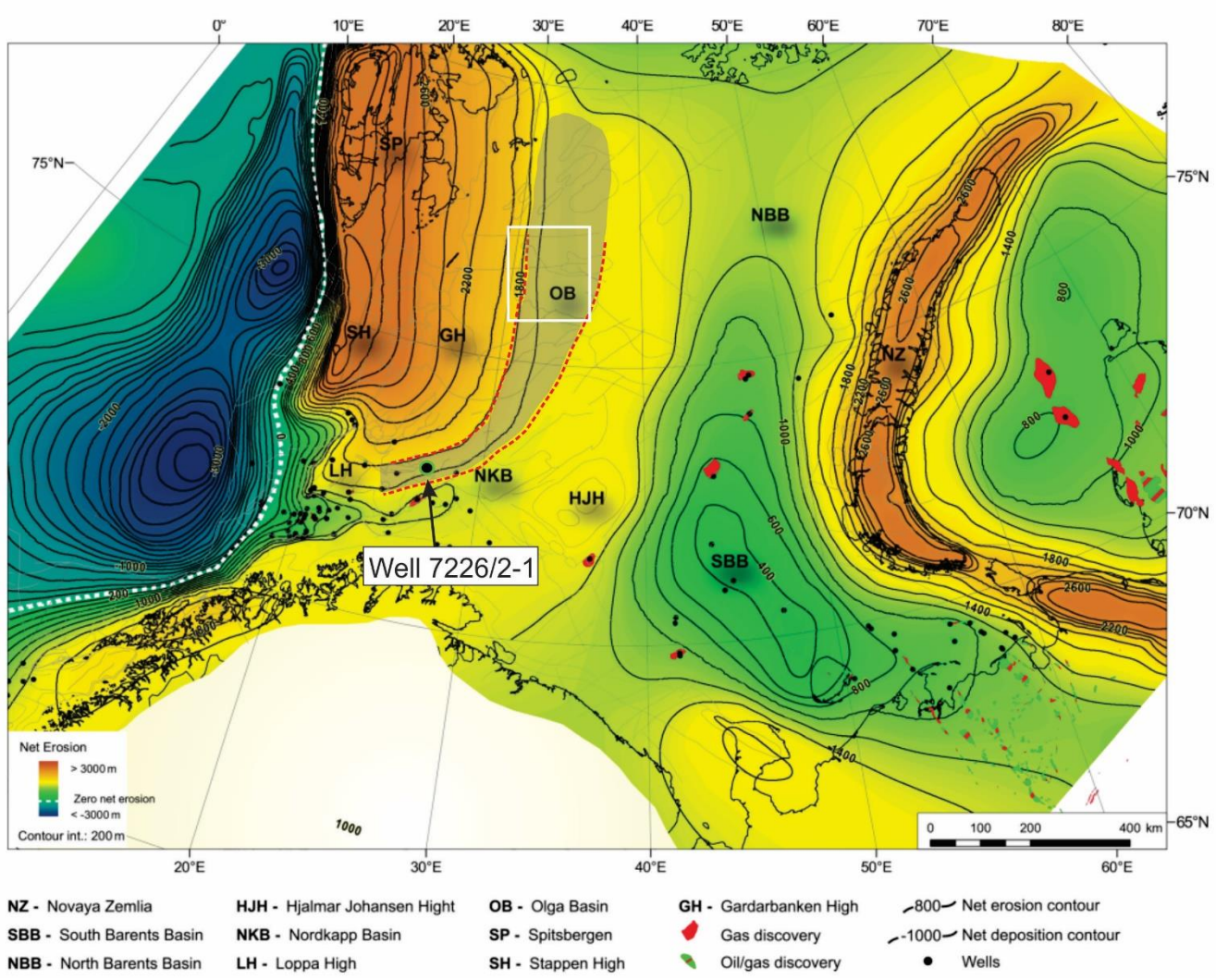

Fig.4.7: Overview of the net erosion in the Barents Sea, the shaded polygon indicates the similar erosion interval between the Bjarmeland Platform (well 7226/2-1) and the Olga basin and Storbanken high. The white square delineates the study area. Figure modified from: (Henriksen et al., 2011a).

Table 4.5: Mean interval velocities for formations in the northern Barents Sea correlated with formations at the Bjarmeland Platform in the Barents Sea South. () indicates the assumed velocity for the Botneheia Formation. Velocities for Flatsalen Formation, Triassic, Permian and Carboniferous from (Ktenas et al., 2018) *Appendix B.*.

Formation name Barents Sea South	Formation name northern Barents Sea	Mean Interval Velocity
Hekkingen- and Fuglen FM	Agardhfjellet FM	2650 m/s
Fruholmen- and Tubåen FM	Realgrunnen Subgroup	3000 m/s
Upper Triassic	Flatsalen FM	3100 m/s
Snadd FM	Snadd/De Geerdalen FM	3300 m/s
Kobbe FM	Botneheia FM?	3600 m/s (3200 m/s)
Lower Triassic	Lower Triassic	4800 m/s
Permian - Carboniferous	Permian - Carboniferous	5800 m/s

4.2.4 Gas hydrate stability zone modeling

The gas hydrate stability zone (GHSZ) was modeled for the study area using the CSMHYD program by Sloan & Koh (2008) which generate pressure-temperature phase boundary curves for hydrates with mixed gas compositions. The program calculates the GHSZ based on the following parameters: water depth, bottom water temperature, thermal gradient, pore water salinity and gas composition of the gas hydrate. A little change in one or several of these parameters will affect the presence or depth of the GHSZ.

Recent gather CTD (conductivity, temperature and depth) data from the CAGE-18-1 cruise which examines the physical properties of the water was utilized for the GHSZ model (Appendix C). The velocity of the sediments to determine depth was utilized based on the velocity correlation of the stratigraphy between the Barents Sea North and Barents Sea South (Table 4.5). Since the geothermal gradient in the Barents Sea is highly variable and there is no available information regarding geothermal gradient in the northern Barents Sea there had to be assumed an average geothermal gradient of 35 ^{o}C/km in the study area (Fig.4.8).

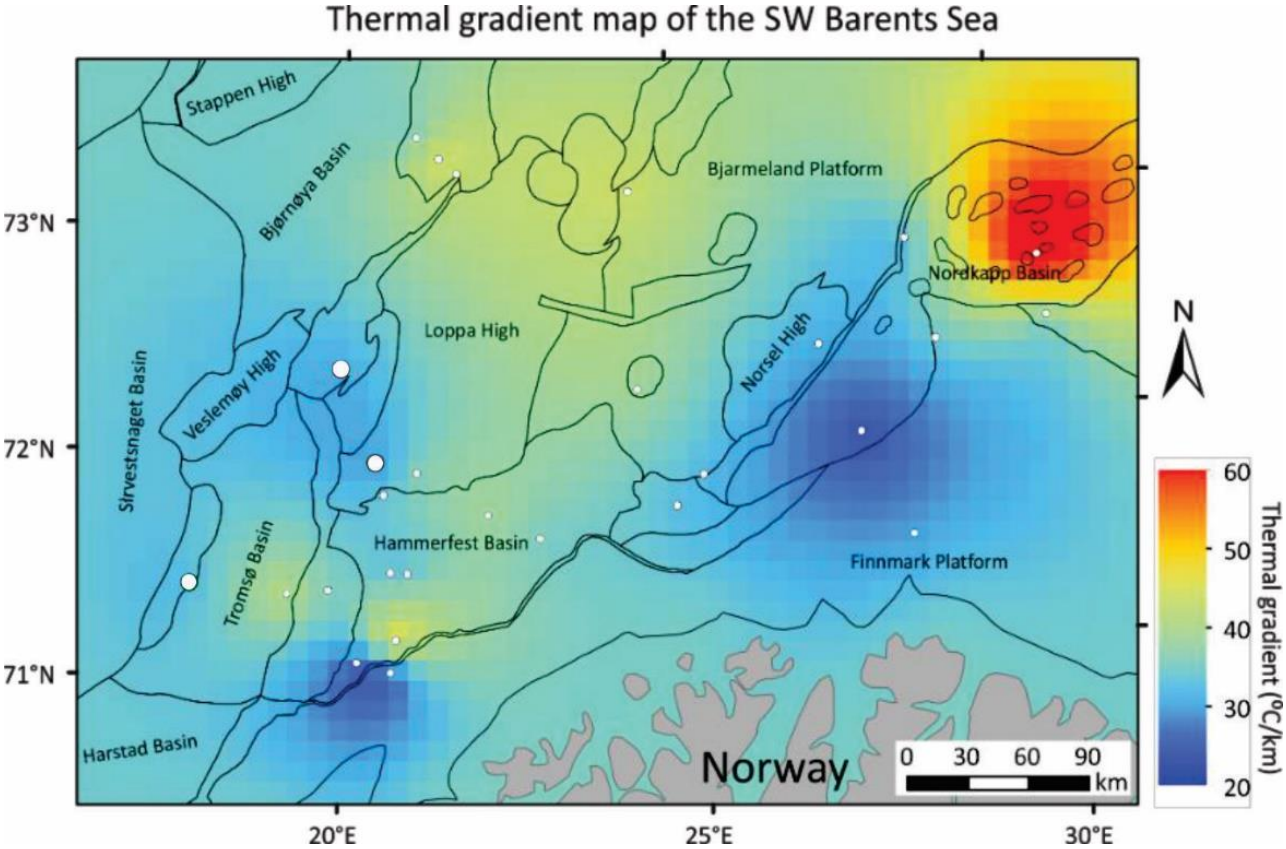

Fig.4.8: Geothermal gradient model of the SW Barents Sea based on bottom hole measurements from wells indicated as white dots and published data by (Bugge et al., 2002). *Modified from* (Vadakkepuliyambatta et al., 2017a).

5 Results

This Chapter is dedicated to documenting all observations and interpretations in the study area. The main focus has been to interpret formations, faults, geomorphology and seismic amplitude anomalies. Identification of a potential Bottom simulating reflector (BSR) was also done which will be used for further discussion of the gas hydrate potential in the study area.

5.1 Stratigraphy

This Chapter is dedicated to present the stratigraphy and the reflectors interpreted within the study area (Fig.5.1). The main emphasis of this study will be on the formations within Mesozoic, as several publications have indicated this era as containing the majority of petroleum plays in the study area (Grogan et al., 1999; Worsley, 2008; NPD, 2017).

5.1.1 Top Billefjorden Group

The Top Billefjorden Group is represented by a middle Carboniferous reflector. The reflector is interpreted on a peak with two associated strong and continuous troughs (Fig.5.2). The reflector is mainly represented by a positive reflection amplitude, however following the reflector it becomes negative at certain areas with a strong central trough which might explain the local coal bodies of the Billefjorden Group. The Top Billefjorden Group is located as deep as 2900 ms (TWT) at the Olga basin and as shallow as 1700 ms (TWT) at the central parts of Storbanken high (Fig.5.2).

5.1.2 Middle Carboniferous - late Permian

The sediment package from middle Carboniferous to late Permian age is represented by the middle Carboniferous reflector and Top Permian reflector (Fig.5.2-5.3). The Top Permian reflector represents a positive reflection coefficient and is interpreted on a relatively continuous peak, the Top Permian reflector is however, more discontinuous at the Storbanken high imposing some challenges in the interpretation of this reflector (Fig.5.2-5.3). The Top Permian reflector is located as deep as -2550 ms (TWT) at the Olga basin and at depths of -1650 ms (TWT) at the Storbanken high (Fig.5.2-5.3). The middle Carboniferous – Top Permian sedimentary package is relatively uniform throughout the Olga basin with a thickness

of approximately 450 ms (TWT) (Fig.5.2). This sedimentary package thins towards the Storbanken high where it has a thickness of 300 ms (TWT) at the high (Fig.5.3).

5.1.3 Botneheia Formation

The Top Botneheia Formation is represented by a late Anisian reflector, while the base is represented by a late Olenekian reflector in the study area (Fig.5.2). There is great uncertainty in the interpretation of the Botneheia Formation at the Storbanken high due to the quality of the data, chaotic reflections and dens faulting (Fig.5.3-5.4). The interpreted late Anisian reflector is relatively discontinuous with a negative reflection coefficient, while the late Olenekian reflector is indicated by a continuous reflection with a positive reflection coefficient (Fig.5.2). The thickness is relatively uniform throughout the Olga basin and Storbanken high with a thickness of 270 ms (TWT). The base of the formation is identified at depths as deep as 1700 ms (TWT) in the central parts of the Olga basin and 1100 ms (TWT) at the Storbanken high (Fig.5.2-5.3).

5.1.4 De Geerdalen/Snadd Formation

The De Geerdalen/Snadd Formation was interpreted between the Top De Geerdalen/Snadd reflector and the late Olenekian reflector (Fig.5.2-5.4). The Top De Geerdalen/Snadd reflector is represented by a positive reflection coefficient, the reflector is relatively discontinuous throughout the whole study area, with the reflector being slightly more continuous within the Olga basin. This formation constitutes a 250 ms (TWT) thick sedimentary package at the Olga basin, it was difficult to measure the thickness at Storbanken high as the formation was highly affected by faults and chaotic reflections (Fig.5.2-5.4).

5.1.5 Flatsalen Formation

The Top Flatsalen Formation is represented by an early Rhaetian reflector, while the base is represented by the Top De Geerdalen/Snadd reflector from late Carnian age (Fig.5.2). The Top Flatsalen reflector is represented by a positive reflection coefficient, this reflector is relatively discontinuous throughout the study area, with the reflector being a little more continuous at the Olga basin and central parts of Storbanken high within the CAGE seismic. There were challenges related to the interpretation of this formation due to chaotic reflection

patterns and complex faulting especially along the western and northern flanks of Storbanken high (Fig.5.3-5.4). The thickness of the formation is relatively uniform with an approximate thickness of 70 ms at the Olga basin and a thickness of 80 ms further North at Storbanken high. The base of the formation is located at depths of 1200 ms (TWT) at the central parts of the Olga basin, the formation is present throughout the study area except for certain areas at the shallowest parts of the Storbanken high, where the formation is eroded and terminates against the seafloor (Fig.5.3 and 5.5-5.6).

5.1.6 Realgrunnen subgroup

The Top Realgrunnen subgroup is represented by the Base Upper Jurassic reflector, while the base of the formation is represented by the Top Flatsalen reflector (Fig.5.2-5.4). The Realgrunnen subgroup is located between the Flatsalen Formation and Agardhfjellet Formation and has a relatively uniform thickness of 155 ms (TWT) throughout the Olga basin and Storbanken high. The subgroup is present throughout large parts of the study area with the base of the subgroup being located as deep as 1150 ms (TWT) at the central parts of the Olga basin and the group being eroded and outcropping at the seafloor at certain areas of the Storbanken high (Fig.5.2-5.4).

5.1.7 Agardhfjellet Formation

The Top Agardhfjellet Formation is represented by the Base Cretaceous reflector, while the base is represented by the Base Upper Jurassic reflector (Fig.5.2-5.4). The Base Cretaceous reflector is characterized by a strong continuous negative reflector which is easily traced throughout the study area. However, some faulting and outcropping reflectors terminating against the seafloor at the Storbanken high has imposed some challenges for the interpretation (Fig.5.3-5.4). The Formation has a uniform thickness varying from 60-90 ms (TWT) and is located at a maximum depth of 1000 ms (TWT) at the Olga basin. The formation is eroded and outcrops at the seafloor throughout large parts of Storbanken high (Fig.5.7).

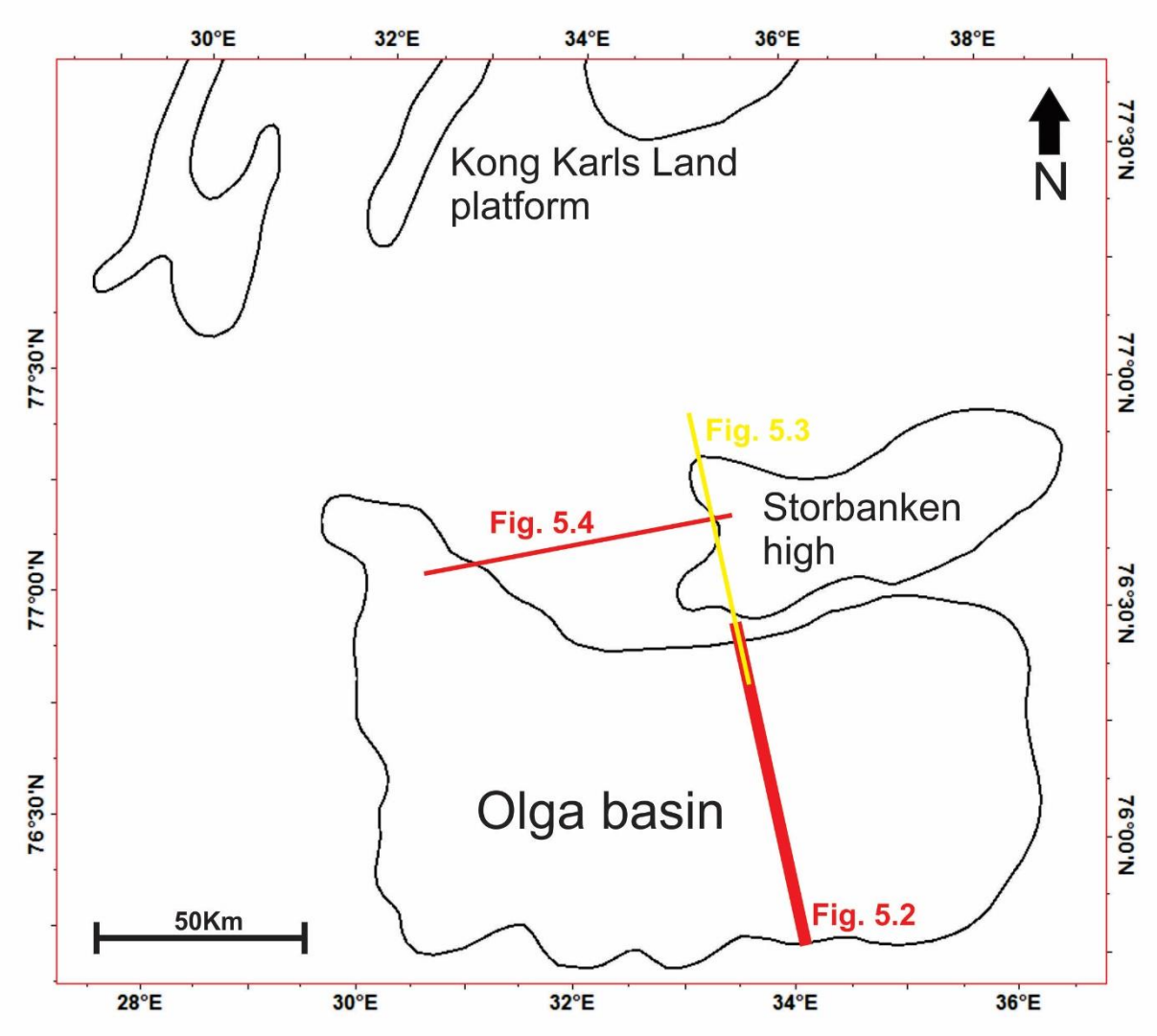

Fig.5.1: Overview of the study area with the main structural elements, the red and yellow lines indicate the location of the illustrated seismic lines. The black polygons delineate the structural elements.

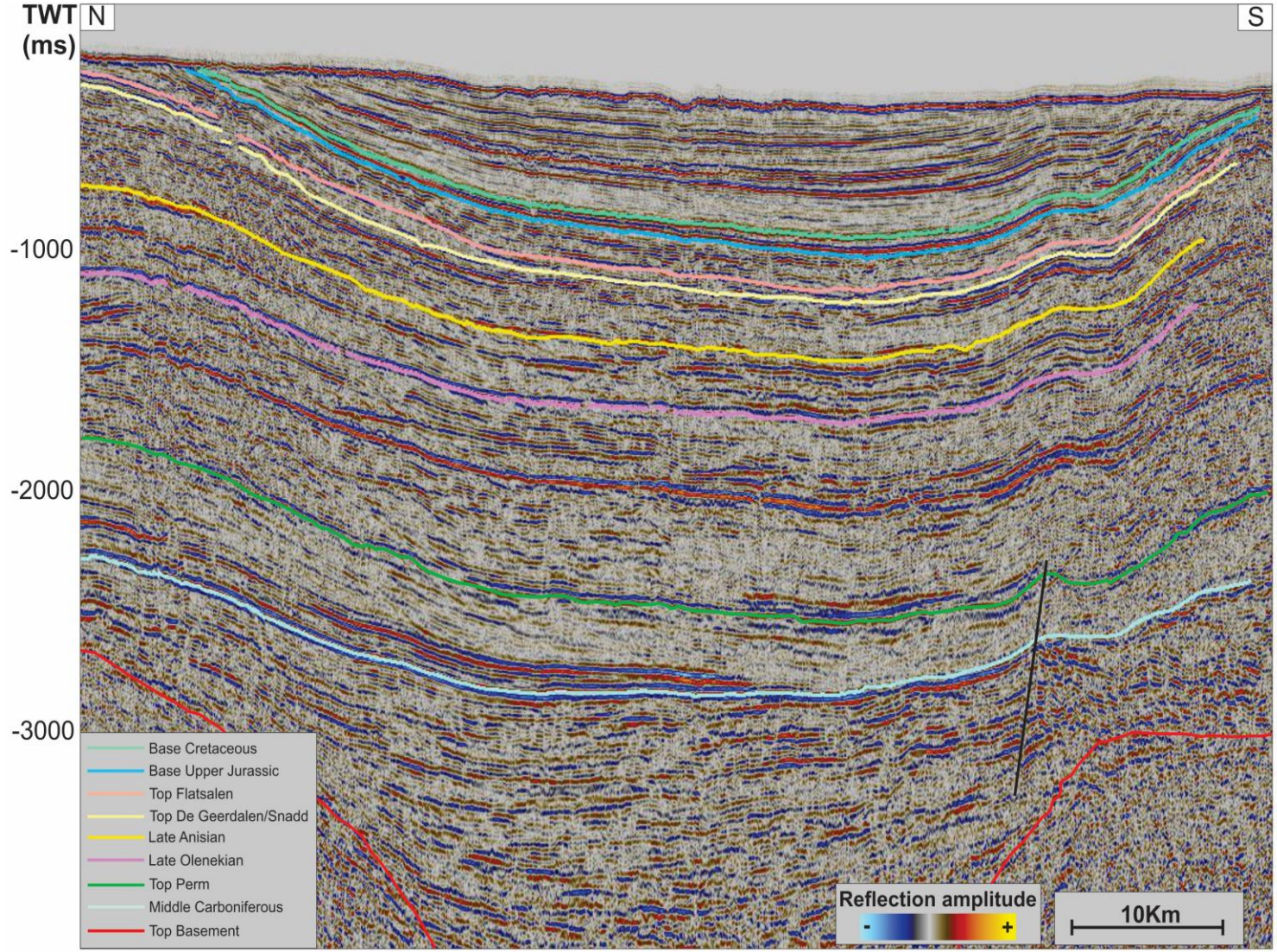

Fig.5.2 Seismic section illustrating the reflectors interpreted, position of the seismic line is indicated in Fig.5.1.

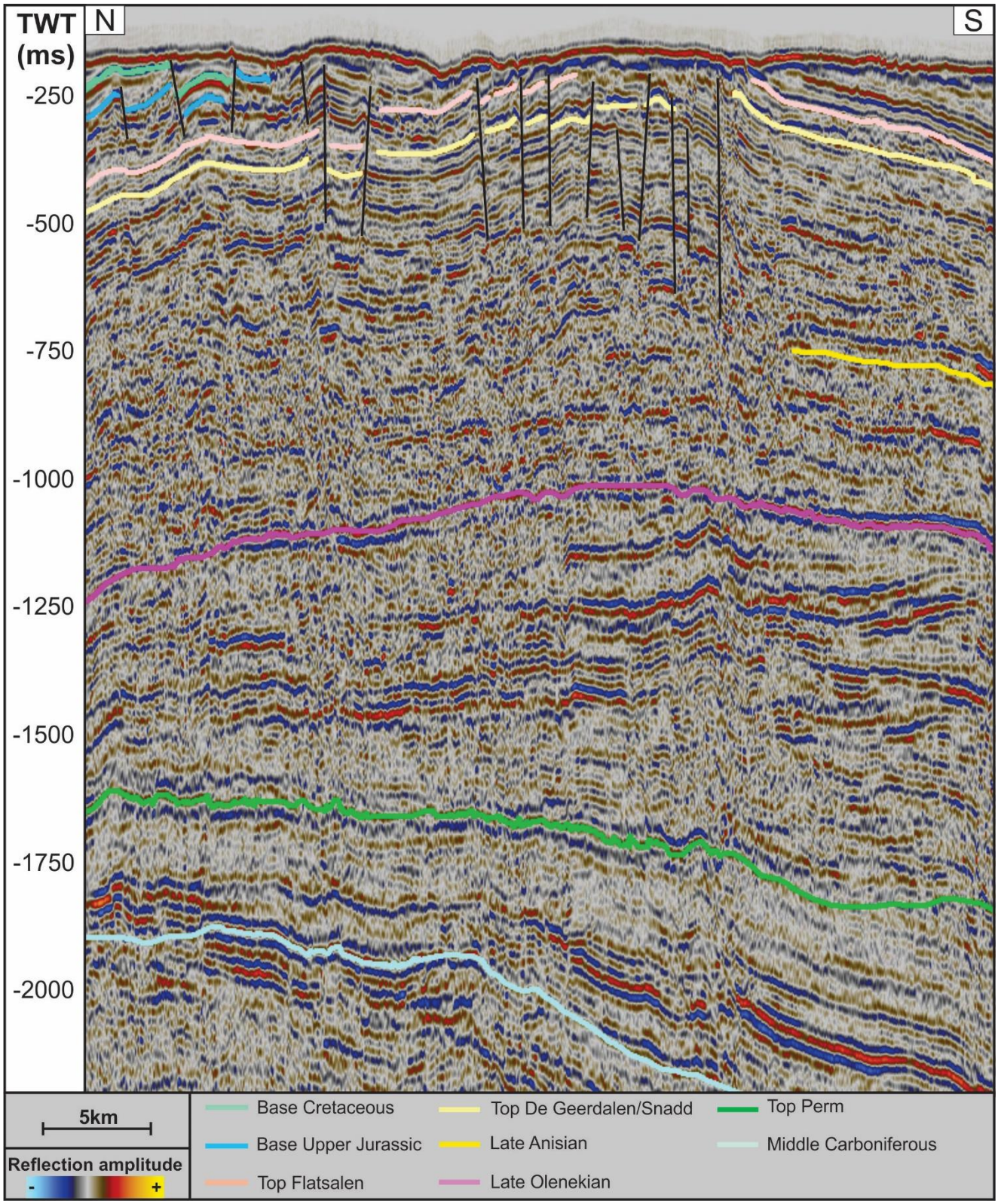

Fig.5.3: Seismic section illustrating the reflectors interpreted, position of the seismic line is indicated in Fig.5.1.

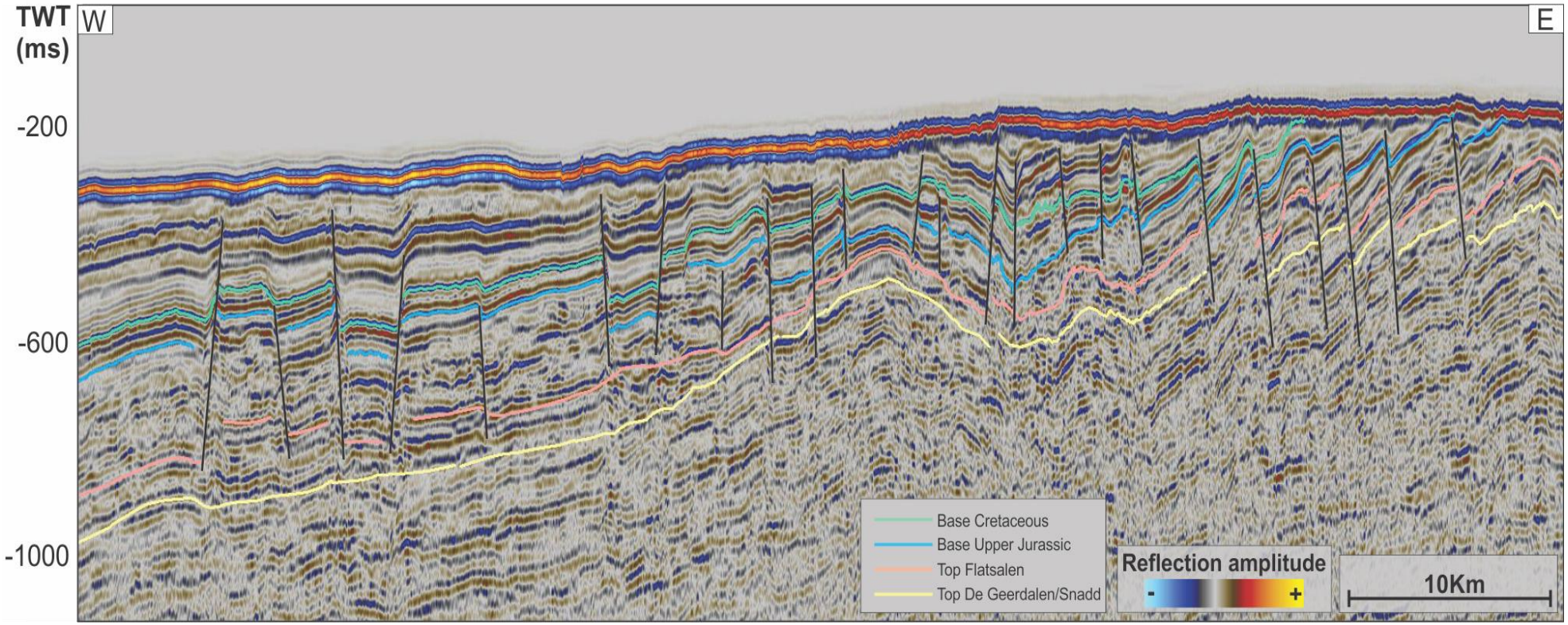

Fig.5.4: Seismic section illustrating the reflectors interpreted, position of the seismic line is indicated in Fig.5.1.

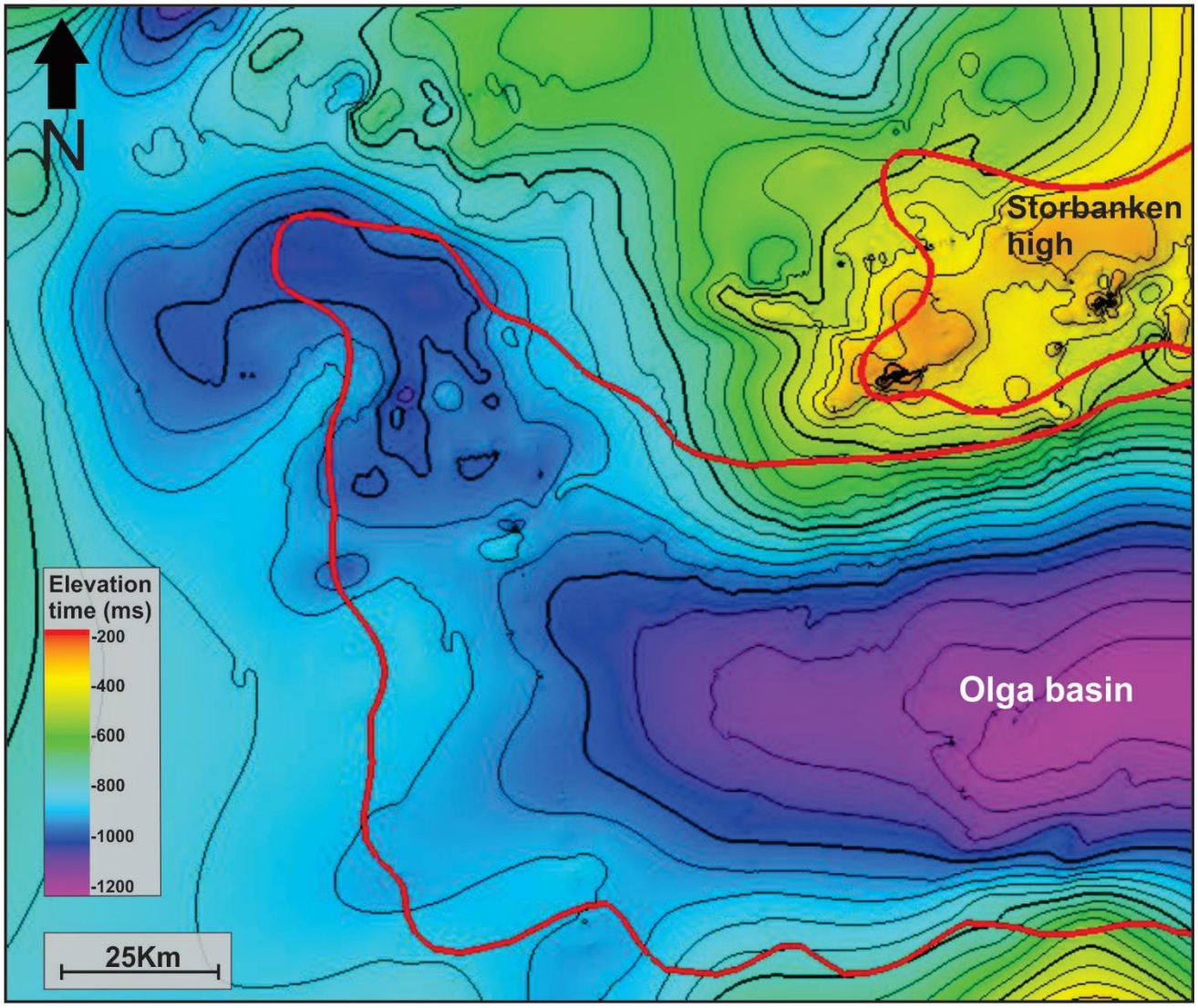

Fig.5.5: Surface map of the interpreted Base Flatsalen Formation displayed in elevation time (ms). The black area indicates areas which the Base Flatsalen Formation is eroded and terminates against the seafloor. The contour line interval is set to 50 ms. Red polygon illustrates the structural elements of the Storbanken high and the Olga basin. The surface map is interpolated between the 2D seismic lines (Fig.4.2-4.3).

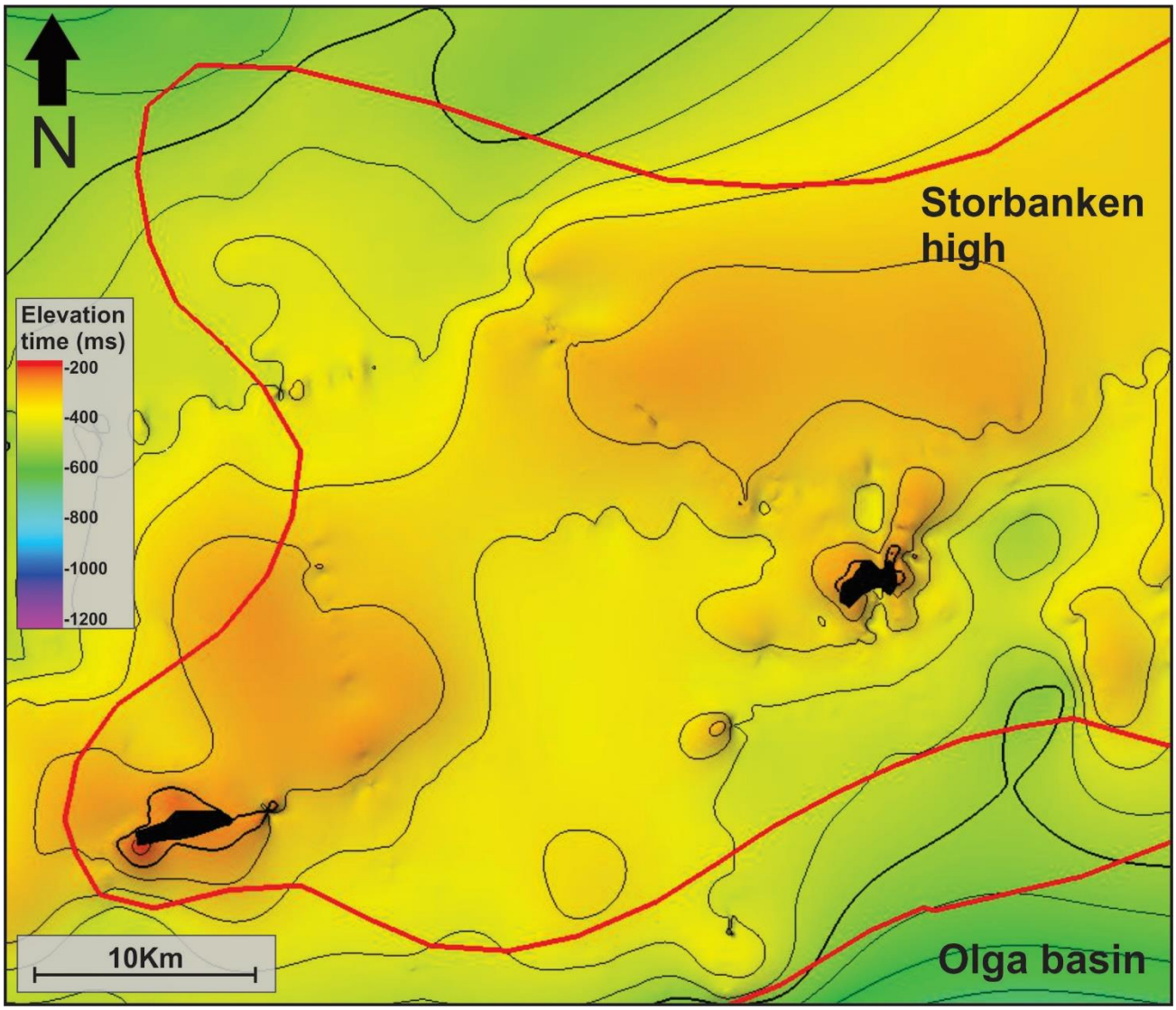

Fig.5.6: A closer overview of the eroded areas of the interpreted Base Flatsalen Formation at the Storbanken high. Red polygon illustrates the structural elements of the Storbanken high and the Olga basin. The contour line interval is set to 50 ms. The surface map is interpolated between the 2D seismic lines (Fig.4.2-4.3). Red polygon delineates the Storbanken high.

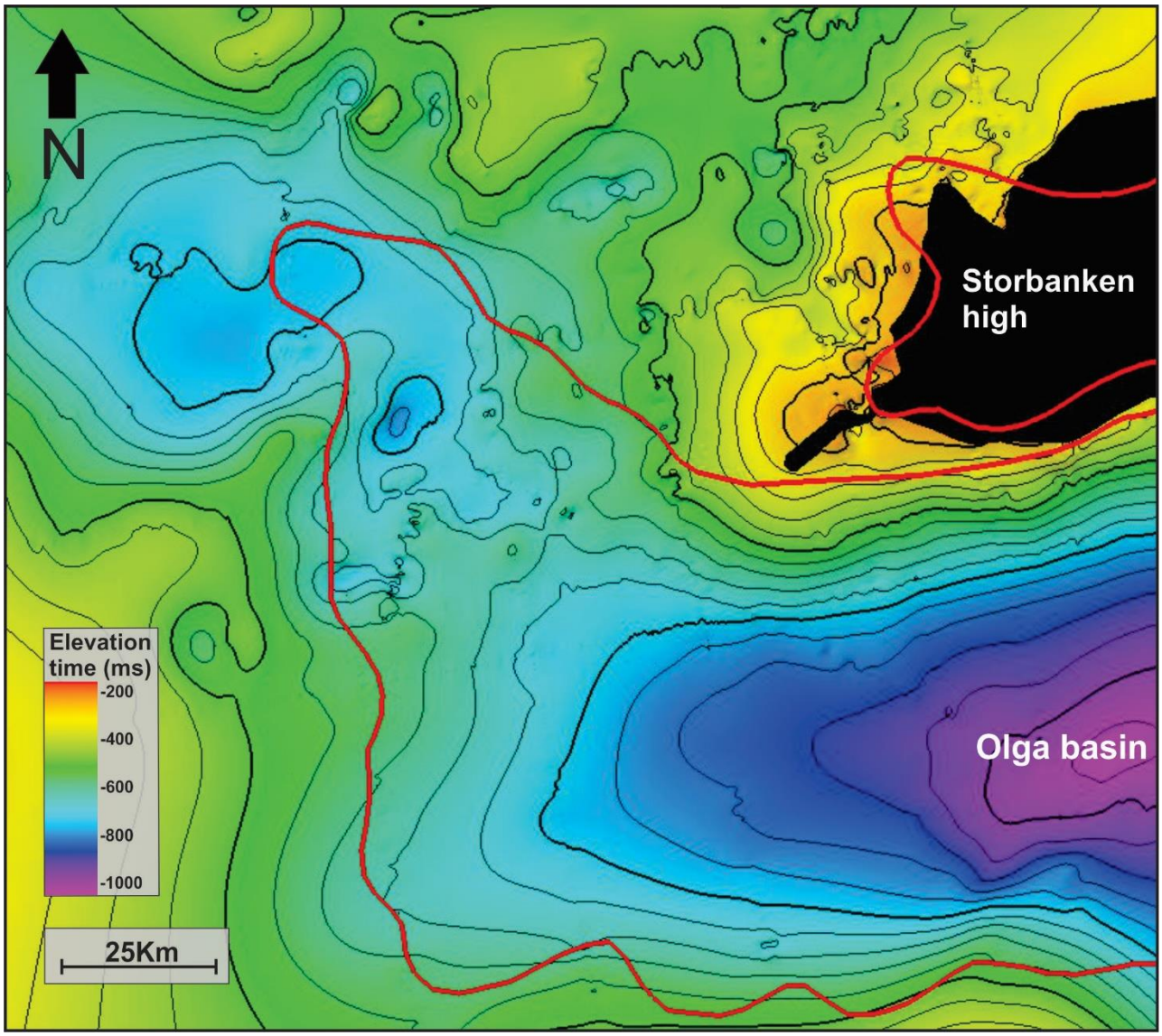

Fig.5.7: Surface map of the interpreted Base Agardhfjellet Formation displayed in elevation time (ms). The black area indicates the area where the Base Agardhfjellet Formation is eroded and terminates against the seafloor. The contour line interval is set to 50 ms. Red polygon illustrates the structural elements of the Storbanken high and the Olga basin. The surface map is interpolated between the 2D seismic lines (Fig.4.2-4.3).

5.2 Faults

The northern Barents Sea has been exposed to a series of different tectonic phases that dates back to the early Carboniferous. The study area has been influenced by severe fault activity, where Storbanken high in particular has a complex faulting pattern indicating evidence of both compressional and extensional forces (Fig.5.8). Several faults have been identified, however there have been some challenges. Due to large distances between the 2D seismic lines it has been difficult to determine strike direction, trace faults laterally and distinguish certain faults from each other. The aim of this chapter has therefore been to distinguish the largest regional faults and fault zones as well as examine faults at the gas flare investigated areas for discussing faults and their relationship to active seepage in the discussion chapter. For simplicity will the faults be annotated as fault zone (FZ) and faults (F) with numbers.

Zone of shallow normal faults (FZ)

The zone of shallow normal faults (FZ) articulates evidence of extensional and potential compressional forces indicated with structures such as horst and graben and half-grabens and internal curved/folded reflectors (Fig.5.8-5.10). It is difficult to determine the strike direction of these faults but the fact that these faults can be identified in both the north-south and east-west direction but not in the seismic line oriented in the northwest-southeast direction might indicate a strike direction parallel to the northwest-southeast seismic lines. The throw of the faults is fluctuating from 50 ms to 90 ms (TWT) (Fig.5.10). There seems to be a dominating dip direction towards the east forming half-grabens for these shallow faults, however the dip direction is more varying further north and east within the zone (Fig.5.9-5.10). The fault segments generally vary from 1 to 3 km with some longer segments up to 10 km (Fig.5.10).

Sediments near the seafloor and the interpreted Base Cretaceous to Flatsalen Formation and well below the Top De Geerdalen/Snadd Formation seems to have been affected by these faults, however due to discontinuous and chaotic reflections it is difficult to determine for certain at what depth these faults terminates (Fig.5.9-5.10). There exist some local variations for the termination of these faults. At the central parts of Storbanken high the faults seem to terminate well below the interpreted Top De Geerdalen/Snadd reflector, while at the northern parts of this zone the faults tend to terminate slightly below the Top De Geerdalen/Snadd reflector (Fig.5.8-5.10). The extent of the shallow fault zone (FZ) is believed to encompass throughout large areas of the Storbanken high (Fig.5.8 and 5.9).

Extensional faults and compressional feature, Storbanken high (F1)

North for Storbanken high three normal faults have been identified which can be traced within the (FZ) based on four seismic lines, these faults are grouped together as (F1) (Fig.5.8). These extensional faults were identified in all the seismic lines except the one oriented in a northwest-southeast direction, it is therefore expected that the strike direction is oriented parallel to this seismic line (Fig.5.8 and 5.11-5.12). The faults of (F1) are identified within the (FZ) and share some of the same characteristics in terms of throw, length of segments and graben structures with curved reflectors (Fig.5.12). There were not identified any dominating dip direction for these faults. In the southeastern parts of the faults there were also identified curved reflectors indicating a compressional feature (Fig.5.11).

Long complex faults, Olga basin (F2 and F3)

From the western flank of the Olga basin to the western flank of Storbanken high there was identified two long extensional faults establishing a graben structure (F2) (Fig.5.8). 20 km further north there was identified two additional normal faults with the same strike direction, establishing another graben structure (F3) (Fig.5.8). The two faults located north (F3) have a shorter extent, they have an extent of at least 25 km as they are identified in two seismic lines, while the longer faults (F2) is extending at least 85 km identified in four seismic lines (Fig.5.8). The faults (F2 and F3) seems to have a strike direction of east-west, with the longer faults (F3) slightly changes their orientation to southwest-northeast when tracing the fault further east (Fig.5.8). For both of the faults (F2 and F3) there seem to be additional deeper faults underneath, all the faults seem to be extensional normal faults, forming a graben structure (Fig.5.13). The deeper faults have reached strata of Carboniferous age, while the uppermost faults seem to have a large vertical extent of approximately 1400 ms (TWT) affecting sediments of Early Cretaceous age to well the interpreted Top De Geerdalen/Snadd reflector (Fig.5.13). It is difficult to determine the vertical extent of these faults as it varies laterally and also due to the very chaotic reflection pattern, but a strong continuous negative reflection might indicate that the faults terminate somewhere above -1800 to -1900 ms (TWT) (Fig.5.13). Tracing the longer faults (F2) in an eastward direction the graben structure tend to be more upward curved, (F2) is traced eastward and is illustrated along with the potential gas chimneys in chapter 5.4 (Fig.5.27).

Extensional faults, northwestern Olga basin (F4)

Between the (F2 and F3) faults there were identified several smaller extensional normal faults (F4) (Fig.5.8 and 5.14). The throw of these faults was varying from 40 to 110 ms (TWT). The faults do not seem to have any dominating dip direction and the segments generally varies from 2-3 km. The faults have reached sediments of Early Cretaceous and Late Jurassic age, it is however difficult to determine the full vertical extent of these faults due to multiples (Fig.5.14). The faults share great resemblance to those identified within the shallow fault zone (FZ) in terms of vertical throw, dip angle, length of segments and the structures of horst and grabens with some curved reflectors (Fig.5.14). They presumably also share the same strike direction as these faults are only identified in the seismic line oriented in a south-north/southwest-northeast direction and not in the line oriented in a northwest-southeast/west-east direction. In association with these faults there has also been identified some seismic anomalies. A potential flat spot was identified at depths of -650 ms (TWT), the flat spot was located -120 ms (TWT) underneath the crest of the fault, above the fault near the seafloor there was also identified a bright spot, acoustic masking and push-downs associated with these faults F4 (Fig.5.14).

Compressional reverse faults, Kong Karls Land platform (F5)

Between the Kong Karls Land platform and Storbanken high there were identified two compressional features (F5) (Fig.5.8). Two large reverse faults were identified, both being located within a depth interval of -1000 ms (TWT) to -2100 ms (TWT) affecting sediments presumably from middle Carboniferous to slightly below the interpreted Top De Geerdalen/Snadd reflector (Fig.5.15). It was challenging to determine the strike and lateral extent of these faults as there were only seismic lines oriented in the north-south and northwest-southeast direction and large distances between the lines. The southernmost reverse fault was identified in two seismic lines and the extent of this fault was therefore interpreted to at least 45 km, the fault located further north, was only identified in one seismic line and it is therefore annotated with a dotted line as there is great uncertainty in the further extent of this fault (Fig.5.8). The seismic line oriented in the northwest-southeast direction had the best defined folds and faults, the strike for the reverse faults was therefore believed to be perpendicular for this line and therefore oriented with a similar strike direction as the compressional feature in (F1) in a southwest-northeast direction. Above the interpreted Base

Cretaceous reflector there was identified to be a thinning towards the Kong Karls land platform and possibly a package of growth strata (Fig.5.15). The strata were measured to be 60 ms (TWT) at its thinnest where it outcrops at the Kong Karls Land platform, while a uniform thickness of 230 ms (TWT) was measured throughout the rest of the seismic line (Fig.5.15).

Faults associated with large depressions, Storbanken high (F6)

At the central parts of Storbanken high (F6) there were identified six normal faults in a west-east/southwest-northeast oriented seismic line (Fig.5.16). It is difficult to determine a dominating strike direction as the faults were only visualized in one additional seismic line oriented in a north-south direction. In association with these faults there were also identified several large depressions at the seafloor (Fig.5.16). The faults are reaching sediments from or near the seafloor and well below the interpreted Top De Geerdalen/Snadd reflector, it was difficult to determine the full vertical extent of these faults due to the multiples (Fig.5.16). These faults generally form half grabens and graben structures, where there is a dominating fault dip to the east and a more symmetrical dip direction in the eastern parts of the seismic line (Fig.5.16). The throw of these faults was relatively small with the half-graben structures having a throw of 10 to 40 ms (TWT) while the graben structure further east had a larger throw of 60 ms (TWT), the fault segments had a relatively uniform length of 2-3 km (Fig.5.16).

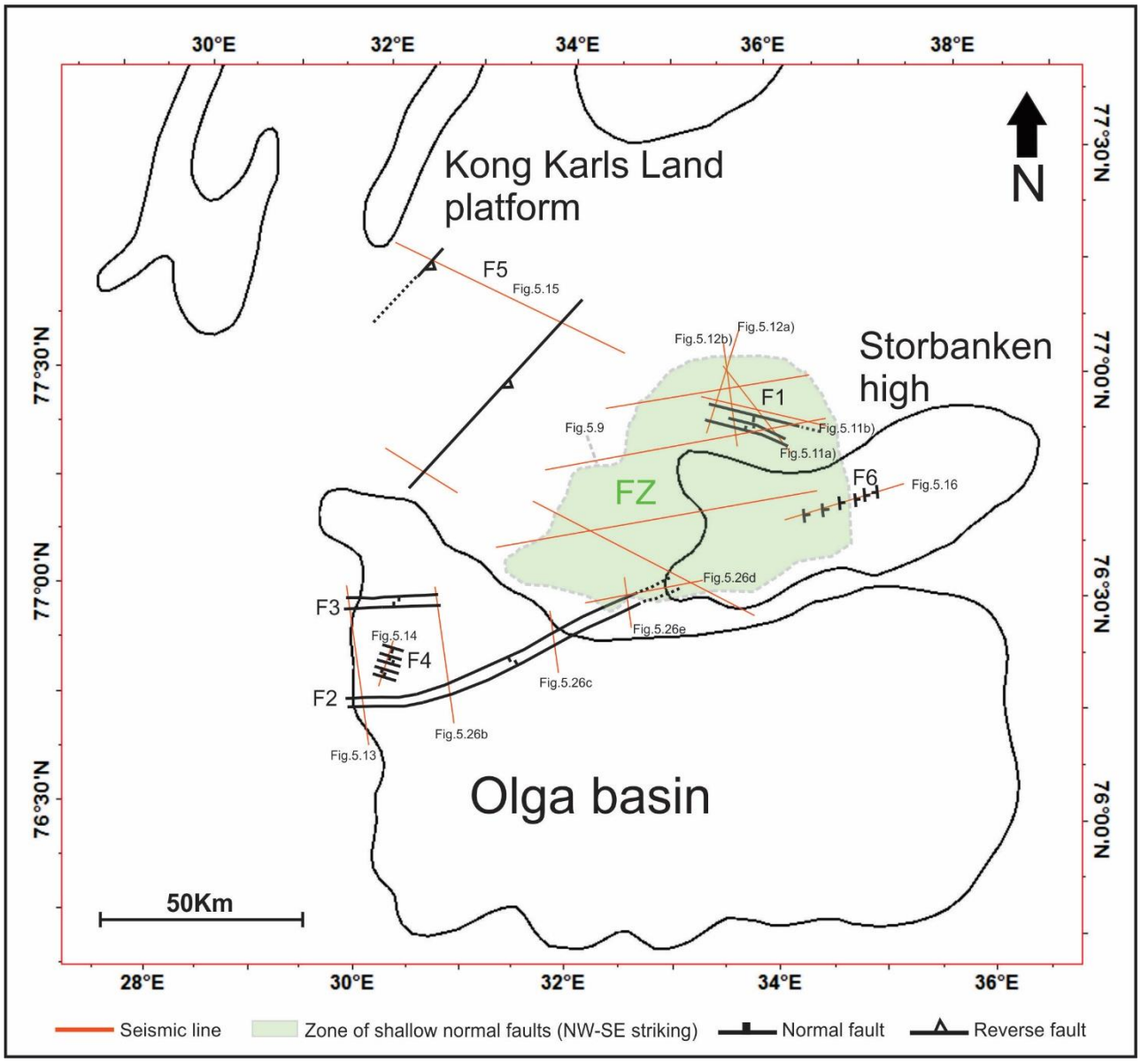

Fig.5.8: Overview map of the main faults in the study area.

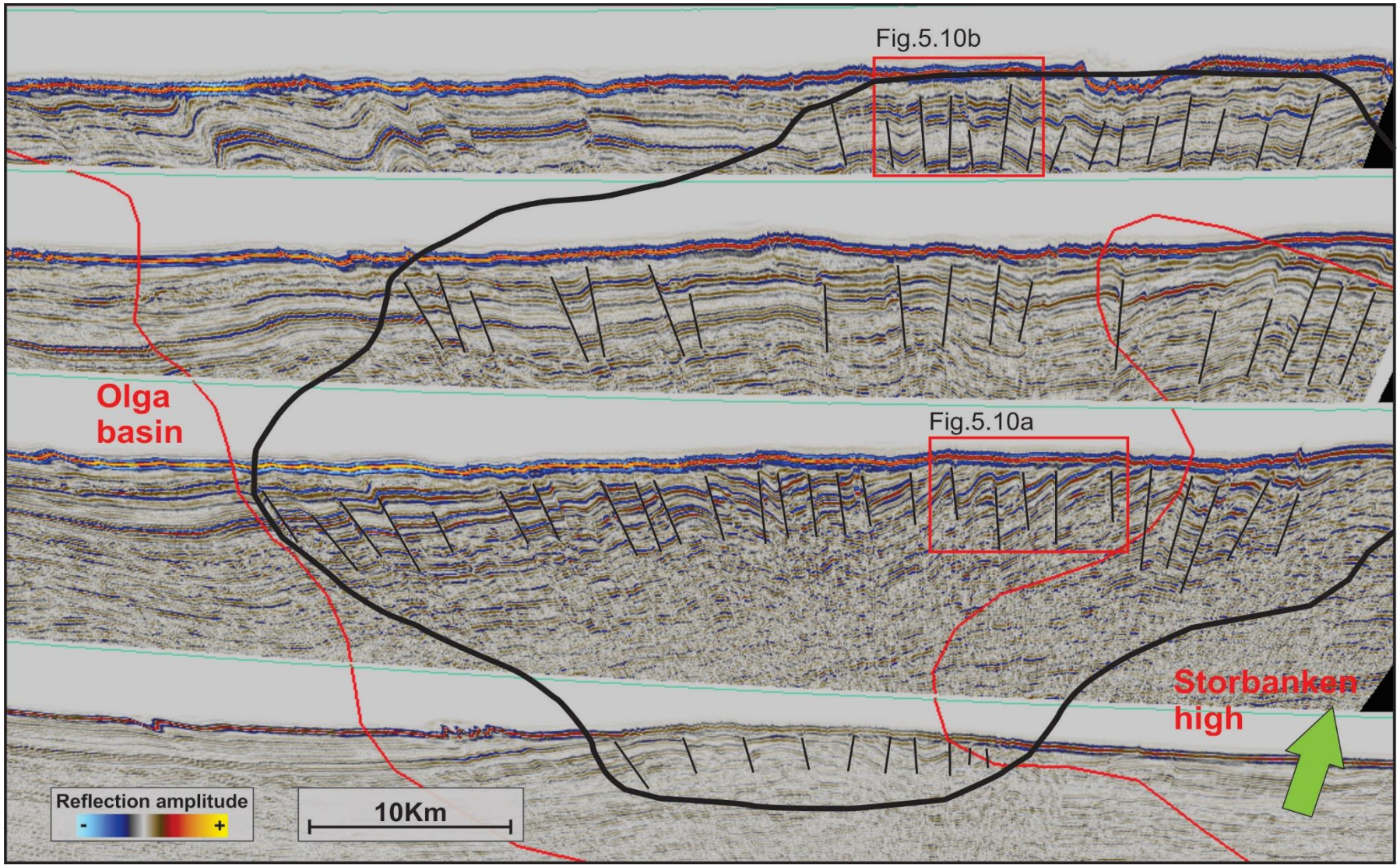

Fig.5.9: Overview of the extent of the shallow fault zone (FZ) as seen in Fig.5.8. The black polygon illustrates the potential fault zone. The red polygons delineates the structural elements of the Olga basin and Storbanken high.

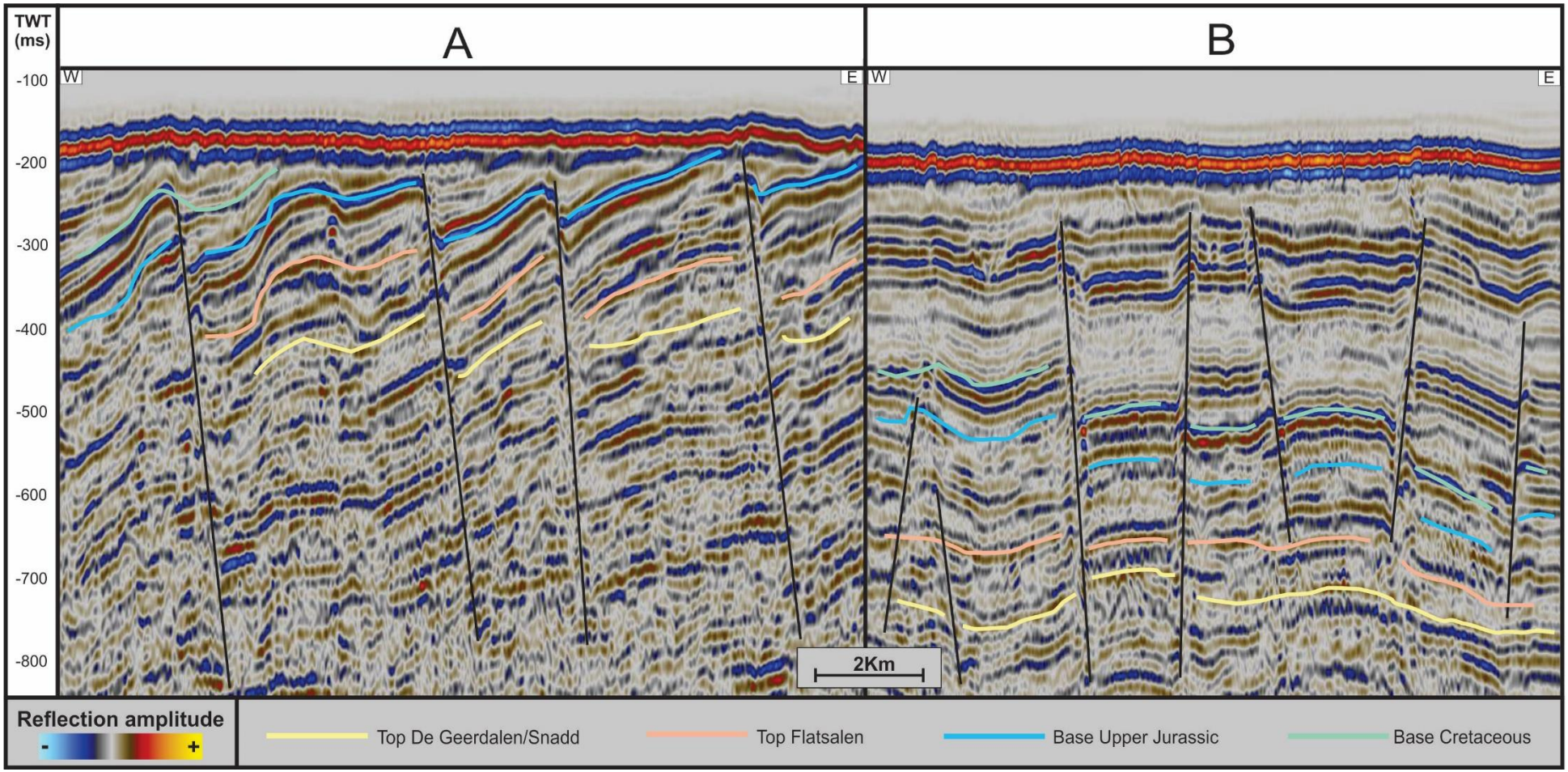

Fig.5.10: seismic section illustrating the faults of two areas located within the shallow fault zone (FZ). Position of the seismic sections is illustrated in Fig.5.9.

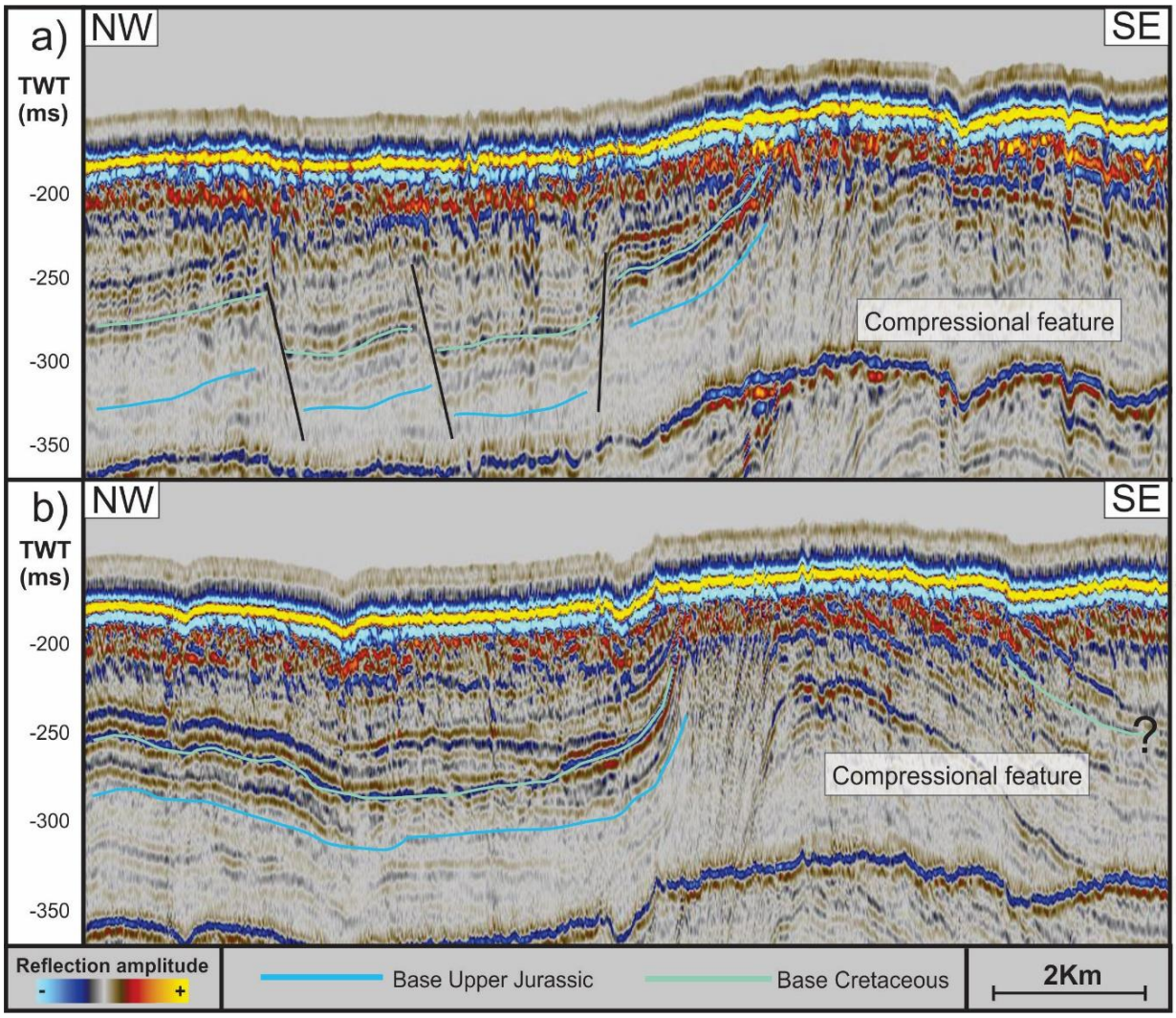

Fig.5.11: Seismic sections illustrating the faults (F1) at two areas. Position of the seismic sections is illustrated in Fig.5.8.

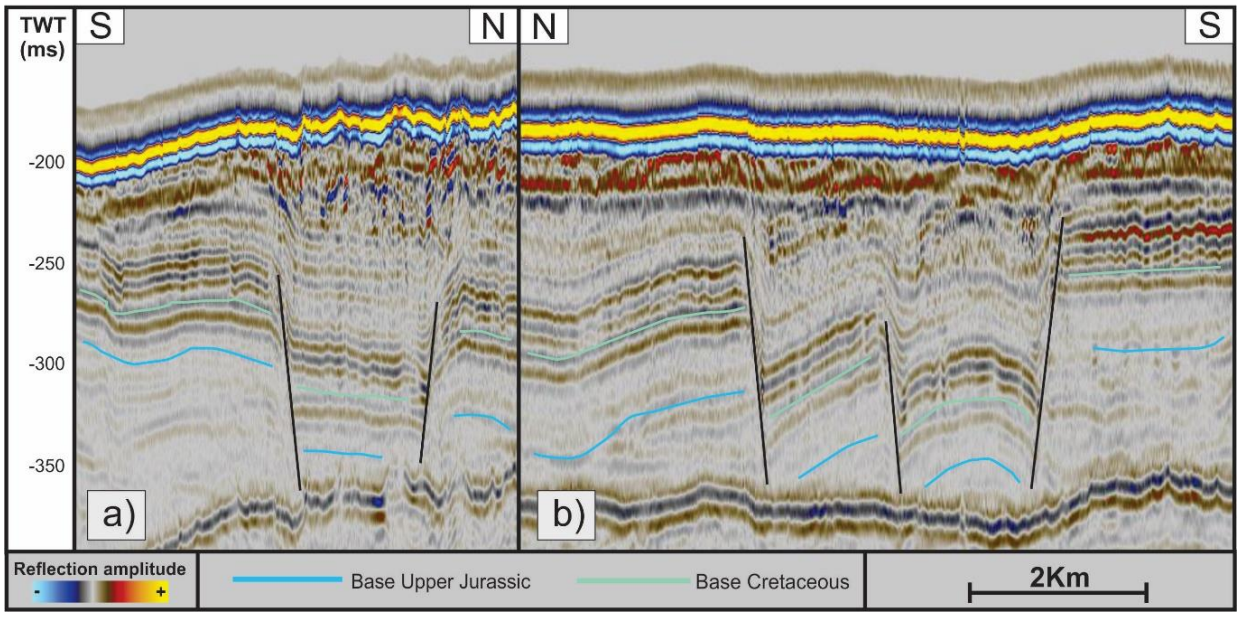

Fig.5.12: Seismic sections illustrating the faults (F1) at two areas. Position of the seismic sections is illustrated in Fig.5.8.

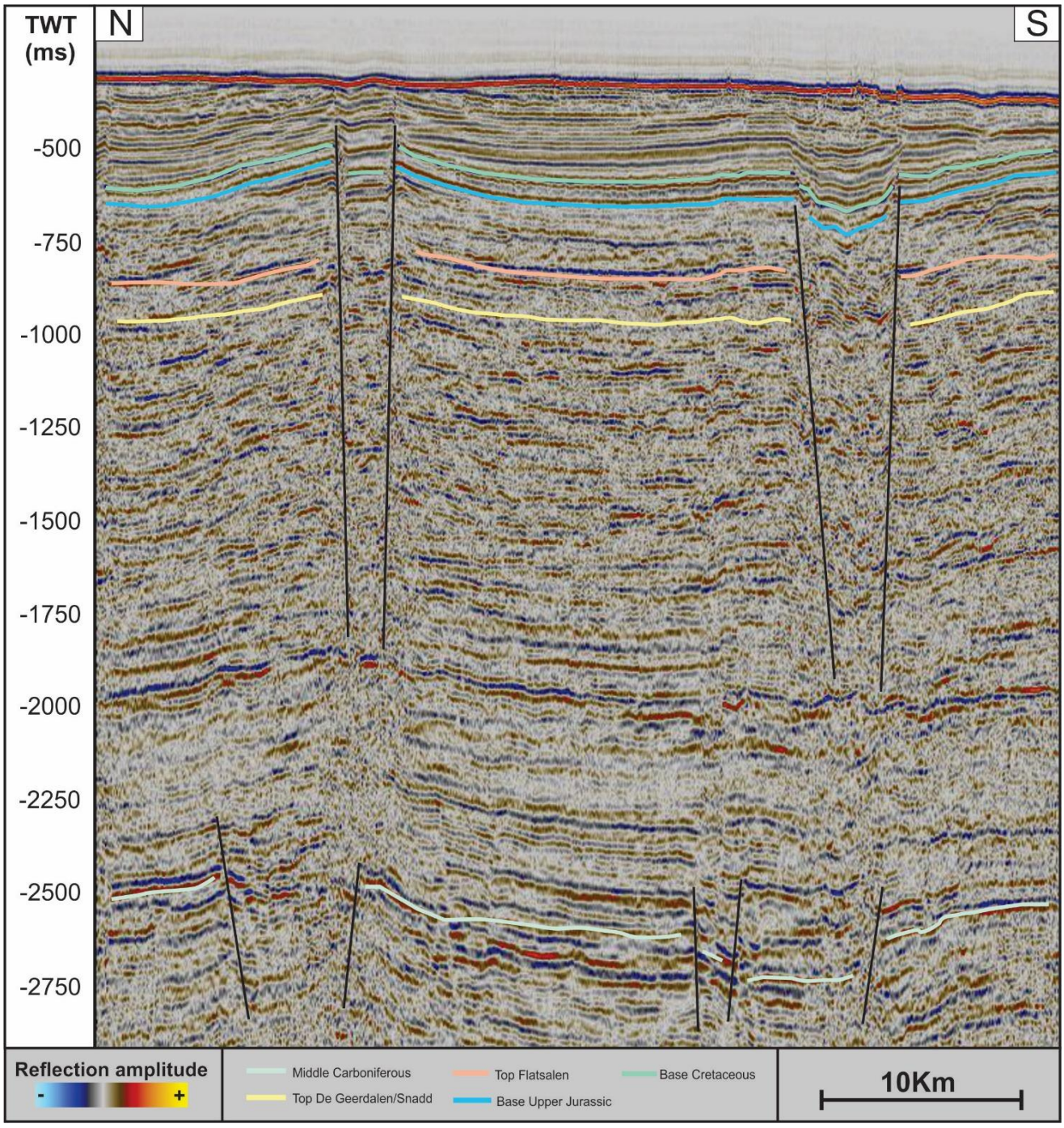

Fig.5.13: Seismic section illustrating the faults (F2) south and (F3) north. Position of the seismic section is illustrated in Fig.5.8.

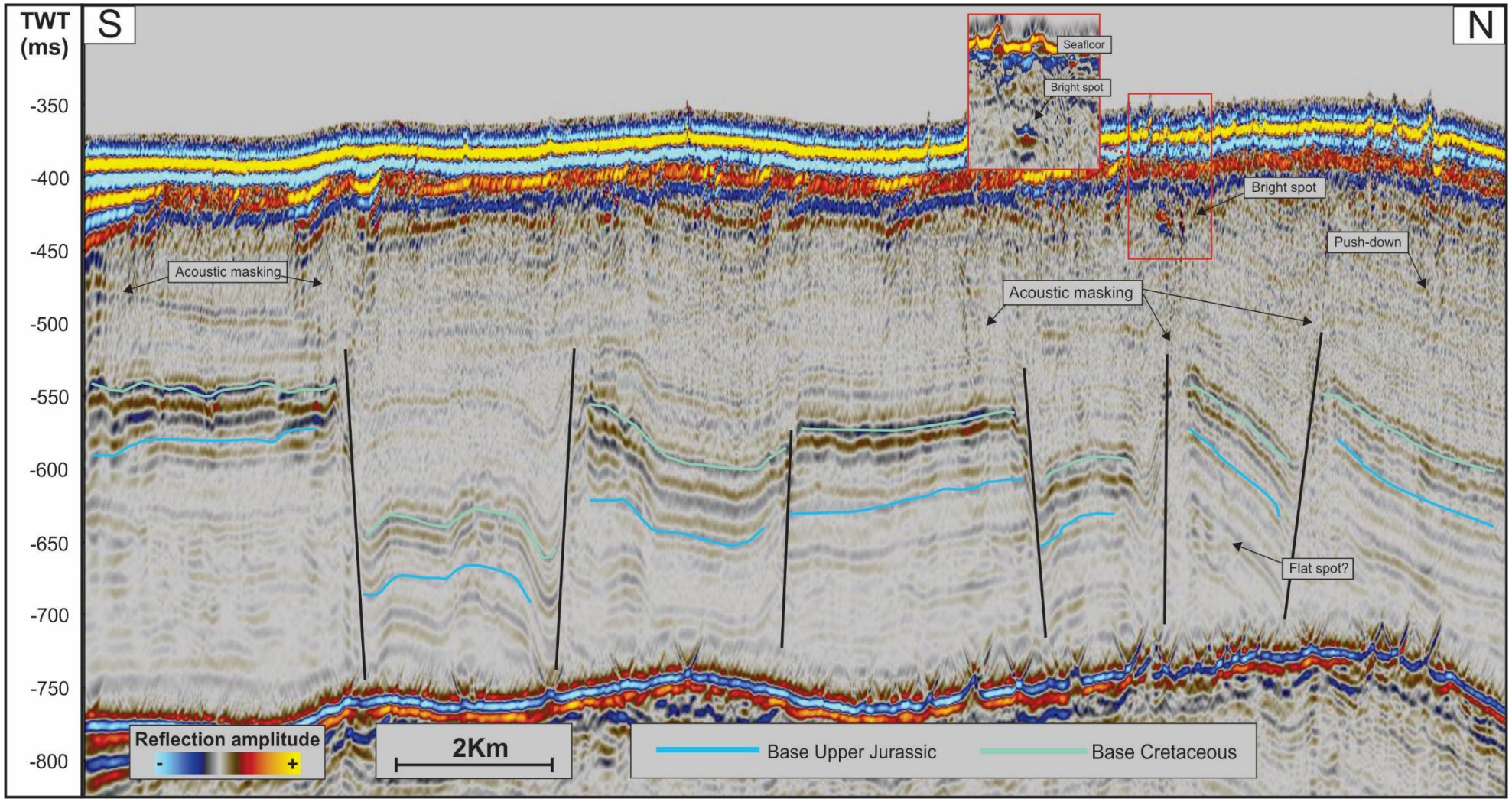

Fig.5.14: Seismic section illustrating the normal faults of (F4) along with amplitude anomalies. Position of the seismic section is illustrated in Fig.5.8. The red square illustrates the brightspot in a reprocessed seismic line.

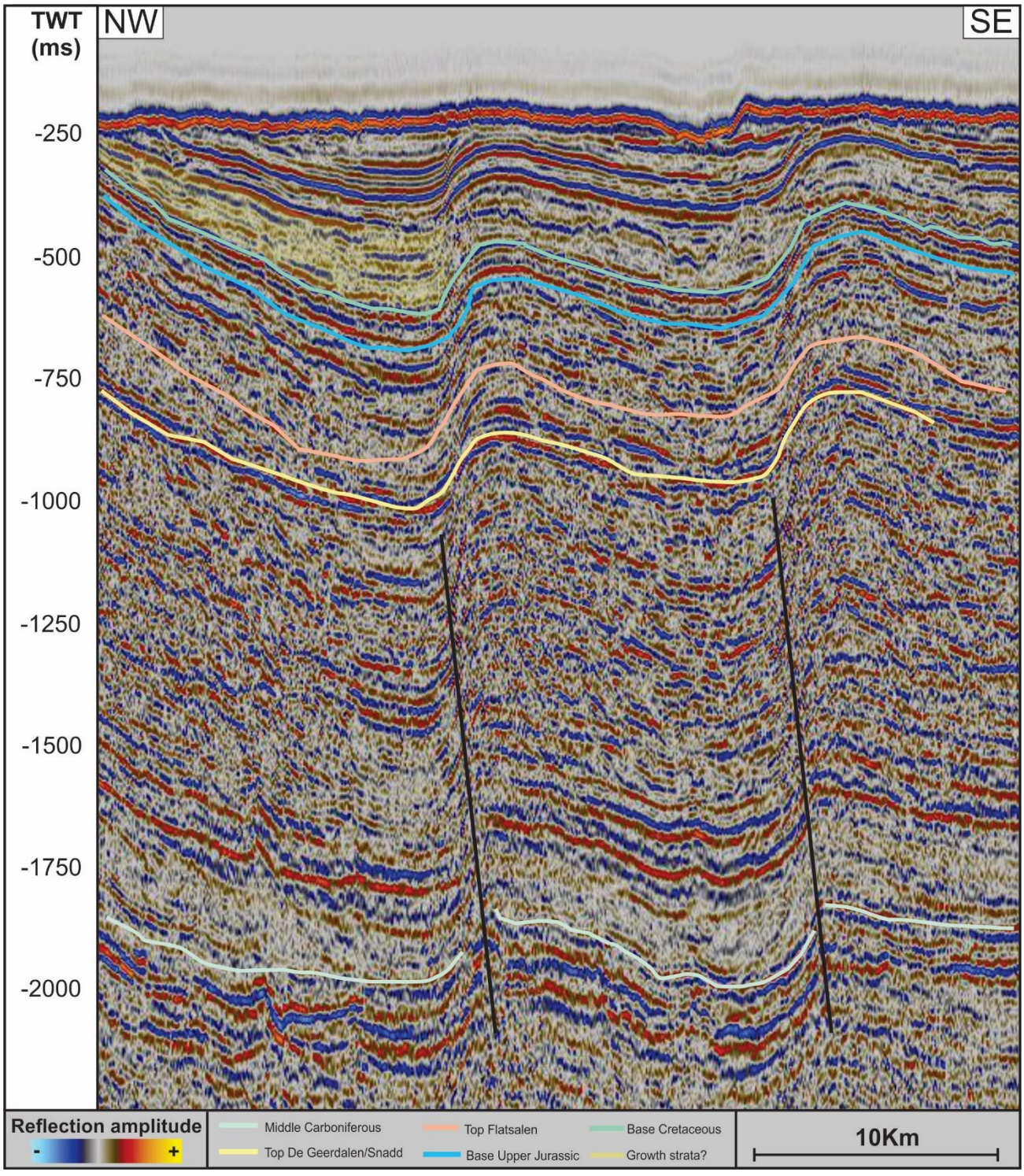

Fig.5.15: Seismic section illustrating the reverse faults (F5). Position of the seismic section is illustrated in Fig.5.8.

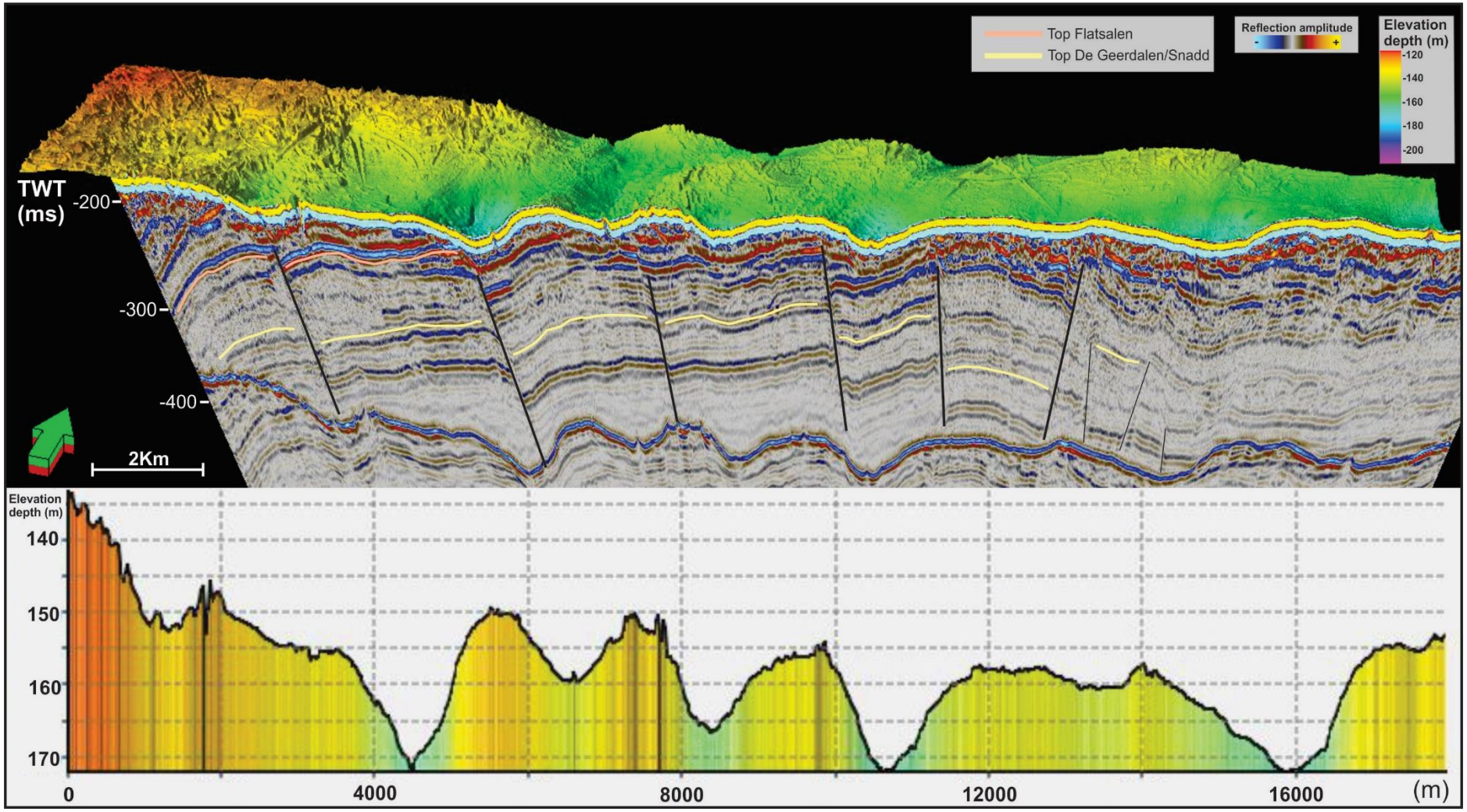

Fig.5.16: Seismic section illustrating the normal faults of (F6) in relation with the large depressions. Position of the seismic section is illustrated in Fig.5.8.

5.3 Geomorphology

During this Study several geomorphological features have been identified, but due to the scope of this thesis the main emphasis will be on the features related to possible gas seepage activity. These include small depressions, craters, craters with associated mounds and single mounds. A quantitative analysis of the small depressions, craters, craters with associated mounds and single mounds has been carried out to examine any potential trends (Appendix D).

5.3.1 Small depressions (pockmarks)

Several small depressions appearing isolated or within groups of varying concentrations was identified at the Storbanken high area (Fig.5.18). The small depressions were found at seafloor depths ranging from 170 - 210 m (Fig.5.17-5.18). The depression depth of these small depressions was measured to be from 1 - 5 m and they had a width ranging from 10 m to 40 m (Fig.5.19-5.20). The features were generally circular to sub-circular with a steep sidewall with no rim, the geometric configuration of the depression was characterized by a V- or U-shape (Fig.5.19 and 5.20).

Similar features have been described by (Chand et al., 2009; Judd & Hovland, 2009; Løseth et al., 2009; Vadakkepuliyambatta et al., 2013) to be pockmarks, these features are therefore successively interpreted as pockmarks. These pockmarks have not been identified elsewhere in the study area except at the Storbanken high. There is an uneven distribution of pockmarks throughout Storbanken high with a general trend of higher pockmark concentration along the southern flanks of Storbanken high. Along the southern flank of Storbanken high there is also observed an long elongated depression which extends in a west-east direction (Fig.5.17). This elongated depression is 30 m at its deepest and reveals variation in steepness (Fig.5.17). It was difficult to comprehend the full extent of this feature as it is present throughout the whole bathymetric section, but the elongated depression is measured to be at least 25 km long and 5 km wide (Fig.5.17).

The pockmarks have been separated into three areas relating to their relative concentration of pockmarks (Fig.5.18). Red represents areas with high concentration of pockmarks, yellow represents areas with medium concentration of pockmarks and no color indicates areas with

very few pockmarks (Fig.5.18-5.20). There has been identified very few pockmarks in the more shallow central parts of the Storbanken high, these areas are however dominated by elongated randomly oriented furrows (Fig.5.17-Fig.5.18). These furrows are only present at the shallowest parts of the study area, at depths shallower than 190 m, they tend to be more dominating as the seafloor is located at shallower depths. The furrows are identified in the bathymetric data of location 1, 2 and 3 but not at location 4 at the north-western Olga basin, as this is an area located at depths of 247 - 301 m (Fig.4.5). The furrows are typically U-shape or V-shape with depression depths ranging from 1 - 12 m, widths from 20 - 220 m and up to ten's of km long, the furrows appear as both single features and in parallel pairs. These features are interpreted to be ploughmarks caused by the decoupling of icebergs from a glacier terminus during the LGM, the keel of the icebergs scratches the seafloor sediments in directions governed by wind and current systems (Barnes et al., 1988; Andreassen et al., 2008).

5.3.2 Craters and mounds

At Storbanken high there were documented a total of 35 features having the characteristics look of a crater, these features had a Sub-circular and elliptical shape with relatively steep walls (Fig.5.17-Fig.5.18). There were also identified 21 craters with associated mounds and two single mounds without associated craters (Fig.5.17-Fig.5.18).

The craters were found at seafloor depths ranging from 157 to 202 m, where most of the craters were located at depths within 160 – 185 m (Chart 5.1). The depression depth of the craters varied from 5 m to 20 m with most of the craters having a depression of 10 - 14 m (Chart 5.2). The craters ranges in length from 80 - 900 m along their long axis and from 60 - 600 m along their short axis, most of the craters had a size within the range of 300 - 400 m along the long axis and 200 - 300 m along the short axis (Appendix D). The relationship between the longest and shortest side of the features was somehow variable with ratios varying from 1 to 0,33 (1 being symmetric circular) however there seemed to be a trending ratio of 0,5 – 0,75 for the features in the study area (Appendix D).

The craters with associated mounds were found at seafloor depths ranging from 160 – 192 m, with most of the craters with associated mounds being located at depths within 165 – 180 m (Chart 5.3). The associated mounds had similar length and width measurements as the craters and the height of the associated mounds somehow corresponded to the depth of the craters (Appendix D) (Chart 5.4).

The craters and mounds were identified to have a trending orientation with the elongated side oriented mainly in an east-west/southeast-northwest direction, except for M2 which the elongated side was oriented north-south (Fig.5.17 and 5.21-5.23). The associated mounds were observed to be located both south relative to the craters and some mounds being located within the craters itself (Fig.5.17 and 5.22-5.24). The craters C22, C23 and C25 and craters with associated mounds CM10, CM11, CM12, CM14, CM15, CM18, CM19 and CM20 which was exposed by seismic was found to have underlying faults (Fig.5.23-5.24).

At the single mound M2 there was identified some ploughmarks on top of the mound, this was also observed at several other mounds associated with craters (Fig 5.21). Underneath the single mound M2 the seafloor reflection seemed to be relatively continuous along the base of the mound, slightly curving upward (Fig.5.21). There were also observed several faults underneath the M2 feature and dipping reflectors (Fig.5.21). The faults were identified to terminate well below the De Geerdalen/Snadd Formation (Fig.5.21). A bright spot was also identified within a fault 3 km southwest for the mound (Fig.5.21). The reflectors underneath (M2) was examined in the seismic to dip from the mound in N-S, W-E, SE-NW and NE-SW direction.

The seismic underneath the crater with associated mound CM6 revealed a strong continuous basal reflector following the base of the mound (Fig.5.22). For the craters with associated mound CM7, CM10, CM11 and CM14 the associated mound was identified to be within the crater itself (Fig.5.22 -5.23). There was also identified no continuous basal reflector following the seafloor underneath these mounds but rather chaotic high amplitude reflections especially underneath CM10 and CM11 (Fig.5.23).

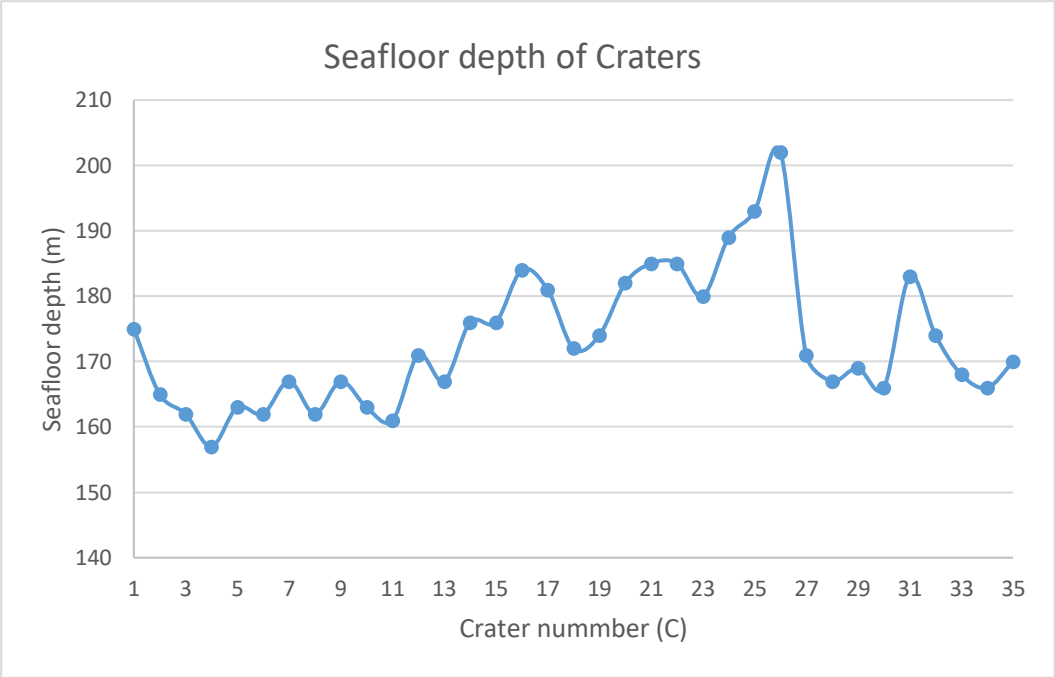

Chart 5.1: Distribution of the craters at different seafloor depths (Fig.5.17-Fig.5.18).

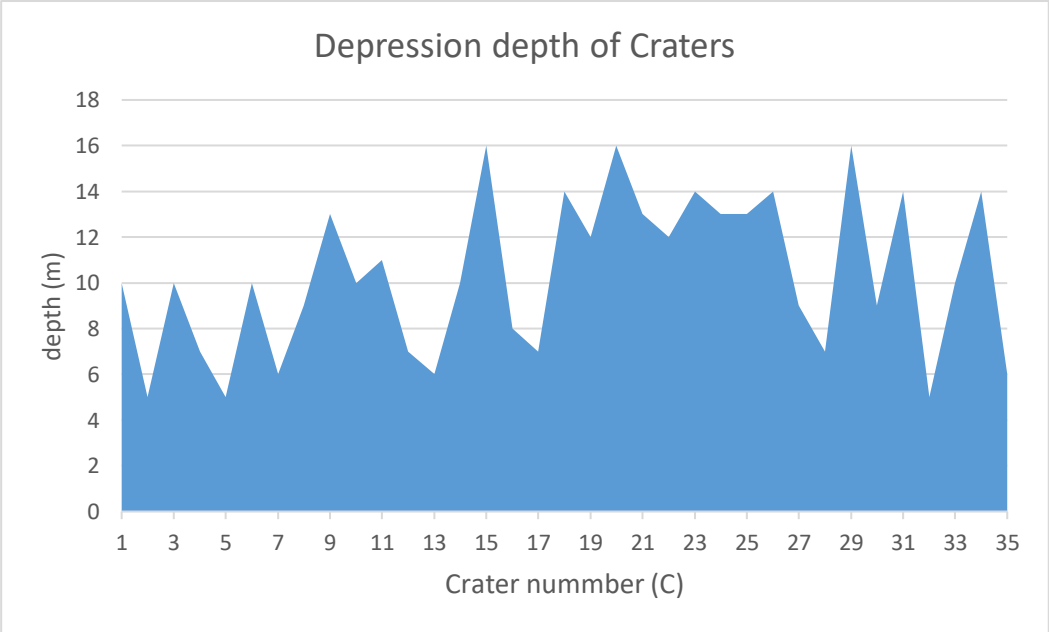

Chart 5.2: Distribution of craters and their depression depth (Fig.5.17-Fig.5.18).

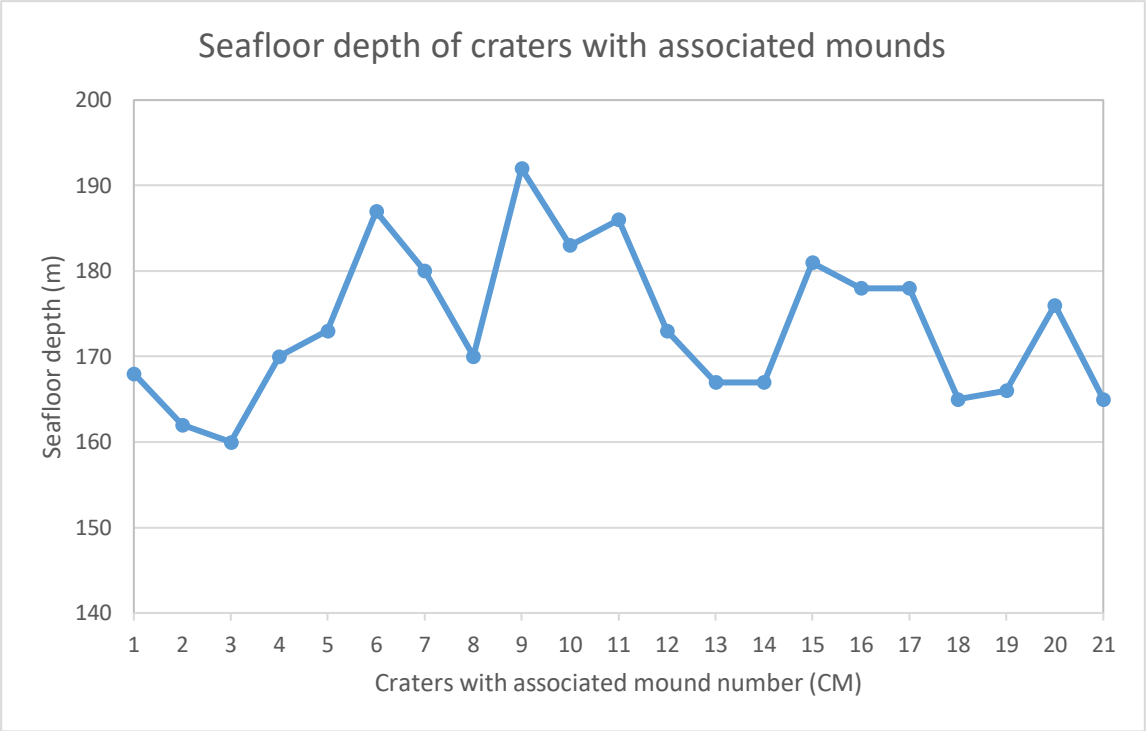

Chart 5.3: Distribution of craters with associated mounds at different seafloor depths (Fig.5.17-Fig.5.18).

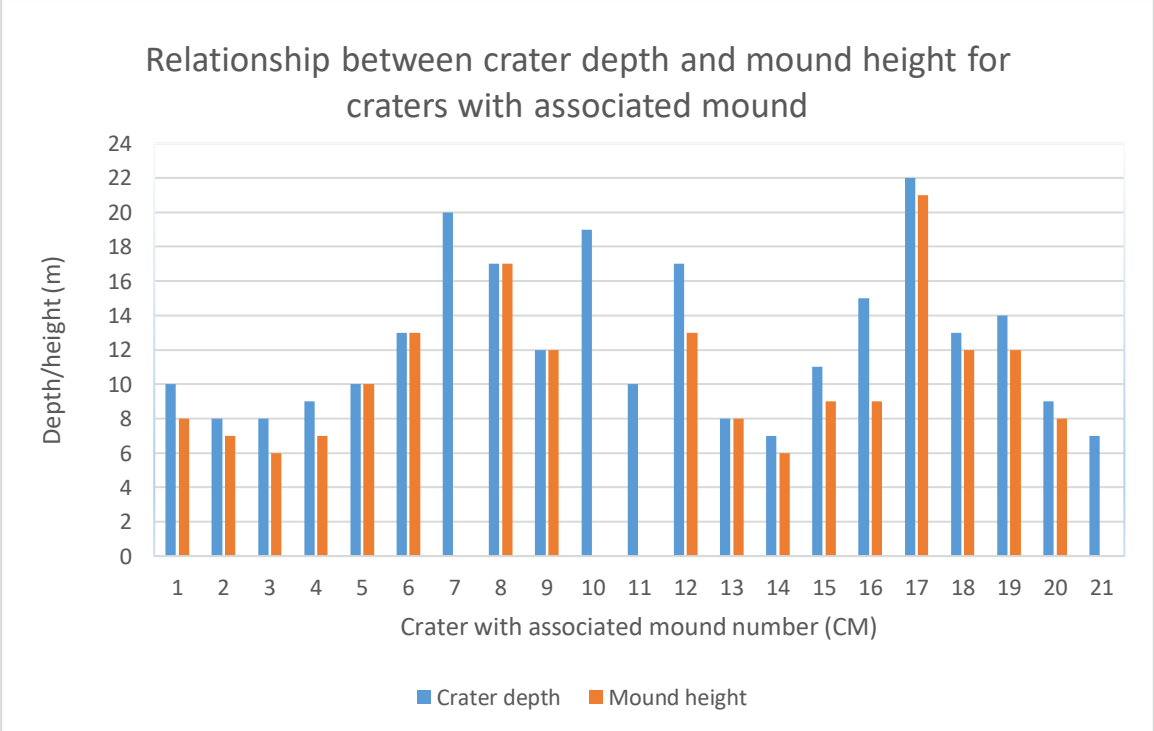

Chart 5.4: Relationship between the depression depth of crater and the height of mound relative to the seafloor for the craters with associated mound (Fig.5.17-Fig.5.18). Craters with an internal mound are indicated with CM without illustrated mound height in the chart.

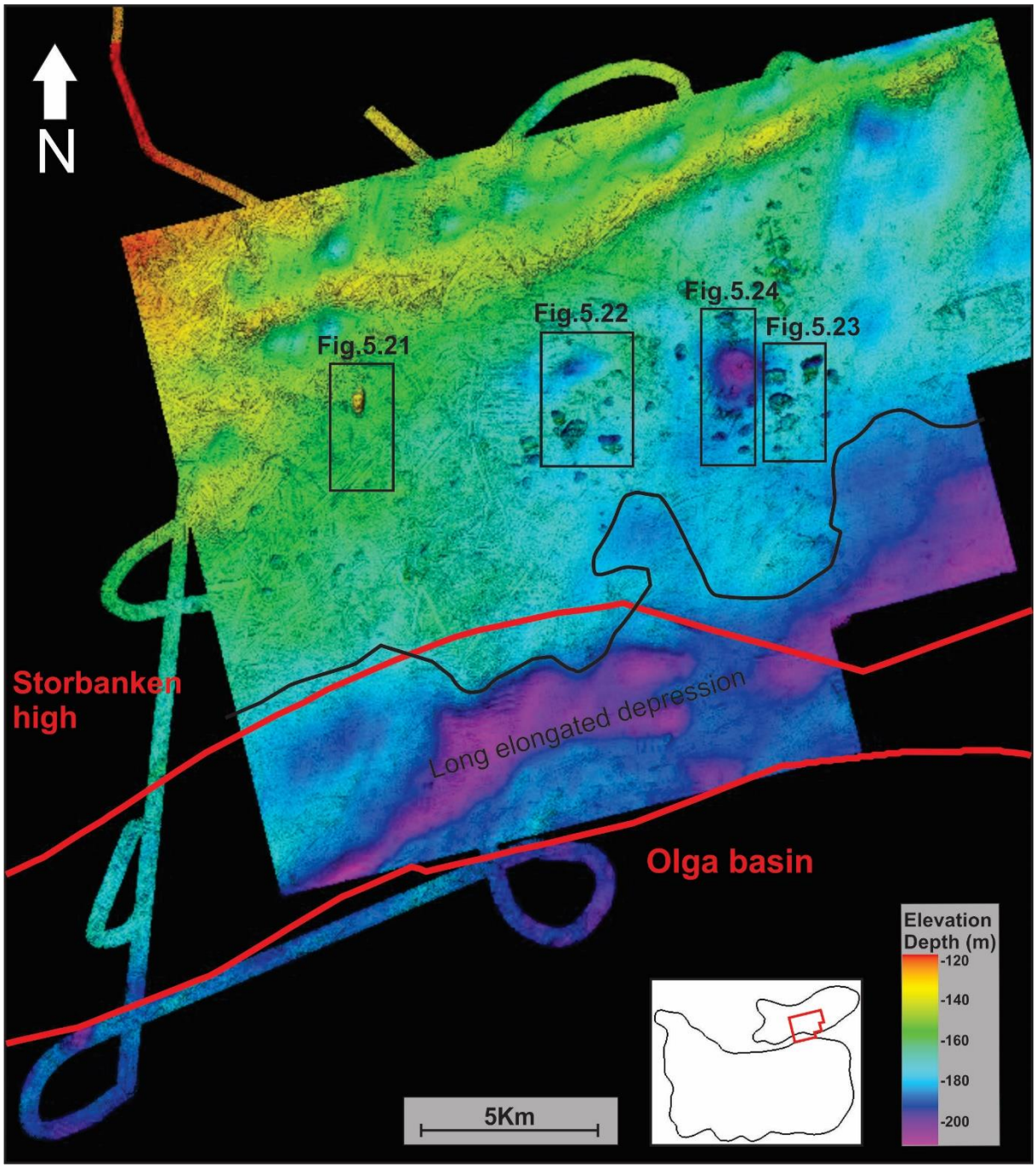

Fig.5.17:Uninterpreted geomorphology. The black line delineates the long elongated depression. The red polygon delineates the structural elements Olga basin and Storbanken high as seen in the inset map.

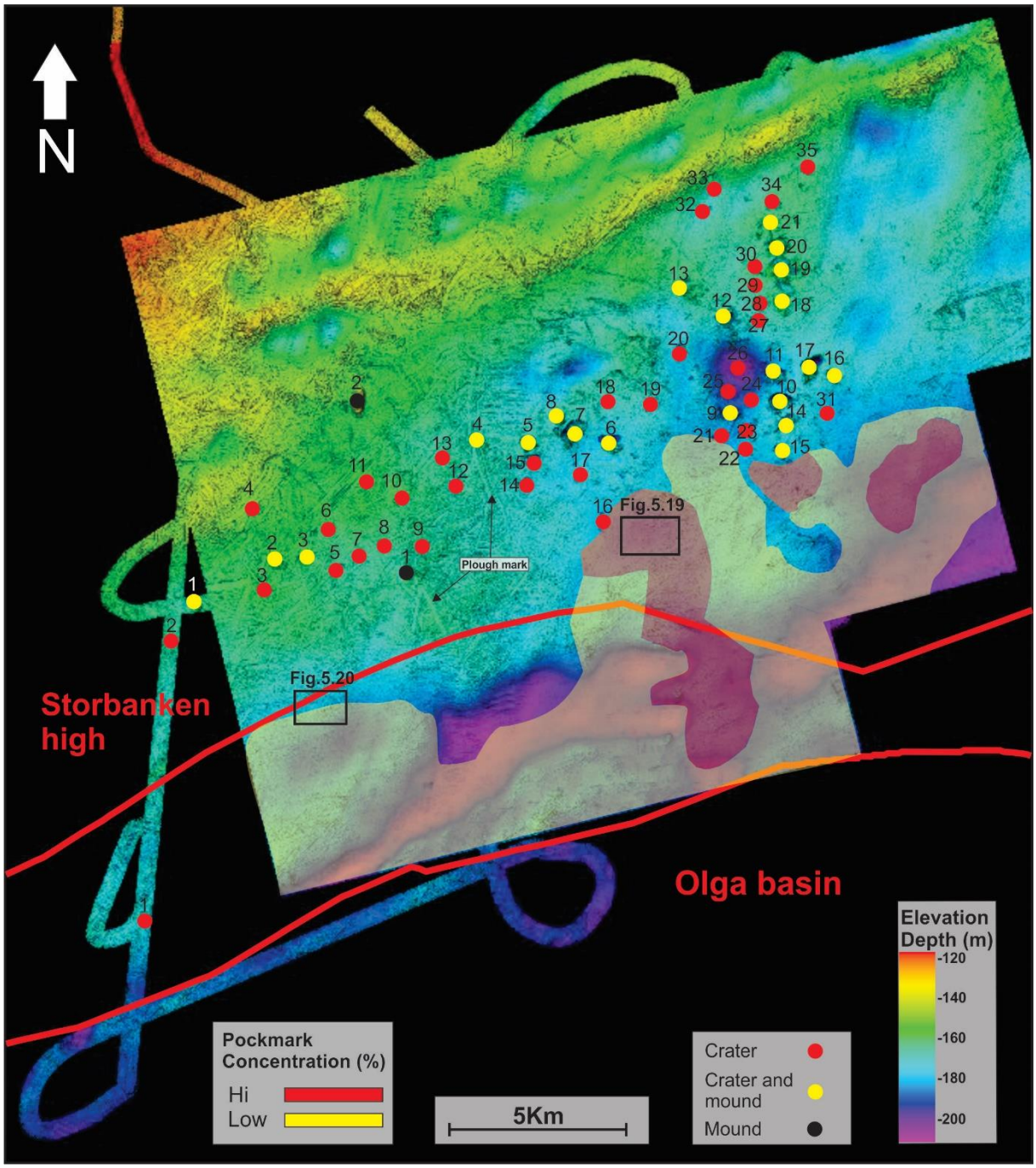

Fig.5.18: Interpreted geomorphological features. The red polygon delineates the structural elements of the Olga basin and Storbanken high. The characteristics of the geomorphological features are displayed in table Appendix D.

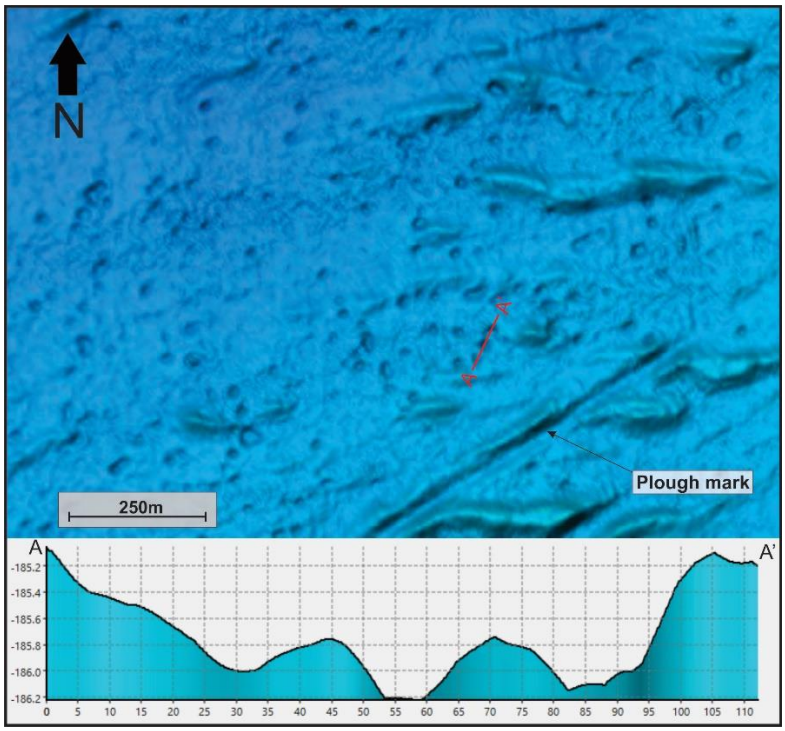

Fig.5.19: Close overview of the area with a high density of pockmarks (red area) as indicated in Fig.5.18, the same scale for elevation depth as used in Fig.5.18, the profile is illustrated in m.

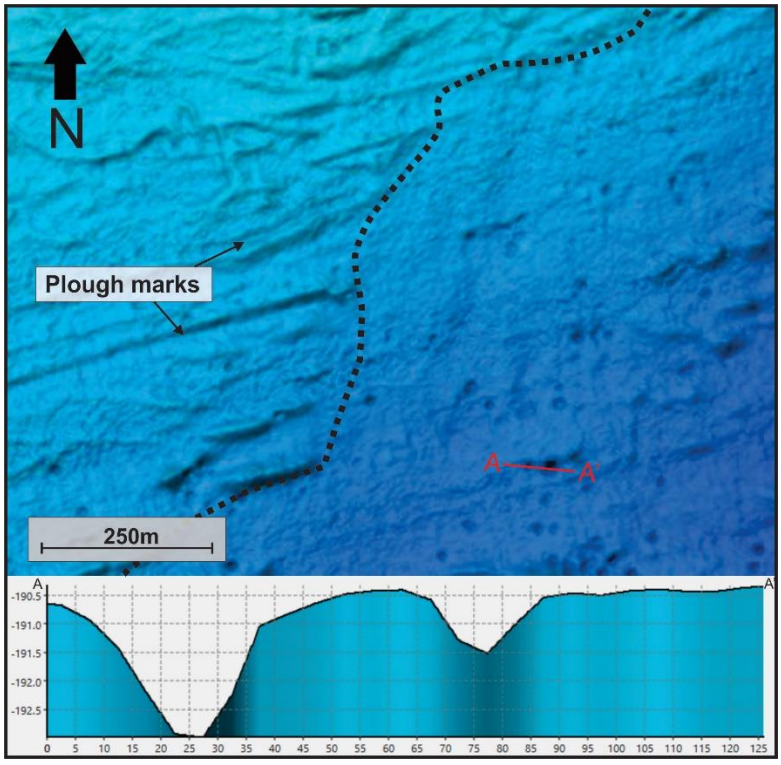

Fig.5.20: Close overview of the transition area from yellow area to area with little to none pockmarks, the same scale for elevation depth as used in Fig.5.18, the profile is illustrated in m.

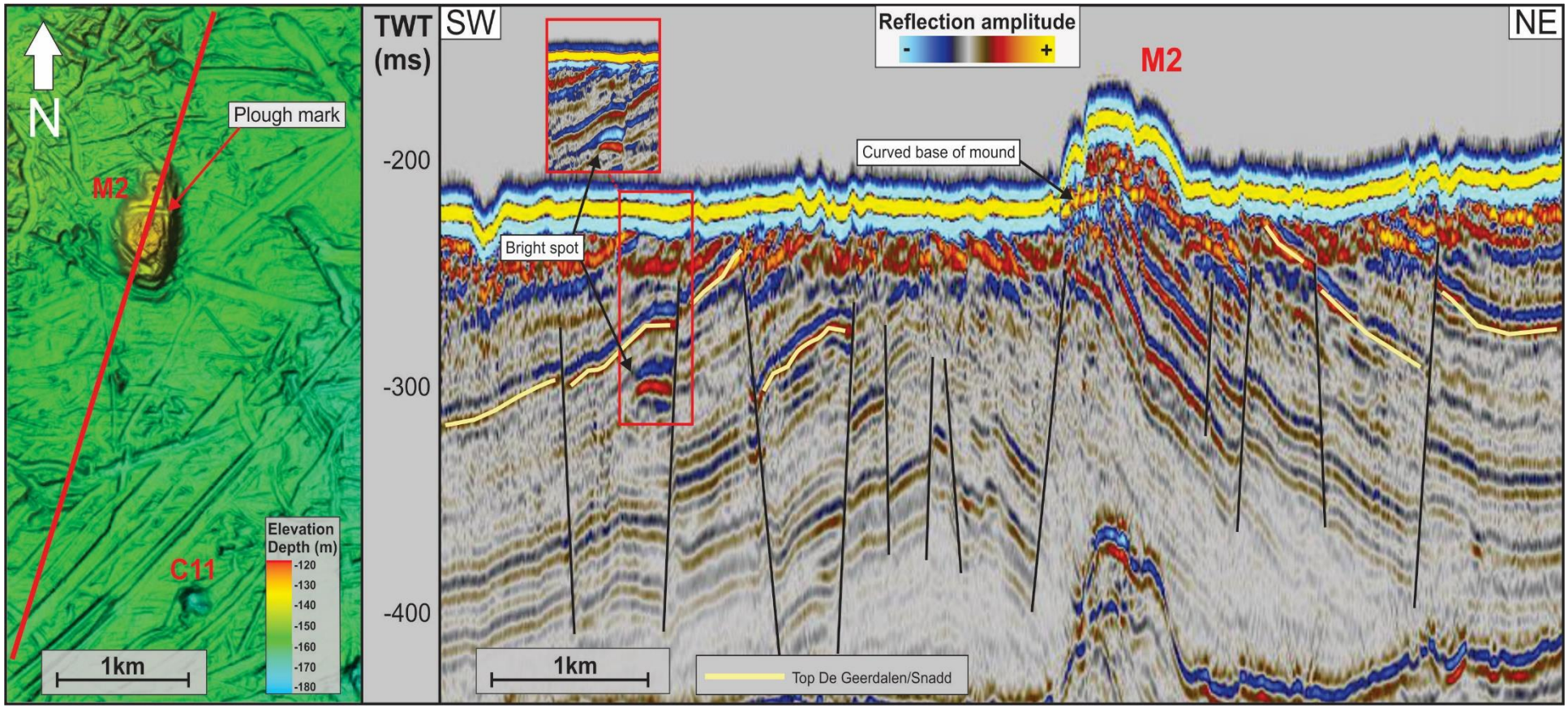

Fig 5.21: Close view of M2 and C11, the red line indicates the orientation of the seismic line. The red square illustrates the brightspot in a reprocessed seismic line. Fig.5.17 for location.

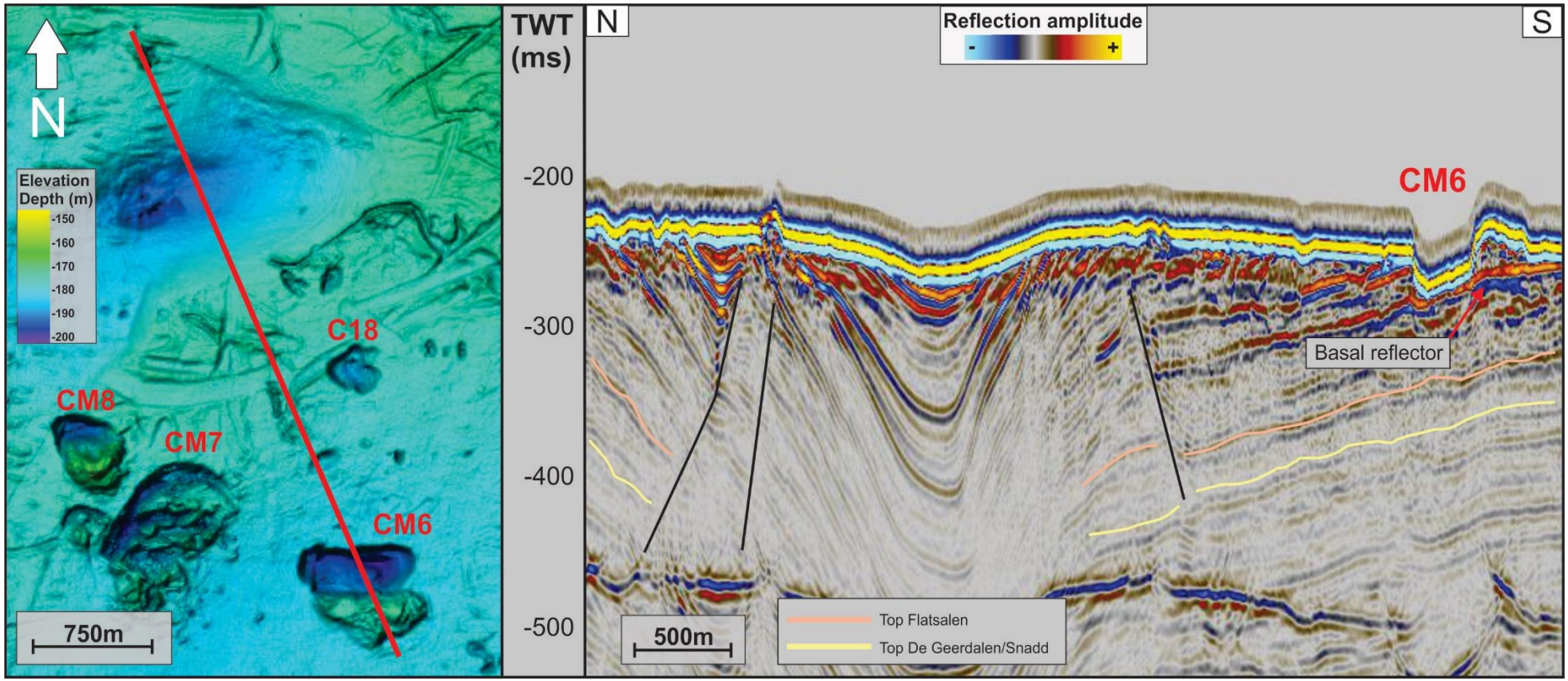

Fig.5.22: Close view of the CM7, CM8 and C18 and the underlying seismic. The red line indicates orientation of the seismic line. Fig.5.17 for location.

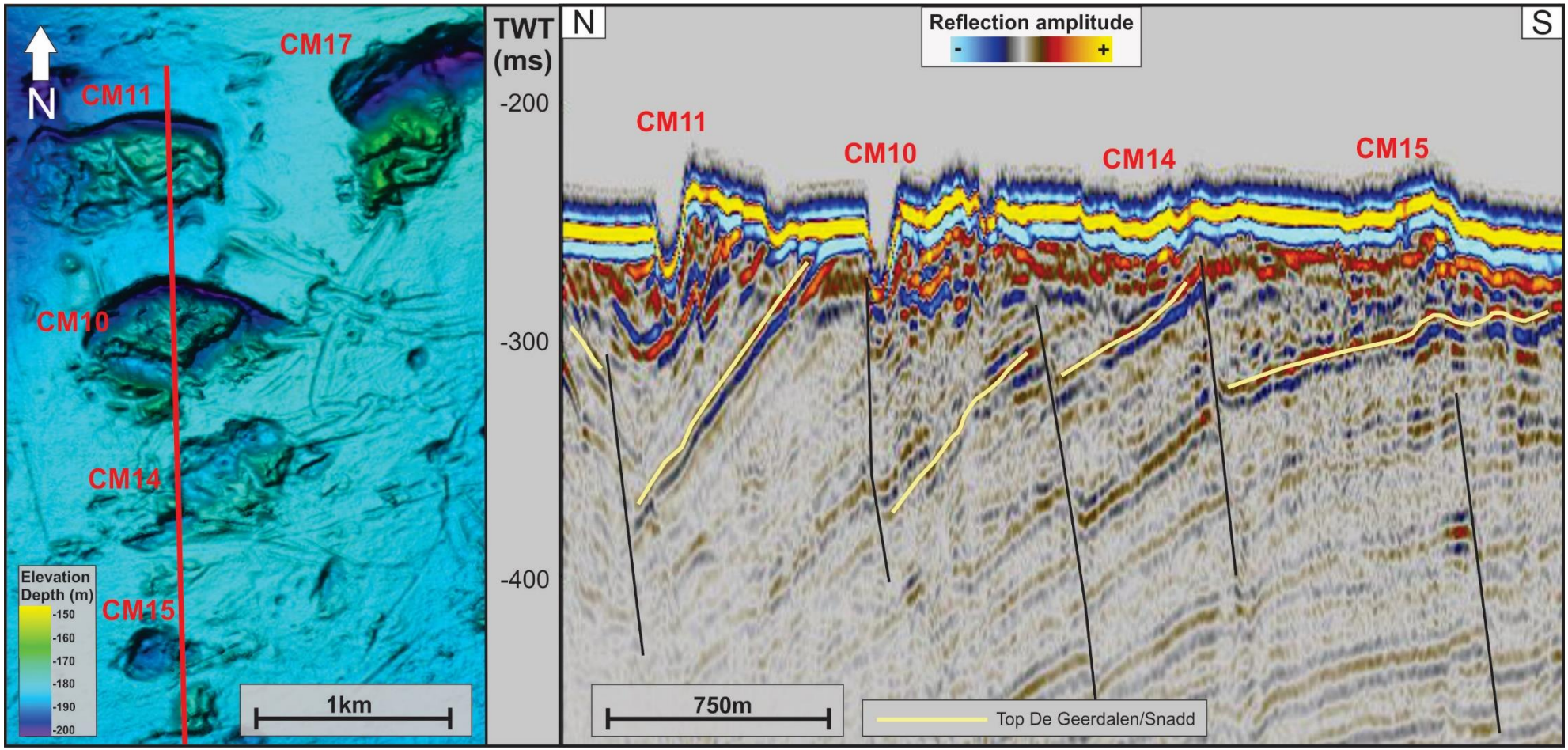

Fig.5.23: Bathymetric and seismic view of craters with internal mounds and associated faults (CM10, CM11, CM14, CM15 and CM17). The red line indicates orientation of seismic line. Fig.5.17 for location.

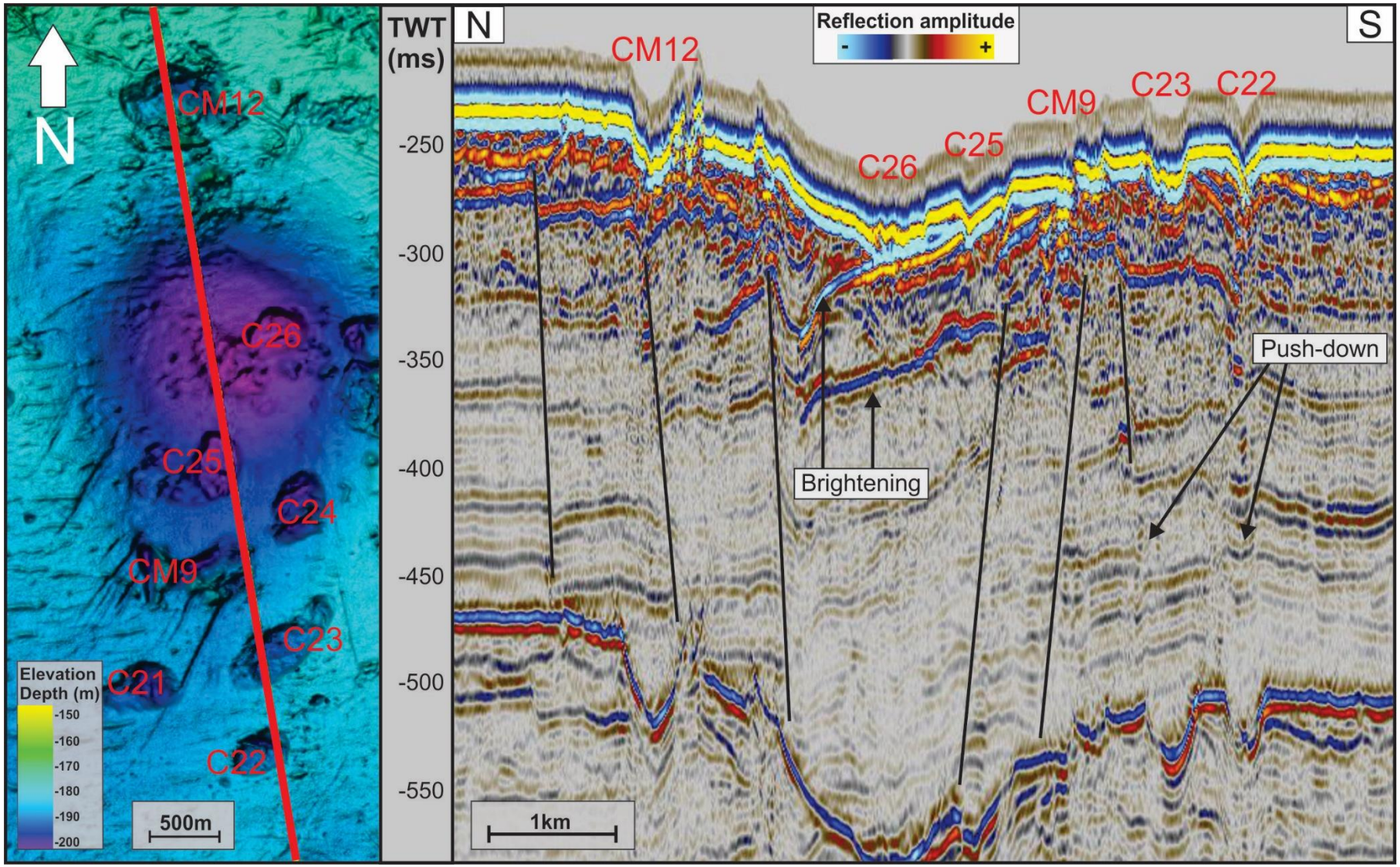

Fig.5.24: Overview of Craters and craters with associated mounds, the seismic reveals complex faulting and seismic amplitude anomalies underneath. Fig.5.17 for location.

5.4 Seismic amplitude anomalies and fluid flow features

The seismic within the study area has revealed amplitude anomalies and fluid flow related features at a presumable zone following the two major faults (F2) and three areas located close to the Kong Karls Land platform (Fig.5.25).

Within the study area there has been identified several vertical zones with disturbed and deteriorated reflections crosscutting other continuous reflectors. Similar features have been suggested to be gas chimneys (chapter 2.2.2) (e.g. Ligtenberg, 2005; Løseth et al., 2009) these features are therefore subsequently referred to as gas chimneys. Within these zones of chaotic seismic reflections and in close proximity there has been identified some push-downs, bright spots and a potential flat spot (Fig.5.26-5.29).

The chaotic reflection pattern of the chimneys was examined by the variance attribute which measures the degree of discontinuity between the reflectors. Reflectors with a high discontinuity are particularly characteristic for the chimneys (Fig.5.27-5.28). It was difficult to distinguish the long and short axis as well as the lateral extent for the gas chimneys based on the limited data available. The potential gas chimneys are annotated for simplicity as gas chimney zone (GCZ) and gas chimney (GC) with numbers (Fig.5.25).

Along the faults (F2) there has been identified some zones of vertical deteriorated reflections which might be a group of potential gas chimneys (GCZ) identified in five different seismic lines, four lines nearly perpendicular and one nearly parallel to the interpreted faults (F2) (Fig.5.25-5.26). Common for the gas chimneys (GCZ) situated along the faults (F2) is that they seem to originate at approximately the same depth, below or slightly above the interpreted middle Carboniferous reflector (Fig.5.26). The chimneys along the faults (F2) also seems to terminate underneath the Top De Geerdalen/Snadd reflector. There is a thickness trend for the chimneys, appearing thinner at deeper parts before increasing in width and thickness at shallower depths (Fig.5.26). The width of the gas chimneys varies from approximately 1 km at the deeper areas and up to 5 km at the shallower areas examined in the north-south direction (Fig.5.26).

The gas chimney examined in the west-east direction had a uniform width of approximately 7.5 km regardless of depth which differs from the chimneys examined in the seismic lines oriented north-south (Fig.5.26d). The seismic line is however oriented relatively parallel to the interpreted faults (F2) which might also explain the large width. East for the potential chimney there was also identified a bright at a depth of 820 ms (TWT).

In addition to the potential gas chimneys (GCZ) identified along the faults (F2), there has also been observed some seismic anomalies suggesting gas chimneys further northwest close to the Kong Karls Land platform (Fig.5.25 and Fig.5.27-5.29).

A gas chimney (GC1) was identified 75 km northwest of the northwestern flank of the Olga basin. This gas chimney seems to originate approximately 200 ms (TWT) above the interpreted middle Carboniferous reflector at a depth of -1850 ms (TWT) (Fig.5.27). However some evidence of chaotic reflections underneath the middle Carboniferous reflector has been identified as well. Special for this chimney is that it is located above an upward curved structure, the reflector on top of the curved structure from where the gas chimney originates indicates brightening with a strong reversed polarity compared to the seafloor reflection (Fig.5.27). Above the terminated gas chimney there is identified a potential flat spot underneath an upward curved structure at shallow depths of -350 to -500 ms (TWT). Above the terminated gas chimney at the seafloor there is identified a distinct depression, the depression is 45 ms (TWT) deep and measures 2,5 km wide (Fig.5.27). The area in which the chimney is identified is upward curving throughout the whole depth as both the Base Cretaceous reflector and the middle Carboniferous reflector is identified to be upward curving. The width of the chimney is varying from 1 km at its smallest and 6 km at its widest, it seems as the gas chimney is concentrated into thinner columns at certain depth intervals (Fig.5.27). It is difficult to determine at what depth the chimney terminates due to the highly folded reflectors, however the chimney seems to terminate within or slightly above the interpreted Flatsalen Formation.

60 km west for the Kong Karls Land platform a potential gas chimney was identified (GC2) (Fig.5.25 and 5.28). This chimney has a uniform width of 7 km. It is difficult to determine the exact depth of origin for this chimney as the chaotic reflection pattern extends to the deepest parts of the seismic and possibly merges with the chaotic reflection exerted by the basement (Fig.5.28). However the chimney is identified to originated underneath the middle Carboniferous reflector (Fig.5.28). The chimney has a bright spot mimicking the seafloor

topography at double the TWT time of the seafloor reflection above where the chaotic reflections terminate. The bright spot is located approximately at the same depth interval as the interpreted Top De Geerdalen/Snadd reflector at a depth of -300 to -400 ms (TWT) (Fig.5.28).

40 km northwest from the northwestern flank of Storbanken high a potential gas chimney was identified (GC3) (Fig.5.25 and 5.29). The gas chimney (GC3) is best visualized at the deeper areas where it seems to originate from depths of -2100 ms (TWT) well below the interpreted middle Carboniferous reflector. It is difficult to determine the upper termination of the gas chimney, however it seems to terminate well below the interpreted Top De Geerdalen/Snadd reflector at depths of -900 ms (TWT) (Fig.5.29). This gas chimney ranges in width from 1 to 4 km, with the wider zone located at the shallower depths. Within the depth interval of -1450 ms (TWT) to -1700 ms (TWT) there was identified more continuous reflectors appearing upward curved within the potential chimney (Fig.5.29).

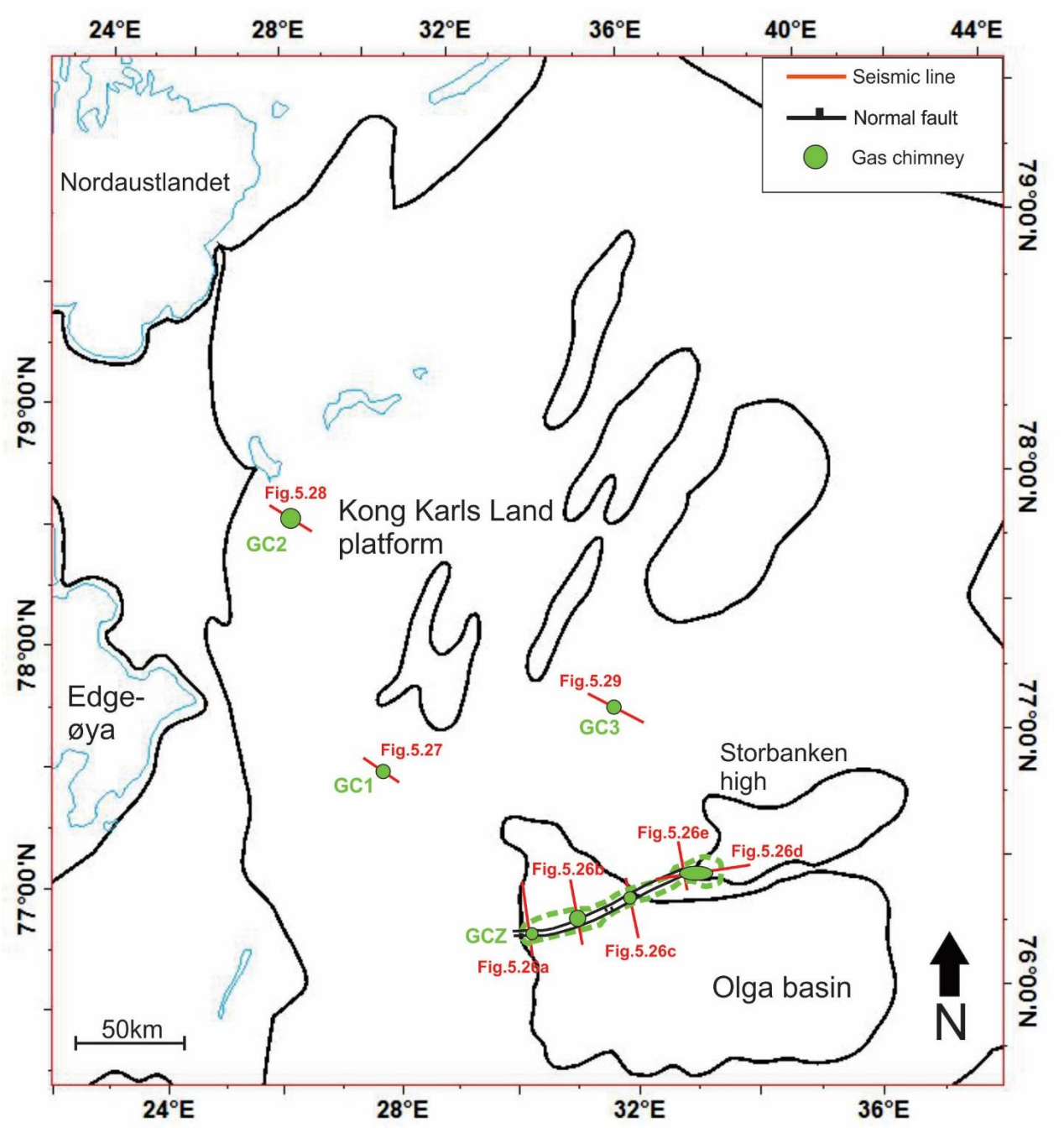

Fig.5.25: overview of the potential gas chimneys. The dotted green line indicates the zone for where there might be gas chimneys within.

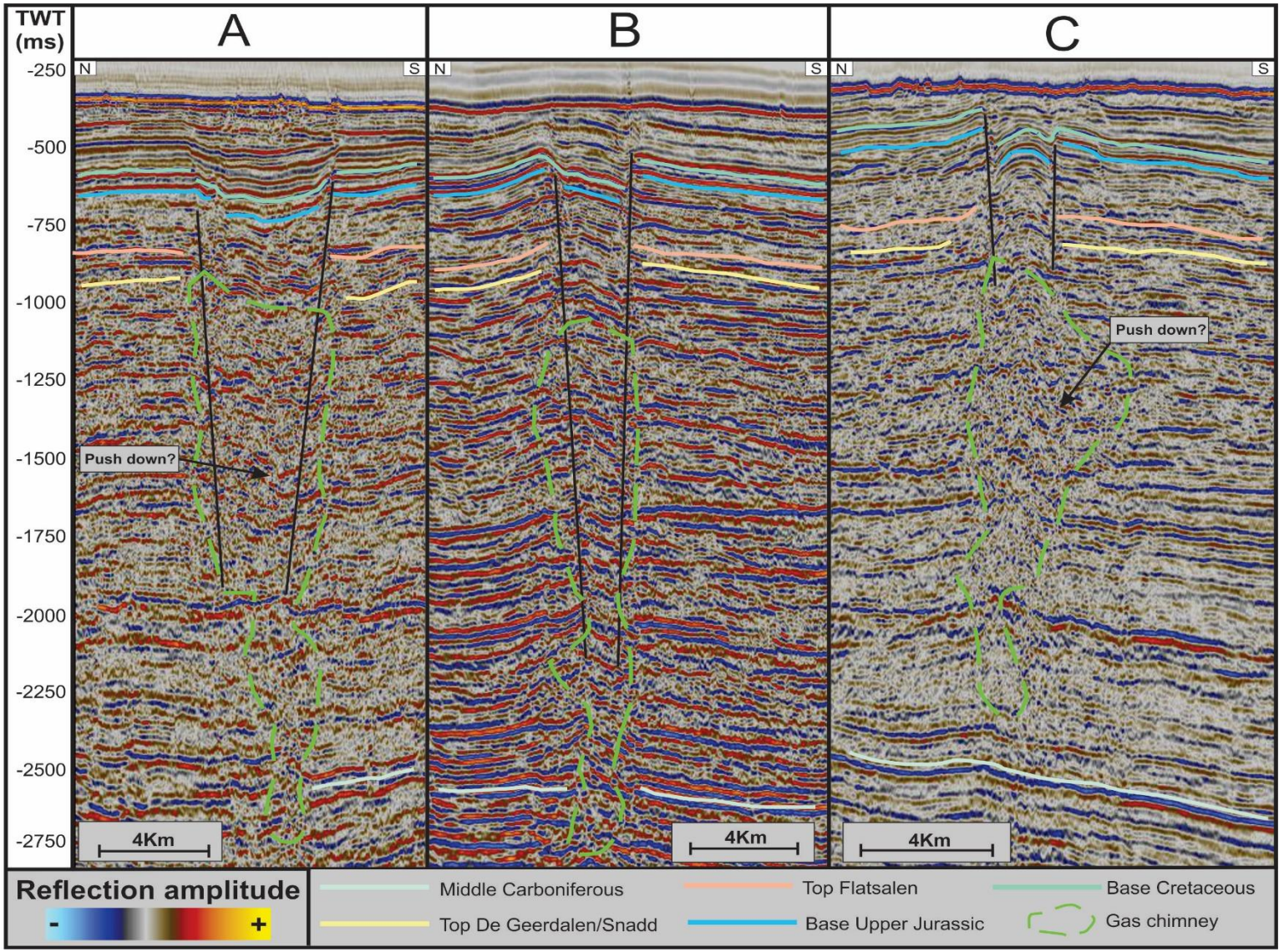

Fig.5.26a-c: Potential gas chimneys (GCZ) identified along the faults (F2). Position of the seismic lines is indicated in Fig.5.25.

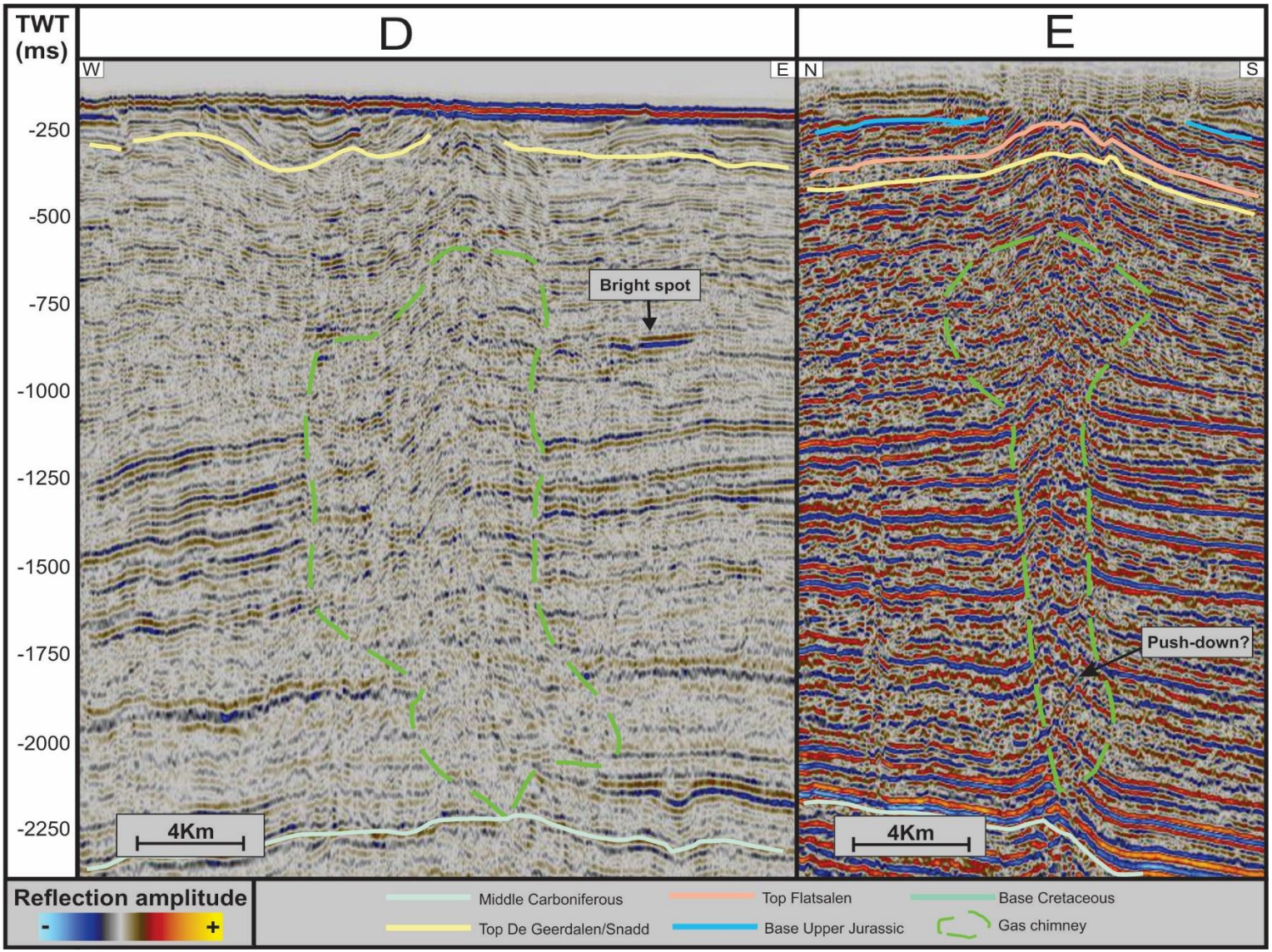

Fig.5.26d-e: Potential gas chimneys (GCZ) identified along the faults (F2). Position of the seismic lines is indicated in Fig.5.25.

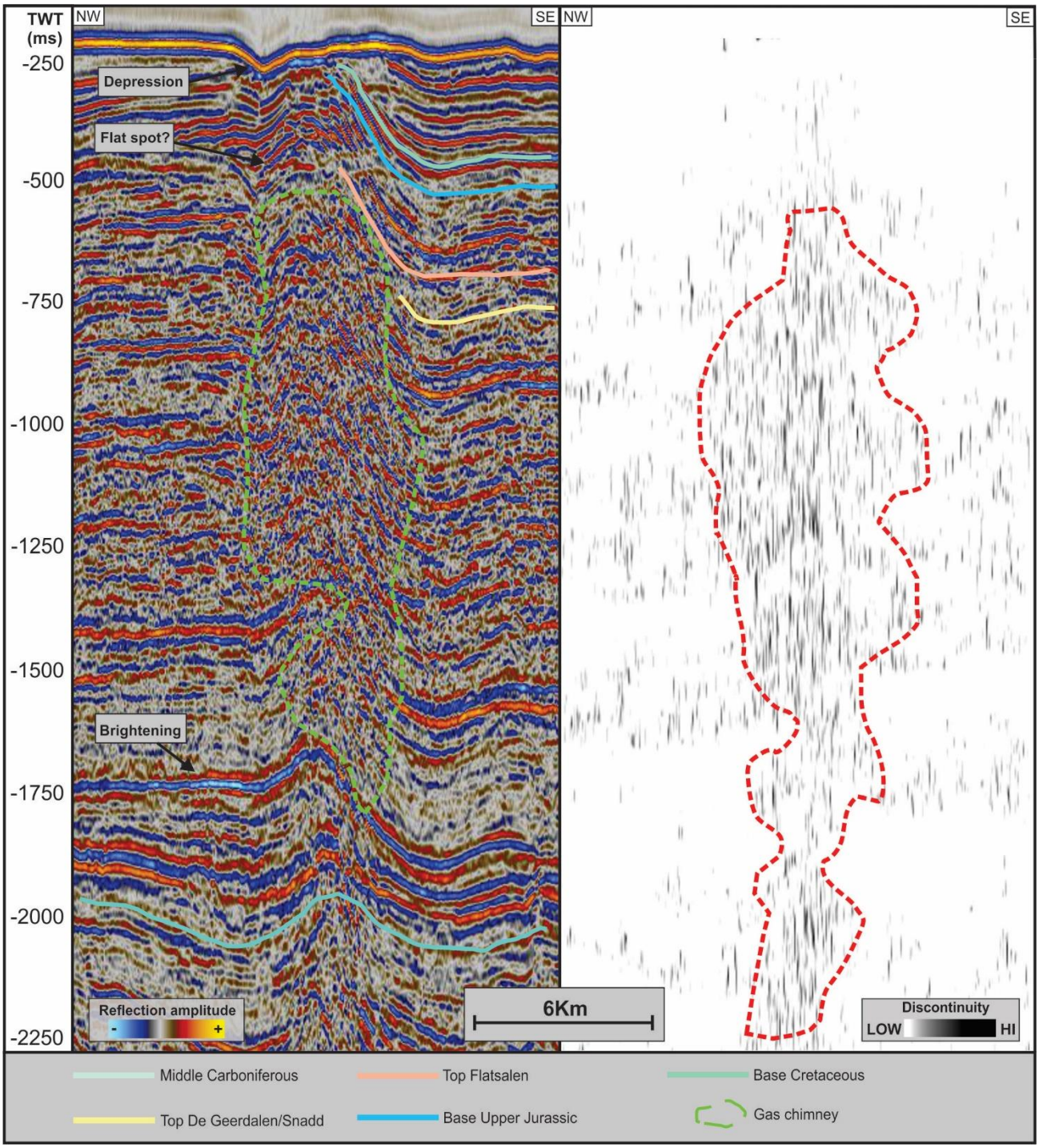

Fig.5.27: Gas chimney (GC1) northwest for the Olga basin illustrated in reflection amplitude and variance edge attribute. Position of the seismic lines is indicated in Fig.5.25.

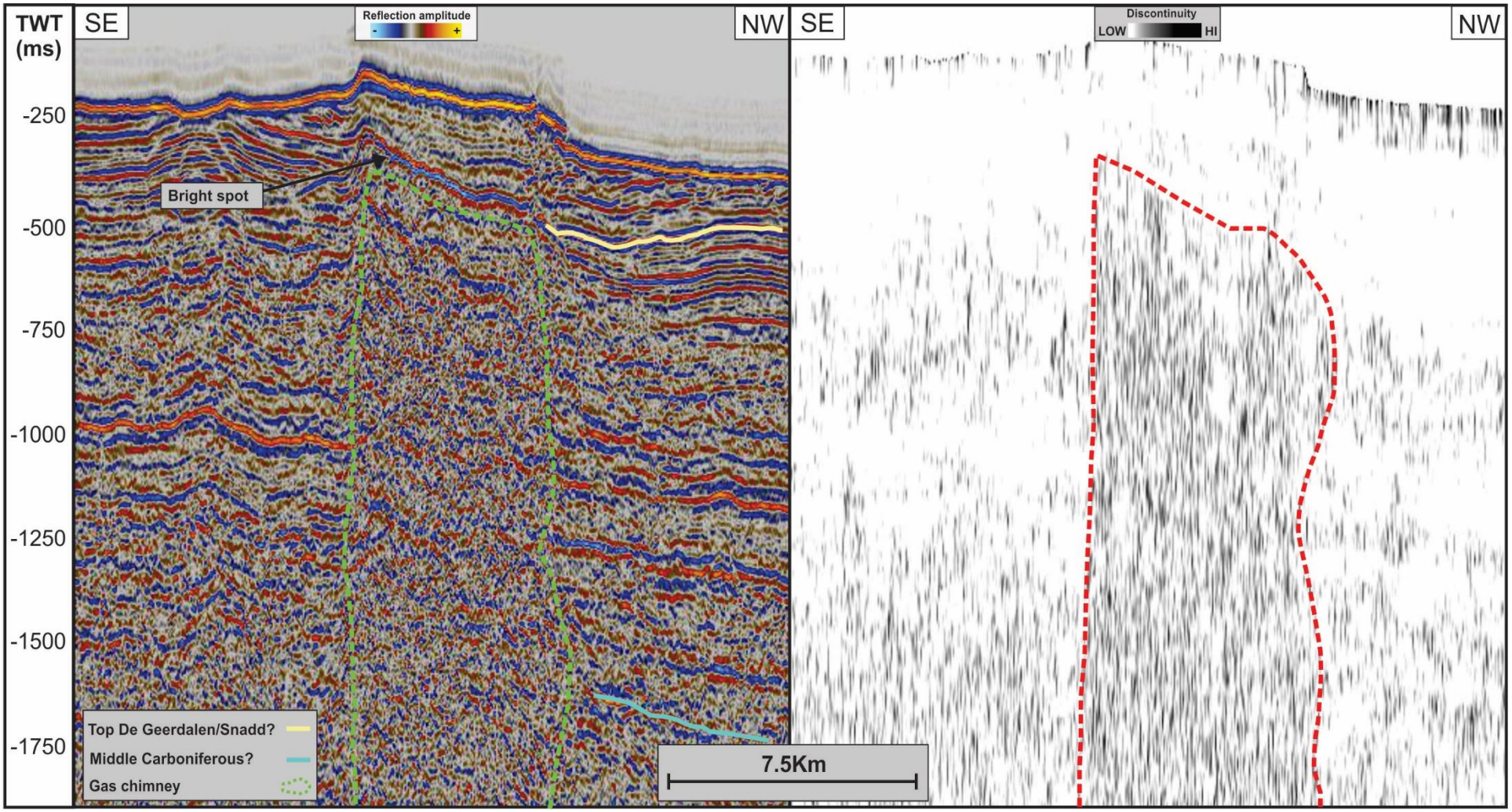

Fig.5.28: Gas chimney (GC2) west for Kong Karls Land platform illustrated in reflection amplitude and variance edge attribute. Position of the seismic lines is indicated in Fig.5.25.

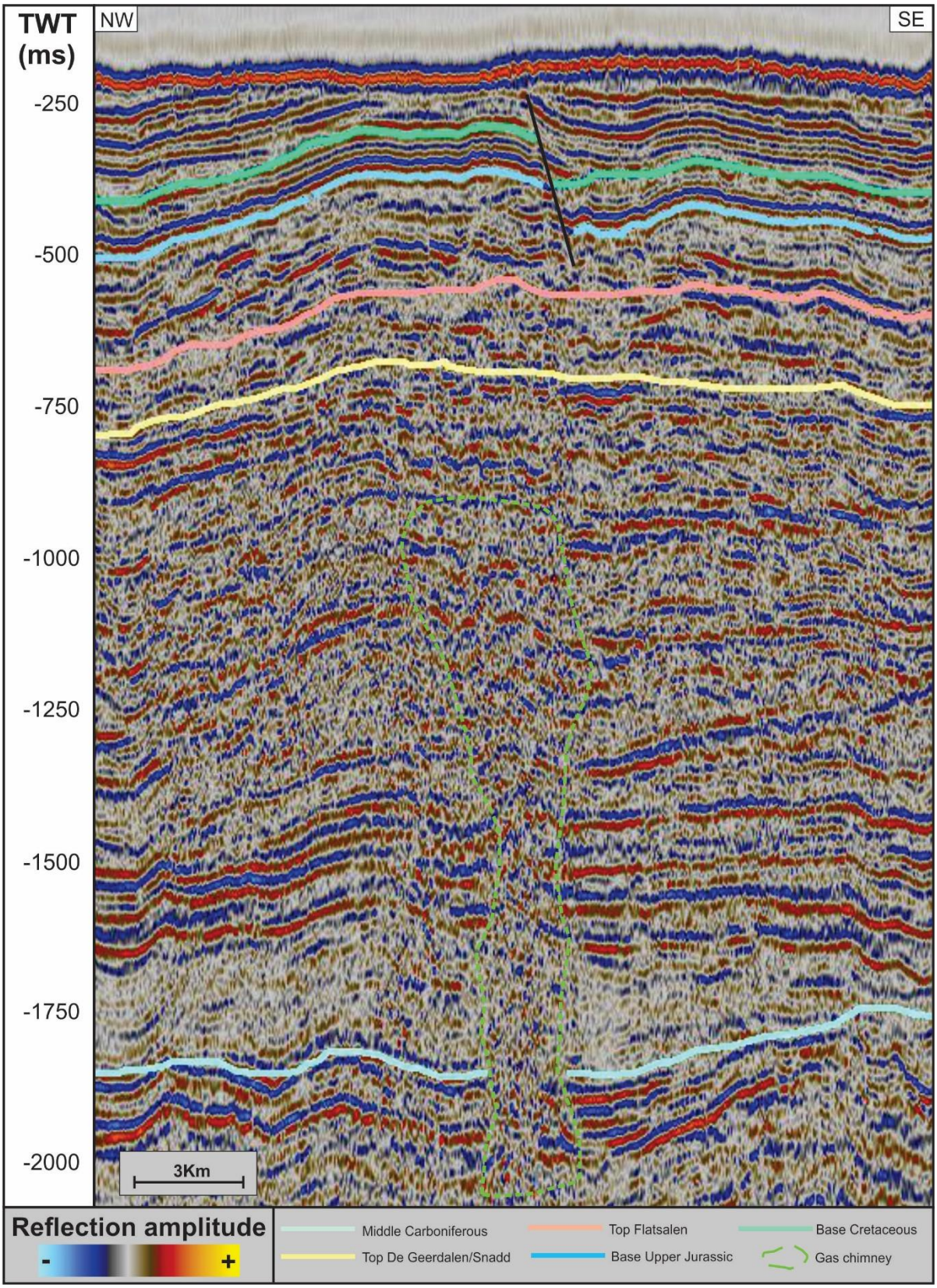

Fig.5.29: Gas chimney (GC3) northwest for Storbanken high. Position of the seismic line is indicated in Fig.5.25.

5.5 Bottom simulating reflector (BSR)

At the central parts of Storbanken high there was identified a reflector with a reversed polarity compared to the seafloor reflection crosscutting other dipping reflectors (Fig.5.30). This reflector is located at depths of -300 ms (TWT), -86 ms (TWT) beneath the seafloor (Fig.5.30). The reflector is identified to be relatively horizontal mimicking the seafloor and reflectors underneath this reversed polarity reflector seem to be faded out with a low reflection amplitude (Fig.5.30). There has not been identified any similar incidents with reflectors crosscutting other reflectors having a reversed polarity compared to the seafloor and a relatively similar topography as the seafloor reflection in the study area. Similar features have been described and interpreted elsewhere on the Norwegian shelf by several authors as the bottom simulating reflector (BSR) (Andreassen et al., 2007; Chand et al., 2008; Klitzke et al., 2016). The reflector is therefore suggested successively to be a potential BSR. To further assess the possibility of this reflection representing a BSR and to examine the gas hydrate potential in the study area there has been conducted a 1D modeling of the Gas hydrate stability zone (GHSZ), this will be further elaborated in chapter 6.5.

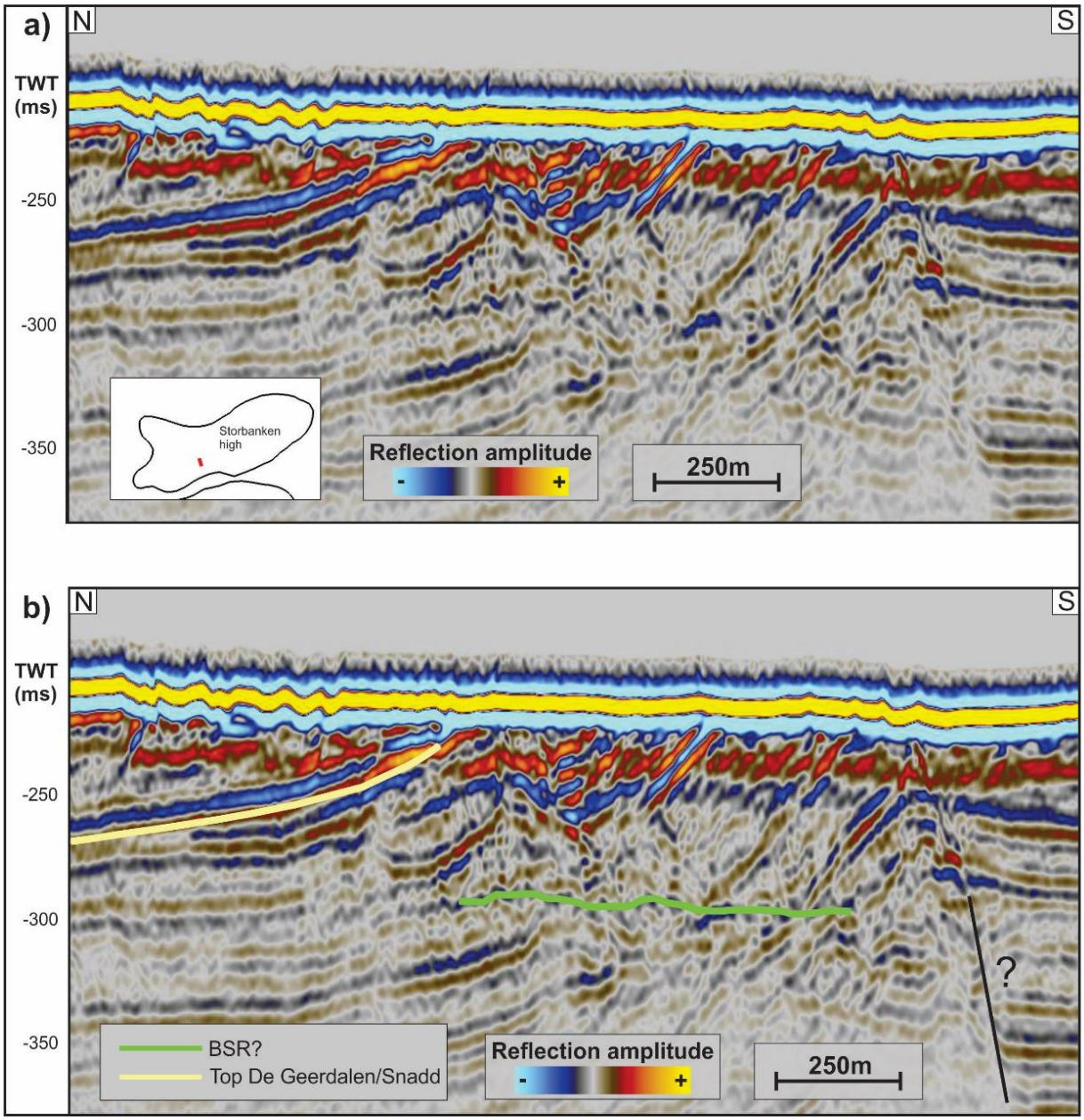

Fig.5.30a) uninterpreted seismic section, inset map in the lower left corner shows the location of the seismic line. b) Interpreted BSR.

5.6 Gas flares

The gas flares represent columnar zones of gas bubbles in the water column. All the recorded gas flares are located at the Storbanken high except four flares which are situated at the NW flank of the Olga basin (Fig.4.6). The Gas flares vary in height from approximately 30 – 200 m extending from the seafloor and into the water column with most of the gas flares having a height ranging within 130 - 160 m (Fig.5.31). The lateral extent of the flares varies between 40 – 250 m with an average width of approximately 120 m. As the flares are detected based on their amplitude anomalies relative to the water column they have their own amplitude properties (Barnard et al., 2015). The amplitudes are measured in raw undefined amplitude values ranging from a minimum of -126 to a maximum of 60, with most values ranging between -90 to -60 (Fig.5.31). A higher positive value represents a higher degree of backscatter and also potentially a higher concentration of bubbles within a flare (Kannberg et al., 2013). The flares identified had generally a higher amplitude in their central and lower parts probably representing a higher concentration of bubbles closer to the area of the leaking source (Fig.5.31). When the gas flares are illustrated in the 2D seismic it's important to keep in mind that there might be some offset in the positioning from the seismic line and the recorded gas flare. The gas flares were found to appear in the seismic within an offset of 1 km perpendicular to the seismic lines. The relationship between the gas flares and subsurface and morphological structures will be further examined in the discussion chapter.

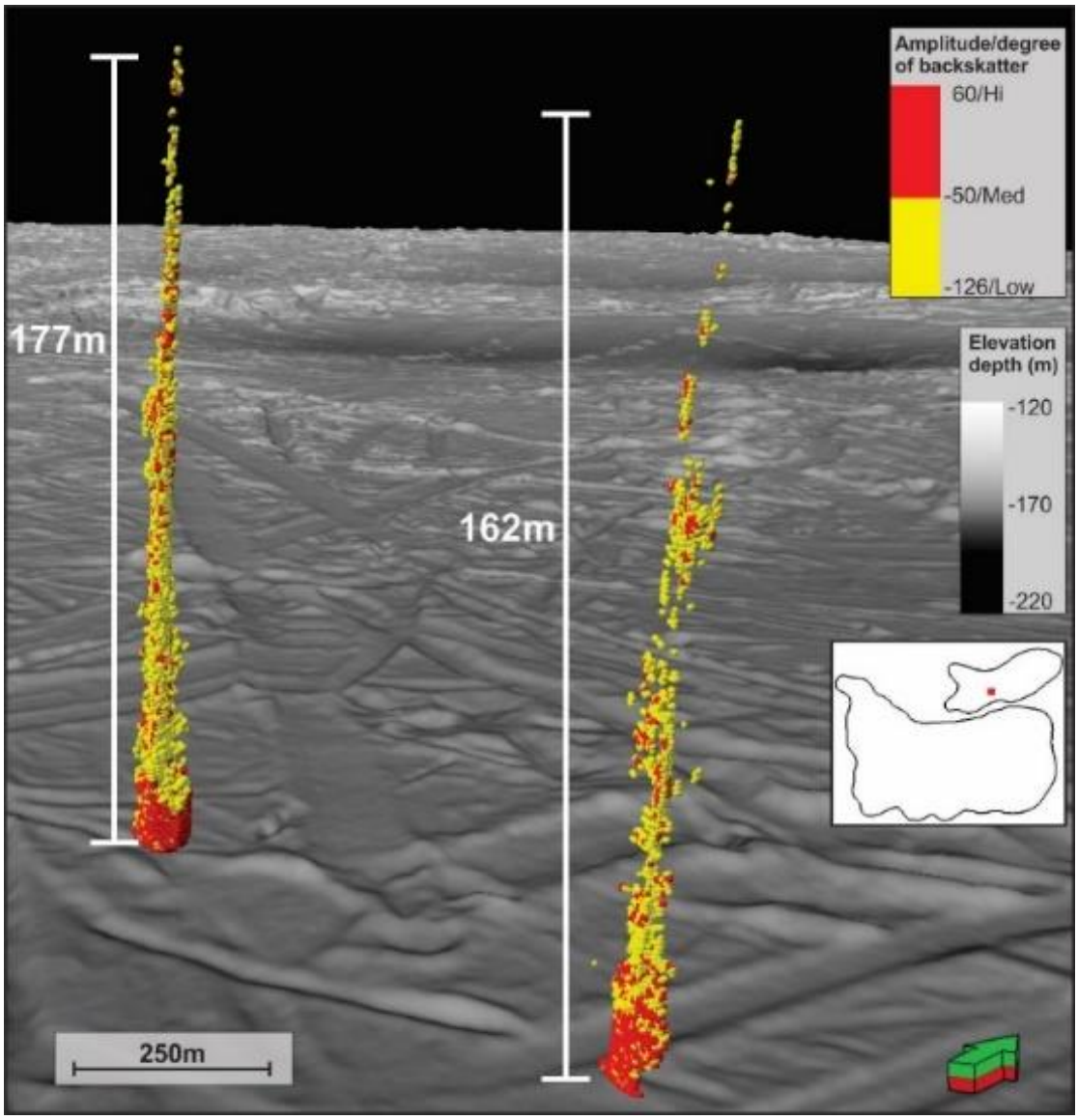

Fig.5.31: Illustration of two gas flares at Storbanken high. Notice how the high amplitudes are dominating closer to the seafloor. The red dot in the inset map indicates the location of the flares.

6 Discussion

This chapter is dedicated to discussing the results and interpreted features in relation to present and former gas seepage activity in the study area.

6.1 Correlation of tectonic events

There have been several tectonic episodes throughout the study area with both compressional and extensional regimes, distinguishing their relative origin and how these features are related to each other is of great interest in relation to the gas seepage activity.

Reverse faults (F5) with growth strata were identified at the Kong Karls Land platform above the interpreted Base Cretaceous reflector indicating compressional movement to been initiated in Early Cretaceous (Fig.5.8 and 5.15). The documented shallow extensional normal faults of (FZ) crosscuts the interpreted Base Cretaceous reflector implying tectonic extension after Early Cretaceous (Fig.5.8-5.10).

The identified NE-SW striking reverse faults interpreted (F5) have a corresponding strike direction to what Kairanov et al, (2018) has classified as Fault family 1 (FF1). These faults are described to be high angled (52-77^{o}) and related to the inversion of late Paleozoic normal faults and the formation of the northeast-southwest oriented anticlines at the Kong Karls Land platform initiated in Late Mesozoic (Grogan et al., 2000; Kairanov et al., 2018). The compressional feature as seen in the faults (F1) is also believed to be part of the same compressional forces as the (FF1) of Kairanov et al, (2018) and the (F5) at the Kong Karls Land platform as the folding of the compressional feature was best defined in the NW-SE direction and the feature was not identified in the NE-SW direction (Fig.5.8 and 5.11-5.12). The easternmost parts of the faults (F2) are also believed to have been influenced by the compressional forces as the graben structure is more curved and folded towards the Storbanken high opposed to the Olga basin (Fig.5.26c-e).

There have been proposed several explanations suggesting the Compression in the study area, Antonsen et al, (1991) has discussed for Late Cretaceous/Paleogene compression being related to the thrust and fold belts as seen on Svalbard caused by the collision of the northeast Greenland and the Northwestern Barents Sea.

More recent studies done by Kairanov et al, (2018) has discussed for three additional potential events in addition to the compression of NE Greenland and NW Barents Sea. The opening of the Amerasia Basin, HALIP or the dextral transpression along the Novaya Zemlya all believed to be initiated in the time span of Late Jurassic – Early Cretaceous (Kairanov et al., 2018).

The interpreted shallow fault zone with NW-SE striking normal faults corresponds to what (Kairanov et al., 2018) has classified as Fault family 3 (FF3), which is described to be high angled normal faults (60-77^{o}) forming horst and graben structures and having throws similar to the interpreted (FZ) of 80 m. The strike direction is however here interpreted to be E-W striking in opposed to the interpretation of NW-SE done for the (FZ) (Fig.5.8). The age of these faults (FF3) is suggested by Kairanov et al, (2018) to be of Post-Early Cretaceous age the same age corresponding to the interpreted (FZ). Studies by Antonsen et al, (1991) has also suggested the normal faults forming horst and graben structures at Storbanken high to be of Post-Jurassic/Early Cretaceous age related to the uplift of the Storbanken high.

Both these tectonic compressional and extensional events are believed to be important factors controlling the gas migration in the study area. The compressional events related to folding and tilting of stratigraphic layers favoring lateral migration along impermeable barriers, while the extensional events might be important for the vertical gas migration along faults.

The geomorphological structures of craters and mounds have indicated to be connected to subsurface tectonic features. There are faults underneath the mound M2, the craters C22, C23 and C25 and the craters with associated internal mounds CM10, CM11, CM12, CM14, CM15, CM18, CM19 and CM20 (Fig.5.21 and 5.23-5.24). This corresponds to every Crater and crater with an associated mound except four craters and one crater with an associated mound to have related faults underneath the areas which are exposed by seismic. This might suggest a linkage between these geomorphological features and the faults. The faults examined underneath the craters and mounds are believed to be part of the interpreted shallow fault zone (FZ) as these are best visualized in the southwest-northeast direction and not visualized in the seismic line oriented in the northwest-southeast direction which most likely corresponds to the direction of the strike (Fig.6.6-6.7). Curved reflectors and a potential dome structure situated underneath (M2) also suggest that compressional forces have been active here potentially related to the same compression as the reverse faults (F5) and compressional feature in (F1) (Fig.6.6-6.7).

6.2 Gas seepage origin

In order to examine the origin of the gas seepage it is essential to understand the source and maturity of the rocks in the study area. The maturity of source rocks is mainly controlled by the thermal history of the sediments which is generally controlled by burial, tectonic activity, sedimentation rate, thermal properties of the sediments and the amount of heat distributed by the sub-lithospheric mantle (Gac et al., 2018).

A simplified 1D maturation modeling based on burial depth and the thermal gradient will be implemented in order to get a broader understanding of the formation source rock potential and the origin of gas seepage in the study area. Both the Olga basin and Storbanken high were examined in order to see whether the source rock is proximal (in proximity to the identified gas flares) or distal (distant from the identified gas flares). The model is based on the measured formation thicknesses in chapter 5.1, the mean formation velocities from Table 4.5 and an assumed geothermal gradient of 35°/km in the study area (Fig.4.8). The location of the evaluated areas is indicated in (Fig.6.1).

The Maturation process of a source rock is an irreversible process, this means once the source rock has been buried at a certain depth and exposed to high temperatures the hydrocarbons might have been expelled (Henriksen et al., 2011a). In the Barents Sea there has been found mature source rocks often at much shallower depths than which expected from vitrinite reflectance measurements, this indicates the source rocks to been located at greater depths than its present and subsequently been exposed to higher temperatures (Henriksen et al., 2011a). A regional uplift event in the Barents Sea caused by late Mesozoic - Cenozoic tectonism has been documented by several authors (Grogan et al., 1999; Smelror et al., 2009; Dallmann et al., 2015). The net erosion model from Henriksen et al, (2011a) is therefore regarded when evaluating burial history pre-uplift (Fig.4.7). Based on the net erosion model of Henriksen et al, (2011a) has the study area been exposed to uplift and erosion of a 1600 m thick succession of sediments (Fig.4.7). A 1600 m thick sediment package is therefore regarded when calculating thermal history for the source rocks before the late Mesozoic – Cenozoic uplift.

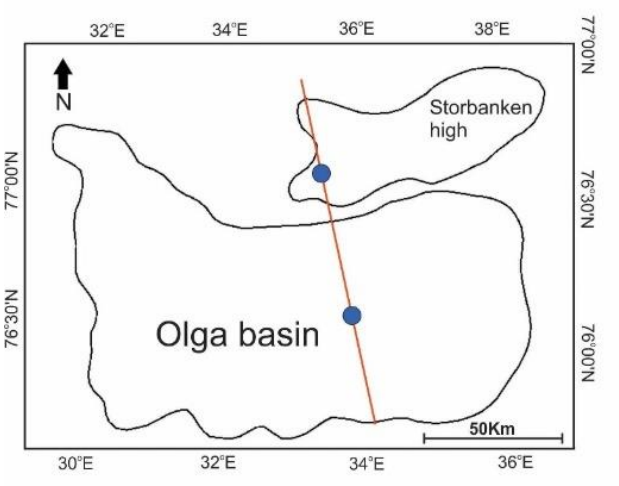

Fig.6.1: The blue dots indicate the areas for where the maturation has been calculated. The red line indicates the seismic line for which formation thicknesses was measured (Fig.5.2-5.3).

6.2.1 Agardhfjellet Formation

There has been documented several working source rocks in the Barents Sea, the most prolific source rock of the Barents Sea is perhaps the Late Jurassic Hekkingen Formation corresponding to the Agardhfjellet Formation in the northern Barents Sea (Dore, 1995; Worsley, 2008). The Hekkingen Formation is documented to have a high TOC content and being an important working source rock in the southwestern parts of the Barents Sea as it is the source rock for several producing fields (Koevoets et al., 2018). However, there is some uncertainty regarding the maturity of this source rock in the study area due to erosion and preservation at relatively shallow depths (Koevoets et al., 2018).

The base of the Agardhfjellet Formation at the Olga basin was found at depths of 863 m, by adding the 1600 m of net erosion the Formation was found to previously been exposed to a maximum burial depth of 2463 m, corresponding to a maximum temperature of 86 ^{o}C pre-uplift (Table 6.1).

Based on the calculations this indicates the Agardhfjellet Formation to potential previously been exposed to favorable temperature conditions for producing oil at the deepest parts of the Olga basin. However, it is worth mentioning that the Agardhfjellet Formation was deposited during Late Jurassic age giving it a short amount of time to be buried, generate and expel hydrocarbons before the regional Cenozoic uplift. The Agardhfjellet Formation as a proximal source rock at the Storbanken high is disregarded as the formation is eroded throughout large parts of this area (Fig.5.7). The Olga basin is a continuous syncline structure which if there

was oil generated it would most likely follow the rim and leak out along the flanks of the basin as the Agardhfjellet Formation outcrops at the seafloor (Fig.5.2). It is therefore very unlikely that the present seepage activity has had its origin from the Agardhfjellet Formation. Additionally, has modeling studies by Grogan et al, (1999) suggested that the Agardhfjellet Formation most likely is immature at the highs and platform areas east for Storfjordrenna. Vitrinite reflectance studies across the Olga basin by Grogan et al, (1999) based on shallow boreholes from NPD has also indicated the Agardhfjellet Formation to be a thermally immature source rock. This maturation evaluation however, is based on a 1000 m of net eroded Cenozoic strata. The Formation with its black impermeable shale is however regarded to constitute as a great cap rock in the study area.

6.2.2 Botneheia Formation

The most prominent source rock in the study area is perhaps the Botneheia Formation also known to be the time-transgressive formation of the Steinkobbe Formation in the southern Barents Sea (Bjorøy et al., 2010; NPD, 2017).

The base of the Botneheia Formation at the Olga basin was found at depths of 2050 m, by adding the 1600 m of net erosion the Formation has been exposed to a maximum burial depth of 3650 m, corresponding to a maximum temperature of 128 ^{o}C pre-uplift (Table 6.1).

The base of the Botneheia Formation at the Storbanken high was found at depths of 845 m, by adding the 1600 m of net erosion the Formation has been exposed to a maximum burial depth of 2445 m, corresponding to a maximum temperature of 86 ^{o}C pre-uplift (Table 6.1).

Based on these calculations the Botneheia Formation is believed to be gas mature at the Olga basin. This might suggest this formation to be a potential distal source rock for the gas seepage activity observed at Storbanken high, as gas generated within the Botneheia Formation at the Olga basin could migrate along the rim of the basin syncline towards the Storbanken high (Fig.5.2-5.3). The Botneheia Formation is found to be within the oil window at the Storbanken high. However, it should not be disregarded that the Botneheia Formation could be gas producing in the deeper parts of Storbanken high as the examined area is at the shallowest part of the high.

The Botneheia Formation is a marine Type II and III Kerogen with documented high TOC content (5-10%) proved to be an oil and gas generating source rock at the Hopen deep, Blanknuten in Edgeøya and in the Barents Sea South (Grogan et al., 1999; Abay et al., 2014; NPD, 2017). The upper parts of the Botneheia Formation are documented to be more oil-prone than the lower parts which tend to be mixed oil and gas generating (Bjorøy et al., 2010). Vitrinite reflectance studies across the Olga basin based on shallow boreholes from NPD by Grogan et al, (1999) also supports a thermally mature source rock of Botneheia Formation. This maturation evaluation however, is based on a 1000 m of net eroded Cenozoic strata. 1D basin modeling by Weniger et al, (2019) has indicated the Botneheia Formation to be oil and gas prone suggesting it to be the source for thermogenic bound gas identified in the Olga basin. The Botneheia Formation is therefore regarded to be an important source rock governing the gas seepage activity in the study area.

6.2.3 Billefjorden Group

The deeply buried coal and carbonaceous shale of the Billefjorden Group is regarded to be a potential gas generating source rock in the study area.

The Top Billefjorden Group at the Olga basin was found at depths of 5275 m, by adding the 1600 m of net erosion the Formation has been exposed to a maximum burial depth of 6875 m, corresponding to a maximum temperature of 240^{o}C pre-uplift (Table 6.1).

The Top Billefjorden Group at the Storbanken high was found at depths of 3515 m, by adding the 1600 m of net erosion the Formation has been exposed to a maximum burial depth of 5115 m, corresponding to a maximum temperature of 179^{o}C pre-uplift (Table 6.1).

The Billefjorden Group is well within the gas window at both the Olga basin and the Storbanken high, which might suggest the possibility of both proximal and distal source rock from the Billefjorden Group in the study area. However, the timing of hydrocarbon expulsion in relation to a sealing cap rock should be considered as the thermal history for this source rock could imply the Group to be overmature at this stage in the Olga basin. The Billefjorden Group was deposited in a terrestrial environment and is most likely a Type III source rock favoring gas generation. Despite the Billefjorden source rock being a Type III source rock there has also been evidence of oil generated from this source rock on Svalbard and the Finmark Platform (Van Koeverden., 2011). The Billefjorden Group has also been documented

to constitute large coal deposits on Svalbard and significant volumes of hydrocarbons have been generated from this source rock in the Russian sector of the Barents Sea (Grogan et al., 1999). The Billefjorden Group might therefore be an important source rock in the Study area.

6.2.4 Other source rocks and potential errors for maturity calculation

It should also be noticed that the Lower Permian organic carbonate-rich Gipsdalen Group and the Upper Permian marine dominated shale of the Tempelfjorden Group might also be working source rocks in the study area (NPD, 2017). There exists however some uncertainty for these groups especially the Tempelfjorden Group which is believed to be eroded over large areas at the highs (Fig.3.3) (NPD, 2017). These two groups are believed to be sufficiently buried and might therefore not be excluded to be potential sources for gas seepage activity in the study area.

It's worth noticing as deeper the maturation is calculated the more uncertainty there is for the accuracy of the calculations. The accuracy of the calculations is governed by several factors such as formation velocity, amount of net erosion, timing and degree of uplift and geothermal gradient. The potential for local heath flows in Cretaceous related to (HALIP) is also believed to be a potential contributing factor for source rock maturation in the high Arctic (Polteau et al., 2016; Kairanov et al., 2018). Despite the potential sources of error was this only meant as a simplified model to get a general idea for the potential gas seepage origin.

Table 6.1: Thickness of Cretaceous sediments from (Antonsen et al., 1991). Velocity for Realgrunnen subgroup to the Botneheia Formation is extracted from the velocity log (Appendix A). Velocity for late Early Triassic to Top Bilefjorden Group is extracted from (Ktenas et al., 2018) *(Appendix B). T= two-way travel time and v = mean formation velocity. Assumed geothermal gradient 35°C/km.*

Location	Formation/Group	Measured TWT thickness	Mean Formation velocity	Formation thickness ($\frac{T*v}{2}$)	Maximum burial depth post-uplift	Maximum burial depth pre-uplift (1600 m)	Thermal history (1 km = 35°C)
Olga basin	Cretaceous sediments	-	-	750 m			
	Agardhfjellet Formation	0.085 S	2650 m/s	113 m	863 m	2463 m	86 °C
	Realgrunnen Subgroup	0.155 S	3000 m/s	233 m			
	Flatsalen Formation	0.07 S	3100 m/s	109 m			
	De Geerdalen/Snadd Formation	0.25 S	3300 m/s	413 m			
	Botneheia Formation	0.27 S	3200 m/s	432 m	2050 m	3650 m	128 °C
	late Early Triassic – Top Perm	0.8 S	4800 m/s	1920 m			
	Top Perm – Top Billefjorden Group	0.45 S	5800 m/s	1305 m			
	Top Billefjorden Group				5275 m	6875 m	240 °C
Storbanken high	De Geerdalen/Snadd Formation	0.25 S	3300 m/s	413 m			
	Botneheia Formation	0.27 S	3200 m/s	432 m	845 m	2445 m	86 °C
	late Early Triassic – Top Perm	0.75 S	4800 m/s	1800 m			
	Top Perm – Top Billefjorden Group	0.3 S	5800 m/s	870 m			
	Top Billefjorden Group				3515 m	5115 m	179 °C

6.3 Vertical migration

Vertical migration is an important factor for transporting hydrocarbons from deeper source rocks to shallower reservoir intervals, several faults and potential gas chimneys has been identified and are believed to be important conduits governing the gas seepage activity in the study area.

6.3.1 Vertical migration along faults

Faults are the most common conduits for transportation of deep-seated fluids as the sediments at greater depths often are consolidated or lithified due to compaction and chemical processes and therefore usually have poor permeability (Ligtenberg, 2005). Therefore understanding whether a fault is leaking or sealing is crucial information as this might indicate migration pathways from deeper reservoirs and source rocks or indicate sealing hydrocarbon filled fault structures (Ligtenberg, 2005). Large amounts of gas seepage have been documented along faults further east for the study area along the Hornsund Fracture zone (Mau et al., 2017).

The faults in the study area were examined in the result chapter 5.2, both extensional and compressional faults were identified. The majority of faults identified at the Storbanken high where Post-Early Cretaceous NW-SE striking normal faults. Active gas migration has been observed along the flare investigated area above the faults F1, F2, F4, F6 and within the FZ (especially in proximity of the mound M2) (Fig.4.6; 6.2-6.3; 6.5h-g and 6.7). As the faults within the shallow fault zone (FZ) is documented to reach well below the interpreted Top De Geerdalen/Snadd reflector they might be important conduits for gas migration from the deeper reservoir of the De Geerdalen/Snadd Formation and potentially the source rock of Botneheia Formation (Fig.5.9-5.10). The migration through these faults is regarded not only as a direct migration pathway to the water column but also important conduits for redistributing gas into shallower reservoir intervals such as the Realgrunnen Subgroup (Fig.6.12).

The gas leakage along F1 has gas flares oriented in an NW-SE direction (Fig.6.2). As the seepage occurs along the fault plane the flares are believed to indicate the striking direction of the fault which supports the interpretation of NW-SE striking normal faults within the shallow fault zone (FZ). It is difficult to distinguish the vertical extent of the leaking F1 and F4 as these seismic lines are disturbed by multiples (Fig.5.11-5.12 and 5.14). However, the extent of the F1 and F4 faults might correspond to the termination observed within the shallow fault

zone (FZ) as these share the same strike direction (Fig.5.8). A potential flatspot was identified underneath the leaking fault F4, this might indicate a filled fault structure with constant slow seepage and the bright spot located above the fault might imply gas accumulations trapped underneath the seafloor (Fig.5.14 and 6.3).

The faults F6 at Storbanken high which was identified in relation to the large depressions at the seafloor was identified to leak at three areas (Fig.5.16 and 6.2-6.3). However, the flares were identified with an offset of 1 km to the north which might also suggest a different leaking mechanism. Thus, no distinct fluid flow indications were identified in the bathymetry, suggesting that the faults are the most likely migration pathway (Fig.5.16 and 6.2-6.3).

6.3.2 Vertical migration along gas chimneys

Vertical gas migration along gas chimneys has been studied by several authors in the southern Barents Sea (e.g. Rajan et al., 2013; Vadakkepuliyambatta et al., 2013), however little work has been done in the northern Barents Sea.

Acoustic gas chimneys (GCZ and GC1 – GC3) were identified close to the Kong Karls Land platform and along the faults (F2) stretching throughout the Olga basin, reaching the western flank of Storbanken high (Fig.6.2). The deteriorated seismic which these gas chimneys constitute might indicate an inhomogeneous distribution of gas in the sediments representing vertical migration pathways for free gas (Ligtenberg, 2005; Løseth et al., 2009). However, as there has not been identified any gas flares above the interpreted gas chimneys they cannot be concluded to conduct gas at the present day. Shallow gas accumulations can additionally deteriorate the seismic signal resulting in vertical wipe-out zones below (e.g. Arntsen et al., 2007), however the push-downs, bright spots and flat spot observed in proximity of the chimneys might suggest these to be excluded for such features (Fig.5.26-5.28). Gas chimneys are commonly related to areas which have been exposed to high strain favoring spilling and seal failure (Ligtenberg & Connolly, 2003; Rajan et al., 2013). The gas chimneys GC1-GC3 are located in proximity to the Kong Karls Land platform (Fig.5.25). As discussed in chapter 6.1 is this an area which has been exposed to severe compression in Early Cretaceous age, while the GCZ is identified along the long faults (F2), this might imply the positioning of the chimneys correlating to areas which have been exposed to high strain and tectonic forces. The Kong Karls Land platform is an area additionally influenced by both volcanic intrusions and

salt which also could cause deteriorated seismic, misinterpreted chimneys to be such features should therefore not be disregarded (Grogan et al., 1999; NPD, 2017).

The GC1 was identified to have steeply upturning reflectors along the vertical zone of deteriorated seismic (Fig.5.27). Folding of reflectors along the deteriorated seismic signal is also characteristic for salt structures, the possibility for this chimney to be misinterpreted for a salt structure should therefore not be excluded (Jones & Davison, 2014). However, this potential gas chimney seemed to originate from near the crest of a strong negative amplitude upward curving reflector which could represent gas accumulations within a folded anticline structure and focused fluid migration from a fractured seal (Fig.5.27). Doré & Jensen, (1996) and Tasianas et al, (2016) has discussed for uplift and erosion to be a generating mechanism for gas chimneys caused by gas expansion, hydraulic fracturing of bedrock and subsequently vertical gas migration. When a sealing cap rock is uplifted and the pressure is decreased it deforms easier and fractures at lower strain levels (Doré & Jensen, 1996). This gas chimney (GC1) could therefore potentially represent such failure of the sealing cap rock suggesting leakage from a deeper reservoir. Additionally, there was also identified a potential flat spot located underneath a presumably folded anticline structure near the seafloor which could suggest accumulations of gas within the folded structure fed from the gas chimney (GC1) (Fig.5.27). However, the flat spot was identified at double the two-way traveltime of the seafloor reflection and could therefore also possibly represent a seafloor multiple. The seafloor reflection above this chimney was also identified with a large depression (Fig.5.27). Pockmarks and craters are common seafloor features related to gas chimneys which could imply this depression to been generated by gas from the chimney reaching the seafloor (Cathles et al., 2010).

The gas chimney zone (GCZ) which stretches along the fault (F2) might in addition to being caused by gas in the sediments also potentially be related to the fault structure causing the deteriorated seismic signal or a combination of both as chimneys are commonly related to faults (Fig.5.25) (Rajan et al., 2013). The chaotic reflection pattern might additionally be related to the faults (F2) simply having a very complex structure e.g. a transpressional or transtensional with a complex fracture network, this is however only speculative as the limited data in the area makes it difficult to examine this. Gas seepage is identified above the easternmost part of the GCZ close to the southwestern flank of Storbanken high (Fig.6.2 and 6.5h). The active gas seepage is however identified only at the area which where the cap rock of Agardhfjellet Formation is outcropping, this might also suggest lateral migration along this

formation in addition to migration along the gas chimney or along the fault (F2) (Fig.6.2; 6.4 and 6.5h).

At the upper termination of the GC2 there were identified a strong reflector with a reversed polarity compared to the seafloor reflection (Fig.5.28). This bright reflector is of great interest as it is located underneath the impermeable cap rock of Flatsalen Formation which might suggest potential accumulation of gas. The bright reflector was however identified to mimic the seafloor reflection and was located at double the TWT of the seafloor which might also suggest this bright spot to possibly be misinterpreted for a seafloor multiple (Fig.5.28).

The gas chimney GC3 might be an important feature governing the gas seepage activity at Storbanken high as its upper termination is below the base Flatsalen Formation and it is located in a favorable position related to the northwest dipping stratigraphy. This might imply a shift in migration from vertically migration along the chimney to laterally migration along the impermeable Flatsalen Formation in a southeast direction towards the Storbanken high (Fig.6.11-6.12). The gas fed from this chimney might also migrate further vertically along the leaking normal faults (FZ) and into the reservoir of Realgrunnen Subgroup and laterally along the Agardhfjellet Formation (Fig.6.12). The lateral migration along these cap rocks will however, be further elaborated in the next chapter.

Common for all the gas chimneys identified in the study area is that they are all deep-seated, originating close to the interpreted middle Carboniferous reflector. This might suggest gas originating from the Billefjorden Group and strengthens the theory for a working Billefjorden Group source rock in the study area as earlier discussed in chapter 6.2.3.

The uplift and erosion during the Cenozoic caused by the Paleocene-Eocene uplift related to the opening of the Norwegian-Greenland Sea and repeatedly glaciations with uplift and erosion during the Plio-Pleistocene have been described by Tasianas et al, (2016) to be the generating mechanism for gas chimneys at the Hammerfest Basin. The vast uplift of the highs in Late Jurassic – Early Cretaceous and regional uplift in Cenozoic in the northern Barents Sea might therefore be an important generating mechanism for the potential gas chimneys identified in the study area.

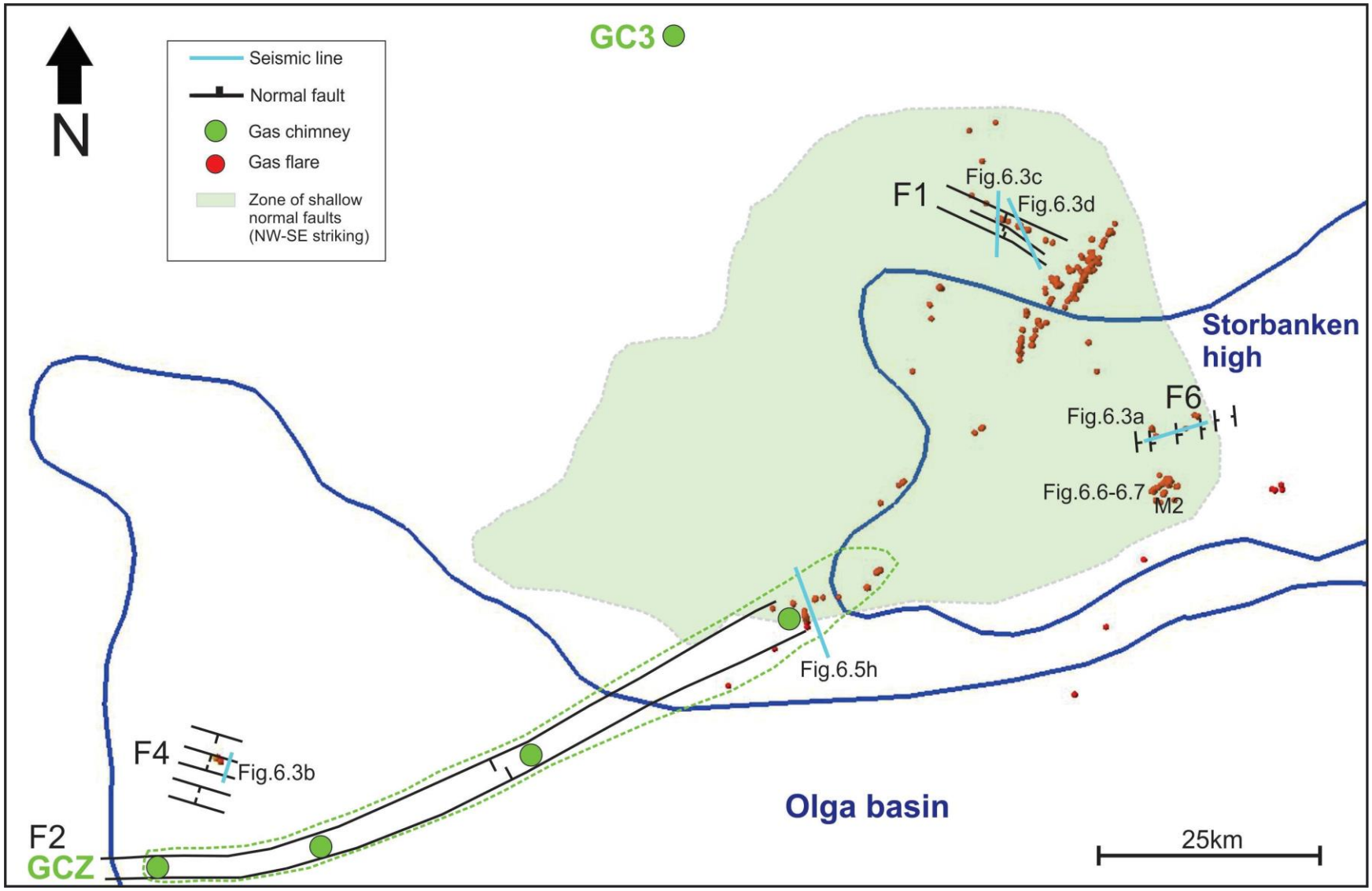

Fig.6.2: overview of vertical migration along gas chimneys and faults and how they correlated to the gas flares identified. See Fig.4.6 for flare investigated area.

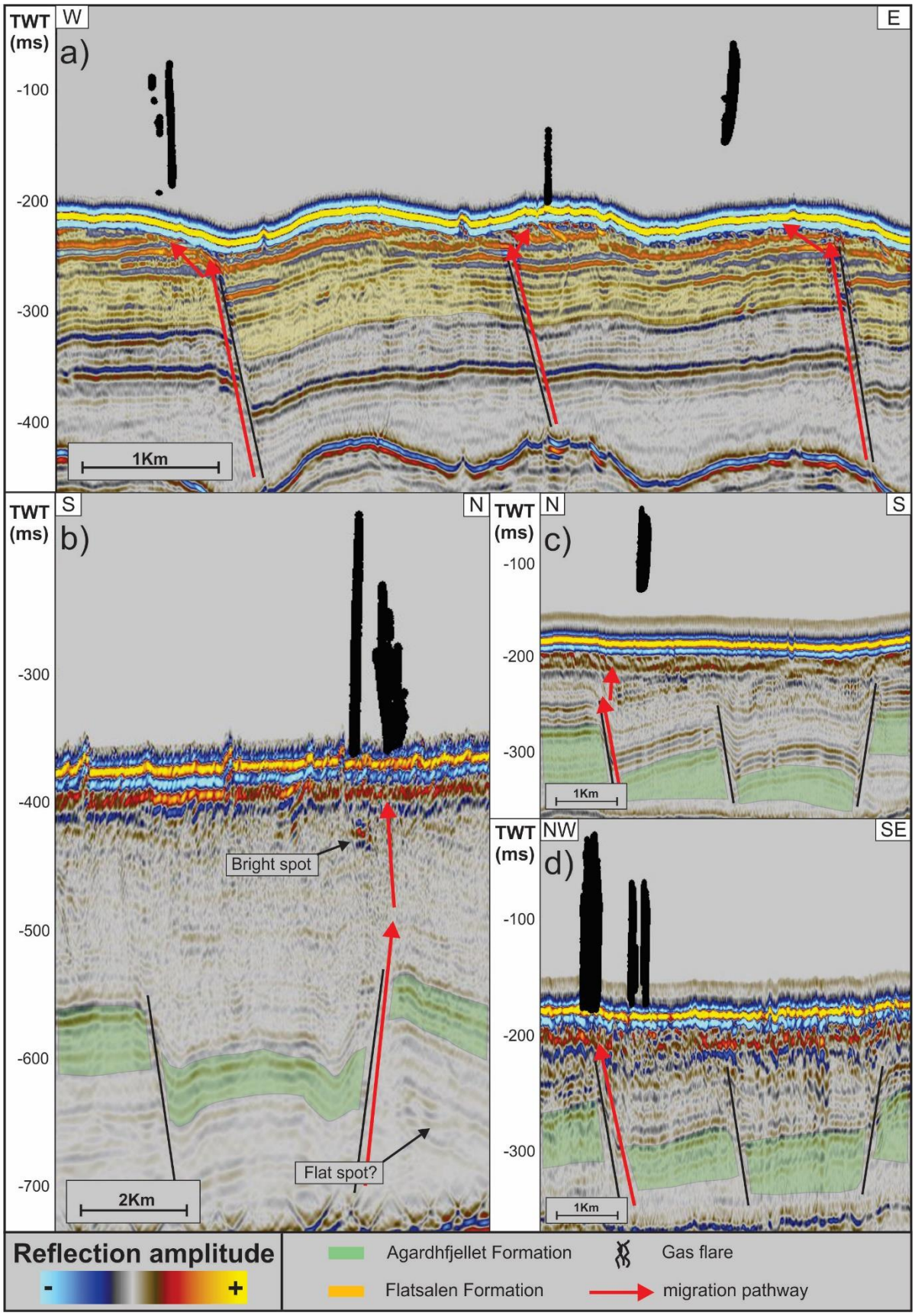

Fig.6.3: Vertical migration along the faults F1, F4 and F6. The black gas flares represent columnar zones of gas bubbles in the water column. Ses Fig.6.2 for position of seismic lines.

6.4 Lateral migration along cap rocks

Lateral migration along impermeable barriers is a common phenomenon where the hydrocarbons migrate for long distances. Along the base of Agardhfjellet Formation and Flatsalen Formation there has been identified several gas flares at the areas where these formations outcrops at the seafloor and is eroded. This might suggest that hydrocarbons have migrated along these impermeable formations. The Lateral migration has been influenced by the tectonic forces which have folded and tilted the stratigraphic layers and concentrated the migration towards the leaking points. It is believed that the tectonic compressional forces initiated in Early Cretaceous tilting the Stratigraphy towards the southeast played an important role for the lateral migration in the northwestern parts of the Storbanken high area (Chapter 6.1).

6.4.1 Agardhfjellet Formation

Migration along the Agardhfjellet Formation is believed to occur within the highly mature and reworked sand of Realgrunnen Subgroup. This formation has proven to be a working reservoir rock at the Snøhvit field in the southern Hammerfest basin and constitutes great reservoir qualities with documented high permeability and porosity (Grogan et al., 1999; Worsley, 2008). For the gas to migrate into the sand of Realgrunnen Subgroup it must migrate through the impermeable cap rock of Flatsalen Formation. Faults within (FZ) have been documented to leak as discussed in chapter 6.3.1 (Fig.6.2 and 6.3c-d). The faults (FZ) are therefore regarded to be important conduits for gas migration from deeper intervals such as the reservoir of De Geerdalen/Snadd Formation and possibly the source rock of Botneheia Formation and into the reservoir of Realgrunnen Subgroup sealed by the Agardhfjellet Formation (Fig.6.12). Most of the active gas seepage is identified along the northwestern flank of the outcropping Agardhfjellet Formation, the absence of gas seepage along the southern flank of this outcropping formation might be related to the absence of leaking normal faults in the Olga basin (Fig.6.2 and 6.4-6.5). The distance from the outcropping Agardhfjellet Formation to the point where the stratigraphy starts to dip towards the southeast which would lead potential hydrocarbons to migrate laterally towards the Kong Karls Land platform is measured to be 45 km. This might suggest a distal generating source rock for the gas seepage within an offset of 45 km to the northwest for the gas seepage identified along the northwestern flank of the outcropping Agardhfjellet Formation. Unfortunately, in a

hydrocarbon exploitation perspective is the Agardhfjellet Formation relatively constant dipping to the point where it outcrops suggesting no trap structures to accumulate hydrocarbons.

Weniger et al, (2019) have suggested the Upper Jurassic Hekkingen source rock also known as the Agardhfjellet Formation to form a regional seal throughout the northern Barents Sea. As areas where this seal is missing or disturbed by faults, there is identified gas migration through the seafloor. A sealing Agardhfjellet Formation is also supported by Sokolov et al, (2017) which has identified high seepage activity in relation to sub-cropping Jurassic layers northeast of Kong Karls Land.

6.4.2 Flatsalen Formation

Migration along the cap rock of Flatsalen Formation occurs within the reservoir of the De Geerdalen/Snadd Formation. The reservoir of the De Geerdalen/Snadd Formation has been proven as a working hydrocarbon reservoir for several producing fields in the southern Barents Sea (Henriksen., et al., 2011b; Klausen & Mørk, 2014).

Gas might migrate into the De Geerdalen/Snadd Formation through the normal faults (FZ) at Storbanken high (Fig.6.2-6.3 and 6.12). Gas might also migrate directly from the Botneheia Formation to the reservoir of De Geerdalen/Snadd Formation in the Olga basin and potentially the deeper parts of the Storbanken high where the Botneheia Formation is gas mature (Fig.6.12).

The majority of gas seepage observed along the outcropping Flatsalen Formation is associated with the mound feature M2 which is located in the center of the eroded Flatalen Formation (Fig.6.6). It is believed that the mound is situated on the crest of a presumable dome structure as indicated by the seismic with tilted stratigraphy dipping from the mound in every direction, focusing the lateral migration to this area (Fig.6.6). A distal source rock within the Olga basin generating gas could be possible as there has been identified gas seepage at the southern flank of the outcropping Flatsalen Formation (Fig.6.6-6.7). Direct migration from the Botneheia source rock to the reservoir of De Geerdalen/Snadd Formation is most likely for the lateral migration along the Olga basin as there has not been identified leaking faults in the eastern parts of the Olga basin (Fig.6.12). There is also identified lots of leaking faults in proximity of the mound (M2), which might imply lateral migration along the Flatsalen Formation followed

by vertical migration into the water column through the leaking normal faults (FZ) (Fig.6.7). The Botneheia Formation is perhaps the most likely source for the gas migrating laterally along the Flatsalen Formation. However, it should not be disregarded with a Billefjorden Group source rock migrating vertically through the potential gas chimneys of GC3 and GCZ or along the faults of (F2) and into the reservoir of De Geerdalen/Snadd Formation (Fig.6.2 and 6.12).

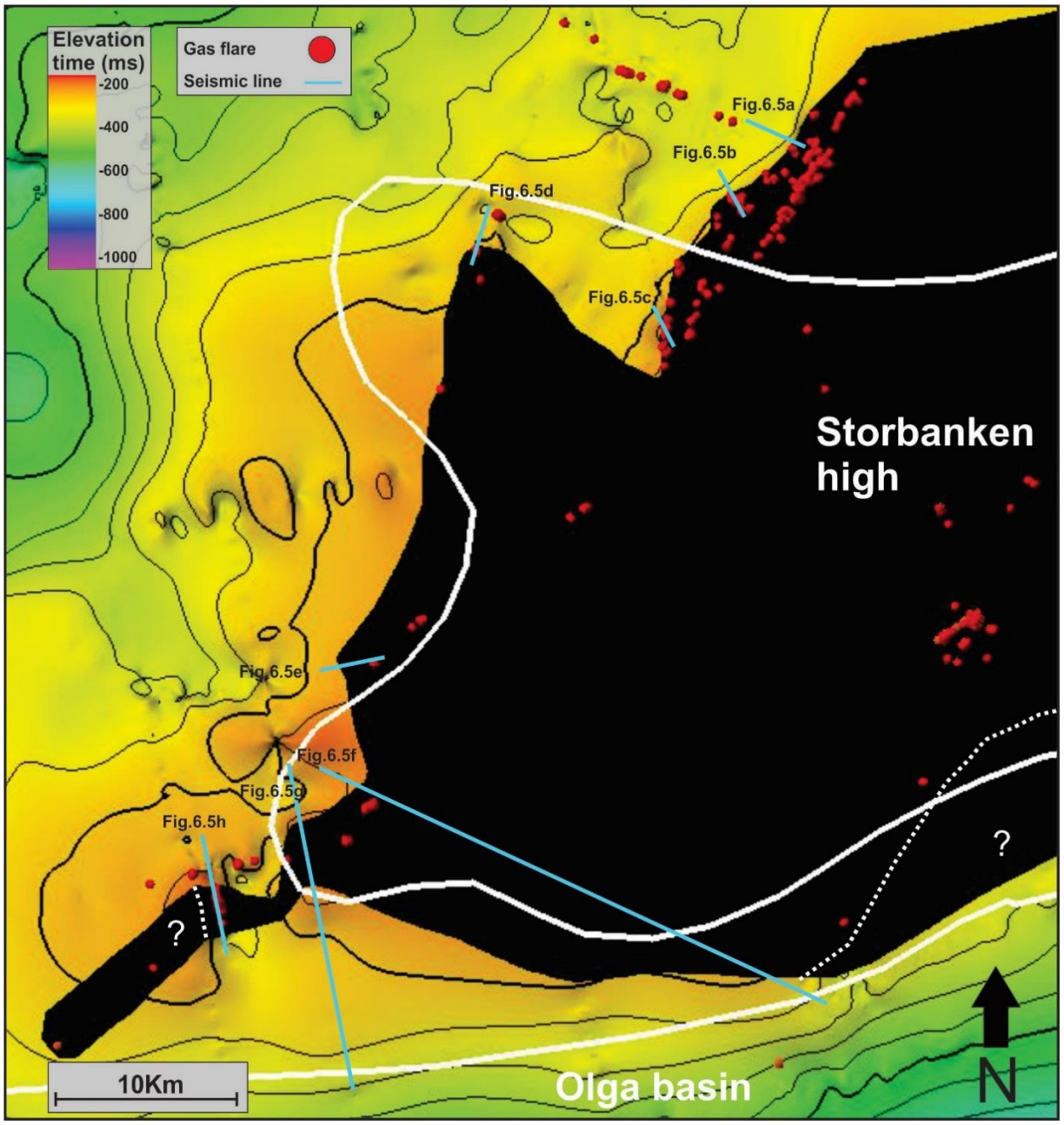

Fig.6.4: Surface map of the interpreted base Agardhfjellet Formation displayed in elevation time (ms) illustrating active gas seepage along the outcropping Agardhfjellet Formation. See Fig.4.6 for flare investigated area. Areas within the dotted white lines indicate areas where the Base Agardhfjellet Formation is believed to be eroded based on the gas flare pattern but no seismic lines to confirm it.

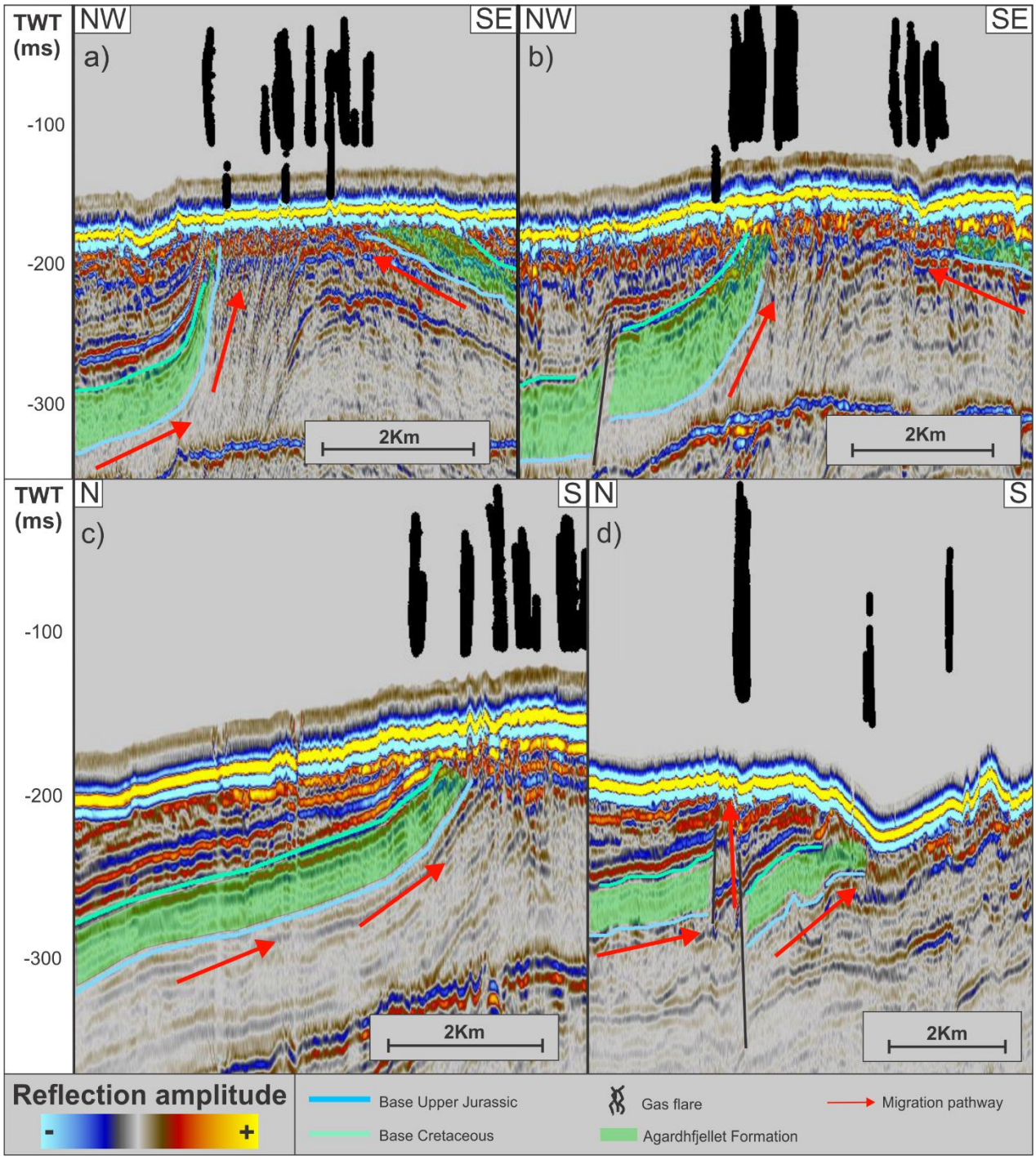

Fig.6.5a-d): Lateral migration along the base of the Agardhfjellet Formation. Position of seismic lines is indicated in Fig.6.4. The black gas flares represent columnar zones of gas bubbles.

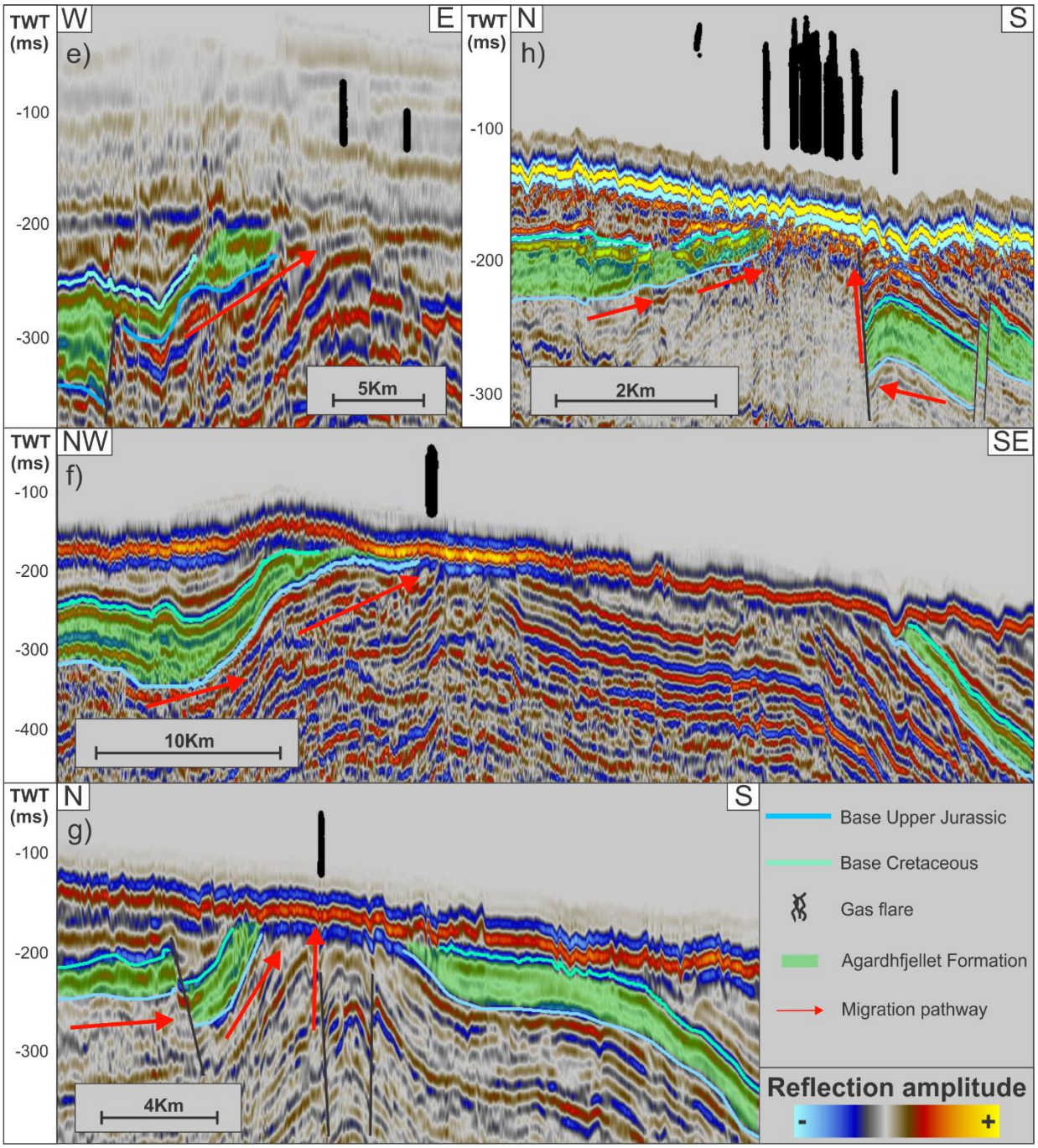

Fig.6.5e-h: Lateral migration along the base of the Agardhfjellet Formation. Position of seismic lines is indicated in Fig.6.4. The black gas flares represent columnar zones of gas bubbles.

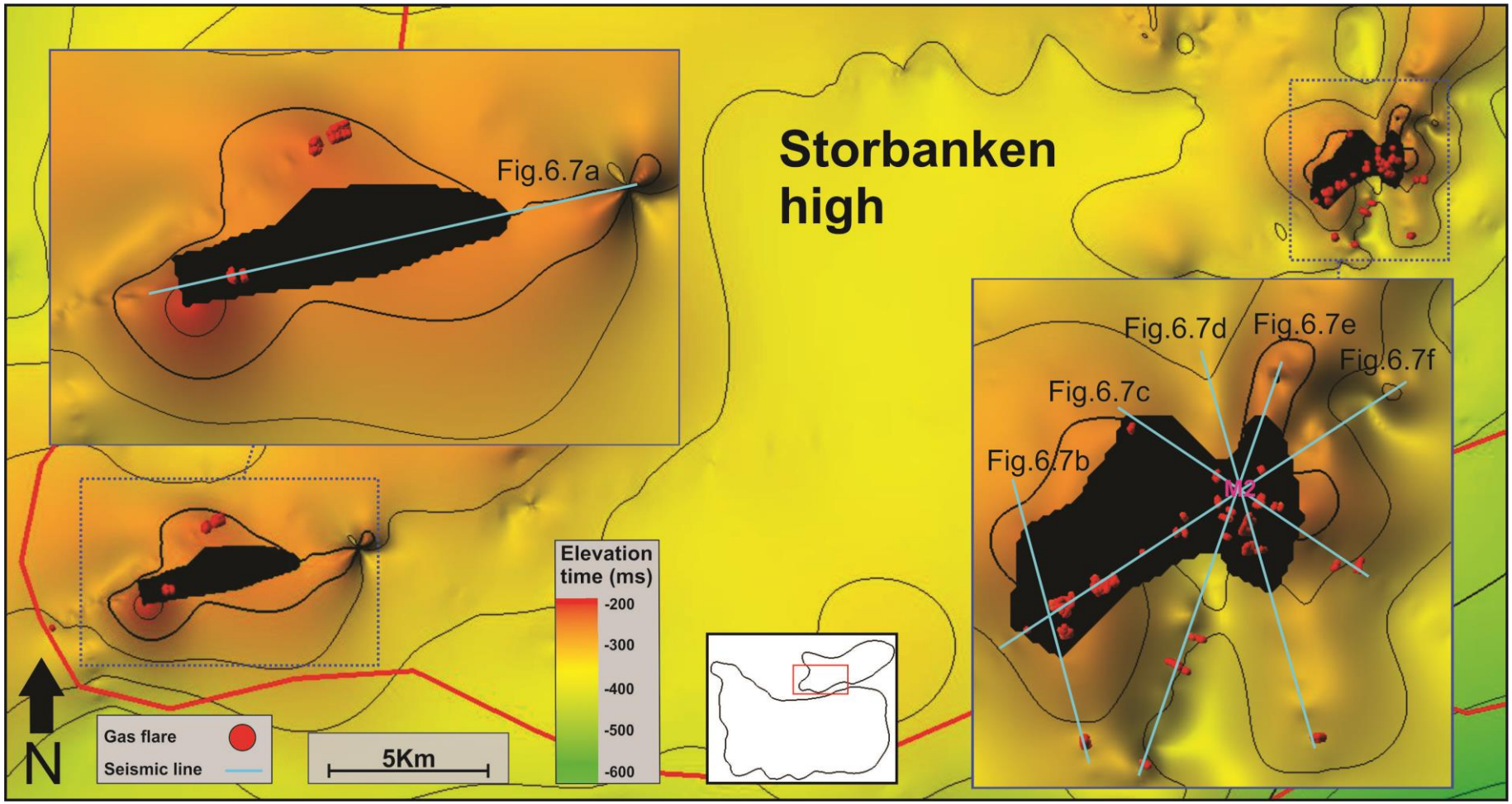

Fig.6.6: Surface map of the interpreted base Flatsalen Formation displayed in elevation time (ms) illustrating active gas seepage along the outcropping Flatsalen Formation. See Fig.4.6 for flare investigated area.

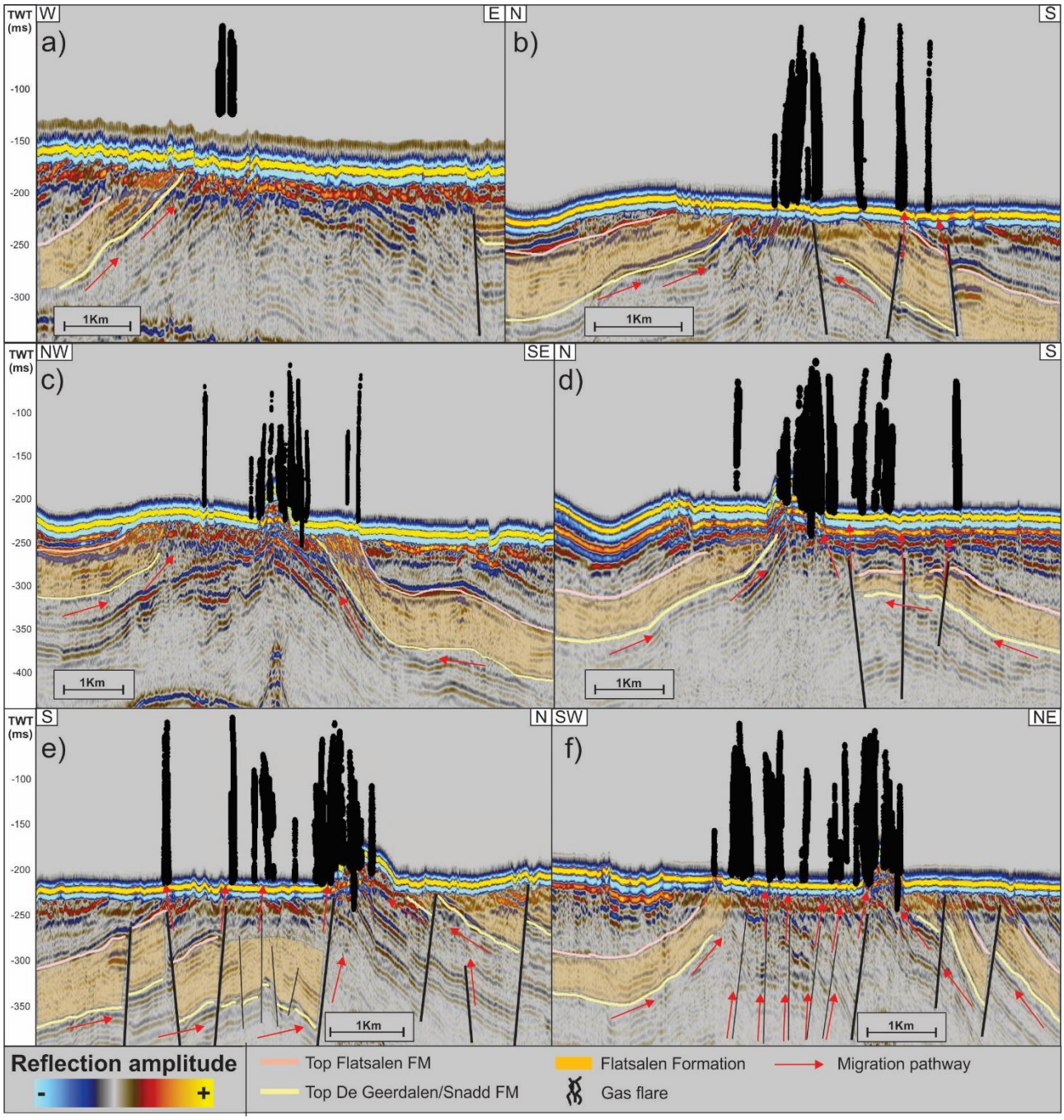

Fig.6.7: Lateral gas migration along the Flatsalen Formation and vertical migration along faults (FZ). See Fig.6.6 for position of seismic lines. The black gas flares represent columnar zones of gas bubbles.

6.5 Gas hydrate potential

Gas hydrates and stability zones have been studied and modeled by several authors in the Southwestern Barents Sea (Chand et al., 2012; Klitzke et al., 2016; Vadakkepuliyambatta et al., 2017b) and in the outer parts of Storfjordrenna trough, south for Svalbard (Waage et al., 2019). However little work has been done in the eastern parts of the northern Barents Sea.

The potential BSR found at Storbanken high was located at an area with a water depth of -0.214 S (TWT) which corresponds to a water depth of 160 m assuming a water velocity of 1500 m/s (Fig.5.30). The BSR is located within the De Geerdalen/Snadd Formation at a depth of -0.3 S (TWT), 0.086 S (TWT) below the seafloor which corresponds to 142 m below the seafloor assuming the interval velocity of the De Geerdalen/Snadd Formation of 3300 m/s (Table 4.5) (Fig.5.30). Due to the lack of well data examining the geothermal gradient in the study area the geothermal gradient was assumed to be 35ºC/km which is generally accepted throughout the Barents Sea (Fig.4.8). The bottom water temperature and pore water salinity were extracted from the CTD data acquired during the CAGE-18-1 cruise and found to be -1.7 ºC and 34.65 psu (Appendix C).

The potential BSR examined is found to potentially represent gas hydrates of structure II as pure methane hydrates (Structure I) is outside the stability zone at this shallow water depth (Fig.5.30 and 6.8a) (Table 6.2).

By constructing a conceptual gas composition it was possible to examine a potential gas mixture of heavier gases such as ethane and propane along with the methane to represent the potential BSR. A conceptual gas mixture of 97.54 % methane, 2,26% ethane and 0,2% propane would have a gas hydrate stability zone corresponding to the depth of the identified BSR (Fig.6.8b). It is worth mentioning that a slight increase in the composition of heavier gases such as ethane and propane would cause significant growth of the gas hydrate stability zone. Given the physical properties of the water and a geothermal gradient of 35 ºC/km the water depth in the study area needs to be deeper than 240.5 m in order for pure methane hydrates to be stable (Table 6.2). This might suggest the presence of pure methane hydrates in the deeper areas of the Olga basin given the same physical properties of the water and geothermal gradient as used for calculation at Storbanken high.

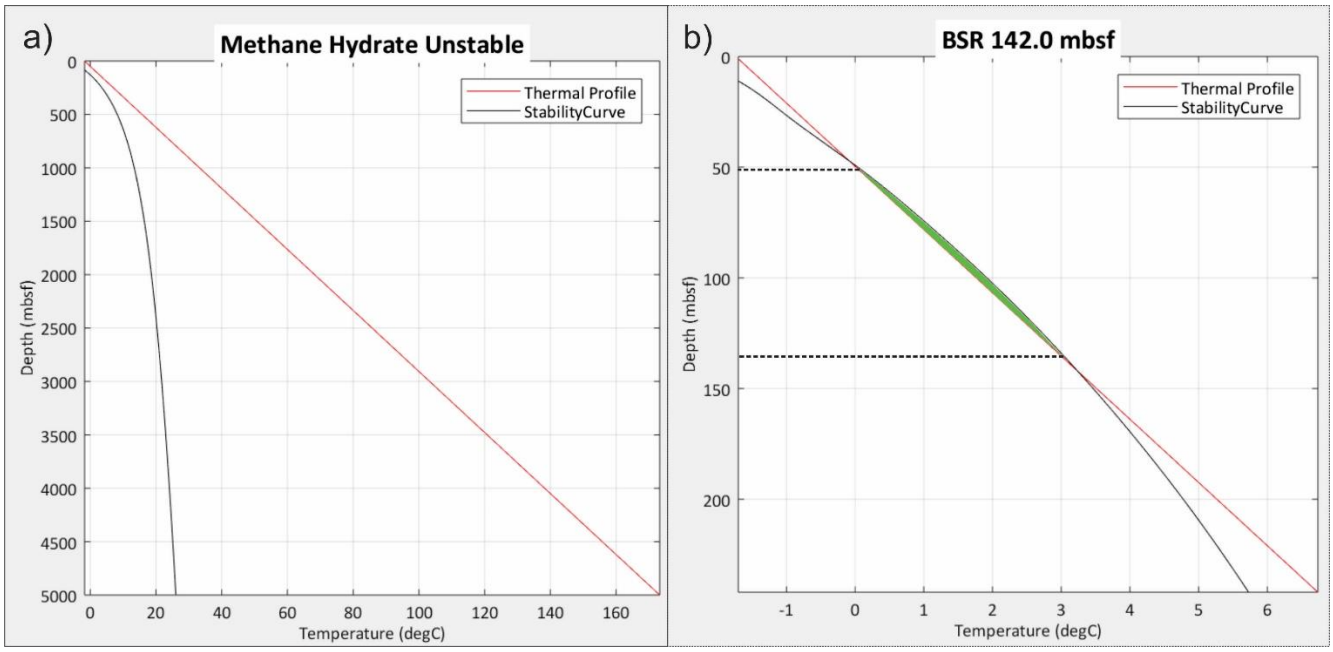

Fig.6.8: Modeled gas hydrate stability zone based on the CSMHYD program by Sloan & Koh (2008). a) GHSZ modeled for pure methane gas composition based on the BSR from (Fig.5.30). b) Conceptual gas composition of 97.54 % methane, 2.26 % ethane and 0.2 % propane to correlate to the depth of identified BSR (Fig.5.30). The green area indicates the depth of the gas hydrate stability zone while the dotted black lines illustrate the upper and lower boundary of the stability zone.

Table 6.2: Illustration of the modeled gas hydrate stability zones given different water depths and gas compositions. Bottom water temperature and pore water salinity were extracted from Appendix C. mbsf = meters below the seafloor.

	Water depth	Thermal gradient	Bottom water temperature	Pore water salinity	Methane	Ethane	Propane	Stability zone
BSR Methane hydrate Strcuture I	160 m	35 ^{o}C/km	-1.7 ^{o}C	34.65 psu	100%	0	0	Unstable
BSR (Conceptual gas composition)	160 m	35 ^{o}C/km	-1.7 ^{o}C	34.65 psu	97.54%	2.26%	0.2%	142 mbsf
BSR Methane hydrate Structure I (Conceptual water depth)	240.5 m	35 ^{o}C/km	-1.7 ^{o}C	34.65 psu	100%	0	0	63 mbsf

The interpreted potential BSR might not be a typical high amplitude clear BSR reflection (Fig.5.30). However gas hydrates might still be present in the study area without the presence of a BSR as the high amplitude reflections is caused by the free gas underneath the hydrates opposed to the gas hydrates themselves (Holbrook et al., 2001; Chand et al., 2008).

It is not uncommon for gas hydrates to consist in mixtures with heavier order gases. Vadakkepuliyambatta et al, (2017a) have documented high local variations in the gas composition of sediments based on various exploration wells in the Southwestern Barents Sea. Bound gases in near-surface sediments at the Olga basin have also indicated mixed gas composition of methane, ethane and propane (Weniger et al., 2019). It is therefore not unlikely with the presence of gas hydrates with a mixture of heavier gases (structure II) at Storbanken high. The interpreted potential BSR with its conceptual gas composition might suggest the presence of such gas hydrates (Fig.5.30). Gas seepage related to the ongoing dissociation of gas hydrates Structure II at the Storbanken high should therefore not be disregarded.

6.6 Seafloor expressions of gas seepage

The Barents Sea has through the Quaternary experienced multiple glaciations which have caused periods of ice sheet loading, erosion and subsequent uplift. These glaciations also caused growth of the theoretical GHSZ to hundreds of meters below the ice sheet throughout large areas of the Arctic due to high pressure and low temperatures imposed by the km's thick ice sheet (Ostanin et al., 2013; Crémière et al., 2016; Andreassen et al., 2017; Serov et al., 2017). This might suggest the presence of sub-glacial gas hydrates formed under the glacial conditions. When the ice sheet started to retreat after the LGM it imposed pressure decrease, sea level rise, a warmer seabed and isostatic rebound which caused the GHSZ to shrink, gas hydrates to dissociate and successively release of free gas into the water column (Ostanin et al., 2013; Wallmann et al., 2018). Several geomorphological features have been proposed to be generated by sub-glacial gas hydrate dissociation (Serov et al., 2017). Gas hydrate dissociating after the LGM can be linked to the formation of pockmarks (e.g. Portnov et al., 2016), authigenic carbonate mounds (e.g. Cremiere et al., 2011) and craters with associated mounds (e.g. Andreassen et al., 2017). All which are abundant seafloor features in the study area at Storbanken high. However, the geomorphological features identified at Storbanken high is not bound to gas hydrate dissociation as other generating mechanisms might also have contributed to the formation of these features.

6.6.1 Origin of pockmarks

A variety of mechanisms exists which can have triggered the formation of pockmarks in the study area at Storbanken high, however the most likely cause is that the pockmarks are focused fluid flow related features (Chand et al., 2009; Judd & Hovland, 2009). The type of fluid and triggering mechanism of the pockmarks could however be many. Harrington (1985) suggests the formation of pockmarks to be a result of pore water escape as he did not identify any pockmarks at areas influenced by mass movement. As there has been identified abundant gas seepage activity in the study area the most possible explanation is perhaps expulsion of gas which has been generated in the subsurface thermogenic or at shallower depths as biogenic (Hovland, 1982; Judd et al., 2002; Chand et al., 2009). The discharge of gas through the seafloor can either occur as constant flowing or as sudden rapid episodes, where the sediments get transported by the fluids into the water column and get redistributed at the seafloor (Hovland et al., 2005). Solheim & Elverhøi (1985) has suggested biogenic decay of

organic matter underneath glacial sediments to generate an insufficient amount of gas to produce the pockmarks. Gas generating source rocks has been documented in the study area (chapter 6.2) favoring the expulsion of thermogenic gas as the most likely developing mechanism for these pockmarks.

The distribution of pockmarks is quite distinctive with the pockmarks distributed only in the southern parts of the Storbanken high, near the intersection of Storbanken high and the Olga basin (Fig.5.18). The pockmarks were also found to be distributed in the proximity to a long elongated depression (Fig.5.17-5.18). It was difficult to determine any seismic evidence for this unique distribution of pockmarks as only a few lines were acquired above the pockmark distributed areas, however, the seismic indicated tilted layers towards the Olga basin and outcropping formations (Fig.5.2). Studies done by Chand et al, (2009, 2012) at the Southwestern Barents Sea found that pockmarks were mainly restricted to soft fine-grained sediments which acted as a better recording medium indifference to coarser consolidated sediments. Glacigenic sediments are believed to be scarce in the study area as there has not been identified an Upper regional Unconformity in the seismic representing the transition from soft glacigenic deposits to more consolidated sediments. In addition has there been reported to be little quaternary sediments in the northern Barents Sea whereas most of the glacigenic sediments were deposited to the west near the continental slope (Svendsen et al., 2004a).

The position of the long elongated west-east oriented depression relative to the outcropping Agardhfjellet Formation at the intersection of the Olga basin and Storbanken might suggest a linkage (Fig.5.7 and 5.17-5.18). Two depressions related to the outcropping Agardhfjellet Formation was identified at the Storbanken high, which might suggest the Agardhfjellet Formation due to its soft high-organic rich shale to be less resistance to erosion in comparison to its adjacent groups and formations (Fig.6.5d and 6.5f). This makes the Agardhfjellet Formation prone to glacial erosion which might explain the orientation and location of this elongated depression. The long depression might therefore be a potential glacial trough, formed exclusively at the seafloor where the Agardhfjellet outcrops explaining the uneven geometry. Glacial troughs are formed by the carving of grounded ice during glaciations, these features are extensive across the Barents shelf (Hogan et al., 2016; Newton & Huuse, 2017). As fine-grained and soft glacigenic sediments are believed to accumulate within the trough the distinct distribution of pockmarks might be related to the higher distribution of glacigenic sediments in proximity of this glacial trough than the adjacent areas (Fig.5.18). This might

imply the pockmark distribution to be lithologically controlled by the glacial erosion of the Agardhfjellet Formation. There exists however some uncertainty in this theory as sparse seismic coverage in the area makes it difficult to examine this relationship.

The lack of identified gas flares and seismic evidence for fluid flow features in relation to the pockmarks suggest that these are not actively leaking at the present day. Potential explanations for the pockmark generation in the study area could therefore be from direct gas release associated with the removal of the sealing ice sheet or dissociation of sub-glacial gas hydrates after the LGM (Fig.6.9). The free gas from dissociated gas hydrates is believed to have migrated through fractures presumably imposed by glacial unloading and isostatic rebound and by deglaciated-induced increase of pore pressure related to the dissociation of sug-glacial gas hydrates (Crémière et al., 2016) (Fig.6.9). Pockmarks related to dissociation of sub-glacial gas hydrates has been discussed by other authors at the western shelf of Svalbard (e.g. Portnov et al., 2016) and in the Southwestern Barents Sea (Chand et al., 2012; Ostanin et al., 2013). Studies by Crémière et al, (2016) has indicated the main methane expulsion episodes to have culminated between 17 and 7 Ka BP in the Southwestern Barents Sea based on Uranium-thorium dating of authigenic carbonate crust. This timing is favorable for the interpretation of sub-glacial gas hydrate dissociation and timing of pockmark formation at Storbanken high (Fig.6.9).

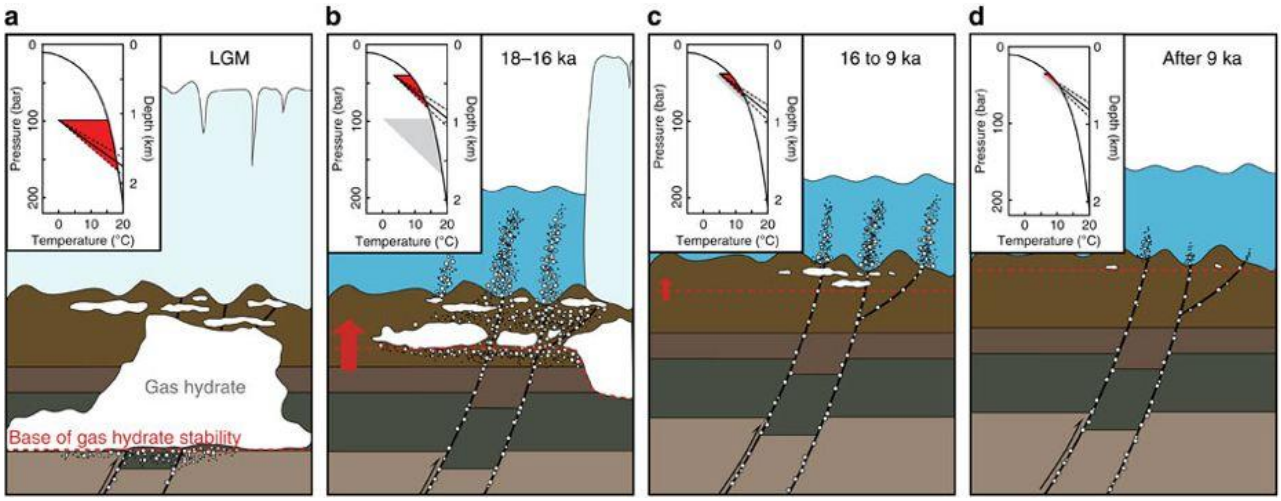

Fig.6.9: conceptual model of pockmark generation from sub-glacial gas hydrate dissociation after the LGM. From (Crémière et al., 2016).

6.6.2 Origin of craters and mounds

There have been several authors discussing the structures at the seafloor referred to as craters and craters with associated mounds (Fig.5.22-5.24). Explanations such as meteorites, man-made activity, biological activity, water discharge and impacts from ice-boulders were suggested by King & Maclean, (1970) in the early discovery of these structures. In more recent days the processes governing the craters are more regarded to be caused by rapid gas expulsions related to gas hydrate dissociation (e.g. Andreassen et al., 2017) and glaciotectonic processes (e.g. Sættem, 1990).

Craters (C22, C23, C25, C26) and craters with associated mounds (CM10, CM11, CM12, CM14, CM15) are exposed by two seismic lines which indicates associated normal faults (FZ) (Fig.5.23-5.24). Common for these craters and mounds is that there are identified no basal reflection at the base of the mounds following the seafloor, suggesting that these features were not deposited upon the seafloor but rather generated from the subsurface (Fig.5.23-5.24). Chaotic reflections and identified brightening and push-downs along the craters and craters with associated mound along with two gas flares located above the craters C21 and C23 might suggest the presence of gas in the sediments (Fig.5.23-5.24). The associated mounds were also identified to have ploughmarks implying that these had to be generated either before or rapidly after the retreat of the ice sheet after LGM.

Similar crater and mound structures have been studied at the northern Bjørnøyrenna (Andreassen et al., 2017). These craters and mounds were described to also have underlying faults and chaotic seismic reflections, and the base of the associated mounds was identified to have no clear basal paleo-seafloor reflection. As the ice shelf retreated after the LGM sediment pore pressure was reduced which led to deeper gas hydrates to decompose, migrate upward and recrystallize at shallower depths (Fig.6.10b) (Andreassen et al., 2017). The increasing volume of gas concentrated within an area along with a gradual thinning of the gas hydrate stability zone led to local volume expansion related to regrowth of gas hydrates and underlying buildup of pressurized gas forming mounds also referred to as gas-hydrate pingos (Fig.6.10b) (Andreassen et al., 2017). Eventually when the pressure was high enough the gas-hydrate pingo exploded and formed a crater with additionally smaller adjacent gas-hydrate pingos (Fig.6.10c-d) (Andreassen et al., 2017).

This process is believed to be widespread across previously glaciated margins which constitute hydrocarbon generating capabilities (Andreassen et al., 2017). These craters and mounds in the study area of Storbanken high might therefore have had the same generating mechanism where the normal faults (FZ) could have acted as migration pathway for the dissociating gas hydrates (Fig.5.23-5.24 and 6.10).

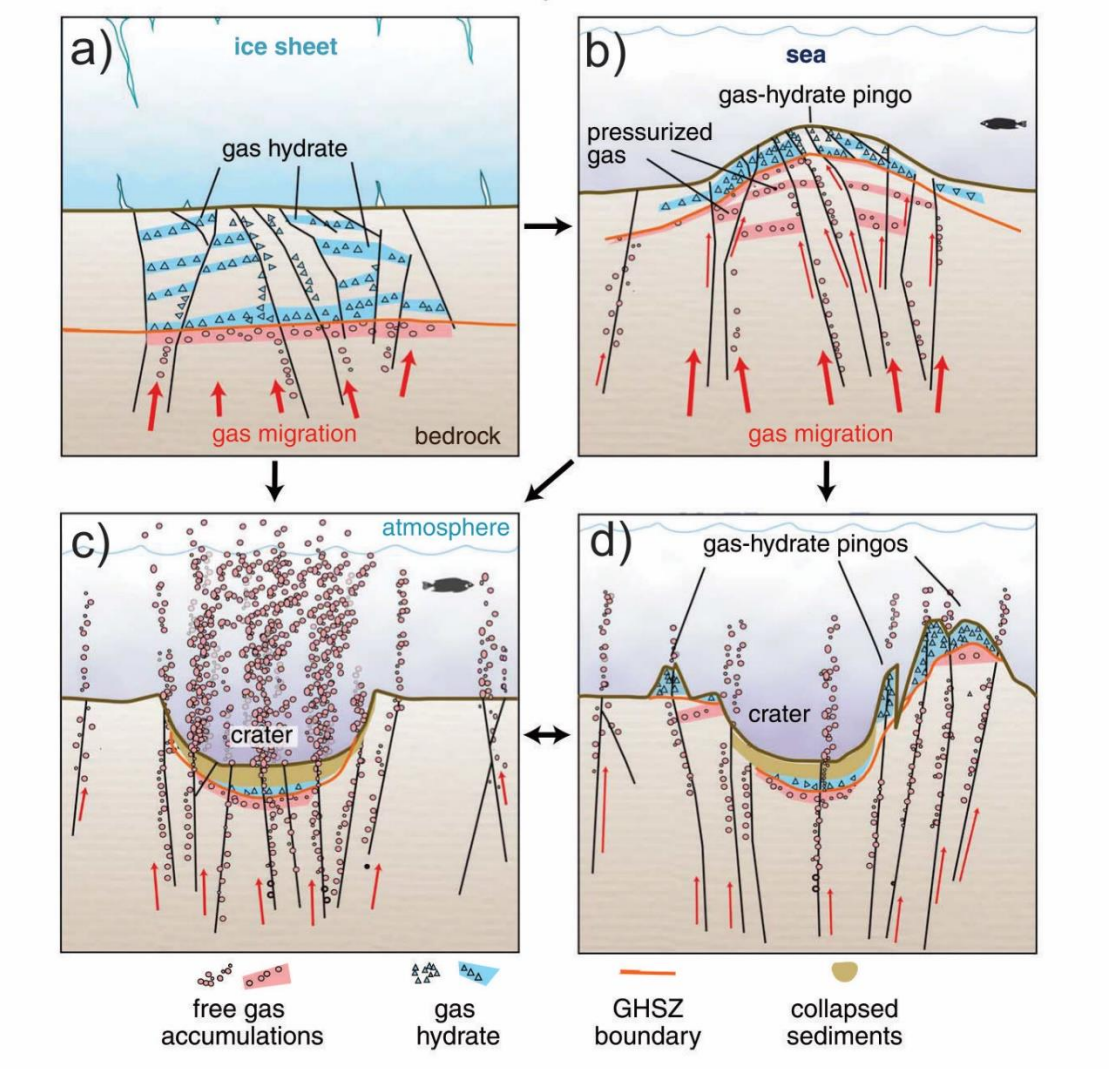

Fig.6.10a-d: Conceptual model for sub-glacial gas hydrate dissociation related to the formation of craters and mounds. Modified from (Andreassen et al., 2017).

The craters with associated mounds (CM5, CM6, CM8 and CM17) all share a mound oriented south relative to the crater (Fig.5.17 and 5.18). CM6 is exposed by a seismic line and show evidence of a continuous basal reflection following the base of the mound (Fig.5.22). This might suggest the formation mechanism of this mound to be deposited upon the seafloor rather than the result of uplifted subsurface sediments. In addition, the craters had similar length and width measurements as the mound, and the depth of the depression corresponded to the height of the associated mound (Chart 5.4). This might suggest this to be an erosional feature redepositing the sediments from the crater as an adjacent mound.

A potential generating mechanism for these craters and mounds (CM5, CM6, CM8 and CM17) could be hill-hole pairs. Hill-hole pairs represents an ice-scooped depression and an ice-shoved hill, the mound is located in short distance from the depression in the down-glacier direction, the depression represents the material deposited as the hill, this material is usually equal to the missing sediments from the depression (Aber., 1989; Dowdeswell et al., 2016; Winsborrow et al., 2016). The hill-hole pairs are a great indicator for paleo-direction for the previously ice sheet, as sediments freeze underneath the ice sheet during still-stand periods and get shoved downstream as the ice sheet readvances (Dowdeswell et al., 2016). The hill is therefore always located in the downstream direction relative to the depression. The location of the hills relative to the craters in the study area suggests a downstream direction to the south, this correlates to the orientation of the moving ice sheet during the LGM, as it advanced southwards and retreated northwards (Svendsen et al., 2004b).

These hill-hole pairs might also be linked to sub-glacial gas hydrates, as gas-hydrate-hosting sediments tend to enhance the basal friction between the sediments and the ice sheet as the gas hydrate-bearing sediments easier freezes to the ice sheet and thereby increasing the resistance for the overlying ice (Winsborrow et al., 2016).

It is therefore suggested that the craters and craters with associated mounds might be related to both fluid flow and glaciotectonic generating processes in the study area as none of these mechanisms can be ruled out.

6.6.3 Origin of single Mounds

Two single mounds were identified at Storbanken high (M1 and M2) (Fig.5.17-5.18 and 5.21). There was identified numerous gas flares implying high gas seepage activity in association to the mound M2. The stratigraphic layers were identified to be tilted in such a manner that the M2 seemed to be situated on top of a presumably eroded dome structure concentrating the lateral migration along the Flatsalen Formation to this mound (Fig.6.7). Vertical migration along the faults (FZ) and direct migration through the permeable reservoir of De Geerdalen/Snadd Formation from the source rock of Botneheia Formation are also processes believed to have governed the gas migration at the mound M2 (Fig.6.7 and 6.12). The mound could potentially be, as earlier defined a pressurized gas-hydrate pingo (Fig.6.10b) (Andreassen et al., 2017). However, the basal curved reflection of this mound following the seafloor might suggest a different generating mechanism (Fig.5.21). Carbonate accretions have been proven to be common at gas seepage sites as complex chemical processes oxides methane and generate authigenic carbonate crust (Naeth et al., 2005; Naehr et al., 2007; Blumenberg et al., 2015). The focused flow of gas in relation to this mound might therefore cause carbonate accretions to form this mound. The curved basal paleo-seafloor reflection indicating a positive reflection amplitude might potentially represent the base of the carbonate mound indicating the transition to more consolidated bedrock. As there was identified ploughmark on top of this mound it is suggested that the mound had to be formed either before the LGM or rapidly after the retreat of the ice sheet. This mound might be more resistant to erosion than the adjacent seafloor due to cementing and diagenetic processes as a result of constant fluid flow and the oxidation of methane, suggesting it to be formed before the LGM (Kauffman el al., 1996). However, studies by Cremiere et al, (2011) indicated a relationship between carbonate mounds and dissociating gas hydrates, which could also imply this mound to be rapidly initiated after the LGM as a result of dissociated sub-glacial gas hydrates.

6.7 Conceptual model

The conceptual model integrates the main migration pathways believed to be governing the gas seepage activity in the study area (Fig.6.12). The model also indicates the direction of lateral migration based on the tilted stratigraphy and gas leakage observed above the outcropping cap rocks (Fig.6.4-6.7 and 6.11).

Vertical migration along the faults (FZ) is believed to transport gas from the reservoir of De Geerdalen/Snadd formation and potentially from the source rock of Botneheia Formation to the shallower reservoir of Realgrunnen Subgroup or directly into the water column (Fig.6.12). The lateral migration along the outcropping cap rock of Agardhfjellet Formation is restricted to the north as there is an absence of leaking faults in the Olga basin transporting the gas to the Realgrunnen Subgroup reservoir (Fig.6.2 and 6.12). Lateral migration along the Flatsalen Formation and migration along faults are believed to have concentrated gas to the location of the mound M2, which might be a mound of carbonate accretion (Fig.6.12). The gas chimney GC3 could be an important migration pathway for deep-seated gas originating from the source rock of Billefjorden Group (Fig.6.12). Based on the GHSZ modeling there were favorable conditions for generating gas hydrate Structure II at Storbanken high (Fig.5.30 and 6.8). The gas hydrates might therefore act as seals or be dissociating governing the seepage activity at the Storbanken high (Fig.6.12). Direct migration from the Botneheia Formation to the De Geerdalen/Snadd Formation is possible in the Olga basin and potentially the deeper parts of the Storbanken high where this formation is gas mature (Fig.6.12) (Table 6.1). The pockmarks are mainly restricted to the intersection of the Olga basin and the Storbanken high potentially controlled by the higher distribution of glacigenic sediments which might be related to the lithological controlled glacial erosion of the outcropping Agardhfjellet Formation (Fig.5.17-5.18 and 6.12).

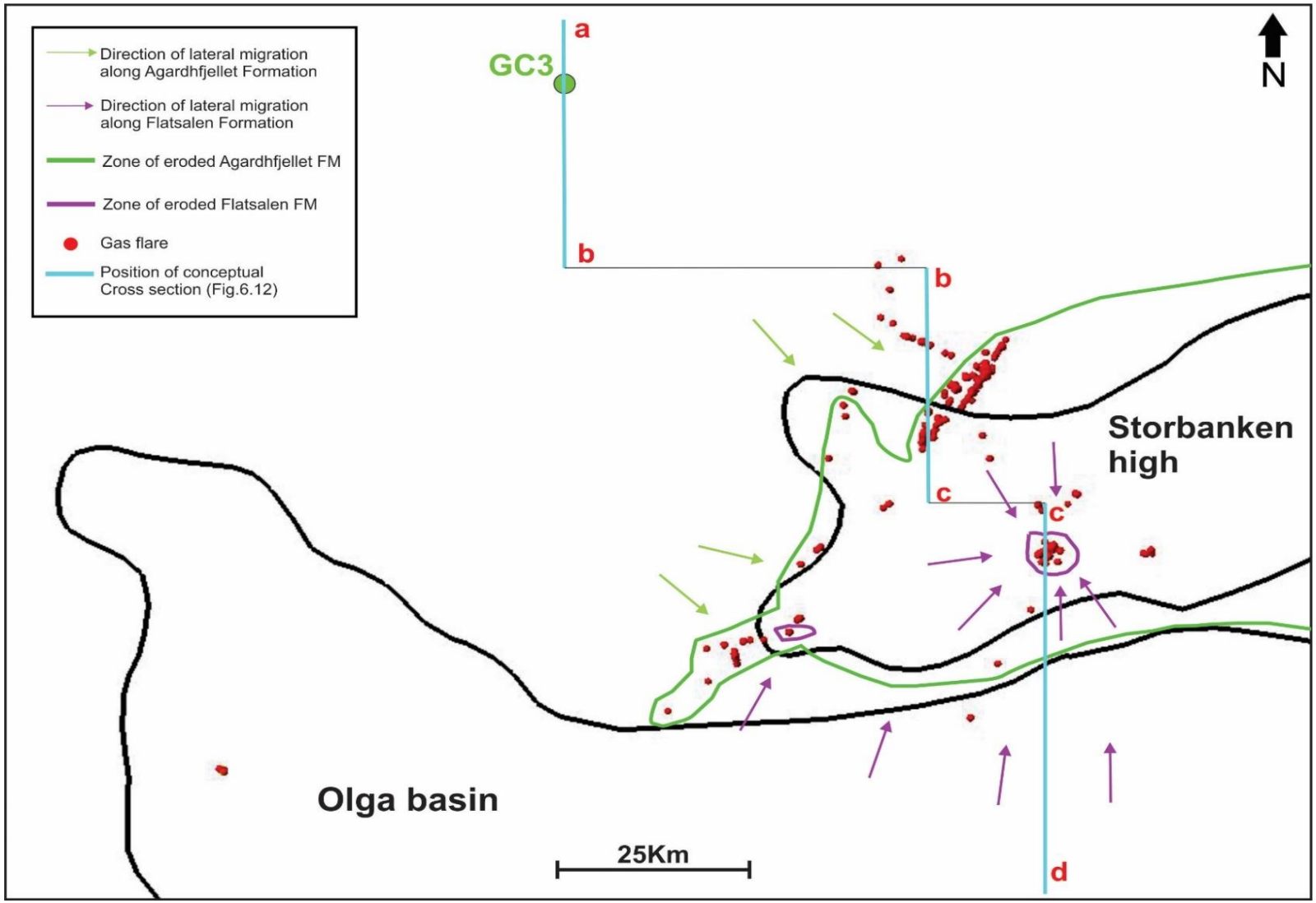

Fig.6.11: Overview of the outcropping cap rocks of the Flatsalen Formation and the Agardhfjellet Formation. Directional lateral migration along the cap rocks of the Flatsalen Formation and the Agardhfjellet Formation is illustrated with arrows.

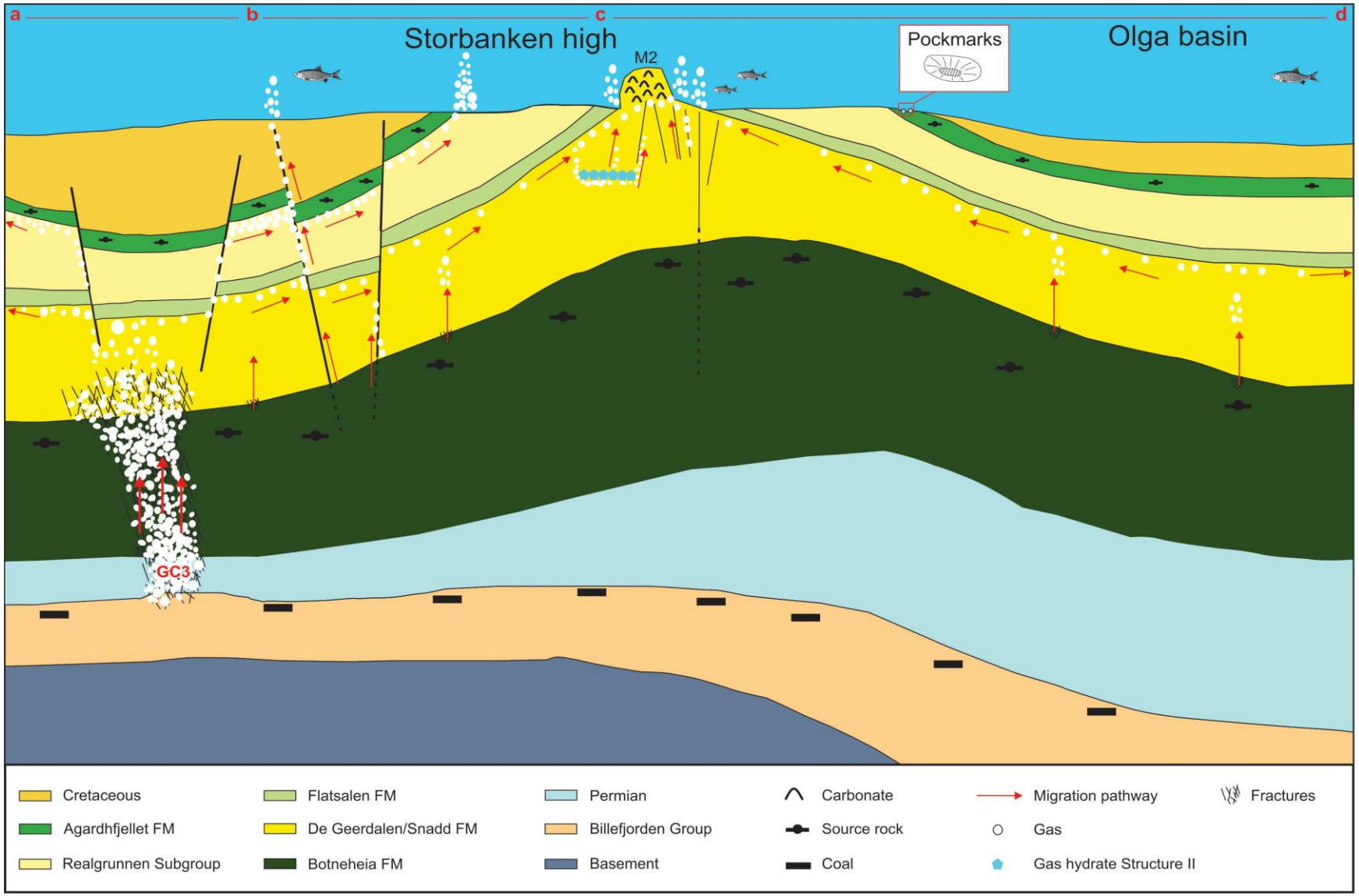

Fig.6.12: Conceptual model of the seepage activity in the study area. Model not to scale.

7 Conclusion

Gas seepage activity was studied at the Olga basin and Storbanken high by using 2D seismic data, bathymetric data and water acoustic data. The data has revealed several faults, outcropping stratigraphic units, seismic amplitude anomalies and seafloor expressions indicating evidence for gas seepage. The main findings during this study have suggested the following for the study area:

- Normal and reverse faults were identified in the study area. The majority of the NW-SE striking normal faults (FZ) are believed to be of Post-Early Cretaceous age related to the uplift of Storbanken high. The reverse faults (F5) of Early Cretaceous age are believed to be related to NW-SE compression and the inversion of Paleozoic normal faults at the Kong Karls Land platform. These are believed to be important tectonic events governing the vertical and lateral gas migration in the study area.
- A simplified 1D maturity modeling has indicated an immature Agardhfjellet Formation and potential gas generating source rocks of Botneheia Formation and Billefjorden Group.
- Seepage activity was identified along the normal faults (FZ, F1, F2, F4 and F6). The (FZ) is believed to be important vertical migration pathways potentially transporting gas from the Botneheia Formation source rock and distributing gas from the reservoir of the De Geerdalen/Snadd Formation to the Realgrunnen Subgroup.
- Deep-seated gas chimneys identified in the study area could be important conduits for vertical gas migration and might suggest a deep-seated gas generating source rock of the Billefjorden Group.
- Gas seepage identified above the outcropping cap rocks of Agardhfjellet Formation and Flatsalen Formation suggests lateral migration along these formations.
- Gas might migrate directly from the source rock of Botneheia Formation and into the reservoir of De Geerdalen/Snadd Formation in the Olga basin and potentially in the deeper parts of the Storbanken high where the Botneheia Formation is gas mature.

- Gas hydrate modeling has indicated the potential for gas hydrates S_{II} at the Storbanken high and favorable conditions for pure methane hydrates at the deeper parts of the Olga basin, leakage related to ongoing gas hydrate dissociation should therefore not be disregarded.
- Pockmarks are believed to been preserved in glacigenic sediments which accumulated within a glacial trough carved by the lithologically controlled erosion of the Agardhfjellet Formation.
- Seafloor expressions of inactive seeping pockmarks and craters with associated mounds might suggest earlier massive gas expulsion related to the retreating ice sheet acting as a seal or the dissociation of sub-glacial gas hydrates after the LGM. Faults underneath the craters and mounds might suggest earlier migration pathway for the free gas.
- The craters with associated mounds cannot be excluded to have a glaciotectonic generating mechanism as these features shares characteristics of hill-hole pairs.

Further research

For further studies at Storbanken high and the Olga basin it is recommended to conduct 3D seismic data. This would provide a broader understanding for the structural geology and better confidence in the interpretation of fluid flow features such as gas chimneys and the outcropping cap rocks of Agardhfjellet Formation and Flatsalen Formation in the study area. As there have not been any available wells in the study area for this thesis it would also be of great interest to correlate well data with the stratigraphy. Conducting well data along with core samples would also allow for a more precise calculation for maturation and GHSZ modeling. For further studies with the seismic data utilized in this thesis the reader is referred to Appendix E.

8 Refrences

Abay, T. B., Karlsen, D. A., & Pedersen, J. H. (2014). Source Rocks at Svalbard : An Overview of Jurassic and Triassic Formations and Comparison with Offshore Barents Sea Time Equivalent Source Rock Formations. *AAPG International Conference & Exhibition*, *30372*(January). Retrieved from https://www.researchgate.net/publication/311818909_Source_Rocks_at_Svalbard_An_Overview_of_Jurassic_and_Triassic_Formations_and_Comparison_with_Offshore_Barents_Sea_Time_Equivalent_Source_Rock_Formations

Aber, J. ., Croot, D. ., & Fenton, M. . (1989). Hill-Hole Pair. in: Glaciotectonic Landforms and Structures. In *Glaciology and Quarternary Geology* (Vol. 5, pp. 13–14). Dordecht: Springer. https://doi.org/https://doi.org/10.1007/978-94-015-6841-8_2

Andreassen, K., Hubbard, A., Winsborrow, M., Patton, H., Vadakkepuliyambatta, S., Plaza-Faverola, A., … Bünz, S. (2017). Massive blow-out craters formed by hydrate-controlled methane expulsion from the Arctic seafloor. *Science*, *356*(6341), 948–953. https://doi.org/10.1126/science.aal4500

Andreassen, K., Laberg, J. S., & Vorren, T. O. (2008). Seafloor geomorphology of the SW Barents Sea and its glaci-dynamic implications. *Geomorphology*, *97*, 157–177. https://doi.org/10.1016/j.geomorph.2007.02.050

Andreassen, K., Nilssen, E. G., & Ødegaard, C. M. (2007). Analysis of shallow gas and fluid migration within the Plio-Pleistocene sedimentary succession of the SW Barents Sea continental margin using 3D seismic data. *Geo-Marine Letters*, *27*(2–4), 155–171. https://doi.org/10.1007/s00367-007-0071-5

Andreassen, K., Nilssen, L. C., Rafaelsen, B., & Kuilman, L. (2004). Three-dimensional seismic data from the Barents Sea margin reveal evidence of past ice streams and their dynamics. *Geology*, *32*(8), 729–732. https://doi.org/10.1130/G20497.1

Anell, I., Braathen, A., & Olaussen, S. (2014). Regional constraints of the Sørkapp Basin: A Carboniferous relic or a Cretaceous depression? *Marine and Petroleum Geology*, *54*, 123–138. https://doi.org/10.1016/j.marpetgeo.2014.02.023

Anka, Z., di Primio, R., Loegering, J., Marchal, D., Vallejo, E., & Rodgriguez, J. . (2014). Distribution and origin of natural gas leakage in the Colorado Basin, offshore Argentina Margin, South America: seismic interpretation and 3D basin modelling. *Geologica Acta*, *12*, 269–285. Retrieved from https://www.researchgate.net/publication/271824161_Distribution_and_origin_of_natural_gas_leakage_in_the_Colorado_Basin_offshore_Argentina_Margin_South_America_seismic_interpretation_and_3D_basin_modelling

Antonsen, P., Elverhoi, A., Dypvik, H., & Solheim, A. (1991). Shallow bedrock geology of the Olga Basin area, northwestern Barents Sea. *The American Association of Petroleum Geologists*, *75*(7), pp.1178-1194. Retrieved from http://archives.datapages.com/data/bulletns/1990-91/images/pg/00750007/0000/11780.pdf

Arntsen, B., Wensaas, L., Løseth, H., & Hermanrud, C. (2007). Seismic modeling of gas chimneys. *Geophysics*, *72*(5), SM251-SM259. https://doi.org/10.1190/1.2749570

Badley, M. (1985). *Practical Seismic Interpretation*. *Badley, Ashton, and Associates Ltd.* Springer. https://doi.org/10.1029/EO067i047p01342-06

Barnard, A., Sager, W. W., Snow, J. E., & Max, M. D. (2015). Subsea gas emissions from the Barbados Accretionary Complex. *Marine and Petroleum Geology*, *64*, 31–42. https://doi.org/10.1016/j.marpetgeo.2015.02.008

Barnes, P. W., & Lien, R. (1988). Icebergs rework shelf sediments to 500 m off Antarctica. *Geology*, *16*(December), 1130–1133. Retrieved from https://watermark.silverchair.com/i0091-7613-16-12-1130.pdf?token=AQECAHi208BE49Ooan9kkhW_Ercy7Dm3ZL_9Cf3qfKAc485ysgAAAmMwggJfBgkqhkiG9w0BBwagggJQMIICTAIBADCCAkUGCSqGSIb3DQEHATAeBglghkgBZQMEAS4wEQQMEtH0KtsaEswaIIDLAgEQgIICFhvCu6vYz-igvXx-jLzHJqmM53-30x9K_

Berndt, C. (2005). Focused fluid flow in passive continental margins. *Philosophical Transactions of the Royal Society A: Mathematical, Physical and Engineering Sciences*. https://doi.org/10.1098/rsta.2005.1666

Berndt, C., Bünz, S., & Mienert, J. (2003). Polygonal fault systems on the mid-Norwegian margin: a long-term source for fluid flow. *Geological Society, London, Special Publications*. https://doi.org/10.1144/GSL.SP.2003.216.01.18

Bjørlykke, K. (2015). *Petroleum geoscience: From sedimentary environments to rock physics, second edition*. *Petroleum Geoscience: From Sedimentary Environments to Rock Physics, Second Edition*. Springer Berlin Heidelberg. https://doi.org/10.1007/978-3-642-34132-8

Bjorøy, M., Hall, P. B., Ferriday, I. L., & Mørk, A. (2010). Triassic source rocks of the Barents Sea and Svalbard. *Search and Discovery*, *10219*(10219), 7pp. Retrieved from http://www.searchanddiscovery.com/pdfz/documents/2009/10219bjoroy/ndx_bjoroy.pdf.html

Blumenberg, M., Walliser, E. O., Taviani, M., Seifert, R., & Reitner, J. (2015). Authigenic carbonate formation and its impact on the biomarker inventory at hydrocarbon seeps - A case study from the Holocene Black Sea and the Plio-Pleistocene Northern Apennines (Italy). *Marine and Petroleum Geology*, *66*, 532–541. https://doi.org/10.1016/j.marpetgeo.2015.05.013

Brown, A. R. (1999). Interpretation of Three-Dimensional Seismic Data. *AAPG Memoir Series*, *42*(5). https://doi.org/10.3109/10903127.2012.717167

Bugge, T., Elvebakk, G., Fanavoll, S., Mangerud, G., Smelror, M., Weiss, H. M., … Erik, S. (2002). Shallow stratigraphic drilling applied in hydrocarbon exploration of the Nordkapp Basin , Barents Sea, *19*. https://doi.org/https://doi.org/10.1016/S0264-8172(01)00051-4

Cartwright, J., Huuse, M., & Aplin, A. (2007). Seal bypass systems. *AAPG Bulletin*, *91*(8), 1141–1166. https://doi.org/10.1306/04090705181

Cathles, L. M., Su, Z., & Chen, D. (2010). The physics of gas chimney and pockmark formation, with implications for assessment of seafloor hazards and gas sequestration. *Marine and Petroleum Geology*, *27*(1), 82–91. https://doi.org/10.1016/j.marpetgeo.2009.09.010

Chand, S., Mienert, J., Andreassen, K., Knies, J., Plassen, L., & Fotland, B. (2008). Gas hydrate stability zone modelling in areas of salt tectonics and pockmarks of the Barents Sea suggests an active hydrocarbon venting system. *Marine and Petroleum Geology*. https://doi.org/10.1016/j.marpetgeo.2007.10.006

Chand, S., Rise, L., Ottesen, D., Dolan, M. F. J., Bellec, V., & Bøe, R. (2009). Pockmark-like depressions near the Goliat hydrocarbon field, Barents Sea: Morphology and genesis. *Marine and Petroleum Geology*, *26*(7), 1035–1042. https://doi.org/10.1016/j.marpetgeo.2008.09.002

Chand, S., Thorsnes, T., Rise, L., Brunstad, H., Stoddart, D., Bøe, R., … Svolsbru, T. (2012). Multiple episodes of fluid flow in the SW Barents Sea (Loppa High) evidenced by gas flares, pockmarks and gas hydrate accumulation. *Earth and Planetary Science Letters*, *331–332*, 305–314. https://doi.org/10.1016/j.epsl.2012.03.021

Chong, Z. R., Yang, S. H. B., Linga, P., Babu, P., & Li, X.-S. (2015). Review of natural gas hydrates as an energy resource: Prospects and challenges. *Applied Energy*, *162*, 1633–1652. https://doi.org/10.1016/j.apenergy.2014.12.061

Crémière, A., Lepland, A., Chand, S., Sahy, D., Condon, D. J., Noble, S. R., … Brunstad, H. (2016). Timescales of methane seepage on the Norwegian margin following collapse of the Scandinavian Ice Sheet. *Nature Communications*, *7*(May), 1–10. https://doi.org/10.1038/ncomms11509

Cremiere, A., Pierre, C., Aloisi, G., Blanc-Valleron, M.-M., Henry, P., Zitter, T., & Cagatay, N. (2011). Authigenic carbonates related to thermogenic gas hydrates in the Sea of Marmara (Turkey). *International Conference on Gas Hydrates (ICGH 2011)*, *33*(0). Retrieved from https://www.pet.hw.ac.uk/icgh7/papers/icgh2011Final00277.pdf

Dallmann, W. ., Blomeier, D., Elvevold, S., Grundvåg, S. ., Mørk, A., Olaussen, S., … Hormes, A. (2015). Historical geology. *Geoscience Atlas of Svalbard*, *6 edition*, 89–131.

Deming, D. (2002). *Introduction to hydrology* (1st ed.). McGraw-Hill.

DiPietro, J. A. (2013). *Landscape Evolution in the United States: An introduction to the geography, geology and natural history*. *Landscape Evolution in the United States*. San Diego: Elsevier. https://doi.org/10.1016/C2011-0-05551-5

Dore, A. G. (1995). Barents Sea Geology, Petroleum Resources and Commercial Potential. *Arctic*, *48*(3), 207–221. Retrieved from https://www.jstor.org/stable/40511656?seq=1#metadata_info_tab_contents

Doré, A. G., & Jensen, L. N. (1996). The impact of late Cenozoic uplift and erosion on hydrocarbon exploration; offshore Norway and some other uplifted basins.; Impact of glaciations on basin evolution; data and models from the Norwegian margin and adjacent areas. *Global and Planetary Change*, *12*(1–4), 415–436. Retrieved from https://www.sciencedirect.com/science/article/pii/0921818195000313

Døssing, A., Jackson, H. R., Matzka, J., Einarsson, I., Rasmussen, T. M., Olesen, A. V., & Brozena, J. M. (2013). On the origin of the Amerasia Basin and the High Arctic Large Igneous Province-Results of new aeromagnetic data. *Earth and Planetary Science Letters*. https://doi.org/10.1016/j.epsl.2012.12.013

Dowdeswell, J. A., Canals, M., Jakobsson, M., Todd, B. ., Dowdeswell, E. ., & Hogan, K. (2016). Atlas of Submarine Glacial Landforms: Modern, Quaternary and Ancient. *Geological Society, London, Memoirs*, *46*. https://doi.org/10.1144/m46

England, W. A., Mackenzie, A. S., Mann, D. M., & Quigley, T. M. (1987). The movement and entrapment of petroleum fluids in the subsurface. *Journal of the Geological Society*. https://doi.org/10.1144/gsjgs.144.2.0327

Fanchi, J. R. (2006). *Principles of Applied Reservoir Simulation* (3rd ed.). Gulf Professional Publishing. https://doi.org/10.1016/B978-0-7506-7933-6.X5000-4

Fossen, H., & Gabrielsen, R. H. (2005). *Strukturgeologi*. Bergen: Fagbokforlaget.

Gac, S., Hansford, P. A., & Faleide, J. I. (2018). Basin modelling of the SW Barents Sea. *Marine and Petroleum Geology*, *95*(April), 167–187. https://doi.org/10.1016/j.marpetgeo.2018.04.022

Golonka, J., Bocharova, N. Y., Ford, D., Edrich, M. E., Bednarczyk, J., & Wildharber, J. (2003). Paleogeographic reconstructions and basins development of the Arctic. *Marine and Petroleum Geology*, *20*(3–4), 211–248. https://doi.org/10.1016/S0264-8172(03)00043-6

Grogan, P., Nyberg, K., Fotland, B., Myklebust, R., Dahlgren, S., & Riis, F. (2000). Cretaceous magmatism south and east of Svalbard: Evidence from seismic reflection and magnetic data. *Polarforschung*, *68*(1–3), 25–34.

Grogan, P., Østvedt-Ghazi, A. M., Larssen, G. B., Fotland, B., Nyberg, K., Dahlgren, S., & Eidvin, T. (1999). Structural elements and petroleum geology of the Norwegian sector of the northern Barents Sea. *Petroleum Geology of Northwest Europe: Proceedings of the 5th Conference*, (July 2016), 247–259. https://doi.org/10.1144/0050247

Gudlaugsson, S. T., Faleide, J. I., Johansen, S. E., & Breivik, a. J. (1998). Late Palaeozoic structural development of the South-western Barents Sea. *Marine and Petroleum Geology*, *15*(1), 73–102. https://doi.org/10.1016/S0264-8172(97)00048-2

Guzzetta, G., & Cinquegrana, R. E. (1987). "Fluid tectonics": a little appreciated facet of buoyancy tectonics. *Tectonophysics*, *139*, 321–324. https://doi.org/10.1016/0040-1951(87)90106-5

Harrington, P. K. (1985). Formation of Pockmarks by Pore-Water Escape. *Geo-Marine Letters*, *5*, 193–197. Retrieved from https://link.springer.com/content/pdf/10.1007%2FBF02281638.pdf

Harris, N. B. (2015). Shale Velocity and Density as Functions of TOC and Thermal Maturity: Upper Devonian Woodford Shale, Permian Basin, Texas*. Retrieved from http://www.searchanddiscovery.com/pdfz/documents/2015/51124harris/ndx_harris.pdf.html

Henriksen, E., Hals, T. ., Heide, T., Kiryukhina, T., Larssen, G. B., Ryseth, A. E., … Exploration, S. (2011a). Chapter 17 Uplift and erosion of the greater Barents Sea: impact on prospectivity and petroleum systems, (2004), 271–281. https://doi.org/10.1144/M35.17

Henriksen, E., Ryseth, A. E., Larssen, G. B., Heide, T., Ronning, K., Sollid, K., & Stoupakova, A. V. (2011b). Chapter 10 Tectonostratigraphy of the greater Barents Sea: implications for petroleum systems. *Geological Society, London, Memoirs*, *35*(1), 163–195. https://doi.org/10.1144/M35.10

Hindle, A. D. (1997). Petroleum migration pathways and charge concentration: a three-dimensional model. *American Association of Petroleum Geologists Bulletin*. https://doi.org/10.1306/3B05BB1E-172A-11D7-8645000102C1865D

Hogan, K. A., Dowdeswell, J. A., & Noormets, R. (2016). Assemblages of submarine landforms in the glacial troughs of the northern Barents Sea, east of Svalbard. *Geological Society, London, Memoirs*. https://doi.org/10.1144/m46.170

Holbrook, W. S., Paull, C. K., & Dillon, P. W. (2001). Seismic studies of the blake ridge: Implications for hydrate distribution, methane expulsion, and free gas dynamics, *124*, 235–256. https://doi.org/10.1029/GM124p0235

Hovland, M. (1982). A coast-parallel depression, possibly caused by gas migration, off western Norway. *Marine Geology*, *50*(1–2). https://doi.org/10.1016/0025-3227(82)90055-X

Hovland, M., Svensen, H., Forsberg, C. F., Johansen, H., Fichler, C., Fosså, J. H., … Rueslåtten, H. (2005). Complex pockmarks with carbonate-ridges off mid-Norway: Products of sediment degassing. *Marine Geology*, *218*(1–4), 191–206. https://doi.org/10.1016/j.margeo.2005.04.005

Ingólfsson, ólafur, & Landvik, J. Y. (2013). The Svalbard-Barents Sea ice-sheet-Historical, current and future perspectives. *Quaternary Science Reviews*, *64*, 33–60. https://doi.org/10.1016/j.quascirev.2012.11.034

Jansson, P. (2018). *Methane bubbles in the Arctic Ocean*. University of Tromsø. Retrieved from https://munin.uit.no/bitstream/handle/10037/14485/thesis.pdf?sequence=5&isAllowed=y

Judd, A. G., Hovland, M., Dimitrov, L. I., García Gil, S., & Jukes, V. (2002). The geological methane budget at continental margins and its influence on climate change. *Geofluids*, *2*(2), 109–126. https://doi.org/10.1046/j.1468-8123.2002.00027.x

Judd, A., & Hovland, M. (2009). *Seabed fluid flow - impact on geology, biology and the marine environment.* Cambridge University Press.

Kairanov, B., Escalona, A., Mordasova, A., Śliwińska, K., & Suslova, A. (2018). Lower Cretaceous tectonostratigraphic evolution of the northcentral Barents Sea. *Journal of Geodynamics*, *119*(March 2017), 183–198. https://doi.org/10.1016/j.jog.2018.02.009

Kannberg, P. K., Tréhu, A. M., Pierce, S. D., Paull, C. K., & Caress, D. W. (2013). Temporal variation of methane flares in the ocean above Hydrate Ridge, Oregon. *Earth and Planetary Science Letters*, *368*, 33–42. https://doi.org/10.1016/j.epsl.2013.02.030

Kauffman, E. G., Arthur, M. A., Howe, B., & Scholle, P. A. (1996). Widespread venting of methane-rich fluids in Late Cretaceous (Campanian) submarine springs (Tepee Buttes), Western Interior seaway, U.S.A. *Geology*, *24*(9), 799–802. https://doi.org/10.1130/0091-7613(1996)024<0799:WVOMRF>2.3.CO;2

Kearery, P., Brooks, M., & Ian, H. (2002). *An Introduction to Geophysical Exploration*. *Eos, Transactions American Geophysical Union* (Third). London: Blackwell science. https://doi.org/10.1029/EO067i011p00132-01

King, L. H., & Maclean, B. (1970). Pockmarks on the Scotian Shelf. *Geological Society of America Bulletin*, *81*, 3141–3148. Retrieved from https://pubs.geoscienceworld.org/gsa/gsabulletin/article/81/10/3141/6732/pockmarks-on-the-scotian-shelf

Klausen, T. G., & Mørk, A. (2014). The Upper Triassic paralic deposits of the De Geerdalen Formation on Hopen: Outcrop analog to the subsurface Snadd Formation in the Barents Sea. *AAPG Bulletin*, *98*(10), 1911–1942. https://doi.org/10.1306/02191413064

Klausen, T. G., Ryseth, A. E., Helland-Hansen, W., Gawthorpe, R., & Laursen, I. (2015). Regional development and sequence stratigraphy of the Middle to Late Triassic Snadd Formation, Norwegian Barents Sea. *Marine and Petroleum Geology*, *62*(APRIL 2015), 102–122. https://doi.org/10.1016/j.marpetgeo.2015.02.004

Klitzke, P., Cacace, M., Jacquey, A. B., Schicks, J. M., Luzi-Helbing, M., Sippel, J., … Faleide, J. I. (2016). Gas Hydrate Stability Zone of the Barents Sea and Kara Sea Region. *Energy Procedia*, *97*, 302–309. https://doi.org/10.1016/j.egypro.2016.10.005

Klitzke, P., Franke, D., Ehrhardt, A., Lutz, R., Reinhardt, L., Heyde, I., & Faleide, J. I. (2019). The Paleozoic Evolution of the Olga Basin Region, Northern Barents Sea: A Link to the Timanian Orogeny. *Geochemistry, Geophysics, Geosystems*. https://doi.org/10.1029/2018GC007814

Knies, J., Matthiessen, J., Vogt, C., Laberg, J. S., Hjelstuen, B. O., Smelror, M., … Vorren, T. O. (2009). The Plio-Pleistocene glaciation of the Barents Sea-Svalbard region: a new model based on revised chronostratigraphy. *Quaternary Science Reviews*, *28*(9–10), 812–829. https://doi.org/10.1016/j.quascirev.2008.12.002

Koevoets, M. J., Hammer, Ø., Olaussen, S., Senger, K., & Smelror, M. (2018). Integrating subsurface and outcrop data of the Middle Jurassic to Lower Cretaceous Agardhfjellet Formation in central Spitsbergen, *98*(4), 1–34. Retrieved from https://njg.geologi.no/images/NJG_articles/NJG_Vol98_Nr4_Art1_Koevoets.pdf

Krajewski, K. P. (2008). The Botneheia Formation (Middle Triassic) in Edgeøya and Barentsøya, Svalbard: lithostratigraphy, facies, phosphogenesis, paleoenvironment. *Polish Polar Research*. Retrieved from https://www.researchgate.net/publication/237473434_The_Botneheia_Formation_Middle_Triassic_in_Edgeoya_and_Barentsoya_Svalbard_lithostratigraphy_facies_phosphogenesis_paleoenvironment

Ktenas, D., Meisingset, I., Henriksen, E., & Nielsen, J. K. (2018). Estimation of net apparent erosion in the SW Barents Sea by applying velocity inversion analysis. *Petroleum Geoscience*, petgeo2018-002. https://doi.org/10.1144/petgeo2018-002

Ligtenberg, H., & Connolly, D. (2003). Chimney detection and interpretation, revealing sealing quality of faults, geohazards, charge of and leakage from reservoirs. *Journal of Geochemical Exploration*, *78–79*, 385–387. https://doi.org/10.1016/S0375-6742

Ligtenberg, J. H. (2005). Detection of Fluid migration pathways in seismic data: Implications for fault seal analysis. *Basin Research*. https://doi.org/10.1111/j.1365-2117.2005.00258.x

Løseth, H., Gading, M., & Wensaas, L. (2009). Hydrocarbon leakage interpreted on seismic data. *Marine and Petroleum Geology*, *26*(7), 1304–1319. https://doi.org/10.1016/j.marpetgeo.2008.09.008

Løseth, H., Wensaas, L., Gading, M., Duffaut, K., & Springer, M. (2011). Can hydrocarbon source rocks be identified on seismic data? *Geology*, *39*(12), 1167–1170. https://doi.org/10.1130/G32328.1

Lundschien, B., Høy, T. and Mørk, A. (2014). Triassic hydrocarbon potential in the northern Barents Sea; integrating Svalbard and stratigraphic core data. *Norwegian Petroleum Directorate Bulletin*, *11*(11), 3–20.

Magoon, L. B., & Dow, W. G. (1994). The Petroleum System-From Source to Trap. *American Association of Petroleum Geologists*, *60*. https://doi.org/10.1306/M60585

Mareano. (2017). Bathymetric mapping. Retrieved March 16, 2019, from http://www.mareano.no/en/topics/bathymetric_mapping

Marin, D., Escalona, A., Sliwihska, K. K., Nøhr-Hansen, H., & Mordasova, A. (2017). Sequence stratigraphy and lateral variability of Lower Cretaceous clinoforms in the southwestern Barents Sea. *AAPG Bulletin*, *101*(9), 1487–1517. https://doi.org/10.1306/10241616010

Mau, S., Römer, M., Torres, M. E., Bussmann, I., Pape, T., Damm, E., … Bohrmann, G. (2017). Widespread methane seepage along the continental margin off Svalbard-from Bjørnøya to Kongsfjorden. *Scientific Reports*, *7*(February), 1–13. https://doi.org/10.1038/srep42997

Minakov, A., Faleide, J. I., Glebovsky, V. Y., & Mjelde, R. (2012). Structure and evolution of the northern Barents-Kara Sea continental margin from integrated analysis of potential fields, bathymetry and sparse seismic data. *Geophysical Journal International*, *188*(1), 79–102. https://doi.org/10.1111/j.1365-246X.2011.05258.x

Mørk, A., & Elvebakk, G. (1999). Lithological description of subcropping Lower and Middle Triassic rocks from the Svalis Dome, Barents Sea. *Polar Research*, *18*(1), 83–104. https://doi.org/10.1111/j.1751-8369.1999.tb00278.x

Naehr, T. H., Eichhubl, P., Orphan, V. J., Hovland, M., Paull, C. K., Ussler, W., … Greene, H. G. (2007). Authigenic carbonate formation at hydrocarbon seeps in continental margin sediments: A comparative study. *Deep-Sea Research Part II: Topical Studies in Oceanography*, *54*(11–13), 1268–1291. https://doi.org/10.1016/j.dsr2.2007.04.010

Naeth, J., di Primio, R., Horsfield, B., Schaefer, R. G., Shannon, P. M., Bailey, W. R., & Henriet, J. P. (2005). Hydrocarbon seepage and carbonate mound formation: A basin modelling study from the Porcupine Basin (offshore Ireland). *Journal of Petroleum Geology*, *28*(2), 147–166. https://doi.org/10.1111/j.1747-5457.2005.tb00077.x

Nanda, N. C. (2016). *Seismic Data Interpretation and Evaluation for Hydrocarbon Exploration and Production: A Practitioner's Guide.* Springer International. https://doi.org/10.1007/978-3-319-26491-2

Newton, A. M. W., & Huuse, M. (2017). Glacial geomorphology of the central Barents Sea: Implications for the dynamic deglaciation of the Barents Sea Ice Sheet. *Marine Geology*, *387*(March), 114–131. https://doi.org/10.1016/j.margeo.2017.04.001

NPD. (2017). Geological assessment of petroleum resources in eastern parts of Barents Sea north 2017, 40. Retrieved from http://www.npd.no/en/Publications/Reports/Geological-assessment-of-petroleum-resources---Barents-Sea-north-2017/

NPDfactpages. (n.d.). Wellbore 7226/2-1. Retrieved from http://factpages.npd.no/FactPages/Default.aspx?nav1=wellbore&nav2=PageView%7CExploration%7CAll&nav3=5807

Osborne, M. J., & Swarbrick, R. E. (1997). Mechanisms for Generating Overpressure in Sedimentary Basins: A Reevaluation. *AAPG Bulletin*, *81*(6), 1023–1041. Retrieved from http://archives.datapages.com/data/bulletns/1997/06jun/1023/Images/97_1023.PDF

Ostanin, I., Anka, Z., di Primio, R., & Bernal, A. (2012). Identification of a large Upper Cretaceous polygonal fault network in the Hammerfest basin: Implications on the reactivation of regional faulting and gas leakage dynamics, SW Barents Sea. *Marine Geology*, *332–334*, 109–125. https://doi.org/10.1016/j.margeo.2012.03.005

Ostanin, I., Anka, Z., di Primio, R., & Bernal, A. (2013). Hydrocarbon plumbing systems above the Snøhvit gas field: Structural control and implications for thermogenic methane leakage in the Hammerfest Basin, SW Barents Sea. *Marine and Petroleum Geology*, *43*, 127–146. https://doi.org/10.1016/j.marpetgeo.2013.02.012

Paganoni, M., Cartwright, J. A., Foschi, M., Shipp, R. C., & Van Rensbergen, P. (2016). Structure II gas hydrates found below the bottom-simulating reflector. *Geophysical Research Letters*, *43*(11), 5696–5706. https://doi.org/10.1002/2016GL069452

Patton, H., Hall, A. M., Heyman, J., Stroeven, A. P., Shackleton, C., Auriac, A., … Winsborrow, M. (2017). Deglaciation of the Eurasian ice sheet complex. *Quaternary Science Reviews*, *169*, 148–172. https://doi.org/10.1016/j.quascirev.2017.05.019

Plaza-Faverola, A., Vadakkepuliyambatta, S., Hong, W. L., Mienert, J., Bünz, S., Chand, S., & Greinert, J. (2017). Bottom-simulating reflector dynamics at Arctic thermogenic gas provinces: An example from Vestnesa Ridge, offshore west Svalbard. *Journal of Geophysical Research: Solid Earth*, *122*(6), 4089–4105. https://doi.org/10.1002/2016JB013761

Polteau, S., Hendriks, B. W. H., Planke, S., Ganerød, M., Corfu, F., Faleide, J. I., … Myklebust, R. (2016). The Early Cretaceous Barents Sea Sill Complex: Distribution, 40Ar/39Ar geochronology, and implications for carbon gas formation. *Palaeogeography, Palaeoclimatology, Palaeoecology*, *441*, 83–95. https://doi.org/10.1016/j.palaeo.2015.07.007

Portnov, A., Vadakkepuliyambatta, S., Mienert, J., & Hubbard, A. (2016). Ice-sheet-driven methane storage and release in the Arctic. *Nature Communications*, *7*. https://doi.org/10.1038/ncomms10314

Rajan, A., Bünz, S., Mienert, J., & Smith, A. J. (2013). Gas hydrate systems in petroleum provinces of the SW-Barents Sea. *Marine and Petroleum Geology*, *46*, 92–106. https://doi.org/10.1016/j.marpetgeo.2013.06.009

Ramberg, I. B., Bryhni, I., & Nøttvedt, A. (2007). *Landet blir til*. Trondheim: Norsk Geologisk Forening.

Riis, F., Lundschien, B. A., Høy, T., Mørk, A., & Mørk, M. B. E. (2008). Evolution of the Triassic shelf in the northern Barents Sea region. *Polar Research*, *27*(3), 318–338. https://doi.org/10.1111/j.1751-8369.2008.00086.x

Ryseth, A. E. (2014). Sedimentation at the Jurassic-Triassic boundary, south-west Barents Sea: indication of climate change. https://doi.org/10.1002/9781118920435.ch9

Sættem, J. (1990). Glaciotectonic forms and structures on the Norwegian continental shelf: observations, processes and implications. *Norsk Geologisk Tidsskrift*, *70*, 81–94.

Schlumberger. (2011). *Petrel 2010: interpreter's guide to seismic attributes*. Houston.

Selley, R. C., & Sonnenberg, S. A. (2014). *Elements of Petroleum Geology: Third Edition*. *Elements of Petroleum Geology: Third Edition*. https://doi.org/10.1016/C2010-0-67090-8

Serov, P., Vadakkepuliyambatta, S., Mienert, J., Patton, H., Portnov, A., Silyakova, A., … Hubbard, A. (2017). Postglacial response of Arctic Ocean gas hydrates to climatic amelioration. *Proceedings of the National Academy of Sciences*, *114*(24), 6215–6220. https://doi.org/10.1073/pnas.1619288114

Sheriff, R. E. (1985). Seismic Stratigraphy II: An Integrated Approach to Hydrocarbon Exploration (pp. 1–10). Houston: AAPG. Retrieved from http://archives.datapages.com/data/specpubs/seismic1/data/a167/a167/0001/0000/0001.htm

Sloan, D. E., & Koh, C. A. (2008). *Clathrate Hydrates of Natural Gases* (3rd ed.). Boca Raton: CRC Press.

Smelror, M., Petrov, V. O., Larsen, G. B., & Werner, S. (2009). Atlas: Geological History of the Barents Sea Geological History of the Barents Sea, 1–138. Retrieved from http://issuu.com/ngu_/docs/atlas_-_geological_history_of_the_b/1?e=3609664/9026048

Sokolov, S. Y., Moroz, E. A., Abramova, A. S., Zarayskaya, Y. A., & Dobrolubova, K. O. (2017). Mapping of sound scattering objects in the northern part of the Barents Sea and their geological interpretation. *Oceanology*, *57*(4), 593–599. https://doi.org/10.1134/s000143701704018x

Solheim, A., & Elverhøi, A. (1985). A pockmark field in the Central Barents Sea; gas from a petrogenic source? *Polar Research*, *3*(1), 11–19. https://doi.org/10.1111/j.1751-8369.1985.tb00492.x

Steel, R., Gjelberg, J., Helland-Hansen, W., Kleinspehn, K., Nøttvedt, A., & Rye-Larsen, M. (1985). The Tertiary Strike-Slip Basins and orogenic belt of Spitsbergen. *Strike-Slip Deformation, Basin Formation, and Sedimentation*, (January), 339–359. https://doi.org/10.2110/pec.85.37.0339

Svendsen, J. I., Alexanderson, H., Astakhov, V. I., Demidov, I., Dowdeswell, J. A., Funder, S., … Stein, R. (2004b). Late Quaternary ice sheet history of northern Eurasia. *Quaternary Science Reviews*, *23*(11–13), 1229–1271. https://doi.org/10.1016/j.quascirev.2003.12.008

Svendsen, J. I., Mangerud, J., Polyak, L., & Gatullin, V. (2004a). The glacial history of the Barents and Kara Sea Region. *Quaternary Glaciations- Extent and Chronology. Vol 1: Europe*, 369–378. Retrieved from https://folk.uib.no/ngljm/PDF_files/Svendsen-2003-in-Ehlers.pdf

Tasianas, A., Martens, I., Bünz, S., & Mienert, J. (2016). Mechanisms initiating fluid migration at Snøhvit and Albatross fields, Barents Sea. *Arktos*, *2*(1). https://doi.org/10.1007/s41063-016-0026-z

Thrasher, J., Fleet, A. J., Hay, S. J., Hovland, M., & Dueppenbecker, S. (1996). Understanding geology as the key to using seepage in exploration: the spectrum of seepage styles. *Hydrocarbon Migration and Its Near-Surface Expression*.

Twiss, R. J., & Moores, E. M. (2007). *Structural Geology*. New York: W, H. Freeman Co.

Vadakkepuliyambatta, S., Bünz, S., Mienert, J., & Chand, S. (2013). Distribution of subsurface fl uid- fl ow systems in the SW Barents Sea. *Marine and Petroleum Geology*, *43*, 208–221. https://doi.org/10.1016/j.marpetgeo.2013.02.007

Vadakkepuliyambatta, S., Chand, S., & Bünz, S. (2017a). Supporting Information for: The history and future trends of ocean warming-induced gas hydrate dissociation in the SW Barents Sea Sunil. *Geophysical Research Letters Supporting*, 1–14.

Vadakkepuliyambatta, S., Chand, S., & Bünz, S. (2017b). The history and future trends of ocean warming-induced gas hydrate dissociation in the SW Barents Sea. *Geophysical Research Letters*, *44*(2), 835–844. https://doi.org/10.1002/2016GL071841

Van Koeverden, J. H., Karlsen, D. A., & Backer-Owe, K. (2011). carboniferous non-marine source rocks from spitsbergen and bjørnøya: Comparison with the western arctic. *Journal of Petroleum Geology*, *34*(1), 53–66. https://doi.org/10.1111/j.1747-5457.2011.00493.x

Veeken, P. (2007). *Seismic Stratigraphy, Basin Analysis and Reservoir Characterisation*. *Handbook of Geophysical Exploration: Seismic Exploration*. https://doi.org/10.1016/S0950-1401(07)80032-2

Veeken, P. (2013). *Seismic Stratigraphy and Depositional Facies Models*. *Seismic Stratigraphy and Depositional Facies Models*. https://doi.org/10.1016/C2013-0-12810-3

Vigran, J. O., Mangerud, G., Mørk, A., Worsley, D., & Hochuli, P. A. (2014). *Palynology and geology of the Triassic succession of Svalbard and the Barents Sea*. *Geological Survey of Norway Special Publication* (Vol. 14). Geological Survey of Norway. Retrieved from https://www.ngu.no/upload/Publikasjoner/Special publication/SP14.pdf

Waage, M., Portnov, A., Serov, P., Bünz, S., Waghorn, K. A., Vadakkepuliyambatta, S., … Andreassen, K. (2019). Geological Controls on Fluid Flow and Gas Hydrate Pingo Development on the Barents Sea Margin. *Geochemistry, Geophysics, Geosystems*, 630–650. https://doi.org/10.1029/2018GC007930

Wallmann, K., Riedel, M., Hong, W. L., Patton, H., Hubbard, A., Pape, T., … Bohrmann, G. (2018). Gas hydrate dissociation off Svalbard induced by isostatic rebound rather than global warming. *Nature Communications*, *9*(1). https://doi.org/10.1038/s41467-017-02550-9

Weniger, P., Blumenberg, M., Berglar, K., Ehrhardt, A., Klitzke, P., Krüger, M., & Lutz, R. (2019). Origin of near-surface hydrocarbon gases bound in northern Barents Sea sediments. *Marine and Petroleum Geology*, *102*(November 2018), 455–476. https://doi.org/10.1016/j.marpetgeo.2018.12.036

Winsborrow, M., Andreassen, K., Hubbard, A., Plaza-Faverola, A., Gudlaugsson, E., & Patton, H. (2016). Regulation of ice stream flow through subglacial formation of gas hydrates. *Nature Geoscience*, *9*(5), 370–374. https://doi.org/10.1038/ngeo2696

Worsley, D. (2008). The post-Caledonian development of Svalbard and the western Barents Sea. *Polar Research*, *27*(3), 298–317. https://doi.org/10.1111/j.1751-8369.2008.00085.x

Zhou, H.-W. (2014). *Practical Seismic Data Analysis*. New York: Cambridge University Press.

Appendix

8.1 A)

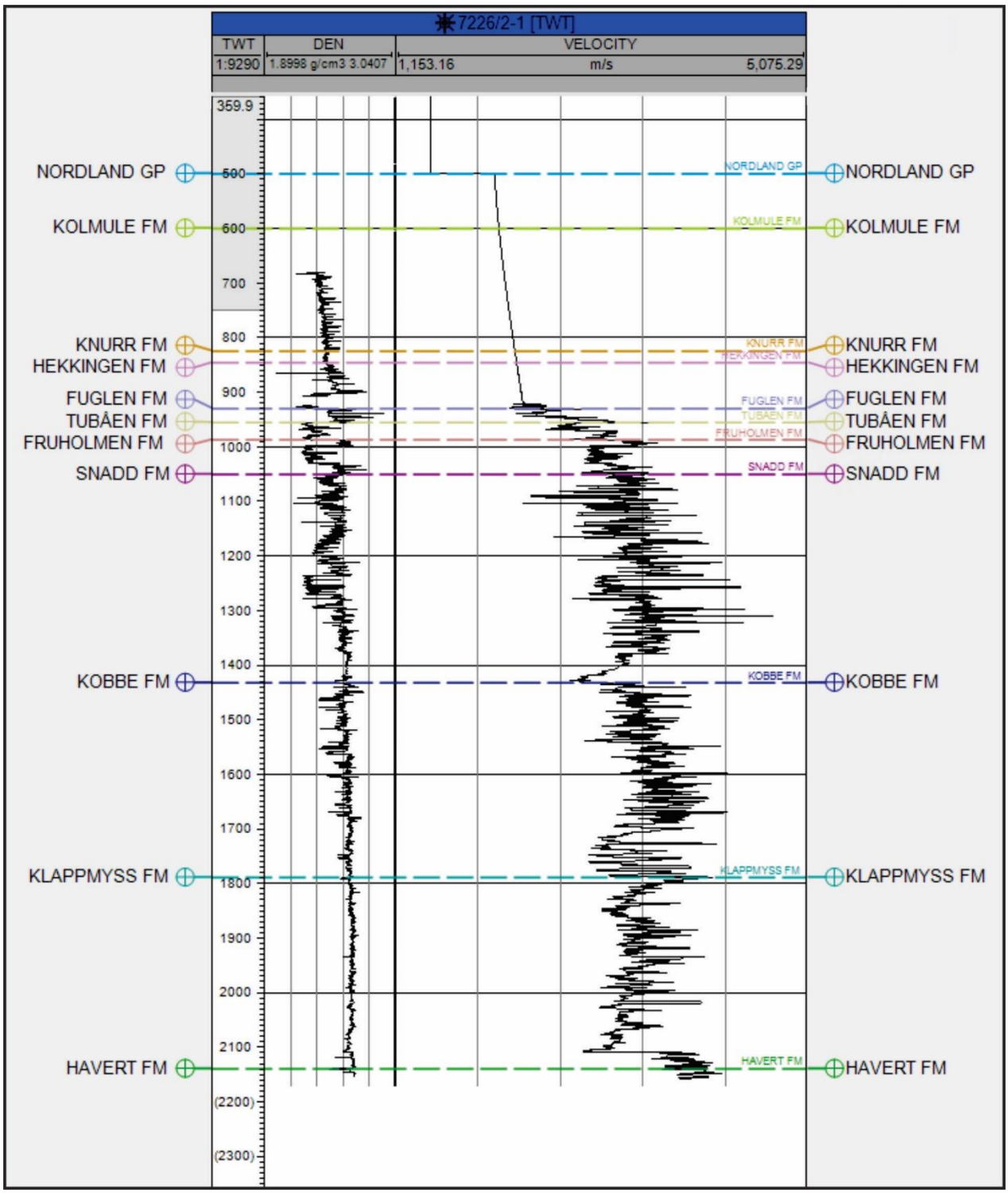

Fig.9.1: Sonic log illustrating the velocity of the formations located at the Bjarmeland Platform (Well 7226/2-1) used to correlate interval velocities for formations in the northern Barents Sea.

8.2 B)

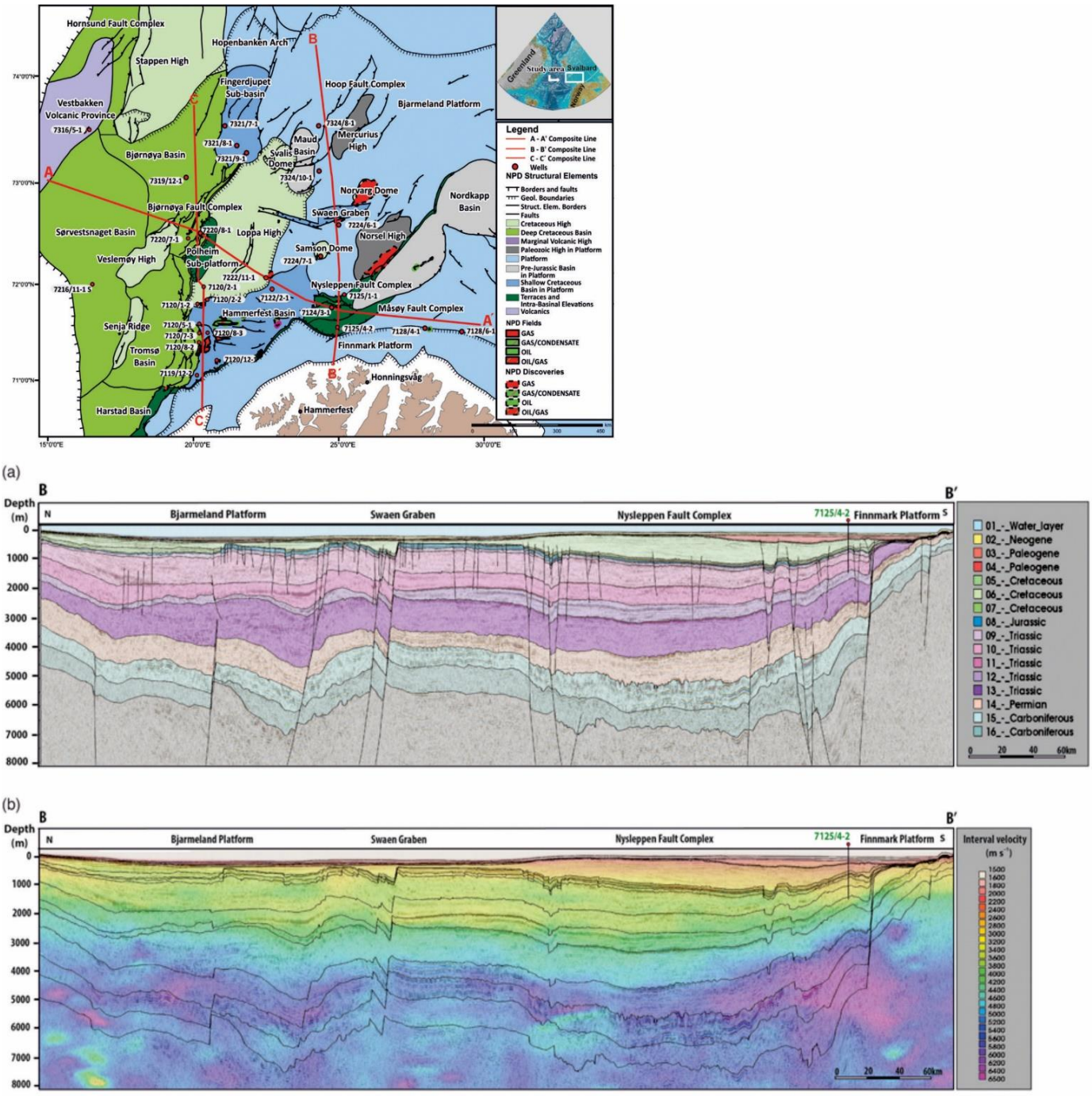

Fig.9.2: Interval velocities at the Bjarmeland Platform from (Ktenas et al., 2018).

8.3 C)

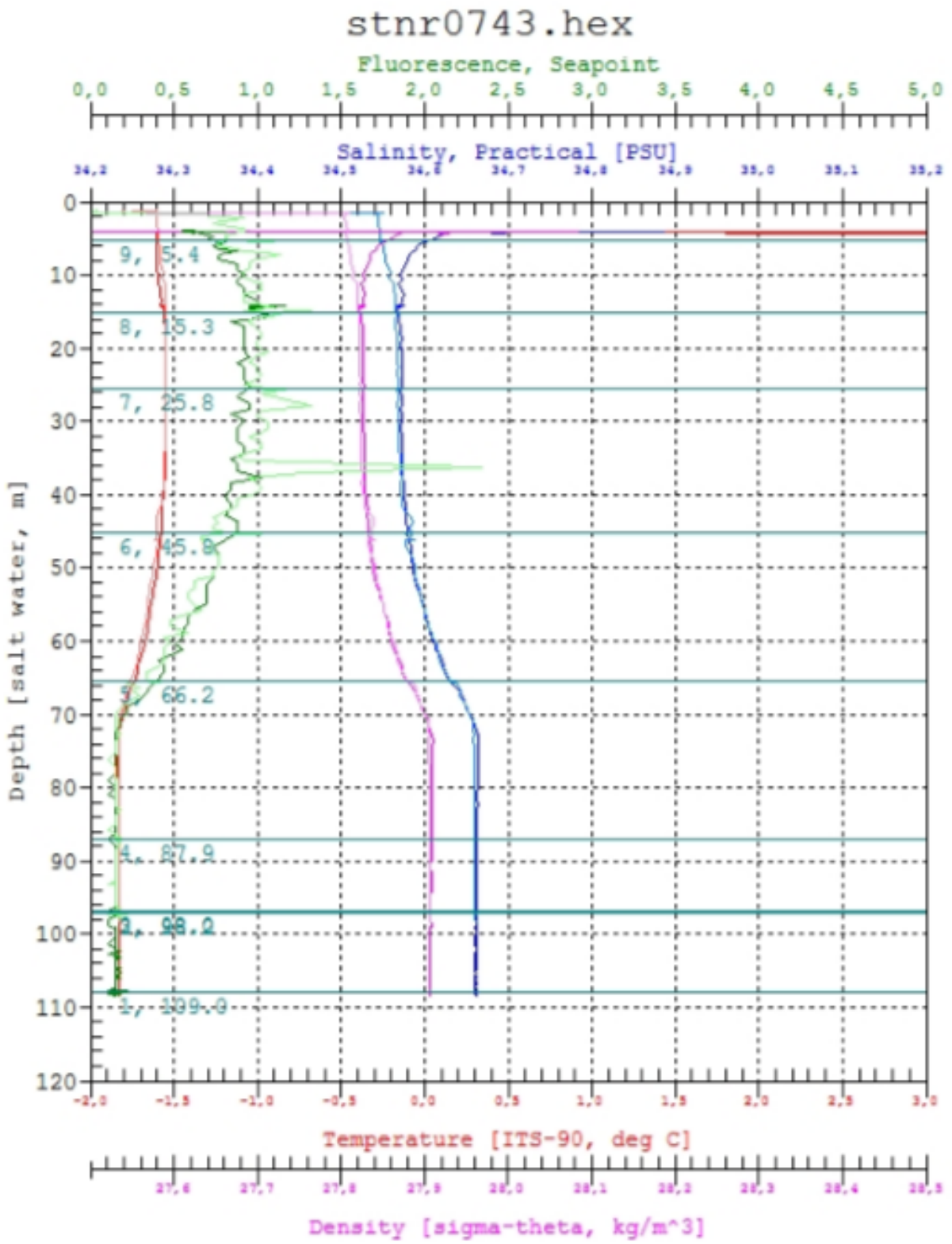

Fig.9.3: CTD profile from Storbanken high at 77,0013º N, 34,9604º E, used for GHSZ modeling.

8.4 D)

Table 9.1: Overview of the craters and mounds features identified in the study area. The features are divided into four categories: craters, craters with an associated mound and single mounds. C= craters, CM= craters and mound, and M= single mound.

Feature	**Long axis (m)**	**Short axis (m)**	**Short - long axis ratio**	**Seafloor depth (m)**	**Crater depth and (Mound height) (m)**
C1	130	95	0,70	175	10
C2	85	60	0,71	165	5
C3	450	400	0,88	162	10
C4	280	220	0,79	157	7
C5	320	120	0,38	163	5
C6	260	250	0,96	162	10
C7	250	250	1	167	6
C8	300	240	0,8	162	9
C9	360	240	0,66	167	13
C10	340	250	0,74	163	10
C11	260	240	0,92	161	11
C12	280	160	0,57	171	7
C13	260	200	0,77	167	6
C14	320	300	0,94	176	10
C15	525	320	0,61	176	16
C16	180	140	0,77	184	8
C17	550	240	0,44	181	7
C18	310	280	0,9	172	14
C19	360	270	0,75	174	12
C20	500	310	0,62	182	16
C21	490	325	0,66	185	13
C22	390	280	0,72	185	12
C23	500	325	0,65	180	14
C24	450	390	0,87	189	13
C25	475	320	0,67	193	13
C26	410	300	0,73	202	14
C27	650	220	0,33	171	9
C28	580	240	0,41	167	7

C29	390	240	0,62	169	16
C30	285	120	0,42	166	9
C31	420	210	0,5	183	14
C32	310	150	0,48	174	5
C33	320	290	0,9	168	10
C34	320	240	0,75	166	14
C35	250	110	0,44	170	6
CM1	380	220	0,57	168	10 (8)
CM2	450	380	0,84	162	8 (7)
CM3	400	200	0,5	160	8 (6)
CM4	430	170	0,4	170	9 (7)
CM5	500	150	0,3	173	10 (10)
CM6	725	300	0,41	187	13 (13)
CM7	800	650	0,81	180	20 (inside crater)
CM8	275	210	0,76	170	17 (17)
CM9	400	240	0,6	192	12 (12)
CM10	785	550	0,7	183	19 (inside crater)
CM11	780	470	0,6	186	10 (inside crater)
CM12	890	500	0,56	173	17 (13)
CM13	460	290	0,63	167	8 (11)
CM14	475	270	0,57	167	7 (6)
CM15	260	180	0,69	181	11 (9)
CM16	360	230	0,64	178	15 (9)
CM17	780	490	0,63	178	22 (21)
CM18	800	340	0,43	165	13 (12)
CM19	825	320	0,39	166	14 (12)
CM20	525	480	0,91	176	9 (8)
CM21	625	400	0,64	165	7 (Inside crater)
M1	400	260	0,65	168	(12)
M2	920	600	0,65	163	(30)

8.5 E)

Table 9.2: Name of the seismic lines used in this thesis for further research in the study area.

Figure	**Name of Seismic line**
Fig.5.2	NPD-STOB-91.MIG_FIN.3415-91.-58.10707.POST_STACK.2D.JS-019019
Fig.5.3	NPD-STOB-91.MIG_FIN.3415-91.-58.10707.POST_STACK.2D.JS-019019
Fig.5.4	NPD-STOB-93.MIG_FIN.SB-7655-93.-58.8168.POST_STACK.2D.JS-019019
Fig.5.10a	NPD-STOB-93.MIG_FIN.SB-7655-93.-58.8168.POST_STACK.2D.JS-019019
Fig.5.10b	NPD-STOB-93.MIG_FIN.SB-7715-93.-58.7968.POST_STACK.2D.JS-019019
Fig.5.11a	Cage18_1_2D_20
Fig.5.11b	Cage18_1_2D_22
Fig.5.12a	Cage18_1_2D_6
Fig.5.12b	Cage18_1_2D_5
Fig.5.13	NPD-STOB-89.MIG_FIN.0000003030-89.7203.16461.POST_STACK.2D.JS-019019
Fig.5.14	Cage18_1_2D_1
Fig.5.15	NPD-STOB-89.MIG_FIN.000SB-4-89-A1.-46.8600.POST_STACK.2D.JS-019019
Fig.5.16	Cage18_1_2D_16
Fig.5.21	Cage18_1_2D_12
Fig.5.22	Cage18_1_2D_18
Fig.5.23	Cage18_1_2D_15
Fig.5.23	Cage18_1_2D_16
Fig.5.24	Cage18_1_2D_19
Fig.5.26a	NPD-STOB-89.MIG_FIN.0000003030-89.7203.16461.POST_STACK.2D.JS-019019
Fig.5.26b	NPD-BA-88-GSI.MIG_FIN.00003130-88.-46.12745.POST_STACK.2D.JS-019019
Fig.5.26c	NPD-STOB-89.MIG_FIN.0000003230-89.-46.9870.POST_STACK.2D.JS-019019
Fig.5.26d	NPD-STOB-93.MIG_FIN.SB-7645-93.-58.9550.POST_STACK.2D.JS-019019
Fig.5.26e	NPD-BA-88-GSI.MIG_FIN.00003330-88.10913.17985.POST_STACK.2D.JS-019019
Fig.5.27	NPD-STOB-89.MIG_FIN.0000SB-2-89-A.7950.12098.POST_STACK.2D.JS-019019 - 2

Fig.5.28	NPD-STOB-89.MIG_FIN.000SB-4-89-A2.8549.10854.POST_STACK.2D.JS-019019
Fig.5.29	NPD-STOB-89.MIG_FIN.000SB-4-89-A1.-46.8600.POST_STACK.2D.JS-019019
Fig.5.30	Cage18_1_2D_11
Fig.6.3a	Cage18_1_2D_16
Fig.6.3b	Cage18_1_2D_1
Fig.6.3c	Cage18_1_2D_5
Fig.6.3d	Cage18_1_2D_20
Fig.6.5a	Cage18_1_2D_22
Fig.6.5b	Cage18_1_2D_20
Fig.6.5c	Cage18_1_2D_5
Fig.6.5d	Cage18_1_2D_7
Fig.6.5e	NPD-BA-88-GSI.MIG_FIN.00007650-88.114.12992.POST_STACK.2D.JS-019019
Fig.6.5f	NPD-STOB-89.MIG_FIN.000SB-3-89-A2.9900.13521.POST_STACK.2D.JS-019019 - 2
Fig.6.5g	NPD-STOB-93.MIG_FIN.SB-3345-93.-58.7149.POST_STACK.2D.JS-019019
Fig.6.5h	Cage18_1_2D_23
Fig.6.7a	Cage18_1_2D_25
Fig.6.7b	Cage18_1_2D_11
Fig.6.7c	Cage18_1_2D_17
Fig.6.7d	Cage18_1_2D_8
Fig.6.7e	Cage18_1_2D_12
Fig.6.7f	Cage18_1_2D_13